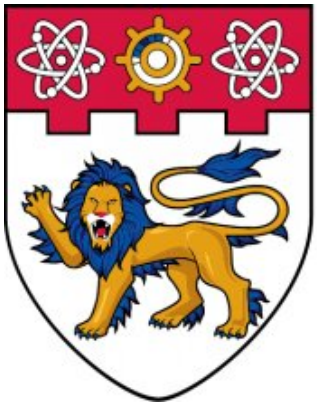

NANYANG TECHNOLOGICAL UNIVERSITY
SINGAPORE

Quantum Photonic Computer and Its Algorithms

Wan Lingxiao

Quantum Science and Engineering Center (QSec)

School of Electrical and Electronic Engineering

A thesis submitted to the Nanyang Technological University in partial fulfillment of the requirement for the degree of Doctor of Philosophy

2021

STATEMENT OF ORIGINALITY

I hereby certify that the work embodied in this thesis is the result of original research, is free of plagiarised materials, and has not been submitted for a higher degree to any other University or Institution.

Jan-03-2022 | Wan Lingxiao

Date | Wan Lingxiao

SUPERVISOR DECLARATION STATEMENT

I have reviewed the content and presentation style of this thesis and declare it is free of plagiarism and of sufficient grammatical clarity to be examined. To the best of my knowledge, the research and writing are those of the candidate except as acknowledged in the Author Attribution Statement. I confirm that the investigations were conducted in accord with the ethics policies and integrity standards of Nanyang Technological University and that the research data are presented honestly and without prejudice.

Jan-03-2022

Date

Professor Liu Ai Qun

AUTHORSHIP ATTRIBUTION STATEMENT

This thesis does not contain any materials from papers published in peer-reviewed journals or from papers accepted at conferences in which I am listed as an author.

Jan-03-2022 

Date Wan Lingxiao

ACKNOWLEDGEMENT

First and foremost, I would like to express the deepest gratitude to my Supervisors, Professor Kwek Leong Chuan and Professor Liu Ai Qun. Professor Liu is the person who leads me to the world of science and provide me unlimited support for pursuing the wonderful research at NTU. Whenever I have any question regarding either my life or research, he is always there to give me support and inspirations.

I would like to thank Kwek Leong Chuan for his selfless guidance of our research. He has no doubt provided me with]the foundation to the quantum optics and physics, in general. He sacrifices most of his Saturday time over the past five years to teach us from the basic concept of quantum mechanics to cutting-edge science in the forefront of publications. He shows great patience in this teaching and I cannot recall how many times he has repeated some of the simplest idea like creation/annihilation operator, coherent state, interference to us so that we get the concepts ingrained in our minds.

I would like to thank Dr Stefano Paesani from University of Bristol. Without him, all those fabulous theories are just equations on paper. Stefano helps me to connect them to experiments in the lab such as the multi-photon interference pattern, the quantum state tomography, the quantum operator expectation value and so on. Starting from scratch, he tells me every detail in the quantum experiments and help me to solve various

seemingly unwieldy problem encountered. The countless email exchanges and online meetings between us provide ample evidence on what I say.

I would like to thank Dr Huang Jianguo, Dr Zhang Gong, Dr Yan Libin, the seniors in our lab and the pioneer generation of quantum experimentalists. I admire their courage to devote themselves to a totally unknown research field. They also help me adopt to the life in Singapore quickly by organizing wonderful activities at weekends.

I would like to thank Zhang Hui. She is the PhD admitted to our group at the same time with me. She is very smart and hardworking and she is able to read many papers and absorb their concepts quickly. She is able to suggest many clever and ingenious ideas and she has given me much inspiration. Our cooperation in experiment is a pleasant journey. I would like to thank Dr Feng Lantian and Dr Zhang Chao from University of Science and Technology of China. They visited us and built up the single photon light source. I have learnt a lot about quantum circuit design from them. They gave me a deeper understanding of the nature of quantum entanglement and etc. I would like to thank Dr Cai Hong, researcher from Institute of Microelectronics and former PhD from our group. She is an expert in silicon photonics fabrication and she has provided many guidance and help for us in chip design, fabrication and package. I would like to thank Dr Zou Jun and Zhu Huihui. They have helped me a lot in silicon photonic structure design process to realize various functions for quantum state manipulation on chip. I would thank many other professors or research fellows: Professor Man Hong-Yun from Southern University of Science and Technology, Zhou Xiaoqi from Sun Yat-sen University, Jin Xianmin from Shanghai Jiaotong University, Su Xiaolong from Shanxi University, Raffaele Santagati from University of Bristol.

I would also like to thank all other current and previous group members for their

help at some parts of my PhD journey. They are Mr Cao Lin, Dr Luo Wei, Mr Li Zhenyu, Dr Shi Yuzhi, Dr Xiong Sha, Dr Chen Yanyu, Dr Wang Xuyang, Dr Wang Xuyang, Dr Su Ping, Dr Feng Shilun, Dr Cao Gaozhe, Dr Wang Bo, Dr Li Sijin, Dr Li Yuan, Mr Lin Hexiang, Mr Ng Siqi and Dr Li Shuyi.

I would thank all the technicians in Valens and QSec lab and the in-house engineers for lending me help in the equipment and for their technical support and resources. I would like to thank Nanyang Technological University for providing me such an excellent platform to conduct study and research.

Finally, I would like to have my gratitude to my family and friends for their support of my PhD life. Their encouragement will always give me power to continue my way on the tough journey of research life. To my girlfriend, Deng Han, I must say that you are my love and I thank you all this while for your company. You have been my strongest mental and psychological support in face of difficulties.

Wan Lingxiao

Contents

Summary

Quantum information has been emerging as a fast-developing subject in recent years. It has shown the potential in bringing revolution to science and technology progress such as absolutely secured encryption for communication, highly accurate and efficient simulation of practical physical system, more compact and faster machine learning models for prediction and advanced quantum computational performance to solve intractable problems for classical supercomputer. These supremacies are all relying on the superposition and entanglement properties of the qubits. Among many candidates like superconducting qubits or trapped ions to realize quantum technologies, photon has demonstrated its prominent advantages for its robustness against decoherence and noise, high clock cycle rate, fast and easy measurement, room temperature working environment, support for quantum network and so on. This thesis mainly focuses on the photonic integrated quantum technologies to produce and manipulate photons on an integrated silicon chip and characterizes its performance along with the demonstration of some quantum computing algorithms.

The thesis first study the design and fabrication of a photonic integrated circuit with spiral waveguides to generate photons on chip and a linear optical circuit to perform unitary operations on the photonic quantum states. The photon is generated via the spon-

taneous four wave mixing process by pumping the waveguide with pulsed laser. The photon source properties of purity, indistinguishability, joint spectra intensity, squeezing parameter and so on are characterised carefully to prove that the on chip photon generation can function as a good resource for quantum computation. Furthermore, the linear optical circuit is calibrated to realize an arbitrary unitary matrix for quantum state manipulation and the photon distribution is measured after it. This can be seen as the basic model of boson sampling experiment and by designing the linear optical circuit, this distribution can be mapped to some practical physical systems so that the photonic quantum circuit can function as a quantum analogue computer for simulation. A Gaussian boson sampling experiment was performed to simulate the graph perfect matching problem is demonstrated as an example.

The quantum photonic integrated circuit can be implemented to perform some digital quantum computing algorithm like the error correction encoding scheme. Reducing error rate is a critical problem for large scale computing in either classical or quantum computing. In this thesis, an error correction scheme is demonstrated to protect single logical qubit with 4 physical photonic qubits and it has been proved experimentally that the quantum information can be retrieved from the state with a single qubit loss or error. This encoding can be used to identify the error type as well by measuring the expectation value of stabilizers for the quantum state to distinguish X, Y, Z errors. Finally, this scheme is applied to realize an error-corrected quantum teleportation that the failed projective measurement or quantum entanglement for teleportation can be recovered under proposed encoding scheme without losing the quantum information. This proof of principle demonstration of quantum error correction code would pave the way for universal quantum error correction scheme on computation process.

The last task implemented on the integrated photonic circuit platform is chip to chip quantum teleportation with auto encoder. This can be seen as a prototype of quantum network model for direct quantum information sharing and encoder for quantum information compression. First, the teleportation between two integrated photonic chips connected with fibre to transport a photonic qubit is realized. Qubit states in different basis are transported to measure its fidelity at the receiving chip and this proves the feasibility of teleportation process. Then the quantum auto encoding process is applied at transmission chip by tuning the linear optical circuit to compress a 3-dimensional qutrit to a qubit and this qubit is sent to the receiving chip via the teleportation channel. Next, the reverse decoding process recovers this qubit back to qutrit on the receiver chip. This experimental demonstration can help the development of quantum network for sharing higher volume of quantum information with auto encoder.

The quantum revolution has started and the possibility to manipulate the quantum information and bring new technology to society is the target of quantum development. Compatible with the state of the art silicon fabrication technology, the photonic platform possesses the potential of scalability and integration for quantum chip. This thesis focuses on the integrated photonic quantum circuit and its application on quantum computing and wished to bring more motivation for future development of quantum technologies.

List of Figures

List of Tables

Nomenclature

BBO Barium Borate

BS Beam Splitter

CNOT Controlled Not

CV Continuous Variable

CZ Controlled Z

DAC Digital-to-Analog Converter

DC Directional Coupler

DV Discrete Variable

EDFA Erbium-Doped Fiber Amplifier

FPGA Field-programmable gate array

FSR Free Spectra Range

FWHM Full Width at Half Maximum

GBS Gaussian Boson Sampling

GHZ Greenberger–Horne–Zeilinger

HOM Hong-Ou-Mandel

HSPS Heralded Single Photon Source

ITU International Telecommunication Union

JSA Joint Spectra Amplitude

JSI Joint Spectra Intensity

LOQC Linear Optical Quantum Computing

MMI Multi-Mode Interferometer

MZI Mach-Zehnder Interferometer

NISQ Noisy Intermediate-Scale Quantum

OSA Optical Spectrum Analyzer

PBS Polarization Beam Splitter

PC Polarization Controller

PCB Printed circuit board

PD Photodiode

PRS Polarization Rotator and Splitter

PS Phase Shifter

QAOA Quantum Approximate Optimization Algorithm

QD Quantum Dot

QKD Quantum Key Distribution

QML Quantum Machine Learning

QST Quantum State Tomography

SFWM Spontaneous Four Wave Mixing

SMF Single Mode Fiber

SMS Single Mode Squeeze

SOI Silicon-on-Insulator

SPDC Spontaneous Parametric Down Conversion

SVD Singular Value Decomposition

TE Transverse Electric

TEC Thermoelectric Cooler

TM Transverse Magnitude

TMS Two Mode Squeeze

WDM Wavelength-division Multiplexer

Chapter 1

Introduction

1.1 Motivation

This thesis focuses principally on photonic integrated quantum computation: Gaussian boson sampling for perfect matching, quantum error correction and quantum teleportation with autoencoder. All schemes have for first time been demonstrated on the integrated photonic platform.

Since rise of quantum mechanic over a hundred years ago, this subject has gone through rapid developments that entirely reshaped humanity's perspective towards fundamental research in the world. It has potentially given rise to many changes in the current modern technologies such as the quantum chemistry analysis, light-emitting diodes, nuclear magnetic resonance imaging for medical diagnose, electron microscopy for research and quantum key distribution for security communication.

Nowadays, quantum science is bringing a revolution to the field of classical information theory, creating a new concept of quantum information theory and computa-

tion. Two of the main ideas are the Shor's algorithm for number factorization [10] in 1994 and the Grover algorithm for database search [11] in 1996. Shor's algorithm is a quantum algorithm that shows how a quantum computer can factorize an n-bit long integer with polynomial time scale of $O(n^3)$ even though a classical algorithm would take $e^{O(n^{1/3})}$, providing a complexity speed-up of $O(n^2 log(n))$. This problem is critical as prime number factorization forms the basis of Rivest-Shamir-Adleman (RSA) encryption method for modern computer communication. RSA is widely used as an encryption protocol to protect most information transmitted over the internet nowadays [12]. With Shor's algorithm, many encryption schemes are no longer safe, especially if a quantum computer can be implemented realistically. Grover's algorithm is an algorithm that searches a particular value in database of size n with $O(\sqrt{n})$ evaluations while the classical counterpart requires $O(n)$ evaluations. Even though the complexity class remains polynomial, yet with larger and larger database, one expects a significant improvement in speed based on the quantum algorithm. These two algorithms are just two typical examples that show the power of quantum computer and algorithms.

To harness the computation power of quantum mechanics, many schemes have been proposed like the superconducting, trapped ion and diamonds. Various organizations in the industry are involved in the search for quantum computer: such as Google, Intel, Microsoft, IBM from Industry and USTC, NUS, MIT from University. Among the numerous technologies, quantum photonics is one of the promising platforms that may achieve quantum computing. The photon has the main advantage of robustness against decoherence and environmental noise. The ease of manipulation comparing with other matter qubits is another important feature. A quantum system requires the generation, manipulation and measurement of quantum state and it can be all done on

the linear optics platform which nowadays can be miniaturized on integrated photonic system. The photon as the carrier of quantum information has been successfully generated on chip via both spontaneous four wave mixing process [8] and quantum dots [13]. The manipulation of photonic qubits can be done with the aid of linear optical circuit with post processing technique currently [14]. The detection of photon on photonic integrated circuit with a high efficiency has also been reported [15]. Thus, a highly integrated photonic platform for computing is feasible with current technologies and it further scales up to achieve a quantum advantage compared to classical computational techniques.

In the process of scaling up a quantum system to more qubits for solving practical realistic problem, the accurate control of quantum state has become more and more critical as the errors can accumulate. Moreover, quantum information itself is also very fragile: on the one hand, individual subsystems need to interact sufficiently strongly to perform computations, and on the other hand, each subsystems should be adequately insulated from its environment [16] to avoid decoherence. Yet, the discovery of quantum error-correcting codes [17–20] convincingly demonstrates the possibility of overcoming memory and transmission errors provided the noise level is below a certain threshold. Recently, the use of cluster states and stabilizers have constituted a sufficient backbone of fault-tolerant quantum computation [21–23]. Most error correcting codes are stabilizer codes. There is a general approach to quantum error correction called operator quantum error correction [24]. With the aid of error correction codes, the quantum computer can go further for practical usage.

The establishment of quantum network is another direction in quantum information theory. It has become increasingly important through the rapid development of

quantum technologies. A quantum network provides a way to build the connection between separate quantum nodes for sharing quantum information and quantum operations among different quantum systems. Key development in this area includes the recent studies of quantum entanglement swap [25], quantum repeaters [26,27]. To realize a practical quantum network, one of the key problems is to transfer a quantum state between different quantum nodes. Quantum teleportation is one of the main techniques to transfer the quantum information over a long distance with high fidelity. For quantum teleportation, two arbitrary nodes within the network only requires a pair of maximally entangled states to share their own quantum information via the quantum channel. If the transmitter and the receiver setup can be integrated to a single silicon photonic chip, this will greatly facilitate the connection of many quantum devices into quantum network and take advantage of existing fiber communication network. However, quantum resource can be expensive. To be able to transfer more information in a quantum channel, information compression is also necessary. By combining this together, a practical quantum network can be possible for implementation.

Overall, integrated photonic quantum chip is an ideal platform for quantum computation and quantum network. It has a great potential to bring the advantage of quantum computing to solve more realistic problems. In this thesis, the design, fabrication and measurement of quantum chip are studied. Our study paves the way for future quantum connectivity with advanced quantum technologies.

1.2 Objective

The objective of this thesis is to implement three quantum algorithms on a silicon photonic chip: the boson sampling for graph perfect matching calculation, the quantum error correction encoding and quantum teleportation with autoencoder.

A generic silicon photonic circuit includes three parts of photon source, quantum state manipulation and detection. The photon source can be realized with the SFWM process. The manipulation of quantum state will be the linear optical circuit consists of phase shifters and multi mode interferometer, the detection part is the superconducting array to perform photon coincidence counts under different measurement basis.

For three quantum applications, the theoretical process is modeled and the underlying physics is analyzed to decide the required function of the chip. The circuit is then designed by mapping each function into the various components of the silicon photonic structures. During the experimental implementation, the circuit is first calibrated to ensure the functionality of each part before the whole device for the algorithm is assembled.

1.3 Major contribution

In this thesis, the integrated photonic quantum computing circuit is carefully studied and three different quantum computing protocols are demonstrated experimentally. The theoretical modeling, photonic integrated circuit design and experimental implementation process are described at length in the following chapters. The major contributions are listed in three parts.

For the Gaussian boson sampling chip, the properties of on-chip photon source and linear optical circuit is carefully studied. The photon source properties are carefully studied both under single pump scheme for two-mode state (TMS) and under dual pump scheme for single mode state (SMS) such as the JSI, g_2, CAR, squeeze parameter and so on. Then, the circuit is used to implement unitary matrices and the results are verified experimentally to get a similarity of 98.44%. Finally, a boson sampling is measured with a random unitary set and a perfect matching problem is studied for a 6-vertex graph. For perfect matching configuration, the achieved photon distribution has a similarity of 0.9783 with the theoretical results and the perfect matching number is also identical with the theory.

In the error correction encoding section, the theoretical model of this scheme is first studied and its photonic implementation is designed. Three possible applications of quantum state reconstruction, error type identification and error corrected quantum teleportation are demonstrated on this photonic integrated circuit. The experiment result proves that the encoding scheme is feasible for the protection of quantum information from propagation loss or quantum operation error with an average state reconstruction fidelity of $\bar{F} = 0.8630$.

A novel quantum information transferring method consuming less quantum resources is proposed and demonstrated with photonic integrated circuit. A quantum autoencoder model is trained with genetic algorithm to map the qutrit subspace to a qubit space. The compressed qubit is then transferred from one photonic integrated circuit to another chip via a 10-meter-long fiber. The original qutrit is recovered by the inverse process of trained autoencoder and an average fidelity of $\bar{F} = 0.9132$ for four random qutrits is achieved to prove the functionality of the full system.

1.4 Organisation

The thesis is divided into 6 chapters. The first chapter is the introduction, it includes the motivation, objective, contribution and organisation of the whole thesis.

Chapter 2 is the literature review, it gives a brief concept of quantum information theory that involved in the following theoretical modeling and experimental analyses. The development of integrated photonic quantum computing and state-of-the-art technologies are reviewed with a listing of some of the critical technological breakthroughs.

Chapter 3 describes the integrated quantum photonic circuit. The theoretical modeling and design of a integrated silicon photonic circuit for implementing quantum protocols on the chip as well as the control of the quantum states within the silicon photonic components are described. The on-chip single photon source and linear optical circuit is calibrated experimentally to explore the purity, indistinguishability, unitary matrix decomposition of the full integrated photonic system. Finally, a Gaussian boson sampling experiment is performed and the graph perfect matching problem is simulated with this integrated quantum photonic chip.

Chapter 4 is the experimental demonstration of quantum error correction encoding scheme. The scheme is first studied theoretically to determine the required initial quantum state for the encoding and the manipulation process. The fabricated chip entangles photonic qubits in the form of a GHZ state and protect a single qubit information with 4 physical qubits. Different error types are simulated on chip to test the functionality of this encoding scheme to recover quantum information and perform fault tolerant teleportation.

Chapter 5 is the quantum teleportation scheme with autoencoder. Two photonic

integrated circuits are designed and fabricated as the encoder chip and decoder chip to demonstrate a quantum network with two nodes. The quantum autoencoder model using linear optical components is optimized with classical algorithm to compress the qutrit information into a qubit, which is then used for teleportation in the quantum network. Finally, the transformed qubit is recovered to its qutrit with an inverse decoder circuit using linear optical components with a high fidelity.

Finally, in Chapter 6, a general outlook and conclusion regarding the contributions are provided in this thesis with further recommendations for future work.

Chapter 2

Literature Review

In this chapter, the basic concepts to understand the thesis is described in first part. This part includes fundamental concepts in quantum information like qubits, quantum logic gates and state tomography. We then introduce the digital and analogue model of quantum computing.

In the second part, the photonic based quantum computing, including the state-of-the-art of quantum photonic devices are surveyed. The main part of this section focuses on linear optical setups based on integrated photonics technology.

2.1 Quantum Computer and Computing

Quantum computer is a device that uses the quantum mechanics properties like superposition and entanglement to realize computing. A general quantum computer usually includes quantum bits and quantum logic gates.

2.1.1 Quantum Computer Qubits and Gates

Qubit, short for ”quantum bit”, is the basic unit in quantum information in analogous to the bit concept in classical information theory. It is a two-energy-level quantum system with the ground state labeled as $|0\rangle$ or the excited state labeled as $|1\rangle$ where ”$|\rangle$” is called the Dirac notation, a standard representation of states in quantum mechanics.

A classical bit is always on a state of either 0 or 1 and when a measurement is performed, it gives an exact result of either 0 or respectively. The measurement process does not change the state. In contrast, a qubit can be in both $|0\rangle$ and $|1\rangle$ states and it can be written as a linear combinations as

$$|\varphi\rangle = \alpha|0\rangle + \beta|1\rangle \tag{2.1}$$

where α and β are, in general, two complex numbers. We say that this state is a superposition of states $|0\rangle$ and $|1\rangle$ and it can be represented as a vector in a two dimensional complex space where $|0\rangle$ and $|1\rangle$ are one set of the orthogonal basis of the vector space. A measurement of state $|\varphi\rangle$ in $|0\rangle$ and $|1\rangle$ basis would give a result of 0 with probability of $|\alpha|^2$ or 1 with probability of $|\beta|^2$. As there are only two possibilities, it is obvious that the two probabilities add up to 1, thus $|\alpha|^2 + |\beta|^2 = 1$. The Equation 2.1 can be rewritten as

$$|\varphi\rangle = e^{i\gamma_1}\cos\frac{\theta}{2}|0\rangle + e^{i\gamma_2}\sin\frac{\theta}{2}|1\rangle) \tag{2.2}$$

where θ, γ_1 and γ_2 are real numbers. The phase $e^{i\gamma_1}$ (or γ_2) can be factorized from the

state $|\varphi\rangle$ so that Equation (2.2) can be rewritten as

$$\begin{aligned} |\varphi\rangle =& e^{i\gamma_1}\left(\cos\frac{\theta}{2}|0\rangle + e^{i(\gamma_2-\gamma_1)}\sin\frac{\theta}{2}|1\rangle\right) \\ =& e^{i\gamma_1}\left(\cos\frac{\theta}{2}|0\rangle + e^{i\phi}\sin\frac{\theta}{2}|1\rangle\right) \end{aligned} \tag{2.3}$$

where θ defines the accounts for the probabilities of the states $|0\rangle$ and $|1\rangle$, γ is the global phase of the state and ϕ represents the relative phase difference between the state $|0\rangle$ and the state $|1\rangle$. The global phase factor has no effect on the state measurement results and can be effectively dropped or ignored, leaving the state as

$$|\varphi\rangle = \cos\frac{\theta}{2}|0\rangle + e^{i\phi}\sin\frac{\theta}{2}|1\rangle. \tag{2.4}$$

This state can then be represented as a point on the surface of a 3D unit sphere with coordinates $(\sin\theta\cos\phi,\ \sin\theta\sin\phi\cos\theta)$ as seen in Figure 2.1. This sphere is the so called Bloch Sphere and it provides to visualize a single-qubit state. Many single-qubit operations can be visualized directly on this sphere for a better understanding. However, such a representation for a high dimensional quantum states or multi-qubit states yet is not so easily available.

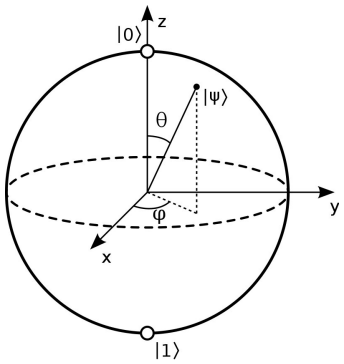

Figure 2.1: qubit on a Bloch Sphere

For two classical bits, there exists 4 different states as $\{00, 01, 10, 11\}$. Similarly, a two-qubit quantum system would also have four basis as $|00\rangle$, $|01\rangle$, $|10\rangle$ and $|11\rangle$ so that any two-qubit states can be written as

$$|\varphi\rangle = \alpha_{00}|00\rangle + \alpha_{01}|01\rangle + \alpha_{10}|10\rangle + \alpha_{11}|11\rangle \tag{2.5}$$

and the complex coefficients $\alpha_{i,j}$ of this state also satisfies the normalization condition that $\sum |\alpha_{i,j}|^2 = 1$. This can be further extended to an N-qubit system with 2^N basis listed from $|00...0\rangle$ to $|11...1\rangle$ and the state can be written as

$$|\varphi\rangle = \alpha_1|00...0\rangle + ... + \alpha_{2^N}|11...1\rangle \tag{2.6}$$

More generally, a quantum bit with d energy levels can be called an d-dimensional quantum bit or qudit with its ith energy level being denoted as $|i-1\rangle$ $(i = 0, \cdots d-1)$. An m qudit quantum system has d^m basis from $|00...0\rangle_m$ to $|d-1, d-1, ..., d-1\rangle_m$ and can be expressed as

$$|\varphi\rangle = \alpha_1|00...0\rangle + ... + \alpha_{d^m}|d-1, d-1, ..., d-1\rangle \tag{2.7}$$

The basis of a single qubit in a vector form can also be expressed as

$$|0\rangle = \begin{bmatrix} 1 \\ \\ 0 \end{bmatrix} |1\rangle = \begin{bmatrix} 0 \\ \\ 1 \end{bmatrix} \tag{2.8}$$

so the state $|\varphi\rangle = \alpha|0\rangle + \beta|1\rangle$ in vector form can be expressed as

$$|\varphi\rangle = \alpha \begin{bmatrix} 1 \\ 0 \end{bmatrix} + \beta \begin{bmatrix} 0 \\ 1 \end{bmatrix} = \begin{bmatrix} \alpha \\ \beta \end{bmatrix} \tag{2.9}$$

The multi-qubit state can be expressed by the tensor product of subsystem expressed as

$$|00\rangle_{12} = |0\rangle_1 \otimes |0\rangle_2 = \begin{bmatrix} 1 \\ 0 \end{bmatrix} \otimes \begin{bmatrix} 1 \\ 0 \end{bmatrix} = \begin{bmatrix} 1 \\ 0 \\ 0 \\ 0 \end{bmatrix} \tag{2.10}$$

and this can be further applied to an arbitrary m qudit ($d-$ quantum level) system.

Classical computing is realized with various logic gates assembled to form different programs in order to implement different functions. One typical single bit classical gate is the logical NOT gate whose action is to change the classical bit $0 \rightarrow 1$ and $1 \rightarrow 0$.

Similarly, an analogous quantum NOT gate would also interchange the quantum state $|0\rangle$ and $|1\rangle$. The NOT gate can be represented as

$$X = \begin{bmatrix} 0 & 1 \\ 1 & 0 \end{bmatrix} \tag{2.11}$$

and acting on an arbitrary quantum state, $|\varphi\rangle = \alpha|0\rangle + \beta|1\rangle$, it simply exchange the

coefficients of the arbitrary state as follows:

$$X \begin{bmatrix} \alpha \\ \beta \end{bmatrix} = \begin{bmatrix} \beta \\ \alpha \end{bmatrix} \tag{2.12}$$

Note that X has been mentioned earlier as the σ_x operator.

All single-qubit quantum gates can be expressed by a 2×2 matrix U and they must obey the rule that $U^\dagger U = I$ to conserve the total probability, and where $U^\dagger$ is the conjugate transpose of U. Such a matrix is also known as a unitary matrix.

There are some other important single qubit gates like Y (corresponding to the σ_y operator), Z (corresponding to the σ_y operator) and the Hadamard gate, H, defined as

$$Y = \begin{bmatrix} 0 & -i \\ i & 0 \end{bmatrix}, Z = \begin{bmatrix} 1 & 0 \\ 0 & -1 \end{bmatrix}, H = \frac{1}{\sqrt{2}} \begin{bmatrix} 1 & 1 \\ 1 & -1 \end{bmatrix} \tag{2.13}$$

The Y gate will swap the two states and give an additional phase ($e^{\pm i\frac{\pi}{2}} = \pm i$) depending on the basis state. Accordingly, $|0\rangle \rightarrow -i|1\rangle$ and $|1\rangle \rightarrow i|0\rangle$. The Z gate will flip the sign of state $|1\rangle$ while maintaining the state $|0\rangle$ unchanged. The H gate will convert the $|0\rangle$ and $|1\rangle$ into a superposition of two states $(|0\rangle + |1\rangle)/\sqrt{2}$ and $(|0\rangle - |1\rangle)/\sqrt{2}$. Indeed, as have already beeb seen, along with Identity matrix I, the I, X, Y, Z are called

Pauli Matrices. In literature, these operators are also denoted as

$$\sigma_0 = \sigma_I = I \tag{2.14a}$$

$$\sigma_1 = \sigma_X = X \tag{2.14b}$$

$$\sigma_2 = \sigma_Y = Y \tag{2.14c}$$

$$\sigma_3 = \sigma_Z = Z \tag{2.14d}$$

The Pauli matrices play an important role in the quantum information theory and they are involved heavily as the basis for qubit measurement, the form of the density matrix and many others, which will be shown in later examples.

The Pauli matrices are also related to the qubit rotation along different axis on the Bloch Sphere. Based on the Euler's formula $e^{i\theta} = \cos\theta + i\sin\theta$ and matrix exponential expansion $e^A = \sum_{n=0}^{\infty} \frac{1}{n!} A^n$, if matrix A satisfies $A^2 = I$, it can deduced that

$$e^{-iA\theta} = \cos\theta \cdot I - i\sin\theta \cdot A \tag{2.15}$$

and the rotation matrix $R_A(\theta)$ is defined as

$$R_X(\theta) = e^{-iX\frac{\theta}{2}} = \cos\frac{\theta}{2} \cdot I - i\sin\frac{\theta}{2} \cdot X = \begin{bmatrix} \cos\frac{\theta}{2} & -i\sin\frac{\theta}{2} \\ -i\sin\frac{\theta}{2} & \cos\frac{\theta}{2} \end{bmatrix} \tag{2.16a}$$

$$R_Y(\theta) = e^{-iY\frac{\theta}{2}} = \cos\frac{\theta}{2} \cdot I - i\sin\frac{\theta}{2} \cdot Y = \begin{bmatrix} \cos\frac{\theta}{2} & -\sin\frac{\theta}{2} \\ \sin\frac{\theta}{2} & \cos\frac{\theta}{2} \end{bmatrix} \tag{2.16b}$$

$$R_Z(\theta) = e^{-iZ\frac{\theta}{2}} = \cos\frac{\theta}{2} \cdot I - i\sin\frac{\theta}{2} \cdot Z = \begin{bmatrix} e^{-i\frac{\theta}{2}} & 0 \\ 0 & e^{i\frac{\theta}{2}} \end{bmatrix} \tag{2.16c}$$

$R_{\vec{n}}(\theta)$ represents different rotation matrices along the corresponding axis $\vec{n} \equiv A$, where $\vec{n}$ is some unit vector on the Bloch sphere. It can be shown as the qubit $|\varphi\rangle$ rotates θ degree along the specific axis in Figure 2.1. Qubit operations can be also represented in a circuit language as shown in Figure 2.2. The circuit wire means a single qubit, the square with A in side means the single qubit operation A and the default circuit runs from left to right.

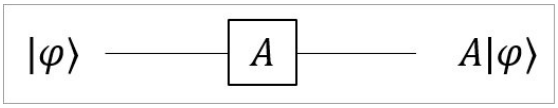

Figure 2.2: Schematic of single qubit gate.

For classical two-bit operations like AND, OR gates, the analogous two-qubit operations in quantum information theory exist. One of the typical operation is called Controlled-Not (CNOT) gate. It operates on a two-qubit state, treating one of qubits as a control qubit and another as a target qubit. The function is to flip (NOT oepration) the target qubit if the control qubit is in state $|1\rangle$ and yet do nothing if the control qubit is in state $|0\rangle$. The logical operations can be summarized as

$$|00\rangle \xrightarrow{CNOT} |00\rangle \tag{2.17a}$$

$$|01\rangle \xrightarrow{CNOT} |01\rangle \tag{2.17b}$$

$$|10\rangle \xrightarrow{CNOT} |11\rangle \tag{2.17c}$$

$$|11\rangle \xrightarrow{CNOT} |10\rangle \tag{2.17d}$$

and its circuit model is represented schematically in Figure 2.3, where the top wire functions as control qubit and the bottom wire is for target qubit.

Quantum entanglement is one of the most unique properties of quantum mechan-

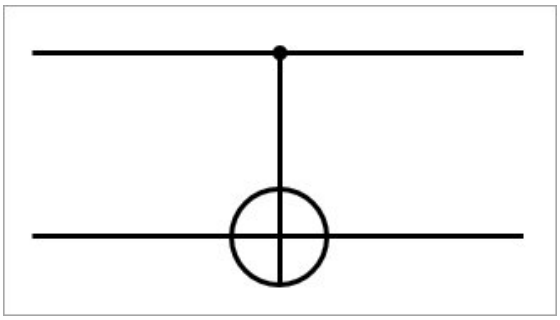

Figure 2.3: Schematic of two-qubit CNOT gate

ics. When a quantum bit is maximally entangled with another qubit then the result of the measurement of the quantum bit is always correlated to the results of the measurement on the other quantum bit, regardless of the distance between the two qubits. For example, if the two-qubit state given by

$$|\varphi\rangle = \frac{1}{\sqrt{2}}(|00\rangle + |11\rangle)_{12}, \tag{2.18}$$

then it can be shown that such a state cannot be written as a tensor product of the state of two individual single-qubit states. In this case, the state of two qubits are maximally entangled and when one of the qubits is measured to be the state $|0\rangle$ (or $|1\rangle$), the other qubit would collapse to a state $|0\rangle$ (or $|1\rangle$) immediately. In fact, if the state is measured in some other orthogonal basis $\{|u\rangle, |u^{\perp}\rangle\}$, the results of the measurements will continue to be fully correlated, i.e. if the first qubit collapse to the state $|u\rangle$ (or state $|u\rangle^{\perp}$) the other qubit will also collapse to state $|u\rangle$ (or state $|u\rangle^{\perp}$). Indeed, if the pure state can be written as tensor product of two single-qubit states, then it is called a pure separable state, otherwise, it is called an entangled state.

The quantum entanglement as a thought experiment was first raised by Albert Einstein, Boris Podolsky and Nathan Rosen, which subsequently gave rise the a state known as the EPR state, in 1935 [28]. The paradox was subsequently known as the

EPR paradox. Through the years, there has been a lot of fundamental studies on how to explain this faster-than-light interaction but, until recently, none of them appears to be convincing. One of the most famous theories that challenge quantum entanglement is called the local hidden variable theory [29] and this theory tries to explain the non-classical correlations resulting from quantum entanglement by introducing the existence of an unobservable variable to account for the indeterministic nature of quantum mechanics. It is interesting to note that the phrase "God does not play dice" appears under this context through the words of Albert Einstein [30].

It is not so easy to explain the EPR paradox satisfactorily. However, John Stewart Bell proposed the famous Bell inequalities in 1964 [31] to illustrate that the quantum mechanics cannot be fully explained with local hidden-variable theories. In short, any correlations arising from quantum theory will violate the Bell inequalities. These inequalities have been experimentally violated over many platforms [32–35]. Yet, these experiments often suffer from loopholes, arising from experimental assumptions. In two recent experiments, the researchers from Havard University manage to remove additional assumptions arising from nonlocality requirement to show the Bell inequalities violation directly [36] and a joint group researchers from all over the world tackle the 'free will' assumption using nearly 100 thousand humans as randomizer for the selection of the measurement basis [37].

Under the Copenhagen interpretation of such faster-than-light EPR paradox, the collapse of wavefunction happens immediately and there is no propagation of any information between the two parties when the state of the two parties is a maximally entangled pair of qubits. The non-classical correlation resulting from the measurement can only be established with a classical channel which is limited by the speed of light.

Corresponding to any pure state $|\varphi\rangle$ as shown in Equation 2.4, one can associate a density matrix denoted by $\rho = |\varphi\rangle\langle\varphi|$. If representing the state $|0\rangle$ and $|1\rangle$ as the vector, the density matrix ρ is given by

$$\begin{aligned}
\rho &= |\varphi\rangle\langle\varphi| \\
&= \begin{bmatrix} \cos\left(\frac{\theta}{2}\right) \\ e^{i\phi}\sin\left(\frac{\theta}{2}\right) \end{bmatrix} \begin{bmatrix} \cos\left(\frac{\theta}{2}\right) & e^{-i\phi}\sin\left(\frac{\theta}{2}\right) \end{bmatrix} \\
&= \begin{bmatrix} \cos\left(\frac{\theta}{2}\right) & e^{-i\phi}\sin\left(\frac{\theta}{2}\right)\cos\left(\frac{\theta}{2}\right) \\ e^{i\phi}\frac{\sin\theta}{2}\cos\left(\frac{\theta}{2}\right) & \sin^2\left(\frac{\theta}{2}\right) \end{bmatrix} \\
&= \begin{bmatrix} \frac{1+\cos(\theta)}{2} & e^{-i\phi}\frac{\sin\theta}{2} \\ e^{i\phi}\frac{\sin\theta}{2} & \frac{1-\cos(\theta)}{2} \end{bmatrix} \\
&= \frac{1}{2}\left(\sigma_I + \cos\theta\,\sigma_Z + \sin\theta\cos\phi\,\sigma_X + \sin\theta\sin\phi\,\sigma_Y\right)
\end{aligned} \tag{2.19}$$

where σ_x, σ_y and σ_z are the Pauli matrices in the $x-$, $y-$ and $z-$ directions.

A practical quantum system is usually a mixture of different states with its the density matrix expressed as [38]

$$\rho = \sum P_i |\varphi_i\rangle\langle\varphi_i| \tag{2.20}$$

where P_i is the probability of getting a state $|\varphi_i\rangle$ in this mixture. It is important to distinguish the difference between the notion of superposition and mixed state. Each pure states $|\varphi_i\rangle$ could be a superposition of some basis states, i.e. $|\varphi_i\rangle = \sum_j a_{ij}|u_{ij}\rangle$ for each i, so that the probability of getting a particular basis state $|u_{ij}\rangle$ is given by $|a_{ij}|^2$. A quantum system in a mixed state has a fixed probability P_i that it will produce the state $|\varphi_i\rangle$. For example, a mixed system to generate state $|0\rangle$ and $|1\rangle$ with an equal probability

50%. For measurement under basis $|0\rangle$, the detector apparatus would have 50% chance get a click and 50% change no click. When switching to a new measurement basis $\{1/\sqrt{2}(|0\rangle+|1\rangle), 1/\sqrt{2}(|0\rangle-|1\rangle)\}$, the results are the same, i.e. the same state can also be written as a convex sum of states $\{1/\sqrt{2}(|0\rangle+|1\rangle), 1/\sqrt{2}(|0\rangle-|1\rangle)\}$ each with 50%. For a superposed pure state $1/Sqrt2(|0\rangle+|1\rangle)$, the measured distribution at basis $|0\rangle$ is the same to have 50% chance for both click and non-click. However, the results with the measurement basis $\{1/\sqrt{2}(|0\rangle+|1\rangle), 1/\sqrt{2}(|0\rangle-|1\rangle)\}$ will always click if the setting is set to $1/\sqrt{2}(|0\rangle+|1\rangle)$. This is clearly different from the earlier mixed state.

Quantum state tomography is an experimental technique to determine the density matrix of a quantum state. A density matrix should satisfy the property given by

$$\rho = \rho^{\dagger}, Tr(\rho) = 1, \langle\varphi|\rho|\varphi\rangle \geq 0 \tag{2.21}$$

For m-qudit system, its density matrix size is d^m. Experimentally, quantum state tomography (QST) method is used to reconstruct density matrix.

Here the QST done on a 2-level quantum system is illustrated. For a single-qubit state $|\varphi\rangle$, its density matrix is represented as

$$\rho = \sum_{i=0}^{3} a_i \sigma_i \tag{2.22}$$

where a_i is the coefficient and σ_i (each i) is the one of the Pauli matrices defined above.

The eigenvector v_i and eigenvalue λ_i of these matrices is given by

$$\sigma_0 |0/1\rangle = |0/1\rangle \tag{2.23a}$$

$$\sigma_1 \frac{1}{\sqrt{2}}(|0\rangle \pm |1\rangle) = \pm \frac{1}{\sqrt{2}}(|0\rangle \pm |1\rangle) \tag{2.23b}$$

$$\sigma_2 \frac{1}{\sqrt{2}}(|0\rangle \pm i|1\rangle) = \pm \frac{1}{\sqrt{2}}(|0\rangle \pm i|1\rangle) \tag{2.23c}$$

$$\sigma_3 |0/1\rangle = \pm |0/1\rangle \tag{2.23d}$$

These basis are usually simplified as $|D/A\rangle = \frac{1}{\sqrt{2}}(|0\rangle \pm |1\rangle)$ and $|R/L\rangle = \frac{1}{\sqrt{2}}(|0\rangle \pm i|1\rangle)$. The corresponding eigenvalue is labeled as λ_1, λ_2, thus the Pauli matrix in the form of eigenvector and eigenvalue can be expressed as

$$\sigma_0 = \lambda_1 |0\rangle\langle 0| + \lambda_2 |1\rangle\langle 1| = |0\rangle\langle 0| + |1\rangle\langle 1| \tag{2.24a}$$

$$\sigma_1 = \lambda_1 |D\rangle\langle D| + \lambda_2 |A\rangle\langle A| = |D\rangle\langle D| - |A\rangle\langle A| \tag{2.24b}$$

$$\sigma_2 = \lambda_1 |R\rangle\langle R| + \lambda_2 |L\rangle\langle L| = |R\rangle\langle R| - |L\rangle\langle L| \tag{2.24c}$$

$$\sigma_3 = \lambda_1 |0\rangle\langle 0| + \lambda_2 |1\rangle\langle 1| = |0\rangle\langle 0| - |1\rangle\langle 1| \tag{2.24d}$$

The coefficients a_i can be expressed as [38]

$$a_0 = \frac{1}{2}(\lambda_1 |\langle\varphi|0\rangle|^2 + \lambda_2 |\langle\varphi|1\rangle|^2) = \frac{1}{2}(|\langle\varphi|0\rangle|^2 + |\langle\varphi|1\rangle|^2), \tag{2.25a}$$

$$a_1 = \frac{1}{2}(\lambda_1 |\langle\varphi|D\rangle|^2 + \lambda_2 |\langle\varphi|A\rangle|^2) = \frac{1}{2}(|\langle\varphi|D\rangle|^2 - |\langle\varphi|A\rangle|^2), \tag{2.25b}$$

$$a_2 = \frac{1}{2}(\lambda_1 |\langle\varphi|R\rangle|^2 + \lambda_2 |\langle\varphi|L\rangle|^2) = \frac{1}{2}(|\langle\varphi|R\rangle|^2 - |\langle\varphi|L\rangle|^2), \tag{2.25c}$$

$$a_3 = \frac{1}{2}(\lambda_1 |\langle\varphi|0\rangle|^2 + \lambda_2 |\langle\varphi|1\rangle|^2) = \frac{1}{2}(|\langle\varphi|0\rangle|^2 - |\langle\varphi|1\rangle|^2). \tag{2.25d}$$

where the inner product $|\langle\varphi|v_i\rangle|^2$ is the projective measurement for state $|\varphi\rangle$ at basis

$|v_i\rangle$. For integrated photonic system, a qubit can be encoded under dual rail encoding with photon at the upper waveguide representing $|0\rangle$ and photon at lower waveguide representing $|1\rangle$, which is also called the experimental basis. For an arbitrary qubit $|\varphi\rangle = \alpha|0\rangle + \beta|1\rangle$, its projective measurement under basis $|0/1\rangle$ is obviously $|\alpha|^2$ and $|\beta|^2$, which corresponds to the direct photon count rate at two waveguides. The project measurement under other other basis requires the state to be transformed under a basis transformation matrix. Take the basis $|D/A\rangle$ as an example, its theoretical result is given by

$$\langle\varphi|D\rangle = \frac{1}{\sqrt{2}}(\alpha+\beta) \tag{2.26a}$$

$$\langle\varphi|A\rangle = \frac{1}{\sqrt{2}}(\alpha-\beta) \tag{2.26b}$$

The original state can also be expressed as

$$|\varphi\rangle = \alpha|0\rangle + \beta|1\rangle = \frac{\alpha+\beta}{\sqrt{2}}|D\rangle + \frac{\alpha-\beta}{\sqrt{2}}|A\rangle \tag{2.27}$$

A projective measurement under basis $|D/A\rangle$ is exactly the coefficient of the state written in the $|D/A\rangle$ basis. By applying a Hadamard gate on this state, it can be expressed as

$$H|\varphi\rangle = \frac{\alpha+\beta}{\sqrt{2}}|0\rangle + \frac{\alpha-\beta}{\sqrt{2}}|1\rangle \tag{2.28}$$

Thus the projective measurement for $|D/A\rangle$ is tantamount to the measurement of $H|\varphi\rangle$ under basis $|0/1\rangle$. For basis $|R/L\rangle$, the corresponding operator is given by

$$U = |0\rangle\langle R| + |1\rangle\langle L| = \frac{1}{\sqrt{2}}\begin{bmatrix} 1 & -i \\ 1 & i \end{bmatrix} \tag{2.29}$$

By performing the appropriate operations on the target state, the projective measurement results P_{v_i} under different basis v_i is expressed as

$$P_{v_i} = |\langle\varphi|0\rangle|^2 = \frac{N_{v_i}}{N_0 + N_1} \tag{2.30}$$

where N_{v_i} is the measured photon counts at basis v_i and N_0, N_1 are for basis $|0/1\rangle$.

For a two-qubit state in Equation 2.5, its density matrix, in general, can be expressed as

$$\rho = \sum_{i=0}^{3}\sum_{j=0}^{3} a_{i,j}\sigma_i \otimes \sigma_j \tag{2.31}$$

where the coefficient $a_{i,j}$ are calculated in similar fashion to the previous case for a single qubit by considering appropriate projective measurements for each term of the density matrix $\sigma_i \otimes \sigma_j$. The eigensystem for each part is expressed as

$$\sigma_i \left|v_{i,1}\right\rangle = \lambda_{i,1}\left|v_{i,1}\right\rangle \tag{2.32a}$$

$$\sigma_i \left|v_{i,2}\right\rangle = \lambda_{i,2}\left|v_{i,2}\right\rangle \tag{2.32b}$$

$$\sigma_j \left|v_{j,1}\right\rangle = \lambda_{j,1}\left|v_{j,1}\right\rangle \tag{2.32c}$$

$$\sigma_i \left|v_{j,2}\right\rangle = \lambda_{j,2}\left|v_{j,2}\right\rangle \tag{2.32d}$$

The eigensystem for $\sigma_i \otimes \sigma_j$ can easily be written as

$$\sigma_i \otimes \sigma_j(\left|v_{i,1}\right\rangle \otimes \left|v_{j,1}\right\rangle) = \lambda_{i,1}\lambda_{j,1}(\left|v_{i,1}\right\rangle \otimes \left|v_{j,1}\right\rangle) \tag{2.33a}$$

$$\sigma_i \otimes \sigma_j(\left|v_{i,1}\right\rangle \otimes \left|v_{j,2}\right\rangle) = \lambda_{i,1}\lambda_{j,2}(\left|v_{i,1}\right\rangle \otimes \left|v_{j,2}\right\rangle) \tag{2.33b}$$

$$\sigma_i \otimes \sigma_j(\left|v_{i,2}\right\rangle \otimes \left|v_{j,1}\right\rangle) = \lambda_{i,2}\lambda_{j,1}(\left|v_{i,2}\right\rangle \otimes \left|v_{j,1}\right\rangle) \tag{2.33c}$$

$$\sigma_i \otimes \sigma_j(\left|v_{i,2}\right\rangle \otimes \left|v_{j,2}\right\rangle) = \lambda_{i,2}\lambda_{j,2}(\left|v_{i,2}\right\rangle \otimes \left|v_{j,2}\right\rangle) \tag{2.33d}$$

The coefficient $a_{i,j}$ is defined as

$$\begin{aligned} a_{i,j} =& \frac{1}{4}(\lambda_{i,1}\lambda_{j,1}|\langle\varphi|v_{i,1}\otimes v_{j,1}\rangle|^2+\lambda_{i,1}\lambda_{j,2}|\langle\varphi|v_{i,1}\otimes v_{j,2}\rangle|^2+ \\ & \lambda_{i,2}\lambda_{j,1}|\langle\varphi|v_{i,2}\otimes v_{j,1}\rangle|^2+\lambda_{i,2}\lambda_{j,2}|\langle\varphi|v_{i,2}\otimes v_{j,2}\rangle|^2) \end{aligned} \tag{2.34}$$

Thus each coefficient $a_{i,j}$ contains four measurement basis, and the unitary operator on the two qubit state is defined as

$$\begin{aligned} U =& |00\rangle\langle v_{i,1}\otimes v_{j,1}| + |01\rangle\langle v_{i,1}\otimes v_{j,2}| + \\ & |10\rangle\langle v_{i,2}\otimes v_{j,1}| + |11\rangle\langle v_{i,2}\otimes v_{j,2}| \end{aligned} \tag{2.35}$$

For m-qubit state, this method can be expanded to measure 4^n coefficients and each coefficient contains 2^n terms of project measurements. If the state is further expanded to an m-level qudit, the Pauli matrix will also be adjusted accordingly to a matrix set of m^2.

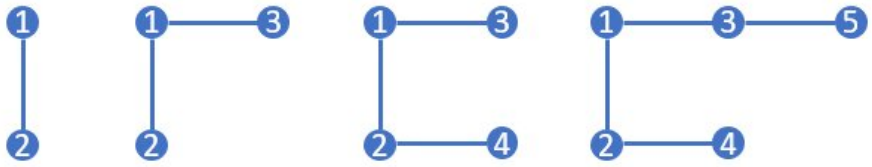

Figure 2.4: Schematic of Linear Cluster State from 2 qubits to 5 qubits. Each vertex represents the state $|+\rangle$ and the connecting edge represents Controlled-Z gate.

Cluster state is an important kind of entangled state in quantum computation. To construct it, the state can start with a series of separable qubits initiated with the state $|+\rangle = \frac{1}{\sqrt{2}}(|0\rangle + |1\rangle)$ and entangle each other by performing controlled-Z gate between them. Linear cluster state is a special kind of cluster states in which qubits are entangled in a chain as shown in Figure 2.4, where each vertex represents the state $|+\rangle$ and the

connecting edge represents Controlled-Z gate. By entangling a $|+\rangle$ qubit to the end of previous state $|L_n\rangle$, the linear cluster chain can be expanded, which is expressed as

$$|L_2\rangle = \frac{1}{\sqrt{2}}(|0+\rangle_{12} + |1-\rangle_{12}) \tag{2.36a}$$

$$|L_3\rangle = \frac{1}{\sqrt{2}}(|+0+\rangle_{312} + |-1-\rangle_{312}) \tag{2.36b}$$

$$|L_4\rangle = \frac{1}{\sqrt{2}}(|+0\rangle_{31}\left|\phi^+\right\rangle_{24} + |-1\rangle_{31}\left|\phi^-\right\rangle_{24}) \tag{2.36c}$$

$$|L_5\rangle = \frac{1}{\sqrt{2}}(\left|\phi^+0\phi^+\right\rangle + \left|\phi^-1\phi^-\right\rangle)_{53124} \tag{2.36d}$$

It is obvious to notice that $|L_2\rangle$ is equivalent to a Bell state under local transform H_2 and $|L_3\rangle$ is equivalent to GHZ state under $H_2 \otimes H_3$. Cluster state plays an important role in quantum computing. Unlike the usual unitary circuit paradigm, entanglement is created right at the start and only single-qubit operations are performed. It can be treated as a quantum resource for universal computing as shown below.

2.1.2 Digital Quantum Computer

The applications of quantum mechanics to computing has completely overhauled the perspective of computation in the world. Computation done on a small quantum system, limited to only tens of qubits, is sufficiently intractable for most of the advanced supercomputers to-date, if the power of superposition and entanglement of quantum bits are properly harnessed. Moreover, since Nature is quantum mechanical, it is an obvious choice to build a controllable quantum computer to mimic quantum systems in Nature. Richard Feynman first suggested this idea in 1982 [39]. Further more, by taking advantage of the entanglement, a quantum computer could show great speed-up

in solving classically hard r intractable problems. This is the case of Shor's algorithm which could in principle factorize a large number that is made up of some large prime numbers and, also Grover's Algorithm for a quadratic speed-up in database search, an ubiquitous protocol in many computational task.

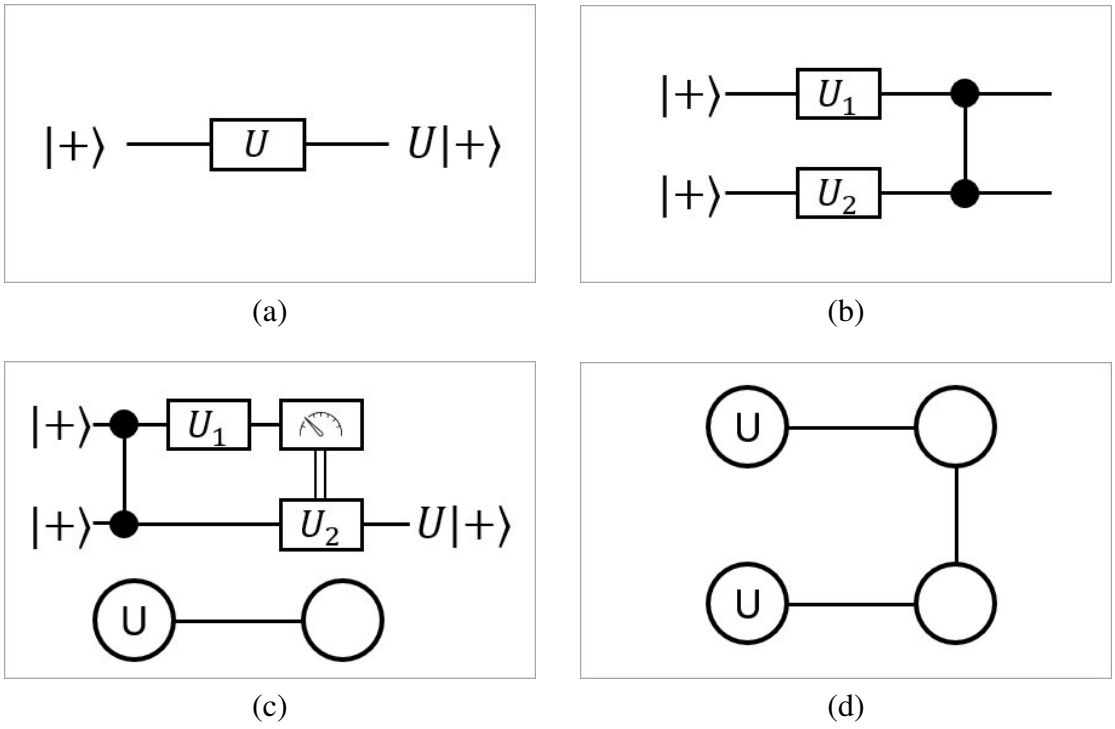

Figure 2.5: Quantum computing models of (a) single qubit gate for circuit model, (b) two qubit gate for circuit model, (c) single qubit gate for cluster state model and (d) two qubit gate for cluster state model.

The basic components for circuit model quantum computing is the single-qubit gate and two-qubit gate as shown in Figure 2.5a and 2.5b. Each horizontal line is for a single qubit and the evolution sequence is from left to right. The square box is for single-qubit operation and the vertical line with two dots are for two-qubit CZ gate. There have been theoretical analysis showing that an arbitrary N-qubit gate can be decomposed into single qubit gate and two qubit gate [40–42]. However, the optimization of gate decomposition process still remains to be an open problem.

The circuit model can also be mapped into the cluster state model to realize a one-way computing, which is typically performed in two stages: preparation of the appropriate highly entangled resource followed by a sequence of single-qubit measurements on the cluster state. These latter measurements are adaptive so that the basis in which a qubit is measured depends on the outcome of earlier measurements [43–46], as shown in Figure 2.5c. A single qubit operation in circuit model can be realized with a 2D linear cluster state. The first qubit would undergo an operator U_1 and then get measured. The measurement results would decide the form of operator U_2 to reconstruct the second qubit as $U|+\rangle$. The simplified drawing is two circles connected with a line as a cluster state and the U means performing operator U and then measure it at $|0/1\rangle$ basis, which is equivalent to measuring under a basis related to U as discussed in QST part. One might be curious why the cluster state is necessary to realize single qubit operator since the cluster computing model itself requires single qubit operation. Actually the advantage of cluster can be shown in two-qubit operation in Figure 2.5d. We use a 4-qubit linear cluster state to simulate a circuit model with two-qubit operators. As it can be seen, only single qubit measurement without any two-qubit gate operation is needed.

A more complicated multi-qubit circuit model is shown in Figure 2.6. The circuit model is a multi-qubit circuit that includes multiple operation steps. Its corresponding cluster model is a universal 2D grid shape cluster state such that part of the entanglement collapses as denoted in dashed line. As before, only single qubit measurement is required to perform the computation. The computational complexity is very low but the computational complexity for a complicated cluster state resource can be demanding and there have been many works reported on this area [47–50].

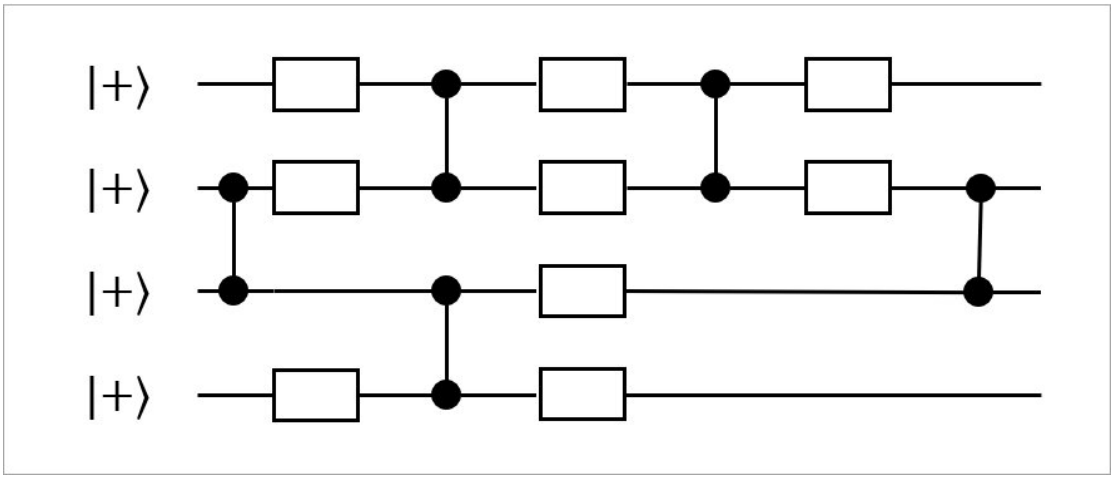

(a)

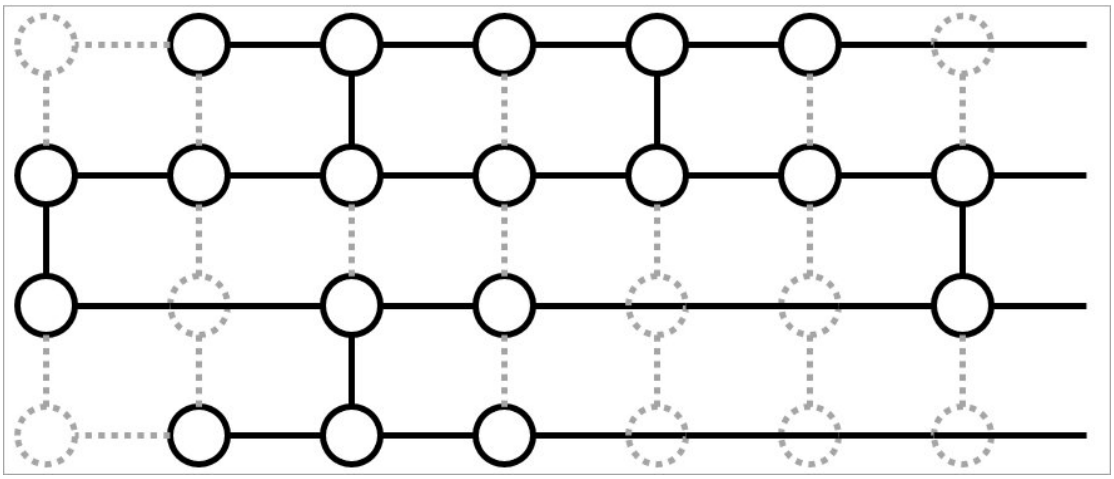

(b)

Figure 2.6: A general multi qubit operation under (a) circuit model and (b) cluster state model.

2.1.3 Analogue Quantum Simulation

Analogue Quantum Computing is another big topic for simulating real problem with a quantum computer. It is more like a dedicated quantum simulator target with a specific type of problem. The main idea is to find a mapping between a hard but real problem and a quantum system. By observing the quantum state, the real problem can be solved. Some typical applications are chemical simulations or graph and network problem.

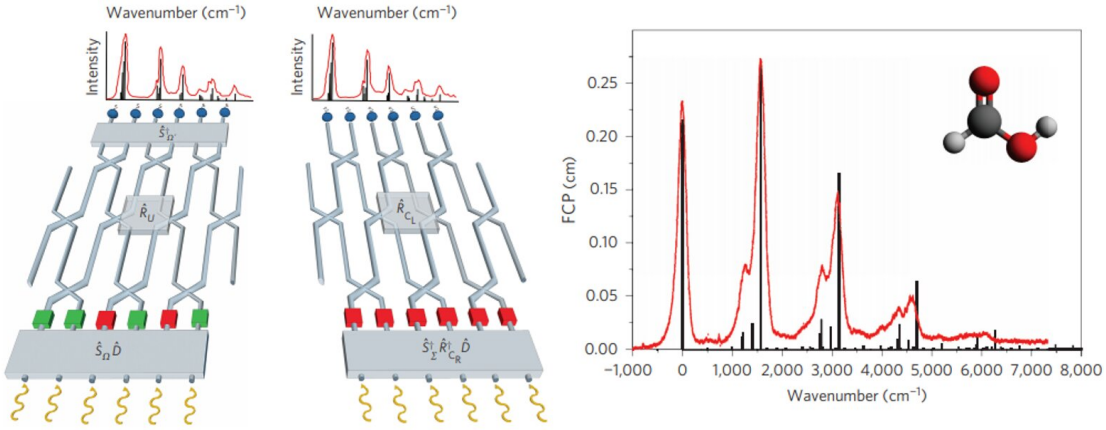

Figure 2.7: Molecular Frank-Condon profile simulation. The molecular vibronic spectra can be mapped to a Boson Sampling distribution [1].

The Figure 2.7 is a good example to demonstrate the analogue quantum simulation of molecular vibronic spectra [1]. The spectra depends on the Frank-Condon Profile, which is described with equation given by

$$FCP(\omega_{vib}) = \sum_{m}^{\infty} |\langle m|\hat{U}_{Dok}|0\rangle|^2 \delta(\omega_{vib} - \sum_{k}^{N} \omega_k' m_k). \tag{2.37}$$

This equation is the sum of the production of two terms to form a full spectra. The wave number of each peak is decided by the second term $\delta(\omega_{vib} - \sum_k^N \omega_k' m_k)$. The intensity of the peak is decided by the first term $|\langle m|\hat{U}_{Dok}|0\rangle|^2$, which is called the Frank-Condon Factor. The main part of calculation is the vacuum state $|0\rangle$ evolution to $|m\rangle$ under the operator $\hat{U}_{Dok}$. This part is computationally intractable for supercomputer but yet it can still be mapped to a quantum boson sampling process given by

$$\hat{U}_{Dok}|0\rangle = \hat{R}_{C_L}\hat{S}_{\Sigma}^{\dagger}\hat{R}_{C_R}^{\dagger}\hat{D}_{\frac{1}{\sqrt{2}}J^{-1}\delta}|0\rangle \tag{2.38}$$

The boson sampling process begins with a squeezed coherent state and evolves in a linear optical circuit $\hat{R}_{C_L}$. The output photon combination corresponds to the state $\langle m|$

and its intensity can be mapped to the peak intensity of spectra. All the parameters like C_L, C_R, Σ, J are extracted from the molecular structure itself.

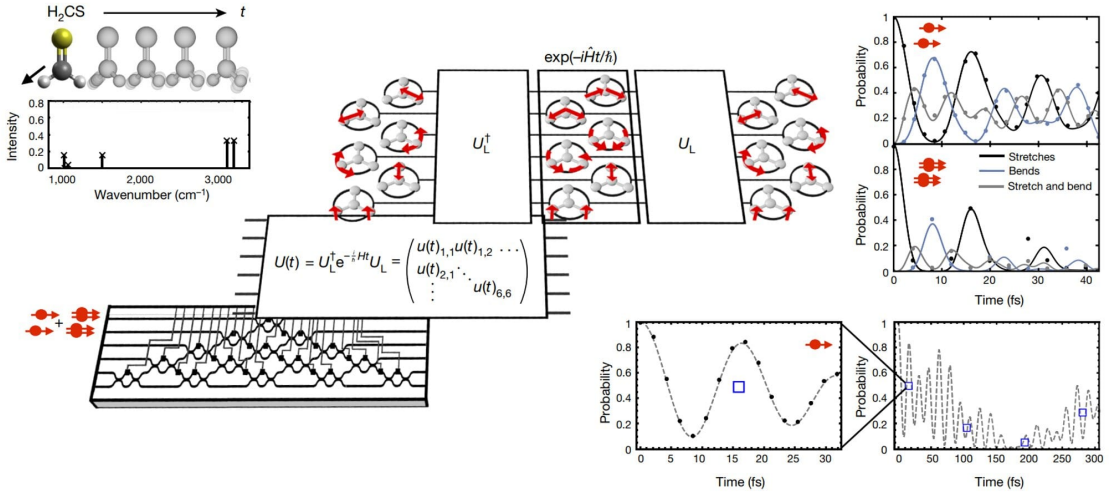

Figure 2.8: Vibronic dynamics process of molecules. The Hamiltonian evolution can be mapped to a unitary matrix to simulate the vibrational modes at time t [2].

Another example for quantum simulation is Figure 2.8 [2]. It simulates the quantum dynamic behaviours of molecules with a reconfigurable linear optical circuit. The main idea is to simulate the Hamiltonian evolution given by

$$\begin{aligned} |\psi\rangle_t &= e^{-i\hat{H}t/\hbar}|\psi\rangle_0 \\ &= U_L^\dagger e^{-i\Sigma t/\hbar} U_L |\psi\rangle_0 \end{aligned} \tag{2.39a}$$

$$\hat{H} = U_L^\dagger \Sigma U_L \tag{2.39b}$$

The Hamiltonian $\hat{H}$ is decided by the target molecule and can be decomposed to the unitary matrix U_L and diagonal term Σ via the singular value decomposition (SVD). Thus the time evolution can be treated by two stationary unitary matrices $U_L^\dagger, U_L$ and a diagonal phase term $e^{-i\Sigma t/\hbar}$ evolution with time t. The input state $|\psi\rangle_0$ is decided

which dynamic process is studied and the sampling results can indicate the probability of a mode at the given evolution time t.

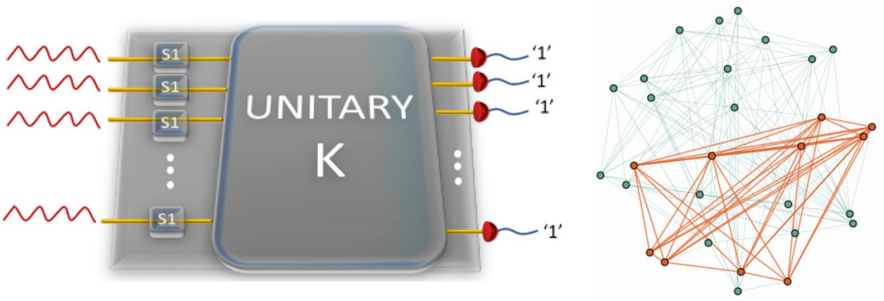

Figure 2.9: Dense graph problem simulated by Gaussian boson sampling process [3, 4] to find the maximum perfect matching numbers of a subgraph.

The graph problem of finding the dense subgraph can also be mapped to a quantum simulator as shown in Figure 2.9 [3, 4]. The dense graph is related to the calculation of maximum perfect matching of a graph. This is a mathematical problem of calculating the Hafnian as

$$Pr(\bar{n}) = \frac{1}{\bar{n}!\sqrt{det\sigma_Q}} hafA_S, \tag{2.40}$$

where $\bar{n}$ is the selected combinations of subgraph, A_S is related to the structure of graph connections. The Hafnian calculation process is hard to solve classically for sufficiently large graph, yet the quantum Gaussian boson sampling model can help to speed up this process. By further combining with some optimization algorithms to search different combinations, the dense subgraph can be found. There are more related quantum simulation algorithms as shown in ref. [51, 52].

2.2 Quantum Photonic Circuits

Quantum computation has become more and more promising with the development of quantum technologies. Superconducting qubits [53], trapped ions [54], diamond nitrogen vacancy (NV) centers [55] and so forth are all practical platforms to realize a quantum computer. The photon is also a promising candidate compared to other platforms with some key advantages.

The photon is very robust against decoherence from the environment (since it hardly interacts at all) and it therefore suffers from very little decoherence and crosstalk. Moreover, it only requires room temperature for operations comparing with other qubit implementation schemes. So that the photonic qubit is an ideal platform for quantum network and quantum communication. The photon propagates at the speed of light and this allows a very fast clock cycle at GHz level with commercial technology. It is also very easy to manipulate the photon to guarantee a very high fidelity with single-qubit gate. Finally, when one considers the integrated photonic qubit on silica-on-insulator (SOI), it is compatible with the current mature CMOS fabrication technologies for scaling up.

Linear optical circuit is able to perform qubit manipulation and it can be used to realize universal quantum computing, using the famous KLM scheme for Linear Optical Quantum Computing (LOQC) [14, 56–61]. Although the continuous variable quantum computing is becoming more and more important in LOQC [62–65], only discrete variable LOQC would be reviewed here. Photonic integrated circuit platform possesses the potential for quantum computation. It is able to integrate photon sources [8, 66–70] by inducing the non-linearity effect via the spontaneous four wave mixing process or

deterministic quantum dot emitters [71, 72]. Photons can be manipulated easily on chip to perform rotation operations and measurements under different basis [5, 6, 73–76] and there are many experimental efforts to integrate better and better single photon detectors on chip [77, 78]. Like bulk optics experiments [79–85], entanglements can also be realized on chip via the post-selection methods [86–89]. With all these advantages, photonic integrated chip sets to challenge other platforms in the Noisy Intermediate-Scale Quantum (NISQ) era to realize quantum supremacy [90–92], quantum machine learning [7, 93–95], quantum key distribution [96–98], quantum simulation [1, 99, 100] and last but not least quantum computation [9, 101–103].

There are many ideal platforms for integrated quantum photonic applications like the silica-on-insulator [104], laser-writing silica [105–108], silicon nitride [76, 109–112], lithium niobate [113–115]. To realize the universal quantum computing that requires the manipulation of many photons simultaneously, the CMOS-compatible integrated photonic chip would be a better choice than the laser writing chip.

Here, a comparison of two mature technologies, the silica and silicon waveguide, are listed in Table 2.1. The typical parameters are obtained from reference paper [5, 116–118] and this research thesis to show the difference of two platforms. The reference paper takes the germanium-doped silica waveguide core embedded in a silica cladding and the thesis takes the silicon waveguide with silica cladding. The mentioned wavelength for two platforms are 800 *nm* and 1550 *nm*. To ensure a single mode propagation in waveguide, the cross section is designed to be $3.5 \times 3.5um$ for silica and $0.22 \times 0.5um$ for silicon, which is mainly designed by the refractive index difference of the core and cladding material. The core of silica waveguide is germanium dopped so that the refractive index difference is only 2.5% difference while for silicon waveg-

Table 2.1: Comparison of silica and silicon platform for photonic chip

	Silica	Silicon
Wavelength	800 nm	1550 nm
Cross Section	$3.5 \times 3.5um$	$0.22 \times 0.5um$
Refractive Index Difference	2.5%	133%
Bending Radius	1 mm	10 um
Propagation Loss	0.85 dB/m	2 dB/cm
Photon Source	SFWM	SFWM
Modulation	Thermo-optics 100 mW	Thermo-optics 2 mW
Coupling	0.4 dB	1.1 dB

uide, the core material is silicon with refractive index $n = 3.5$ and the cladding is silica with $n = 1.5$, corresponding to a 133% difference. This would further cause the footprint difference of the designed chip. Typically, the bending radius is 1 mm for silica and 10 um for silicon. Propagation loss is also affected by the refractive index difference as the roughness of fabrication process has a more serious effect on silicon. Both platforms can take the advantage of nonlinear effect called the spontaneous four wave mixing process to generate the photons on chip. The manipulation of phase is based on thermo-optic effect but the required power for a pi phase shift is slightly different due to the fabrication technology and material property. Finally, the coupling efficiency for silica can reach 0.4 dB with ultraviolet curing epoxy adhesive and for silicon, the corresponding loss is 1.1 dB implemented by aluminum assisted apodized grating couplers.

This thesis would mainly focus on integrated quantum photonic platforms with silicon on insulator (SOI) technology [119]. Two key technologies of linear optical circuit and light source would be introduced and their state-of-the-art developments would be illustrated.

A general roadmap of integrated quantum photonics progress in past decade is

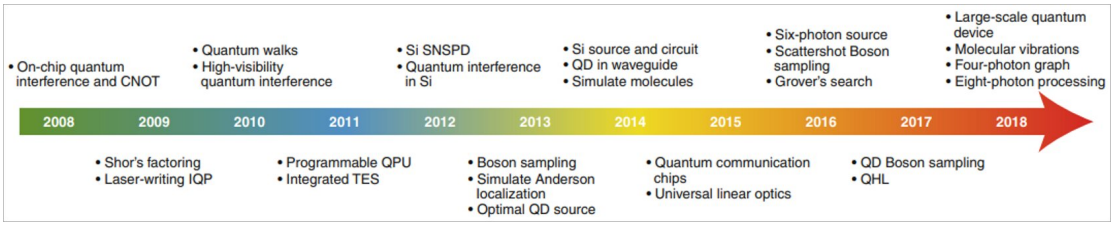

Figure 2.10: Progress of integrated quantum photonic technologies in past decade.

shown in Figure 2.10. The key technologies of the integrated quantum photonics are listed, including on-chip interference and CNOT gate [120], Shor's algorithm [121], laser-writing chip [105], quantum walk [122], high visibility interference [104], programmable QPU [123], integrated TES detector with PNR ability [124], on chip SNSPD [15], interference on SOI [125], boson sampling [126], localization [127], QD source [128], on chip SFWM source [8], on chip QD source [13], molecule simulation [129], quantum communication [130, 131], universal linear optics [5], measurement of 6 photon on chip [132], scatter boson sampling [133], Grover's search algorithm [134], QD boson sampling [135], quantum hamiltonian learning [136], large scale circuit implementation [9], molecular vibronic dynamics [2], four photon graph state [89] and eight photon processing [92].

2.2.1 Linear Optical Quantum Circuits

The development of integrated quantum photonic circuit begins with the basic single-qubit operation and two-qubit operation [120,123,137,138] on silica-on-insulator optical waveguide circuits in 2008 as shown in Figure 2.11. The qubit is encoded in dual rail with one photon travelling on two waveguides. Single-qubit operation is realized by the directional coupler and phase shifters and the two-qubit CNOT gate with bulk op-

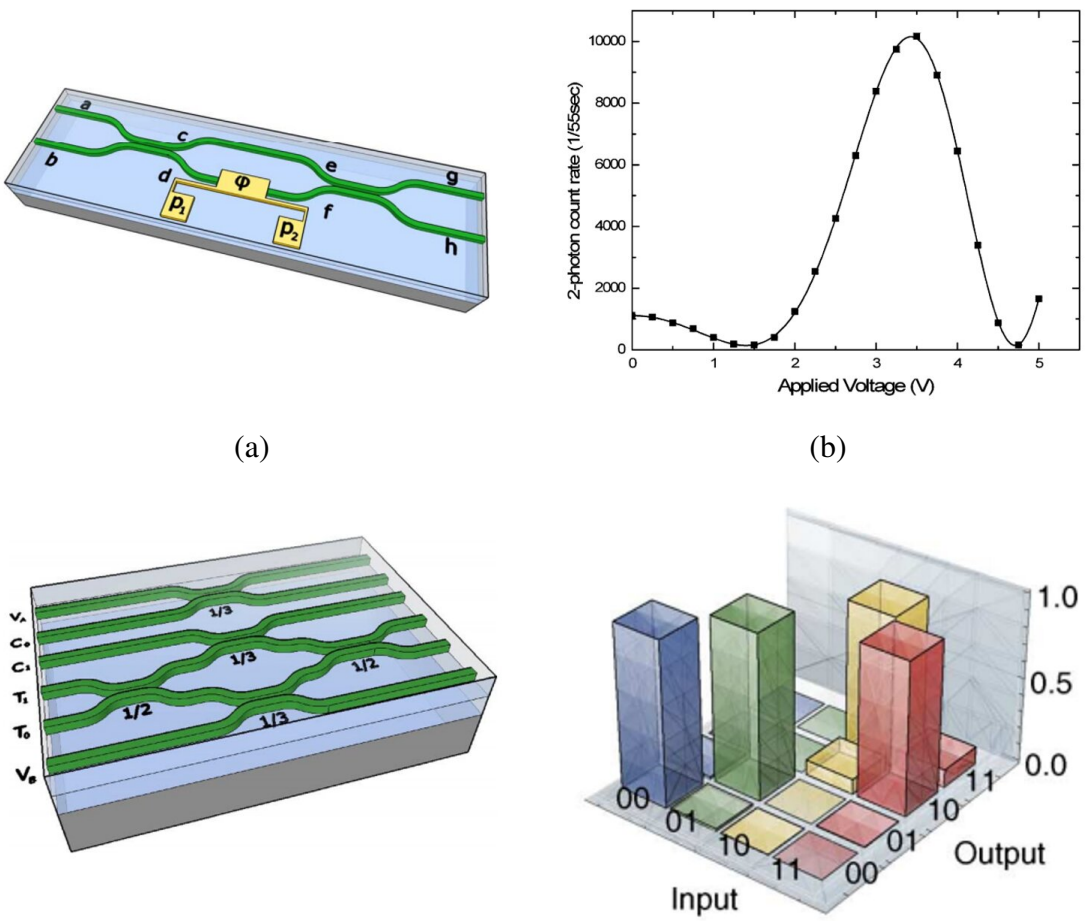

(a) (b)

(c) (d)

Figure 2.11: Qubit operation with integrated quantum photonic chip. (a) Single qubit operation. (b) Interference fringe. (c) CNOT gate. (d) Measured truth table for CNOT gate.

tics schemes has also been demonstrated with the on-chip structure. The corresponding interference fringe and experimental truth table are also plotted.

By scaling these components up, a universal linear optical circuit can be realized to implement an arbitrary unitary matrix as shown in Figure 2.12. The circuit is a 6-mode reconfigurable linear optical circuit with 15 Mach-Zehnder Interferometers (MZIs). Each MZI is formed with 2 directional coupler (DC) and two phase shifters. Photon is generated off chip via the SPDC on BBO Crystal and coupled to chip for com-

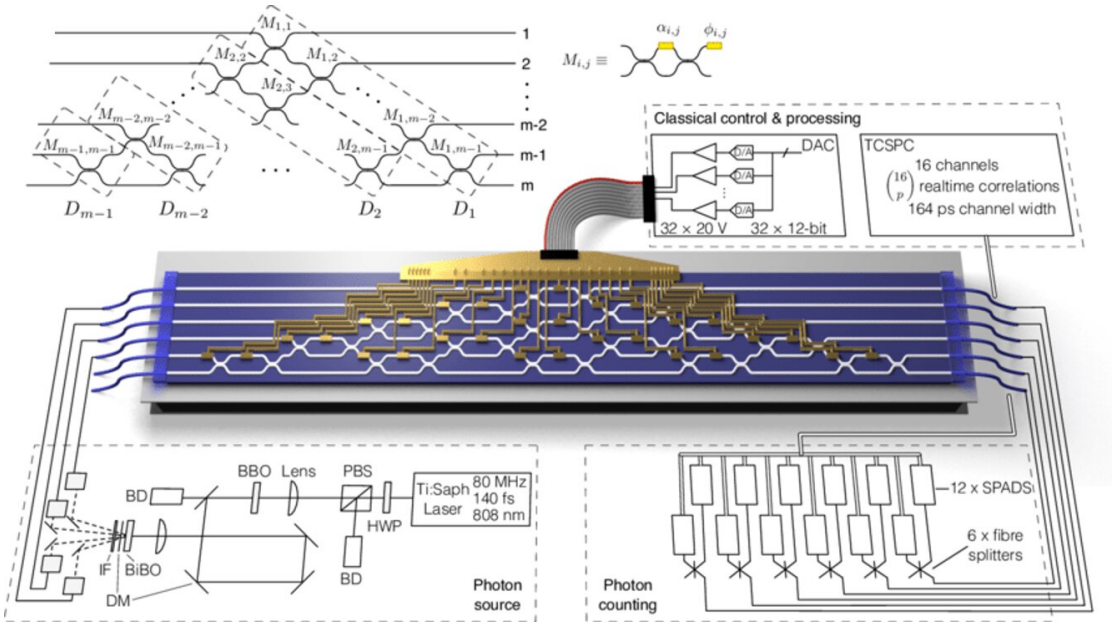

Figure 2.12: A 6-mode universal linear optical circuit to realize arbitrary unitary matrix and perform various quantum computing tasks [5].

putation. The chip is reprogrammed to different configurations to demonstrate multiple tasks like the single qubit rotation operation, two-qubit CNOT gate as well as quantum computation with circuit model and cluster state model, quantum state and process tomography and boson sampling [5].

A larger quantum photonic circuit can have more potentials to realize multiple tasks [6, 7] as shown in Figure 2.13. It is an SOI photonic chip with up to 88 MZIs and a footprint of $4.9mm \times 2.4mm$. A quantum walk is demonstrated to show the Anderson localization and the role of environmental disorder in quantum transport is also studied. Furthermore, the chip is programmed to realize the optical machine learning with fully connected neural network on chip for vowel recognition tasks. Up to two orders of speed up and three orders of energy efficiency than the conventional electrical model is achieved.

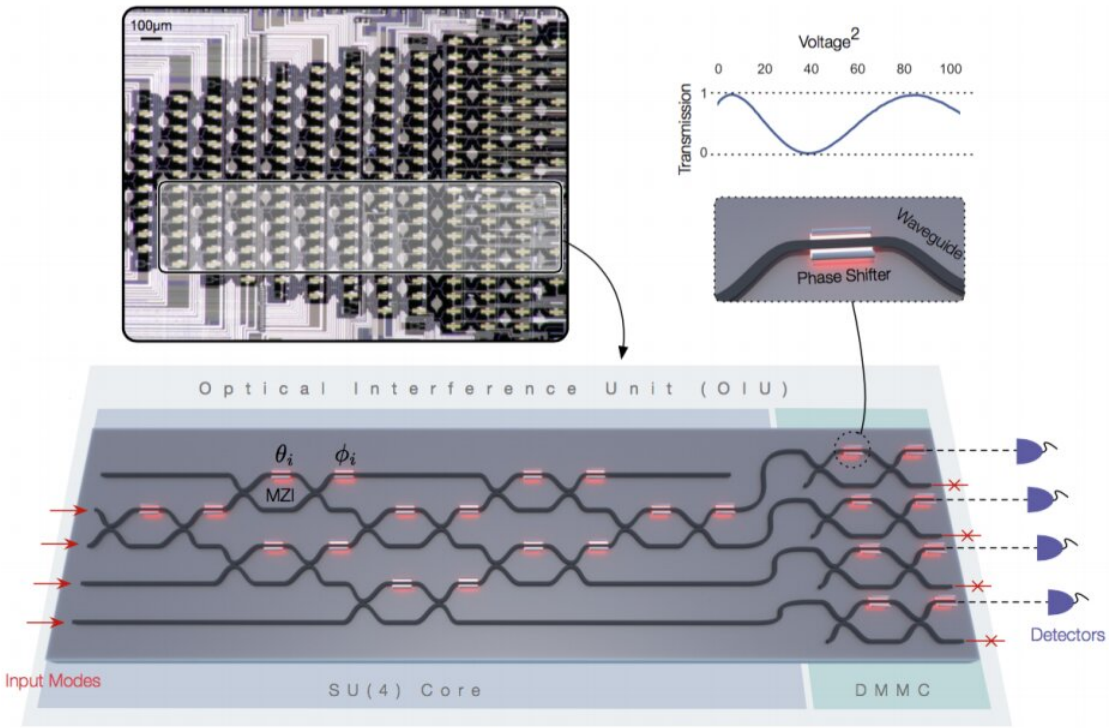

Figure 2.13: A large scale programmable quantum photonic circuit to demonstrate the quantum walk and Anderson localization, quantum transport with noise and quantum machine learning [6, 7].

2.2.2 Quantum Light Source

The first on-chip photon source [8] is demonstrated in Figure 2.14. Quantum interference is measured and exhibits different patterns with the interference of classical light. Such $220nm \times 470nm$ waveguide cross section is specially designed to match the energy conservation and phase matching criteria simultaneously that photon can be generated via the SFWM process. The support photon wavelength also falls at the communication band at around 1550 *nm*, which is compatible with current technologies for optical communication, making SOI platform the most popular candidate for integrated quantum photonics.

Currently, the largest integrated quantum photonic chip is designed by University of Bristol and fabricated in Technical University of Denmark [9] in 2018 to program a

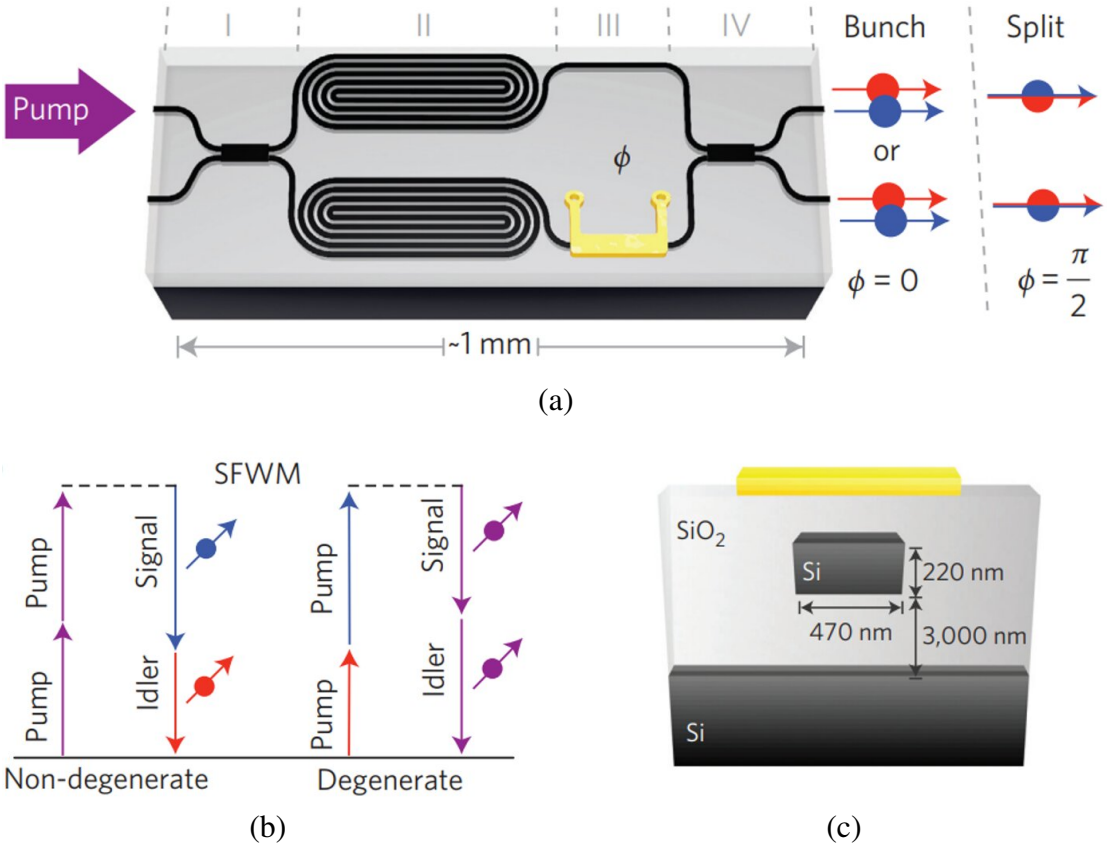

Figure 2.14: First demonstration of on chip photon generation with SFWM process [8]. (a) Schematic of on chip source. (b) Two types of SFWM. (c) Cross section of waveguide.

two photon entangled system of up to 15 dimensions. The chip consists of 16 SFWM sources, 93 tunable phase shifters, 122 MMIs, 256 waveguide cross and 64 grating couplers. The HOM interference between each two pairs of photon source are calibrated with their visibility histogram plotted to shown the indistinguishability. The fidelities in both Z basis and F basis are measured to prove the designed chip is functioning effectively.

Despite all these progresses, the integrated quantum photonic chip is still at the beginning stage of noisy intermediate-scale quantum (NISQ) era [139] with less than 10 logical qubits for demonstrating useful quantum algorithms. Further development of practical quantum computer would require the further studies in following directions:

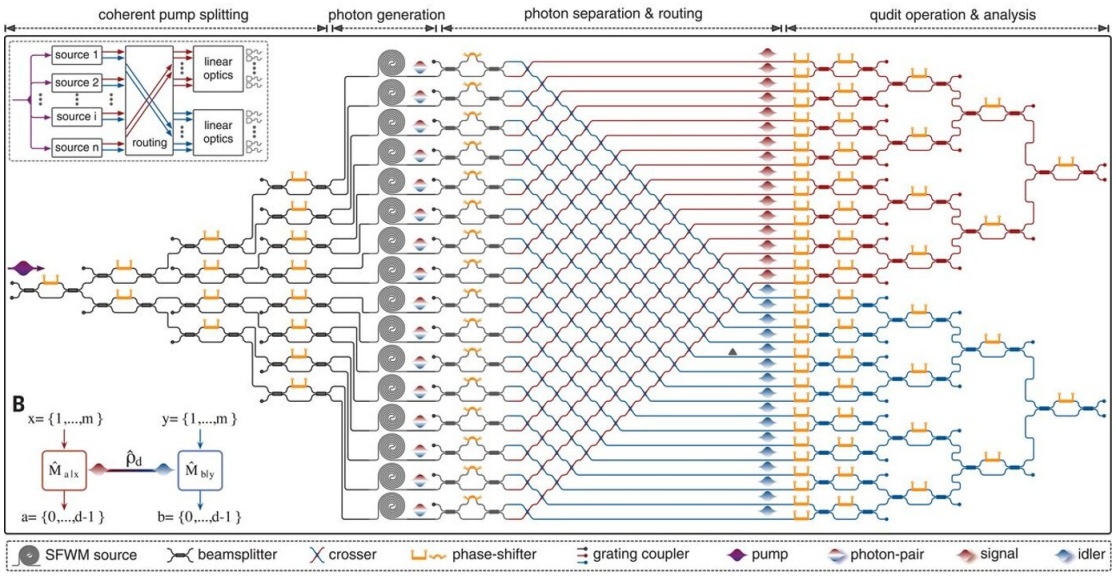

(a)

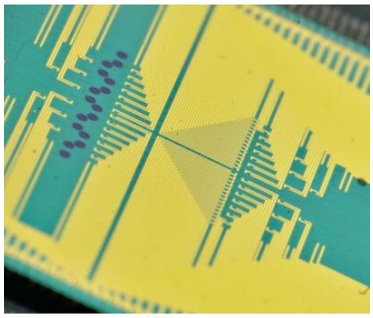

(b)

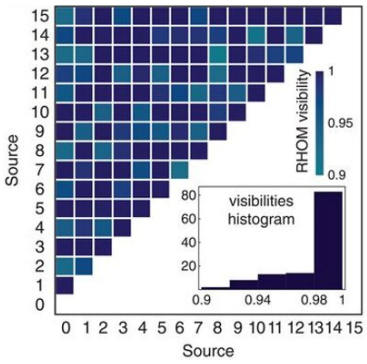

(c)

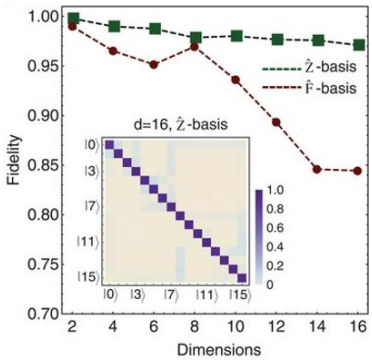

(d)

Figure 2.15: A multi-dimensional qudit generation chip with integrated photon source and over 500 components in a centimeter scale silicon photonic chip [9]. (a) Schematic of chip. (b) Microscope photo of the fabricated chip. (c) Histogram of HOM visibility between arbitrary two sources. (d) Fidelity with the qudit dimension.

reducing error rate of quantum operation to allow the scaling up of quantum computer and the increasing the interconnects of quantum network to allow the direct quantum information flow between different nodes.

2.3 Conclusion

This chapter gives a basic introduction of the quantum information knowledge for an understanding of the thesis and an overall review of the development of integrated quantum photonics for quantum computing. First, the fundamental concept of quantum bit, quantum gate, entanglement, density matrix and tomography is described. Then, two basic models of quantum computer and their implementation method are compared. Next, the previous development of integrated quantum photonic computer chip is illustrated: the two main parts, linear optical circuit and integrated photon source, are reviewed in some detail to show the potential of integrated quantum photonic computer platform. Finally, further exploratory directions in integrated quantum photonic computer are briefly discussed, including the current state-of-art prototypings. Overall, there exists much space for future development of integrated quantum photonic computer.

Chapter 3

Quantum Photonic Circuit

This chapter describes the benchmarks for the quantum photonic integrated circuit parameters. The properties of on-chip single photon sources including purity, distinguishability, squeeze parameter and so on are calibrated. The reconfigurable linear optical circuit to represent arbitrary unitary matrix is also tested on chip to achieve an average fidelity over 98%, which is fundamental for the accuracy of qubit operations on chip. Finally, a boson sampling experiment is conducted to simulate the perfect-matching problem with a high accuracy.

3.1 Theoretical Model of Quantum Photonic Circuit

Quantum photonics is one of the promising platforms to achieve quantum computing. It has the advantage of robustness against decoherence and environmental noise and the ease of manipulation comparing with other matter qubits. In this chapter, the on-chip single photon source and circuit model for photonic integrated circuit model is studied in some detail.

A general quantum integrated circuit mainly includes three parts: a photon source to generate desired quantum state, a photonic circuit to manipulate photons and a detection system to decode quantum information.

3.1.1 Photon Source

An ideal photon source is the key component for quantum computing. It provides the quantum state for various computing models like boson sampling, quantum computing, quantum communication, etc. Currently there are three types of mature technologies for generating photons: the spontaneous parametric down conversion, the spontaneous four wave mixing and quantum dots. The first two methods are realized by inducing the nonlinear properties of material with a pump laser. It is easy to create photons and can maintain a high indistinguishability between photons. However, it is naturally a probabilistic way to create photon pairs and there exist a trade off between generation probability and multi-photon purity. For quantum dot photon sources, the main mechanism is based on the emission of semiconductor material. A pair of carriers, called the exciton, is excited by the injected laser pulse in the quantum dot. The decay of exciton then emits a single photon via the spontaneous emission process. This

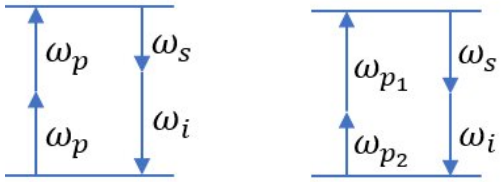

(a) (b)

Figure 3.1: (a) Non degenerated and (b) Degenerated spontaneous four wave mixing process to generate photon pair on chip by absorbing two pump photons.

is a deterministic single photon source that each laser pulse would generate theoretically only one photon each time. There has been reports that the best single photon source has reached the detection efficiency of 0.5 for each laser pulse considering all the collection efficiency, system loss and detection efficiency. However, the single photon source also possesses its own drawbacks, for instance, it requires critical working environment of ultra-low temperature and highly vacuum chambers. It is difficult to maintain the indistinguishability of photons generate from separated quantum dots and people usually take active de-multiplexing technologies to separate a single photon source as a multi-photon source. Quantum dot can only generate single photon, it is unable to generate other non classical quantum state such as the squeeze state, which is another fundamental resource for quantum photonic computing.

In this section, the integrated photon source is studied based on the $\chi^{(3)}$ nonlinear material to induce optical conversion process called the spontaneous four wave mixing (SFWM). It would absorb two pump photons and generate a pair of signal and idler photons. This process is widely used for heralded single photon source, entangled photon pair and squeezed quantum light source with low phase or amplitude noise beneath the standard quantum limit.

Based on the difference of signal and idler photon, the process can be divided into two categories: the non-degenerated SFWM as seen in Figure 3.1a in which the two photons generated have the different wavelengths and, the degenerated SFWM as seen in Figure 3.1b where the two photons have the identical wavelength. From the pump laser point of view, the non-degenerated SFWM is also called the single pump scheme as it only requires a single laser pulse to create the photon pair. The degenerated SFWM is called the dual-pump scheme as the experimental set-up requires two laser pulse working simultaneously to create the photon pair.

The relation between pump frequency and generated photon frequency satisfies the law of energy conservation and momentum conservation as:

$$\omega_{p_1} + \omega_{p_2} = \omega_s + \omega_i \tag{3.1a}$$

$$k_{p_1} + k_{p_2} = k_s + k_i \tag{3.1b}$$

where k is called the wavevector. In waveguide modes, the momentum conservation is also called the phase-matching condition, these wavevectors are the propagation constant $\beta(\omega) = n_{eff}(\omega)\omega$ and $n_{eff}(\omega)$ is the effective index of the corresponding frequency decided by the material nonlinear property.

To realize the photon generation, the main problem is to achieve phase matching condition. Assume the non-degenerated SFWM condition of $\omega_{p_1} = \omega_{p_2} = \omega_p$ and neglecting other nonlinear effects, the difference of propagation constant can be expressed as

$$\Delta\beta = 2\beta(\omega_p) - \beta(\omega_s) - \beta(\omega_i) \tag{3.2}$$

By taking the Taylor expansion of $\beta(\omega_p)$, the phase matching condition can be expressed as

$$\beta = \sum_{n=0}^{\infty} \beta_n \frac{(\omega - \omega_p)^n}{n!}, \tag{3.3a}$$

$$\beta_n = \frac{\partial^n \beta}{\partial \beta^n} \tag{3.3b}$$

where $\Delta\beta$ is expanded in β_n. Due to the limitation of energy conservation law $\omega_{p_1} + \omega_{p_2} = \omega_s + \omega_i$, the difference of frequency can be written as $\delta\omega = \omega_s - \omega_{p_2} = -(\omega_i - \omega_{p_1})$. Therefore, the $\Delta\beta$ can be simplified as

$$\Delta\beta \approx \beta_2(\omega_p)(\Delta\omega)^2 \tag{3.4}$$

where the higher order of terms is ignored. The second order derivative, β_2, is known as group velocity dispersion (GVD) of the waveguide. By selecting the point where GVD $= 0$, $\beta_2 \approx 0$ can be achieved to meet the phase matching condition.

By considering the higher order terms for the derivative of propagation constant [140], the phase matching condition can be written as

$$\Delta\beta \approx \beta_2(\omega_p)(\Delta\omega)^2 + \frac{\beta_4(\omega_p)}{12}(\Delta\omega)^4 \tag{3.5}$$

If the waveguide is designed to make β_2 and β_4 assume opposite sign and the magnitude appropriately adjusted, the phase matching can be achieved.

When the pump photon and generated photon are propagating on different modes, their propagation constant are unrelated to each other [67]. The phase matching condi-

tion can thus be written as

$$\Delta\beta \approx 2\beta_p(\omega_p) - \beta_i(\omega_p) - \beta_s(\omega_p) + \Delta\omega(\beta_{1,i} - \beta_{1,s}) \tag{3.6}$$

If the propagation constant difference $\Delta\beta$ matching with the group velocity $\beta(\omega)$ is found, the phase matching can be realized.

Finally, the waveguide parameter can be modulated periodically with quasi-phase matching conditions [141], which is simplified as

$$\Delta\beta = \Delta\beta_0 + \frac{2\pi}{\Lambda} \tag{3.7}$$

where Λ is the periodicity of poling designed to match $\Delta\beta = 0$.

For simple case of $\beta_2 \approx 0$, the approximation $\omega_p \approx \omega_s \approx \omega_i$ is taken and the energy conservation in wavelength domain is expressed as

$$\lambda_{p_1} + \lambda_{p_2} \approx \lambda_s + \lambda_i \tag{3.8}$$

The probability of two-photon state is decided by the energy conservation and phase matching condition with expression given by

$$|11\rangle \propto \int\int d\omega_s d\omega_i F(\omega_s, \omega_i) |11\rangle_{s,i}. \tag{3.9}$$

This is interpreted as the distribution of two-photon state $|11\rangle_{s,i}$ at mode s and i and the probability amplitude $F(\omega_s, \omega_i)$ is called the Joint Spectra Amplitude (JSA). The latter is dictated the law of energy conservation and phase matching and it can be expressed

as

$$F(\omega_s, \omega_i) = \int d\omega \alpha(\omega_s + \omega_i - \omega)\phi(\omega_s, \omega_i, \omega), \tag{3.10}$$

where $\alpha(\omega_s + \omega_i - \omega)$ is the complex amplitude of the pump ω_p at the frequency $\omega_s + \omega_i - \omega$. Usually the pump spectrum is assumed to be a Gaussian distribution with a bandwidth decided by pump filter or laser property. $\phi(\omega_s, \omega_i, \omega)$ is defined as

$$\phi(\omega_s, \omega_i, \omega) = e^{i\frac{\Delta\beta L}{2}} sinc(\frac{\Delta\beta L}{2}), \tag{3.11}$$

where it is determined by the phase matching condition. The L is the interaction length of waveguide. $|F(\omega_s, \omega_i)|^2$ is the real measured probability of photon pair and is called the Joint Spectra Intensity (JSI).

Taking all these factors into consideration, the state can be expressed as

$$|\phi\rangle = \prod_n \otimes \hat{S}^n_{s,i}(\xi_n) |0\rangle_s |0\rangle_i \tag{3.12}$$

where $\hat{S}^n_{s,i}(\xi)$ is called the squeeze operator on the mode n and ξ_n is the squeeze parameter determined by the material nonlinearity, interaction length, pump energy density and so on. Depending on whether the squeeze parameter condition is filtered or resonated SFWM, the output state is given by

$$\begin{aligned} |\phi\rangle =& \hat{S}_{s,i}(\xi) |0\rangle_s |0\rangle_i \\ =& e^{\xi^* \hat{a}_i \hat{a}_s - \xi \hat{a}_i{}^\dagger \hat{a}_s{}^\dagger} |0\rangle_s |0\rangle_i \end{aligned} \tag{3.13}$$

and by writing $\xi = re^{i\phi}$, the state in photon number basis is expressed as

$$\begin{aligned} |\phi\rangle =& \frac{1}{\cosh r} \sum_{n=0}^{\infty} (-e^{i\phi} \tanh r)^n |n\rangle_s |n\rangle_i \\ =& \sum_{n=0}^{\infty} C_n |n\rangle_s |n\rangle_i \end{aligned} \tag{3.14}$$

The probabilities for detecting n photons at mode s or mode i are the same, which is expressed as

$$P_s(n) = P_i(n) = P(n) = |C_n|^2 = \frac{(\tanh r)^{2n}}{\cosh^2 r} \tag{3.15}$$

Following the Equation 3.12, a maximum entangled two-photon state from SFWM process can be written as

$$|\phi\rangle = \frac{1}{\sqrt{n}} (|1\rangle_{s,1} |1\rangle_{i,-1} + |1\rangle_{s,2} |1\rangle_{i,-2} + |1\rangle_{s,3} |1\rangle_{i,-3} + \cdots + |1\rangle_{s,n} |1\rangle_{i,-n}) \tag{3.16}$$

with different modes from 1 to n. And it is known that the state describing a composition system is decomposed as

$$|\phi\rangle = \sum_{i=1}^{n} \sqrt{\lambda_i} |u_i\rangle \otimes |v_i\rangle \tag{3.17}$$

where $\{|u_i\rangle\}$ and $\{|v_i\rangle\}$ are orthonormal basis states called Schmidt modes. The Schmidt coefficients λ_i are the "weights" of each subsystem satisfying $\sum_i \lambda_i = 1$. Its degree of factorizability is called the Schmidt number K and is defined as

$$K = \frac{1}{\sum_{i=1}^{n} \lambda_i^2} \in [1, n] \tag{3.18}$$

The photon purity P of this state is defined as

$$P = \frac{1}{K} \in [\frac{1}{n}, 1] \tag{3.19}$$

where $p = 1$ represents $K = 1$ and $\lambda_1 = 1$, indicating a perfectly pure two-photon state. If $P < 1$ is measured, it means the state also contains other degree of entangled photon pairs. For a maximally entangled state with the condition that $\lambda_n = \frac{1}{n}$ and $n \to \infty$, $P \to 0$, which indicates that the state has almost no purity (maximally mixed) and is not suitable for a heralded single photon source.

In the weak pump regime, the multi-photon probability $P(n)$ is relatively low and the purity P can be directly estimated as

$$P = \frac{1}{K} = g^{(2)}(0) - 1 \tag{3.20}$$

where $g^{(2)}(0)$ is called the second order correlation. It is an experimentally measurable value that describes the statistics of photon pairs correlations. From the reference [142], the $g^{(2)}$ can be written as

$$g^{(2)}(\Delta t) = \frac{P_{ss}(\Delta t)}{P_s P_s} \tag{3.21}$$

where $P_{ss}(\Delta t)$ is the probability of measuring coincidence counts at the delay time of Δt and P_s is the probability of measuring signal photon at the detector.

With the heralded photon measured, the remaining photon state can be used as a single photon state and the purity of this heralded single photon $g_h^{(2)}(t)$ describes the

quantity of single-photon against the multi-photon emission. It can be written as

$$g_h^{(2)}(\Delta t) = \frac{P_{ssi}(\Delta t)}{P_{s1i}(\Delta t)P_{s2i}(\Delta t)}P_i \tag{3.22}$$

where $P_{ssi}(\Delta t)$ and $P_{si}(\Delta t)$ are the probabilities of measuring coincidence count at the delay time of Δt and P_i is the probability of measuring signal photon.

The noise of the measured photon counts is estimated by coincidence to accidental ratio (*CAR*). Coincidence counts between signal and idler photons from the same pair of photon generation are desired counts while the spurious coincidence between time uncorrelated different pairs or other noises are called the accidental coincidences. The *CAR* is defined as

$$CAR = \frac{R_{si} - R_{ac}}{R_{ac}} \tag{3.23}$$

where R_{si} is the overall coincidence between signal channel and idler channel and R_{ac} is the accidental coincidence.

3.1.2 Photonic Circuit Model of Quantum Photonic Computer

After generating single photon on chip, there are still many other components that are required for manipulating these photons to realize different algorithms and measurements. For the integrated quantum photonic circuit, the degree of freedom to control is the waveguide modes a photon can occupy. Therefore, the beam splitters (BS) and phase shifters (PS) are used to realize the amplitude and phase modulation at each waveguide mode. Each optical component is described with a transformation matrix.

The beam splitter shown in Figure 3.2a is an multi-mode interferometer (MMI)

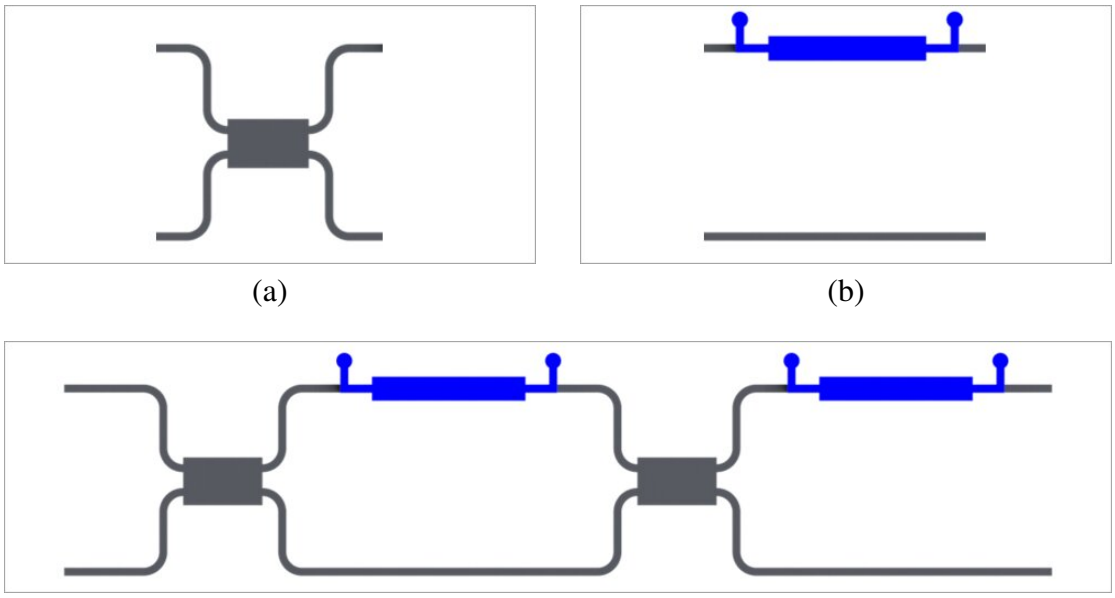

(a) (b)

(c)

Figure 3.2: Schematic of MZI. (a) Multi-mode interferometer to split the light passively with a fixed ratio of 1:1. (b) Phase shifter to induce relative phase change between two arms. (c) Mach-Zehnder Interferometer with two fixed MMI and two tunable Phase shifter to realize arbitrary unitary matrix.

with specially designed interference length and multi-mode area that splits the photon into a superposition state. Its transformation matrix can be written as

$$T_{BS} = \frac{1}{\sqrt{2}} \begin{bmatrix} 1 & i \\ i & 1 \end{bmatrix} \tag{3.24}$$

For phase shifter as shown in Figure 3.2b, it is a waveguide with a TiN resistor on it. A current can flow through it via the Digital-to-Analogue Converter (DAC) to generate heat and change the refractive index of the surrounding waveguide. The optical path different changes and induces a phase difference θ. Its transformation matrix is

written as

$$T_\theta = \begin{bmatrix} e^{i\theta} & 0 \\ 0 & 1 \end{bmatrix} \tag{3.25}$$

If the PS θ moves to the lower arm of waveguide, its transformation matrix is adjusted accordingly so that the element $T_{4,4}$ becomes $e^{i\theta}$.

The Mach-Zehnder Interferometer (MZI) is formed by combining beam splitter and phase shifter together to realize arbitrary splitting ratio and phase difference of a photon. Its transformation can be written as

$$\begin{aligned} T_{MZI} =& T_\phi \cdot T_{BS} \cdot T_\theta \cdot T_{BS} \\ =& \begin{bmatrix} e^{i\phi} & 0 \\ 0 & 1 \end{bmatrix} \cdot \frac{1}{\sqrt{2}} \begin{bmatrix} 1 & i \\ i & 1 \end{bmatrix} \cdot \begin{bmatrix} e^{i\theta} & 0 \\ 0 & 1 \end{bmatrix} \cdot \frac{1}{\sqrt{2}} \begin{bmatrix} 1 & i \\ i & 1 \end{bmatrix} \\ =& \begin{bmatrix} e^{i\phi} & 0 \\ 0 & 1 \end{bmatrix} \cdot \frac{1}{2} \begin{bmatrix} e^{i\theta}-1 & ie^{i\theta}+i \\ ie^{i\theta}+i & -(e^{i\theta}-1) \end{bmatrix} \end{aligned} \tag{3.26}$$

According to Eular's formula, the matrix elements in Equation 3.26 can be simplified as

$$e^{i\theta} - 1 = e^{i\frac{\theta}{2}}(e^{i\frac{\theta}{2}} - e^{-i\frac{\theta}{2}}) = 2ie^{i\frac{\theta}{2}} \sin\frac{\theta}{2} \tag{3.27a}$$

$$e^{i\theta} + 1 = e^{i\frac{\theta}{2}}(e^{i\frac{\theta}{2}} + e^{-i\frac{\theta}{2}}) = 2e^{i\frac{\theta}{2}} \cos\frac{\theta}{2} \tag{3.27b}$$

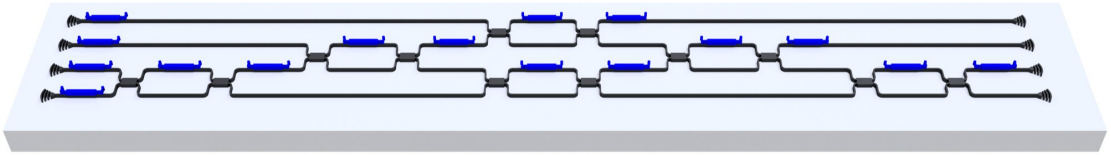

Figure 3.3: Typical schematic of an N-mode photonic integrated circuit to represent an arbitrary $N \times N$ unitary matrix. The final unitary matrix form is the product of matrix for each MZI component.

Therefore, the T_{MZI} can be written as

$$\begin{aligned} T_{MZI} &= \begin{bmatrix} e^{i\phi} & 0 \\ 0 & 1 \end{bmatrix} \cdot ie^{i\frac{\theta}{2}} \begin{bmatrix} \sin\frac{\theta}{2} & \cos\frac{\theta}{2} \\ \cos\frac{\theta}{2} & -\sin\frac{\theta}{2} \end{bmatrix} \\ &= ie^{i\frac{\theta}{2}} \begin{bmatrix} e^{i\phi}\sin\frac{\theta}{2} & e^{i\phi}\cos\frac{\theta}{2} \\ \cos\frac{\theta}{2} & -\sin\frac{\theta}{2} \end{bmatrix} \end{aligned} \tag{3.28}$$

The splitting ratio is determined by the inner PS angle, θ, to be $\sin^2\frac{\theta}{2} : \cos^2\frac{\theta}{2}$ and the phase difference between two output ports is $e^{i\phi}$. When the PS position is changed to add the ϕ at the front of the MZI structure, its transformation matrix can then be expressed as

$$T_{MZI} = T_{BS} \cdot T_{\theta} \cdot T_{BS} \cdot T_{\phi} ie^{i\frac{\theta}{2}} \begin{bmatrix} e^{i\phi}\sin\frac{\theta}{2} & \cos\frac{\theta}{2} \\ e^{i\phi}\cos\frac{\theta}{2} & -\sin\frac{\theta}{2} \end{bmatrix} \tag{3.29}$$

The transformation matrix of BS and PS both satisfies the definition of Unitary matrix given by

$$T \cdot T^{\dagger} = \begin{bmatrix} 1 & 0 \\ 0 & 1 \end{bmatrix} \tag{3.30}$$

and it is obvious to see that T_{MZI} is also a Unitary matrix.

An N-mode integrated quantum photonic circuit is composed of several MZI struc-

tures and it can form a complicated $N \times N$ Unitary matrix as shown in Figure 3.3. The nth MZI between mode i and j is denoted as M_n. Its transformation matrix can be represented as an Identity matrix I_N with four matrix elements $\{a_{i,i}, a_{i,j}, a_{j,i}, a_{j,j}\}$ replaced by T_{MZI}, which is expressed as

$$M_n = \begin{bmatrix} 1 & \cdots & & \\ \vdots & a_{i,i} & a_{i,j} & \\ & a_{j,i} & a_{j,j} & \vdots \\ & & \cdots & 1 \end{bmatrix}_N \tag{3.31}$$

where $a_{i,i} = T_{MZI}(1,1), a_{i,j} = T_{MZI}(1,2), a_{j,i} = T_{MZI}(2,1), a_{j,j} = T_{MZI}(2,2)$. Therefore, the unitary matrix of this N-mode photonic circuit U_N can be represented as the product of MZI transform matrices in the designed orders as

$$U_N = \prod_n M_n \tag{3.32}$$

The detection system is a multi-channel superconducting single photon detector. It can absorb an energy equivalent to a single photon and convert it into electrical signal in the superconducting circuit. Then the signal is then amplified and processed by the time tagger to measure coincidence count.

3.1.3 Boson Sampling and Perfect Matching for Graph

Since the advent of quantum computer, it is well known that the quantum computer can exploit the exponential scaling of Hilbert space and harness its seemingly unlimited computational power [143, 144].

In 2004, Stefan Scheel first discussed the photon distribution after the evolution of a linear optical network [145], showing the capacity of quantum computation with merely single photon and a linear optical circuit. In 2011, Scott Aaronson and Alex Arkhipov further developed this idea to propose the boson sampling [146] to demonstrate such quantum advantage. It is experimentally feasible for quantum photonics relying solely on photon source, linear optical circuit U and detectors to achieve the advantage. M photons are initially prepared (as a separable state) and get injected into a circuit with N waveguide modes so that

$$\sum_{k=1}^{N} s_k = M \tag{3.33a}$$

$$|\psi_{in}\rangle = |s_1, s_2, \cdots, s_N\rangle \tag{3.33b}$$

where s_k is the photon number at waveguide mode k. The output state can then be written as

$$|\psi_{out}\rangle = W\,|s_1, s_2, \cdots, s_N\rangle \tag{3.34}$$

where W is the transformation matrix from input state to output state. The evolved quantum state is hard to predict and the probability for distribution of detecting t_k photons at k mode is described as

$$Pr(t_1, t_2, \cdots, t_N) = |\,\langle t_1, t_2, \cdots, t_N|\psi_{out}\rangle\,|^2 = \frac{|Perm(U_{S,T})|^2}{t_1! \cdots t_N! s_1! \cdots s_N!} \tag{3.35}$$

where $U_{S,T}$ is obtained from the unitary matrix U of linear optical circuit with by taking s_k times the k-th column of U and t_k times the k-th row of U to form an $M \times M$ submatrix $U_{S,T}$.

The nature of this computational complexity lies with the #*P*-hard [147, 148] problem of permanent calculation. There have been benchmarks showing that the computation of a single permanence for matrix size of 48 with a supercomputer would take more than an hour [149] and the largest sampling problem simulated is 50-photon Gaussian boson sampling performed by Sunway TaihuLight Supercomputer [150]. Considering the exponential increase of complexity, matrix size of 50 would be a reasonable limit for current classical supercomputer. To date, there have been many experimental demonstrations of boson sampling [90, 91, 151, 152]. In 2017, high efficiency boson sampling with five photons were performed [135]. The researchers claim that the computation exceeds the first prototype of early electronic computers. The boson sampling has been further optimised to scattershot boson sampling and Gaussian boson sampling with a modified input state to achieve more quantum advantage experimentally. There have also been reports of measurements involving up to 18 photons with integrated quantum photonic chip [153]. In 2020, a tour de force experiment with 76 photons using bulk optics was performed [154].

Boson sampling as a process itself is a mathematical problem without much direct practical applications. However, many problems can be mapped to it as part of the simulation and these problems benefit from the quantum computation power that can achieve speed-up. One of such problem is perfect matching problems in graph theory. The probability of a Gaussian boson sampling distribution with M output photons in an

$N \times N$ circuit is expressed as [155]

$$Pr(\bar{m}) = \frac{1}{\bar{m}!\sqrt{det\,\sigma_Q}} haf(A_S) \tag{3.36a}$$

$$\sigma_Q = \sigma_A + I_{2N}/2 \tag{3.36b}$$

$$A = X_{2N}[I_{2N} - (\sigma_A + I_{2N}/2)^{-1}] \tag{3.36c}$$

$$X_{2N} = \begin{bmatrix} 0 & I_N \\ I_N & 0 \end{bmatrix} \tag{3.36d}$$

where $\bar{m}$ is the output photon distribution limited to 1 photon and 0 photon condition at each mode, σ_A is the covariance matrix of the Gaussian boson sampling circuit, A_S is the submatrix of A decided by the target distribution $\bar{m}$. The calculation of the hafnian $haf(A_S)$ is also a computationally intractable problem for a supercomputer while it is feasible using Gaussian boson sampling on photonic platform. In this thesis, the perfect matching of a graph with 6 vertexes is demonstrated with Gaussian boson sampling circuit.

3.2 Design of Quantum Photonic Circuit

In the design of the experiment, a quantum photonic chip with integrated photon source and a reconfigurable linear optical circuit is fabricated to study the properties of on-chip photon source, linear optical circuit. After the full characterization of the photonic integrated system, a boson sampling experiment for graph perfect matching simulation is conducted.

The detailed schematic of the chip is shown in Figure 3.4a. The coupling of the

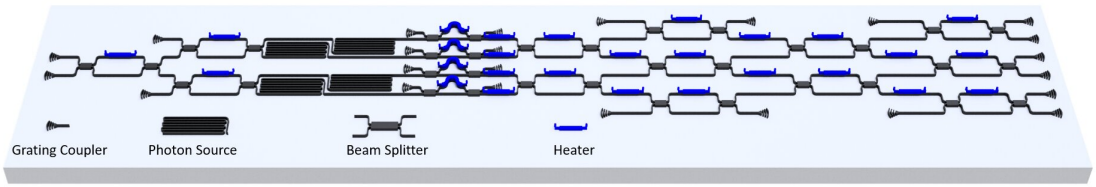

(a)

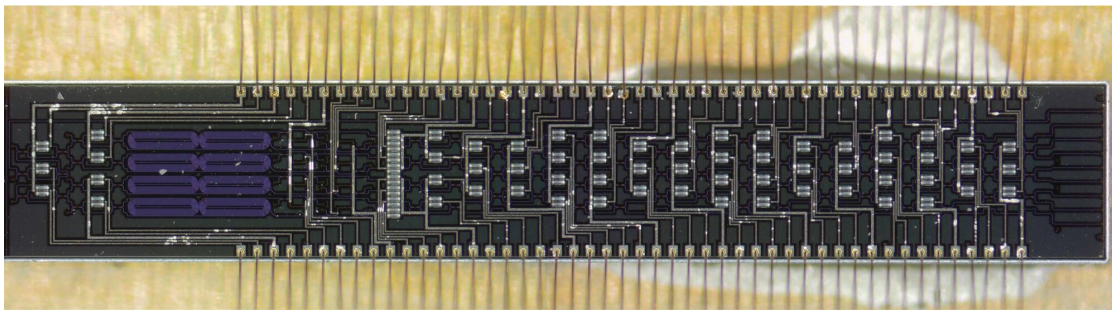

(b)

Figure 3.4: (a) Schematic of the chip to realize squeeze state and unitary matrix. (b) The microscope photograph of the fabricated photonic chip. It contains 8 photon sources and 75 tunable phase shifters.

light between fibre and waveguide is done via a grating coupler. The chip includes two parts: the spiral waveguide sources and a reconfigurable linear optical circuit to represent arbitrary unitary matrix. The pump power for each source is tunable by changing the splitting ratio of MZIs before the spiral waveguides so that each source can be adjusted to a specific squeezing parameter. Then the pump power is filtered out by AMZI and the photons would enter the linear optical cirucit part for quantum simulation based on the implemented algorithm. Finally the photon is coupled outside the chip via a fiber grating array. The photograph of the fabricated chip under a microscope is shown in Figure 3.4b, this 8-mode quantum photonic circuit contains 75 tunable phase shifters in a footprint of $10mm \times 1.6mm$. The two rows of metal pads at upper and lower edges are bonded to PCB with golden wires for external control of each heater with DAC. By implementing the initial quantum states and a target unitary matrix, the circuit can function as a quantum computer to realize some particular tasks.

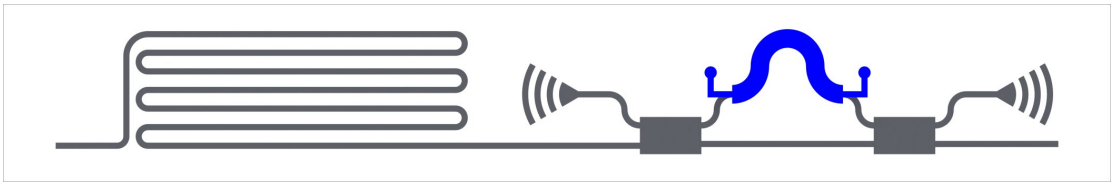

Figure 3.5: Schematic of the on-chip photon source. A spiral waveguide structure is pumped to generate photons. The following AMZI is to remove the pump and reduce the spurious photon.

3.2.1 On Chip Photon Source

For the on-chip light source, the SFWM process is implemented to generate photons on spiral waveguides as shown in Figure 3.5. Both degenerated SFWM and generated SFWM process can be realized with this structure by changing the pump laser. The following AMZI structure is used to filter out the pump laser to reduce the noise photon generated at the linear circuit part of the chip.

3.2.2 Matrix Decomposition Scheme

Under the circuit model, it has been known that a linear circuit model can be mapped to a unitary matrix. An important problem is to realize a given matrix by designing the linear optical circuit parameters. There has been study showing that an arbitrary $N \times N$ Unitary circuit can be decomposed by $\frac{N(N-1)}{2}$ MZIs with specific orders. Two of the main decomposition schemes are the Triangle Circuit [73] and the Square Circuit [75].

The triangle circuit model is shown in Figure 3.6a with its MZI order in a triangle shape. The $\frac{N(N-1)}{2}$ MZIs are distributed in $(N-1)$ lines diagonally with the ith line containing i MZIs. The 4-mode circuit is taken as an example to show how to implement

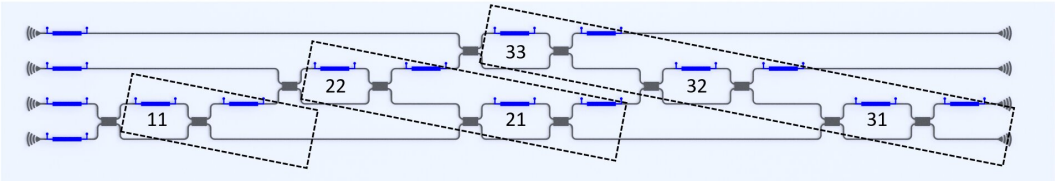

(a)

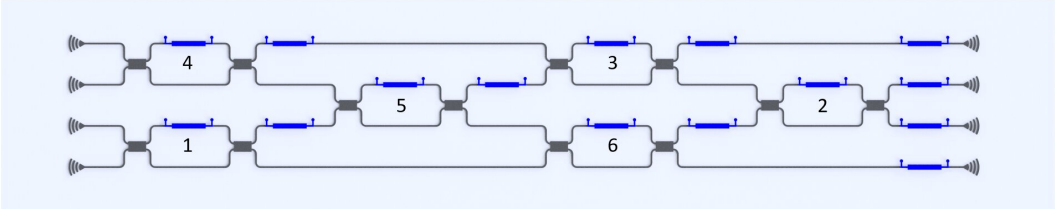

(b)

Figure 3.6: Two typical decomposition schemes of an $N \times N$ unitary matrix. (a) The triangle scheme and (b) the square scheme.

an arbitrary unitary matrix $U_{4\times4}$ with tunable MZI parameters.

When the light is inputted from the first port of the circuit, the distribution at 4 output ports can be expressed as

$$\begin{bmatrix} a_{11} & * & * & * \\ a_{21} & * & * & * \\ a_{31} & * & * & * \\ a_{41} & * & * & * \end{bmatrix} \cdot \begin{bmatrix} 1 \\ 0 \\ 0 \\ 0 \end{bmatrix} = \begin{bmatrix} a_{11} \\ a_{21} \\ a_{31} \\ a_{41} \end{bmatrix} \tag{3.37}$$

where * means unlabeled matrix elements. From the schematic diagram of the triangle circuit in Figure 3.6a it is noticed that the input light from first port would only go through MZI 33, 32, 31. Therefore, the splitting ratio and relative phase of the output light is fully decided by these three MZIs. For the output light a_{31}, and a_{41}, it is split

from MZI 31 with input light from the upper arm, the process can be written as

$$ie^{i\frac{\theta}{2}}\begin{bmatrix} e^{i\phi}\sin\frac{\theta}{2} & e^{i\phi}\cos\frac{\theta}{2} \\ \cos\frac{\theta}{2} & -\sin\frac{\theta}{2} \end{bmatrix}\cdot\begin{bmatrix} 1 \\ 0 \end{bmatrix} = ie^{i\frac{\theta}{2}}\begin{bmatrix} e^{i\phi}\sin\frac{\theta}{2} \\ \cos\frac{\theta}{2} \end{bmatrix} = \begin{bmatrix} a_{31} \\ a_{41} \end{bmatrix} \tag{3.38}$$

Therefore, an appropriate pair of θ and ϕ for MZI 31 should be tuned to match the expression given by

$$\tan\left(\frac{\theta}{2}\right)\cdot|a_{41}| = |a_{31}| \tag{3.39a}$$

$$\arg(a_{31}) - \arg(a_{31}) = \phi \tag{3.39b}$$

where $\arg(a)$ means the phase of a complex number in polar coordinates.

When the unitary matrix is represented as the product of n MZI as U_n, the original target unitary matrix is U_6 and unitary matrix U_5 before MZI 31 can be derived and shown to be

$$M_{31}\cdot U_5 = U_6 \rightarrow U_5 = M_{31}^{-1}\cdot U_6 \tag{3.40}$$

where MZI^{-1} means that the inverse matrix and the matrix element a_{41} of U_5 is 0. Similarly, the parameter of M_{32} can be calculated from matrix elements a_{31}, a_{21} to get $U_4 = M_{32}^{-1}\cdot U_5$. By repeating this step for M_{33}, the U_3 can be deduced as

$$U_3 = \begin{bmatrix} a_{11} & 0 & 0 & 0 \\ 0 & a_{22} & a_{23} & a_{24} \\ 0 & a_{32} & a_{33} & a_{34} \\ 0 & a_{42} & a_{43} & a_{44} \end{bmatrix} \tag{3.41}$$

The element a_{12}, a_{13}, a_{14} would be 0 after applying $U_3 = M_{33}^{-1} \cdot U_4$ because M_n is a unitary transformation and U_n matrix would also remain to be unitary during the decomposition process, which would satisfy the following restriction expressed as

$$U_3 \cdot U_3^{-1} = U_3^{-1} \cdot U_3 = I \tag{3.42a}$$

$$U_3 \cdot U_3^{-1} = I \rightarrow |a_{11}|^2 + |a_{12}|^2 + |a_{13}|^2 + |a_{14}|^2 = 1 \tag{3.42b}$$

$$U_3^{-1} \cdot U_3 = I \rightarrow |a_{11}|^2 = 1 a_{12} = a_{13} = a_{14} = 0 \tag{3.42c}$$

By further calculating the parameter for MZI 21 and 22 from the matrix element a_{42}, a_{32}, a_{22}, the unitary matrix U_1 can be simplified as

$$U_1 = \begin{bmatrix} a_{11} & 0 & 0 & 0 \\ 0 & a_{22} & 0 & 0 \\ 0 & 0 & a_{33} & a_{34} \\ 0 & 0 & a_{43} & a_{44} \end{bmatrix} \tag{3.43}$$

and the last MZI 11 is obtained from a_{33}, a_{43}, simplifying the U_1 to U_0 into a diagonal matrix given by

$$U_0 = \begin{bmatrix} e^{i\phi_1} & 0 & 0 & 0 \\ 0 & e^{i\phi_2} & 0 & 0 \\ 0 & 0 & e^{i\phi_3} & 0 \\ 0 & 0 & 0 & e^{i\phi_4} \end{bmatrix} \tag{3.44}$$

which represents 4-phase shifters at each waveguide mode.

An arbitrary unitary matrix U_6 can be decomposed as

$$U_6 = M_{31} \cdot M_{32} \cdot M_{33} \cdot M_{21} \cdot M_{22} \cdot M_{11} \cdot U_0 \tag{3.45}$$

based on the proposed decomposed scheme, it is easy to understand how each MZI affects the final unitary matrix and how the device can be implemented on chip.

Another decomposition scheme is the square circuit model shown in Figure 3.6b. It is not obvious as the triangle scheme but has a more compact design to shrink the area size (footprint) of the circuit and is a more symmetric structure to balance the loss of each mode.

First, the row operation and column operation of the matrix is introduced as a unitary operation, which is given by

$$T = \begin{bmatrix} 1 & \cdots & & \\ \vdots & a_{i,i} & a_{i,j} & \\ & a_{j,i} & a_{j,j} & \vdots \\ & & \cdots & 1 \end{bmatrix}_N \tag{3.46}$$

and the unitary matrix is expressed as

$$U = \begin{bmatrix} r_1 \\ r_2 \\ \vdots \\ r_N \end{bmatrix}_N = \begin{bmatrix} c_1 & c_2 & \cdots & c_N \end{bmatrix}_N \tag{3.47}$$

where r_i and c_i means the row vector and column vector of the matrix U. The left

multiplexing on the unitary matrix U with operator T can be expressed as

$$T \cdot U = \begin{bmatrix} 1 & \cdots & & \\ \vdots & a_{i,i} & a_{i,j} & \\ & a_{j,i} & a_{j,j} & \vdots \\ & & \cdots & 1 \end{bmatrix} \cdot \begin{bmatrix} r_1 \\ r_2 \\ \vdots \\ r_N \end{bmatrix} = \begin{bmatrix} r_1 \\ \vdots \\ a_{i,i}r_i + a_{i,j}r_j \\ a_{j,i}r_i + a_{j,j}r_j \\ \vdots \\ r_N \end{bmatrix} \tag{3.48}$$

and the right multiplexing on the unitary matrix U with operation T can be expressed as

$$\begin{aligned} U \cdot T &= \begin{bmatrix} c_1 & c_2 & \cdots & c_N \end{bmatrix} \cdot \begin{bmatrix} 1 & \cdots & & \\ \vdots & a_{i,i} & a_{i,j} & \\ & a_{j,i} & a_{j,j} & \vdots \\ & & \cdots & 1 \end{bmatrix} \\ &= \begin{bmatrix} c_1 & \cdots & a_{i,i}c_i + a_{j,i}c_j & a_{i,j}c_i + a_{j,j}c_j & \cdots & c_N \end{bmatrix} \end{aligned} \tag{3.49}$$

It is obvious to conclude that the left multiplexing is performing the row operation on unitary matrix U while the right multiplexing is performing the column operation on the unitary matrix U.

A 4×4 unitary matrix with 6 unitary transformation matrix labeled with $\{ T_1, T_2, T_3, T_4, T_5, T_6 \}$ is shown as an example to illustrate the decomposition process, which is

expressed as

$$U \xrightarrow{U \cdot T1_{3,4}} \begin{bmatrix} \cdots & * & 0_1 \\ & \vdots & \vdots \\ & & \end{bmatrix}_{4\times4} \tag{3.50a}$$

$$\xrightarrow{T3_{1,2} \cdot T2_{2,3} \cdot U \cdot T1_{3,4}} \begin{bmatrix} \cdots & 0_3 & 0_A \\ & * & 0_2 \\ & & * \\ & & \vdots \end{bmatrix}_{4\times4} \tag{3.50b}$$

$$\xrightarrow{T3_{1,2} \cdot T2_{2,3} \cdot U \cdot T1_{3,4} \cdot T4_{1,2} \cdot T5_{2,3} \cdot T6_{3,4}} \begin{bmatrix} * & 0_4 & 0_3 & 0_1 \\ & * & 0_5 & 0_2 \\ & & * & 0_6 \\ & & & \vdots \end{bmatrix}_{4\times4} \tag{3.50c}$$

where the mark * represents the matrix elements involved to simplify other elements to 0 and 0_i to indicate the corresponding operator Ti. The remaining matrix would be a diagonal matrix U_d since all the transformation matrices are unitary. By taking the inverse process, the original unitary matrix U can be written as

$$U_d = T3_{1,2} \cdot T2_{2,3} \cdot U \cdot T1_{3,4} \cdot T4_{1,2} \cdot T5_{2,3} \cdot T6_{3,4} \tag{3.51a}$$

$$U = T2_{2,3}^{-1} \cdot T3_{1,2}^{-1} \cdot U_d \cdot T6_{3,4}^{-1} \cdot T5_{2,3}^{-1} \cdot T4_{1,2}^{-1} \cdot T1_{3,4}^{-1} \tag{3.51b}$$

As it can be seen from Figure 3.6b, this transformation operator order is exactly identical with the MZI sequence for square circle model. If M_i can be used to replace Ti^{-1},

the target unitary matrix can be reconstructed on chip.

Therefore, the form of operator T must be studied. As the unitary matrix elements are all complex values with an amplitude and a phase and the transformation operator $T1, T4, T5, T6$ are right multiplexing and perform column operation as shown in Equation 3.49. To cancel the matrix element to 0, it requires to satisfy the following restriction condition, which is given by

$$\arg(a_{i,i}) \neq \arg(a_{i,j}) \tag{3.52a}$$

$$\arg(a_{j,i}) \neq \arg(a_{j,j}) \tag{3.52b}$$

, and $T2, T3$ are left multiplexing on U to perform row operation in Equation 3.48. The following condition are satisfied as

$$\arg(a_{i,i}) \neq \arg(a_{j,i}) \tag{3.53a}$$

$$\arg(a_{i,j}) \neq \arg(a_{j,j}) \tag{3.53b}$$

Therefore, the MZI transformation unitary operator can be further defined in the form of Equation 3.31, and expressed as

$$M_{L(\theta,\phi)} = ie^{i\frac{\theta}{2}} \begin{bmatrix} e^{i\phi}\sin\frac{\theta}{2} & \cos\frac{\theta}{2} \\ e^{i\phi}\cos\frac{\theta}{2} & -\sin\frac{\theta}{2} \end{bmatrix} \tag{3.54a}$$

$$M_{R(\theta,\phi)} = ie^{i\frac{\theta}{2}} \begin{bmatrix} e^{i\phi}\sin\frac{\theta}{2} & e^{i\phi}\cos\frac{\theta}{2} \\ \cos\frac{\theta}{2} & -\sin\frac{\theta}{2} \end{bmatrix} \tag{3.54b}$$

This is exactly the form of Equation 3.28 and Equation 3.29. Here, the $N \times N$ MZI

matrix is simplified to 2×2 block by only assigning the four elements at index i, j. Since the inverse of a unitary operation T is $T^{-1} = T^{\dagger}$ which can be expressed as

$$M_{L(\theta,\phi)}^{-1} = -ie^{-i\frac{\theta}{2}} \begin{bmatrix} e^{-i\phi}\sin\frac{\theta}{2} & e^{-i\phi}\cos\frac{\theta}{2} \\ \cos\frac{\theta}{2} & -\sin\frac{\theta}{2} \end{bmatrix} = -e^{-i\theta} M_{R(\theta,-\phi)} \tag{3.55a}$$

$$M_{R(\theta,\phi)}^{-1} = -ie^{-i\frac{\theta}{2}} \begin{bmatrix} e^{-i\phi}\sin\frac{\theta}{2} & \cos\frac{\theta}{2} \\ e^{-i\phi}\cos\frac{\theta}{2} & -\sin\frac{\theta}{2} \end{bmatrix} = -e^{-i\theta} M_{L(\theta,-\phi)} \tag{3.55b}$$

The unitary matrix can be expressed as

$$U_d = M_R^{-1}3 \cdot M_R^{-1}2 \cdot U \cdot M_L^{-1}1 \cdot M_L^{-1}4 \cdot M_L^{-1}5 \cdot M_L^{-1}6 \tag{3.56a}$$

$$U = M_R 2 \cdot M_R 3 \cdot U_d \cdot M_L 1 \cdot M_L 4 \cdot M_L 5 \cdot M_L 6 \tag{3.56b}$$

where a group of $\{\theta, \phi\}$ can be determined by solving the Equation 3.39 and the unitary matrix can be decomposed by implementing this group of MZI settings. This problem can be further simplified by exchanging the diagonal matrix U_d and M_R or M_L. Take M_R as an example, M_R acting on the left side of U_d can be expressed as

$$\begin{aligned} M_R(\theta,\phi) \cdot U_d =& ie^{i\frac{\theta}{2}} \begin{bmatrix} e^{i\phi}\sin\frac{\theta}{2} & e^{i\phi}\cos\frac{\theta}{2} \\ \cos\frac{\theta}{2} & -\sin\frac{\theta}{2} \end{bmatrix} \cdot \begin{bmatrix} e^{i\varphi_1} & 0 \\ 0 & e^{i\varphi_2} \end{bmatrix} \\ =& ie^{i\frac{\theta}{2}} \begin{bmatrix} e^{i\phi+i\varphi_1}\sin\frac{\theta}{2} & e^{i\phi+i\varphi_2}\cos\frac{\theta}{2} \\ e^{i\varphi_1}\cos\frac{\theta}{2} & -e^{i\varphi_2}\sin\frac{\theta}{2} \end{bmatrix} \end{aligned} \tag{3.57}$$

and M_L' acting on the right side of U_d' can be expressed as

$$\begin{aligned} U_d' \cdot M_L(\theta', \phi') &= \begin{bmatrix} e^{i\varphi_1'} & 0 \\ 0 & e^{i\varphi_2'} \end{bmatrix} \cdot ie^{i\frac{\theta'}{2}} \begin{bmatrix} e^{i\phi'}\sin\frac{\theta'}{2} & \cos\frac{\theta'}{2} \\ e^{i\phi'}\cos\frac{\theta'}{2} & -\sin\frac{\theta'}{2} \end{bmatrix} \\ &= ie^{i\frac{\theta'}{2}} \begin{bmatrix} e^{i\phi'+i\varphi_1'}\sin\frac{\theta'}{2} & e^{i\varphi_1'}\cos\frac{\theta'}{2} \\ e^{i\phi'+i\varphi_2'}\cos\frac{\theta'}{2} & -e^{i\varphi_2'}\sin\frac{\theta'}{2} \end{bmatrix} \end{aligned} \tag{3.58}$$

where the parameter $\theta', \phi', \varphi_1', \varphi_2'$ can be solved as

$$\theta' = \theta \tag{3.59a}$$

$$\phi' = \varphi_1 - \varphi_2 \tag{3.59b}$$

$$\varphi_1' = \phi + \varphi_2 \tag{3.59c}$$

$$\varphi_2' = \varphi_2 \tag{3.59d}$$

and the unitary matrix can be simplified as

$$U = U_d' \cdot M_L2' \cdot M_L3' \cdot M_L1 \cdot M_L4 \cdot M_L5 \cdot M_L6 \tag{3.60}$$

The U_d can also swap with M_L to the right side of the equation. However, the U_d at the left side of the equation represents a series of phase shifter at the end of the circuit and can be ignored under certain measurement conditions.

3.2.3 Circuit Calibration

The decomposition of an arbitrary unitary matrix into the phase parameters of each MZI is analyzed in the last section. Another important analysis that needs to solved

before any chip implementation is to find the relationship between the heater power needed and induced phase change required for each MZI.

The calibration of phase shifter θ between two BS is first discussed. If the light is input from top arm of the MZI, the output from the two ports can be expressed as

$$ie^{i\frac{\theta}{2}}\begin{bmatrix}\sin\frac{\theta}{2} & \cos\frac{\theta}{2}\\ \cos\frac{\theta}{2} & -\sin\frac{\theta}{2}\end{bmatrix}\cdot\begin{bmatrix}1\\0\end{bmatrix}=ie^{i\frac{\theta}{2}}\begin{bmatrix}\sin\frac{\theta}{2}\\ \cos\frac{\theta}{2}\end{bmatrix} \tag{3.61a}$$

$$P_1=|\sin\frac{\theta}{2}|^2=\frac{1}{2}(1-\cos\theta) \tag{3.61b}$$

$$P_2=|\cos\frac{\theta}{2}|^2=\frac{1}{2}(1+\cos\theta) \tag{3.61c}$$

The output power P_1, P_2 is determined by the phase change and interference fringe can be observed by the increase of phase θ.

From previous analysis, the phase here is intrinsically the optical path difference induced by the effective refractive index change. The thermal phase shifter modulates the refractive index by heating up the TiN resistor and causes proportional temperature change given by

$$\theta=\frac{\Delta n_{eff}L}{\lambda}+\theta_0=\frac{L}{\lambda}\cdot k\cdot P+\theta_0, \tag{3.62}$$

where L is the length of the waveguide affected by heater, λ is the wavelength, θ_0 is the initial phase difference induced by the slight fabrication errors, P is the power added on heater and k is the coefficient to describe the power difference and refractive index change. It is decided by material, size, design and many other factors and can be calibrated experimentally.

For phase shifter ϕ outside the two BS, the phase shifters θ_1 and θ_2 as shown in

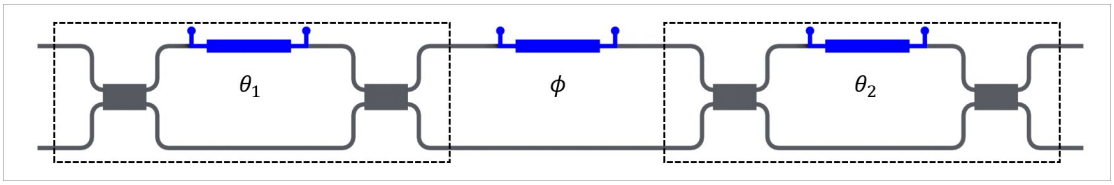

Figure 3.7: Schematic to calibration the phase shifter Φ outside a MZI. Tune the two MZIs before and after the target ϕ to splitting ratio of 50:50 and monitor the interference fringe.

Figure 3.7 are involved together to perform the calibration. By setting $\theta_1 = \theta_2 = \pi/2$, the transformation matrix can be written as

$$\begin{aligned} T =& ie^{i\frac{\theta_2}{2}} \begin{bmatrix} \sin\frac{\theta_2}{2} & \cos\frac{\theta_2}{2} \\ \cos\frac{\theta_2}{2} & -\sin\frac{\theta_2}{2} \end{bmatrix} \cdot \begin{bmatrix} e^{i\phi} & 0 \\ 0 & 1 \end{bmatrix} \cdot ie^{i\frac{\theta_1}{2}} \begin{bmatrix} \sin\frac{\theta_1}{2} & \cos\frac{\theta_1}{2} \\ \cos\frac{\theta_1}{2} & -\sin\frac{\theta_1}{2} \end{bmatrix} \\ =& -ie^{i\frac{\pi}{2}} \begin{bmatrix} \cos\frac{\phi}{2} & i\sin\frac{\phi}{2} \\ i\sin\frac{\phi}{2} & \cos\frac{\phi}{2} \end{bmatrix} \end{aligned} \tag{3.63}$$

If light is inputted from the upper arm of the structure, the output of the two arm can be expressed as

$$-ie^{i\frac{\phi}{2}} \begin{bmatrix} \cos\frac{\phi}{2} & i\sin\frac{\phi}{2} \\ i\sin\frac{\phi}{2} & \cos\frac{\phi}{2} \end{bmatrix} \cdot \begin{bmatrix} 1 \\ 0 \end{bmatrix} = -ie^{i\frac{\phi}{2}} \begin{bmatrix} \cos\frac{\phi}{2} \\ i\sin\frac{\phi}{2} \end{bmatrix} \tag{3.64a}$$

$$P_1 = |\cos\frac{\phi}{2}|^2 = \frac{1}{2}(1+\cos\phi) \tag{3.64b}$$

$$P_2 = |i\sin\frac{\phi}{2}|^2 = \frac{1}{2}(1-\cos\phi) \tag{3.64c}$$

The output power P_1, P_2 is determined by the phase setting of ϕ. By adding current on it, the interference fringe can be observed and the current-phase relationship can be fitted accordingly.

For the triangle circuit, the phase shifters, θ's, are all calibrated in diagonal line order first as shown in Figure 3.6a. The light is inputted from port 1 and the output power is measured at port 4, which is decided independently by three phase shifter $\theta_{33}, \theta_{32}, \theta_{31}$. Then these three θ along the diagonal line 3 are set to identity matrix to measure the light from port 2 to port 4 so that the power is solely decided by phase shifter θ_{22}, θ_{21} and finally θ_{11} can be calibrated using the same way to guide light from input 3 to output 4. The phase shifter ϕ can be easily measured when the calibration for θ is done. For example, the ϕ_{21} can be calibrated by setting $\theta_{21} = \theta_{31} = \pi/2, \theta_{32} = 0$ and measure the fringe at output 4.

For the square circuit, a similar method is taken by measuring light from input port 1 to output 4 and observing the fringes by adding current on the phase shifters $\theta_4, \theta_5, \theta_6$. The MZI 4,5,6 is implemented as identity matrix and phase shifter θ_3, θ_2 are calibrated with light going from input 1 to output 3, θ_1 is calibrated from input 3 to output 4. The phase shifter ϕ can be done the same way as the previous technique for triangle model.

3.3 Experimental Results and Discussions

3.3.1 Experimental Setup

The experimental set up is shown in Figure 3.8. The pump laser is generated from the Ultrafast Optical Clock device (PriTel) with repetition rate of 500 MHz, central wavelength of 1550.116 *nm* and bandwidth of 1.9 *nm*.

For two mode squeeze (TMS) source to generate a pair of signal and idler photons on chip using non-degenerated SFWM, the laser would first go through a 100*G* WDM

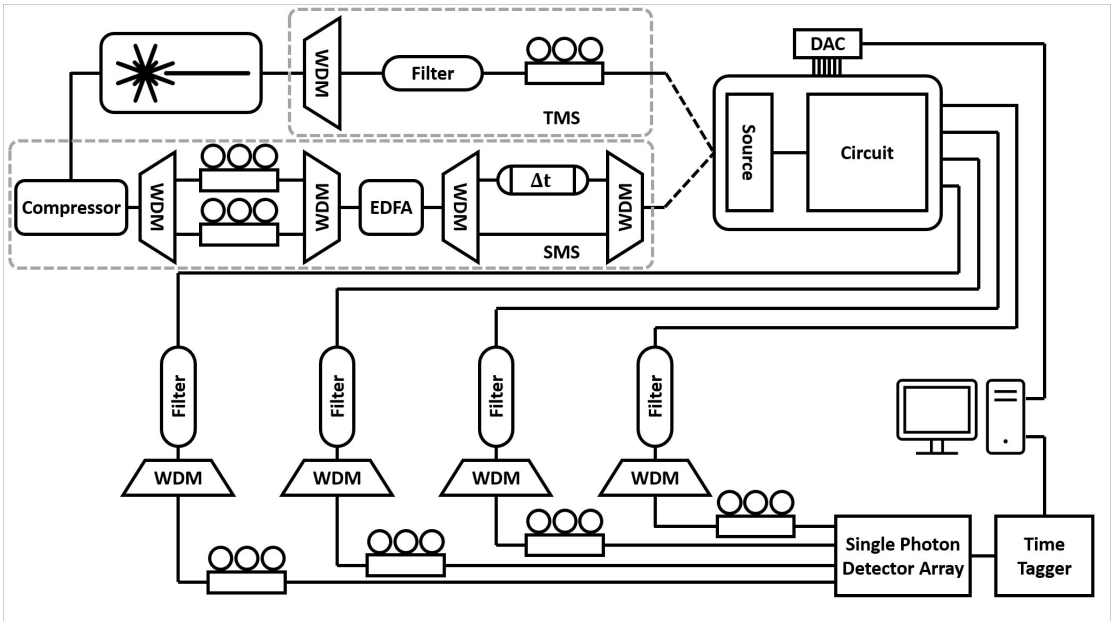

Figure 3.8: Schematic of the experimental setup for quantum photonic circuit.

device and a filter to narrow down the linewidth to 0.5 *nm* and suppress the background noise. Then another three-ring polarization controller is added for polarization control of laser beam to optimize the grating coupler efficiency from fibre to chip.

For single mode squeeze (SMS) source to generate a pair of identical photons with degenerated SFWM process, the spiral waveguide is excited with dual pump scheme. The pulse laser would first go through a compressor to expand the bandwidth to about 10 *nm*. Then, the two pump wavelengths are selected with a 100*G* WDM device and recombine them into a single mode fibre via another WDM. Next, an Erbium dope fibre amplifier (EDFA) is connected to amplify the laser power as the wavelength selection process would only keep the power at selected wavelength and suppress the most part of the spectra. However, the EDFA would also increase much background light and another pair of WDM is required to remove the noise. To balance the optical path difference of two pump wavelength, a tunable delay lines are connected to one arm of the channel to overlap the two pulses. Three-ring polarization controllers are added to

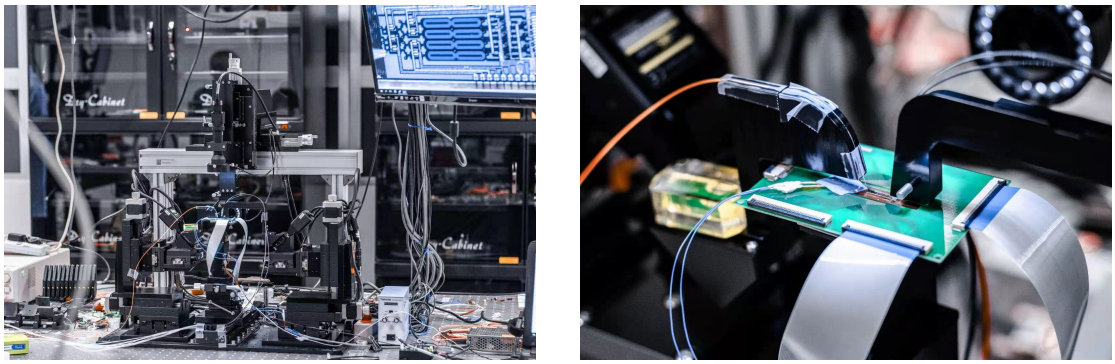

(a) (b)

Figure 3.9: (a) Photo of the experimental setup. (b) Detailed photo of bonded chip.

each path for grating coupler efficiency adjustment.

The pump laser on chip would generate photons via the SFWM process. Different properties of these photon source would be measured by tuning the linear circuit after it. The photon is coupled outside the chip via the grating array and go through some filters and WDMs to remove the background photon. Another polarization controller is placed for adjusting before each superconducting single photon detector channel (PhotonSpot) as these detectors are also polarization-sensitive. The detected photon signal would be converted to electrical signal and processed by Time Tagger (Swabian Instrument) and computer. Finally the computer would send the control signal to each heater on chip via a digital-to-analogue convertor (DAC) device (Qontrol) to manipulate photon for another round of measurement.

Figure 3.9a shows the photo of experimental set up. The chip is set on an alignment stage with 3 translation axis and 3 rotation axis at both sides. The fibre is well aligned to chip via the fine adjustment of these axis. The chip can be monitored from an electrical microscope. Figure 3.9b is the detailed photo of the chip packaging. The two metal arms are for fibre holding and are controlled by the axis. The green board is designed

PCB board for heater control. Gold wires are bonded from chip to PCB metal pad and two 50-ch FFC cables (white flat cable with blue connector) are used to get connected to a DAC. The DAC can be programmed by computer to supply current to each channel individually. The blue wires are thermistor monitoring the temperature of the chip to function as the input signal for a thermoelectric cooler (TEC) attached to the backpanel of PCB, which maintains the temperature of the whole system.

3.3.2 Calibration of Quantum Photonic Circuit

The photon source is first characterized under both non-degenerated SFWM and degenerated SFWM process. Figure 3.10a shows the single pump laser spectra for the non-degenerated SFWM process for generating a two-mode squeezed state, which is measured with an Optical Spectra Analyzer (OSA). The initial output laser spectra has a bandwidth of 1.9 *nm* (blue line), the 100*G* WDM can reshape the bandwidth to 0.7 *nm* and supress the background noise to improve the source quality (orange line). The generated photon pair wavelength are selected to be 1553.329 *nm* (C30) for signal photon and 1546.917 *nm* (C38) for idler photon to match the channels of WDM, which is defined by International Telecommunication Union (ITU). Figure 3.10b is the dual pump spectra for degenerated SFWM to generate a single mode squeezed state. It is selected from a broad band pump laser (blue line) with the C30 and C38 (orange line) channel of the WDM and the generated identical photon pair wavelength is 1550.116 *nm* (C34).

The fiber is coupled with chip via the grating coupler structure and its spectra is seen in Figure 3.10c. The testing structure includes a distance of waveguide with ignorable loss and two grating couplers. By subtracting the output spectra (orange line)

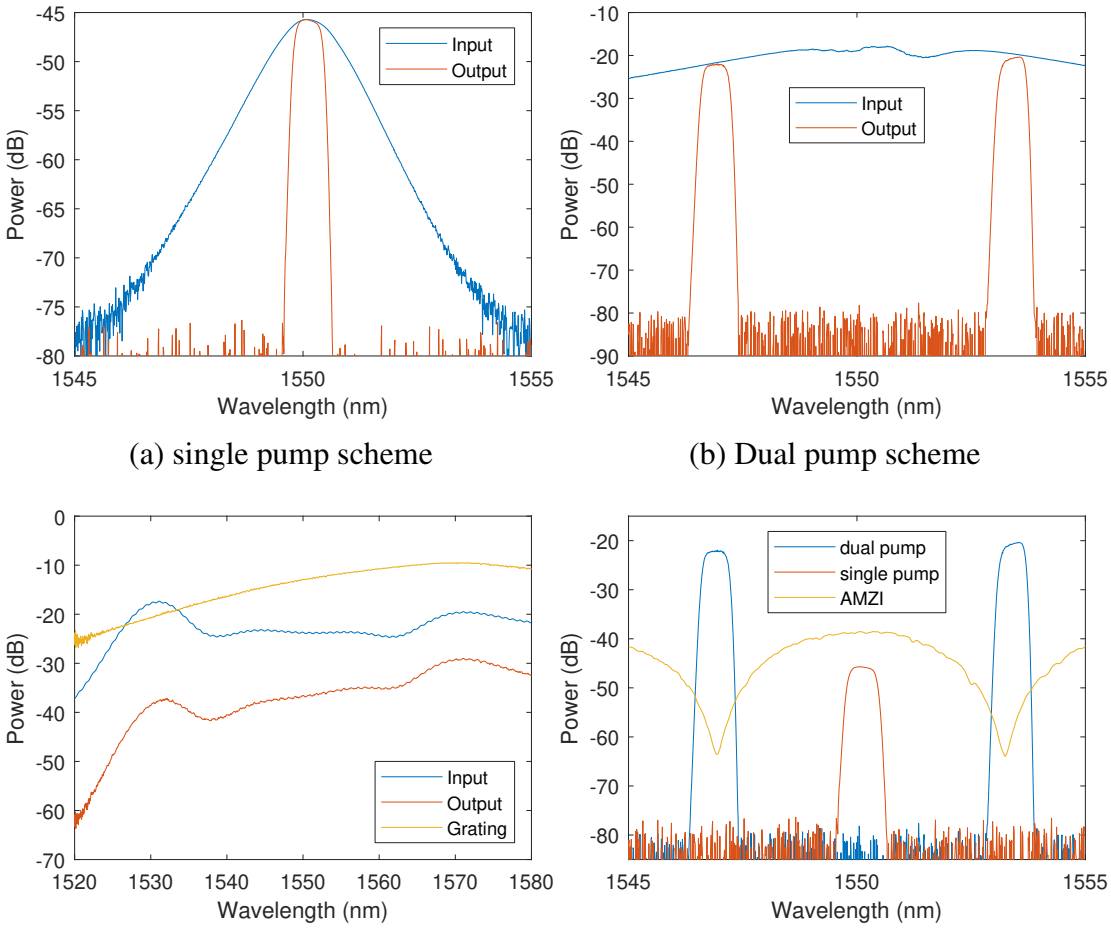

(a) single pump scheme

(b) Dual pump scheme

(c) Grating Coupler

(d) AMZI and pump

Figure 3.10: Spectra of different devices. (a) The spectra of single pump for TMS state. (b) The spectra of dual pump scheme for SMS state. (c) The transmission of grating coupler (yellow line) over the wavelength. (d) The combined spectra of dual pump (blue line), single pump (orange line) and AMZI (yellow line).

from the input spectra (blue line), the transmission of grating coupler with wavelength can be calculated (yellow line). It has the best coupling efficiency of 5 *dB* loss at 1570 *nm* and around the working wavelength of 1550 *nm*, the efficiency is 6 *dB* loss.

The AMZI structure on chip functions as a filter to remove the pump laser in order to reduce the spurious photons generated after the spiral waveguide. As can be seen in Figure 3.10d, the free spectra range (FSR) of the AMZI is 6.4 *nm* (yellow line), which

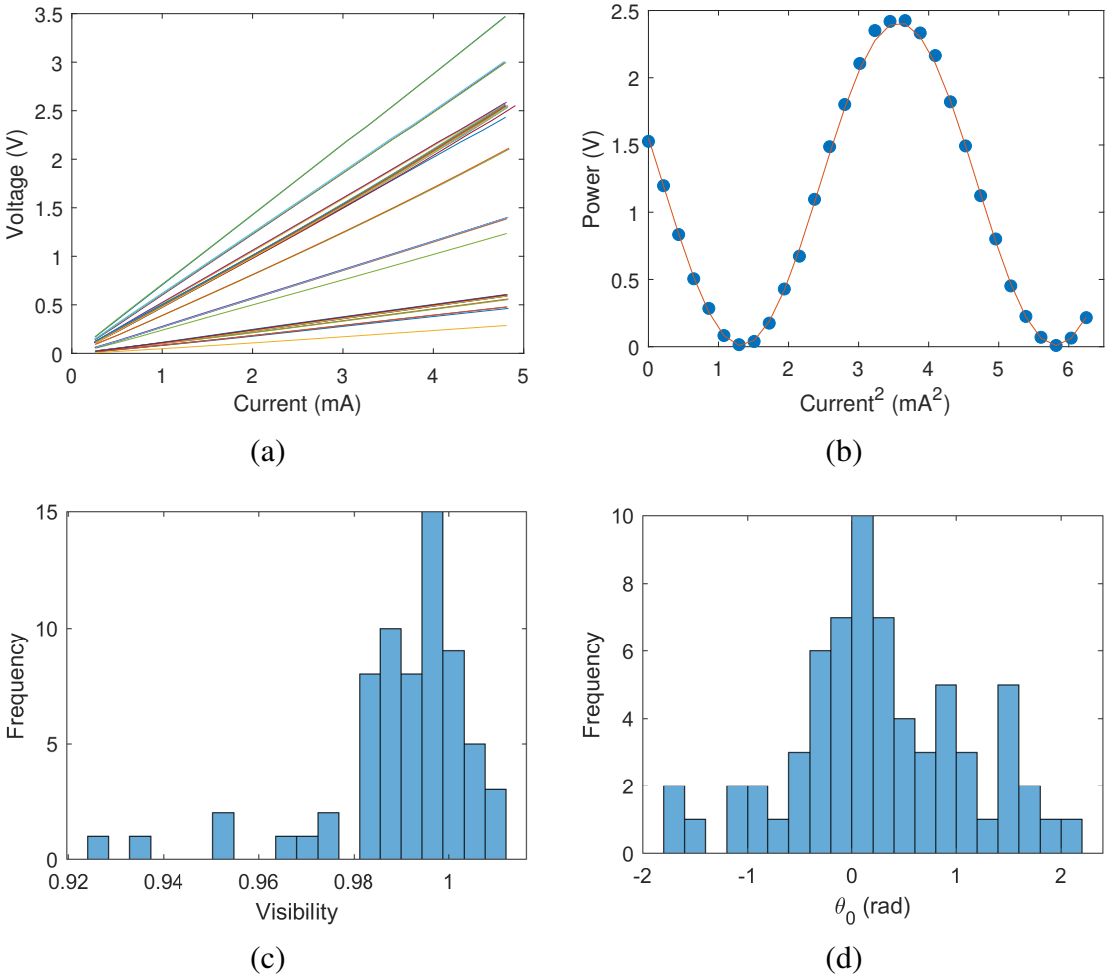

Figure 3.11: Calibration of phase shifters. (a) Voltage-current characteristic of each heaters. (b) Interference fringe of the phase shifter. Blue dots are measured data and orange line is the fitted function. (c) Histogram of the visibilities for all heaters. (d) Histogram of initial phase θ_0 caused by the fabrication heterogeneity.

equals to 8 WDM channels. Therefore, it can split the dual pump laser into one port and SMS state into another (blue line) or split the single pump and TMS state into two ports.

The calibration of phase shifters are shown in Figure 3.11. First, the voltage-current characteristic of each resistance is measured as shown in Figure 3.11a, the voltages are all highly linear with the current, which means the resistor defined as

$R = \delta V / \Delta I$ can be considered as a constant in the experiment. Most of the resistors are around 500 Ω while some of them are smaller. This can be explained that the curve is calibrated by measuring voltages and currents at each metal pad. The chip is designed with multiple heaters sharing one ground pad for space conserving consideration. When measuring from ground pad, the resistor can be considered as the parallel resistors of all the heaters. Plus, the resistor measured here also includes other connection wires including the bounding golden wires from PCB to chip, aluminum wires on chip for conducting with different lengths and ordinary electrical wires.

Since the resistor is measured to be constant, the power added on it can be estimated as $P = I^2 R$ and the Equation 3.62 can be simplified as

$$\theta = \frac{L}{\lambda} \cdot k_0 \cdot I^2 R + \theta_0 = kI^2 + \theta_0 \tag{3.65}$$

Generally, the main variable here is the current added on the heater and all the other parameters can be included into k and get calibrated experimentally. The variable I is selected instead of V is because the power added on heater is not proportional to V, the aluminum wire would share a part of the voltage.

A typical interference fringe of MZI is measured as shown in Figure 3.11b, the coupled fiber is connected to a Photodiode (PD) to convert the light intensity to voltage signal for processing. The blue dots are measured power with increase of current added on heater and the orange fitting line is expressed as

$$P = y_0 V \sin\left(kI^2 + \theta_0\right) + y_0 \tag{3.66}$$

The visibility of the interference fringe is defined as

$$Visibility = \frac{P_{max} - P_{min}}{P_{max} + P_{min}} = \frac{y_0(1+V) - y_0(1-V)}{y_0(1+V) + y_0(1-V)} = V \tag{3.67}$$

where the visibility is exactly the fitting parameter V in the experiment. For all the heaters in circuit, the histograms of the visibilities are shown in Figure 3.11c and 86% of the heaters possess the visibility over 98%. A visibility higher than 1 is just a mathematical artefact due to the optimization of the fitting model. The high visibility can ensure a high fidelity of quantum gate operation and guarantee a better quantum computation accuracy. The Figure 3.11d is the histogram for fitted initial phase θ_0 of heaters. The profile due to the initial phase difference between two arms induced from the fabrication. An ideal MZI should have 0 initial phase and the measured histogram shows that θ_0 distribution is centralized around 0, which indicates that the fabrication difference between two MZI arms is negligible. The θ_0 can be compensated by adding specific initial current on the heater based on the fitting data.

3.3.3 Experimental Results and Discussions

With each module of the chip well calibrated and the general theoretical part discussed, the photon source of the designed chip is then experimentally characterized.

The JSI is used to characterize the spectra correlation of the single photon source and it is represented as the amplitude square of JSA. The measurement setup is shown in Figure 3.12a that the spiral waveguide source is working under a single pump scheme and the generated photon pair is diretcly coupled into a $100G$ WDM device. The measurement range for signal and idler wavelength is each selected to be: signal:

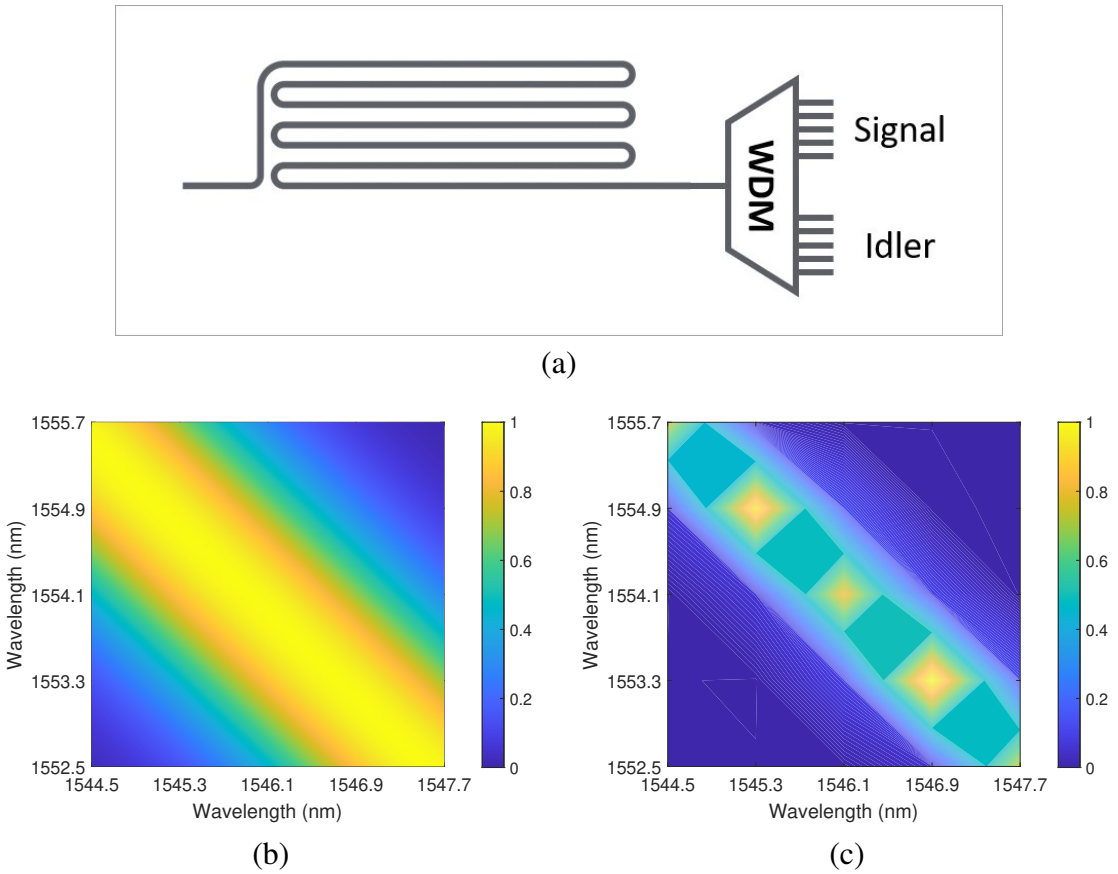

Figure 3.12: Joint spectra intensity of photon source for single pump scheme. (a) Setup for JSI measurement. (b) Theoretical simulation of Joint Spectra Intensity without filter. (c) Measured JSI by selecting different WDM channels.

1544.5 1547.7 *nm* and idler: 1552.5 1555.7 *nm*, which corresponds to 5 WDM channels. Total 25 coincidence counts are measured for all possible combinations of 5 channels and get normalized.

The theoretical value is calculated by Equation 3.10 as seen in Figure 3.12b and the measured data are seen in Figure 3.12c. The discrete result is due to the limit of WDM that the coincidence counts cannot be measured with a very narrow step.

In the weak pump regime, the multi-photon probability $P(n)$ is relatively low and

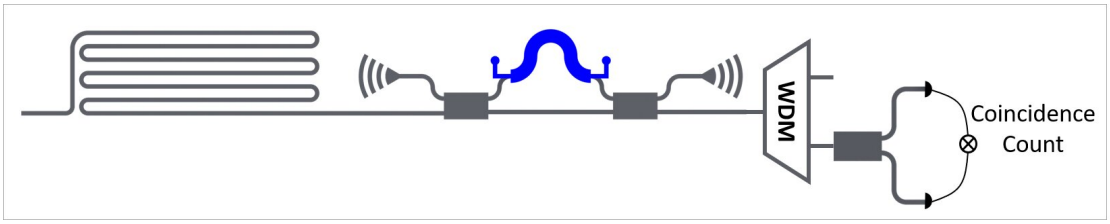

Figure 3.13: Schematic of $g^2(0)$ measurement setup for TMS. The generated signal idler photon pair would be coupled into a WDM for analysis and the idler photon is traced out without detection.

the purity P can be directly estimated as

$$P = \frac{1}{K} = g^{(2)}(0) - 1, \tag{3.68}$$

where $g^{(2)}(0)$ is called the second order correlation. It is an experimentally measurable value to describe the statistics of photon pairs correlations.

Its measurement setup is shown in Figure 3.13 that the photon pair first goes through a WDM to get separated by wavelength. The signal photon is then split by a fibre beamsplitter into two channels and coincidence counts with the delay Δt is measured while the idler photon channel is discard. This is called the unheralded measurement of photon source. The count data is then used to do self-correlation by adjusting the time delay between them to calculate the unheralded $g^{(2)}$ accordingly. The second order correlation $g^{(2)}$ can be written as [142]

$$g^{(2)}(\Delta t) = \frac{P_{cc}(\Delta t)}{P_{s1}P_{s2}} = \frac{R_{cc}(\Delta t)}{R_{s1}R_{s2}}R_p, \tag{3.69a}$$

$$g^{(2)}(0) = \frac{N_{cc}(0)}{N_{cc}(\Delta t \neq 0)} \tag{3.69b}$$

where $P_c(\Delta t)$ is the probability of measuring coincidence count at the delay time of

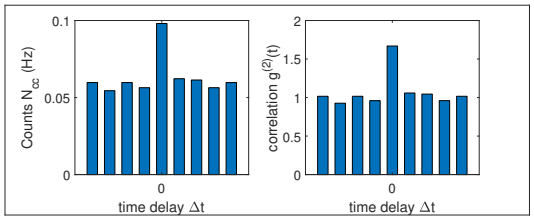

(a) 0.16 mW

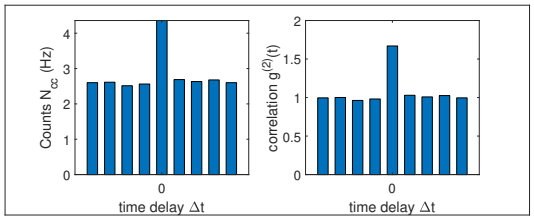

(b) 0.32 mW

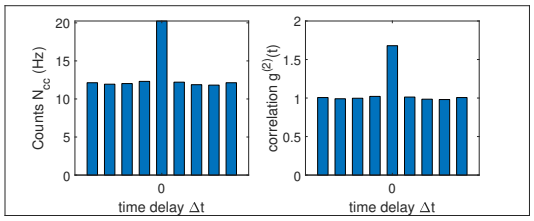

(c) 0.47 mW

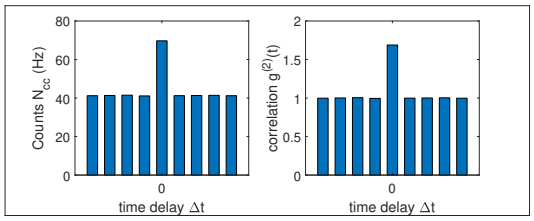

(d) 0.63 mW

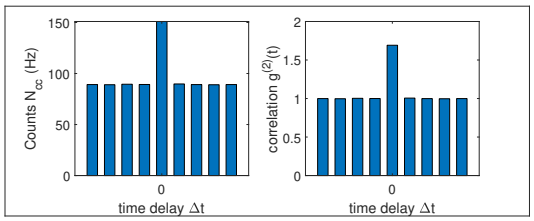

(e) 0.78 mW

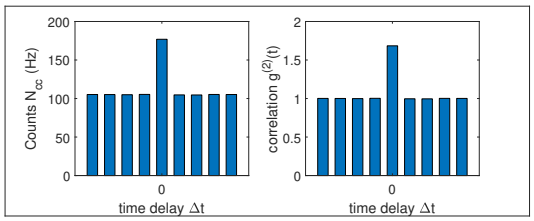

(f) 1 mW

Figure 3.14: The measured $g^{(2)}(t)$ of signal photon source. (a)-(f) Measured raw counting rate over different time delays Δt and the corresponding $g^{(2)}(t)$ under different pump powers.

Δt and P_{s1}, P_{s2} are the probability of measuring signal photon at two detectors. $N_{cc}(\Delta t)$ is the coincidence counts of two detectors at delay Δt. Figure 3.14 lists the measured coincidence count rate and normalized count rate over $N_{cc}(\Delta t \neq 0)$ with different time delays and pump powers.

These two methods are intrinsically equivalent and Figure 3.15 shows the calculated $g_2^{(0)}$ using two equations with different pump power, the average variance over the power difference is merely 0.7%. Thus, it is reasonable to say the $g_2^{(0)}$ remains constant with the change of power. This is due to the properties of squeezed states that if one mode of the photon is traced out, the remaining photon distribution statistic would

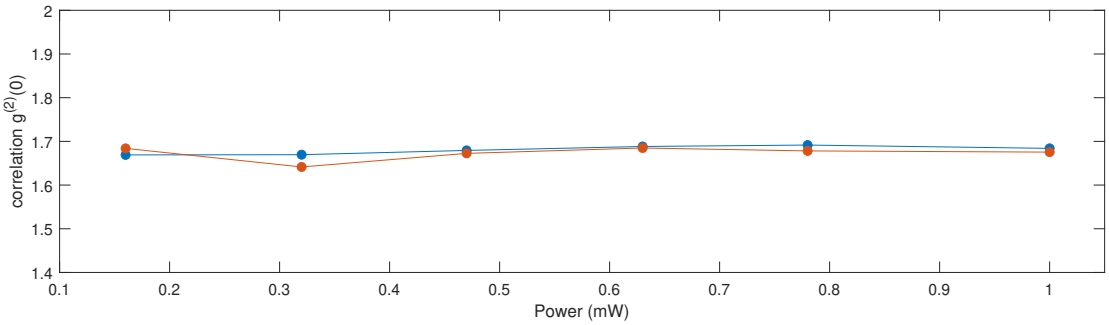

Figure 3.15: $g^{(2)}(0)$ calculated from two equations in Equation 3.69 at different powers. It remains constant with a minor fluctuation due to the super-Poissonian photon number distribution properties of unheralded source.

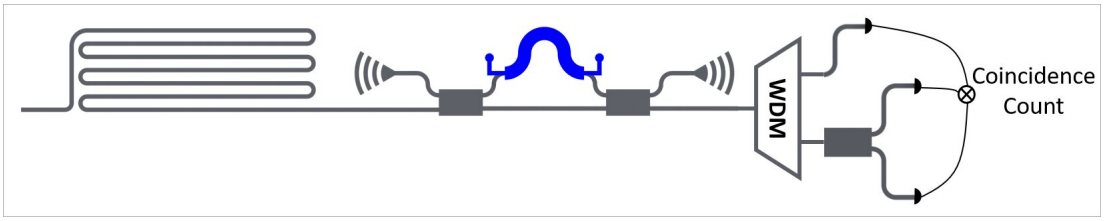

Figure 3.16: Schematic of $g_h^{(2)}(t)$ setup. Coincidences of $s_1 - i$, $s_2 - i$ and $s_1 - s_2 - i$ photons are measured for analysis. With the existence of herald idler photon, the signal photon can be treated as a heralded single photon source.

become super-Poissonian, which corresponds to $g_2^{(0)} = 2$ theoretically regardless of the pump power. The experimental result is measured to be $g_2^{(0)} = 1.68$ and the discrepancy can be explained as the fact that the selected filter bandwidth is not narrow enough and there exists different modes as described in Equation 3.17.

For the heralded photon source purity measurement, the setup is shown in Figure 3.16. The signal and idler photon pair from non-degenerated SFWM process is first separated by a WDM, the idler photon functions as a trigger and the signal photon would be further divided by a beamsplitter into two channels $s1$ and $s2$ for detection and time delay Δt is set at one of the signal channel electrically from the time tagger.

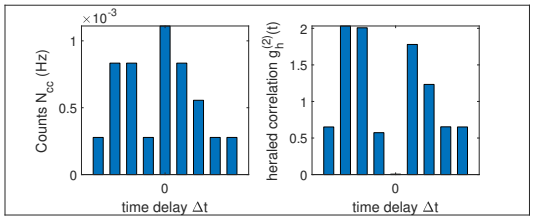

(a) 0.16 mW

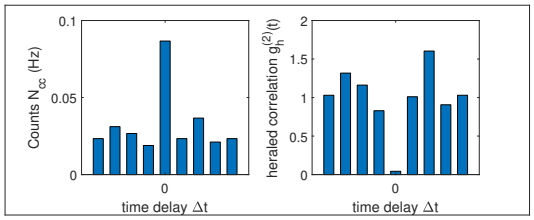

(b) 0.32 mW

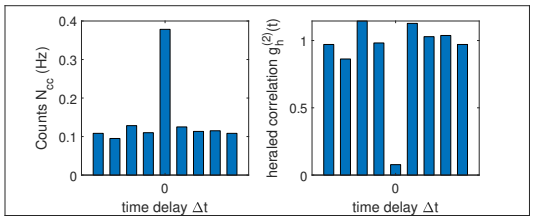

(c) 0.47 mW

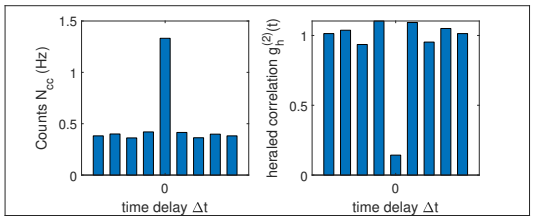

(d) 0.63 mW

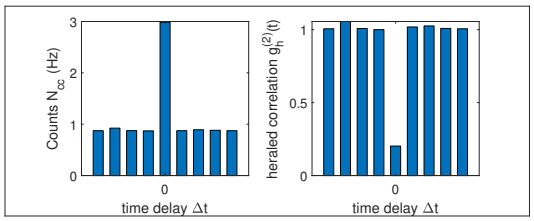

(e) 0.78 mW

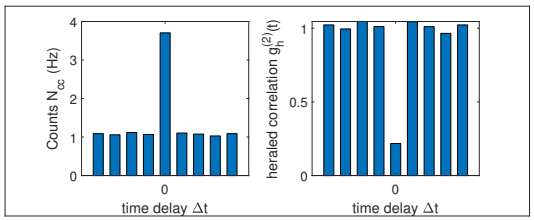

(f) 1 mW

Figure 3.17: Heralded correlation $g_h^{(2)}$ measurement results for TMS state. (a)-(f) The plot of measured signal1, signal2 and idler three photon coincidence rate over the delay time at signal2 channel and the converted $g_h^{(2)}(\Delta t)$ under different input powers.

Thus the Equation 3.22 can be represented by the measured counts expressed as

$$g_h^{(2)}(\Delta t) = \frac{N_{ssi}(\Delta t)}{N_{s1i}(t)N_{s2i}(\Delta t)}N_i. \tag{3.70}$$

$N_{ssi}(\Delta t)$ is the three photon coincidence counts at delayed time Δt, $N_{si}(\Delta t)$ is the two photon coincidence counts at delayed time Δt. N_i is the single channel counts for triggered idler photon.

The measurement results are plotted in Figure 3.17 and the three-photon coincidence counts are first shown with different delays and $g_h^{(2)}(\Delta t)$ are plotted. By increas-

ing of pump power, the $g_h^{(2)}(0)$ increases, which means the purity as single photon source decreases.

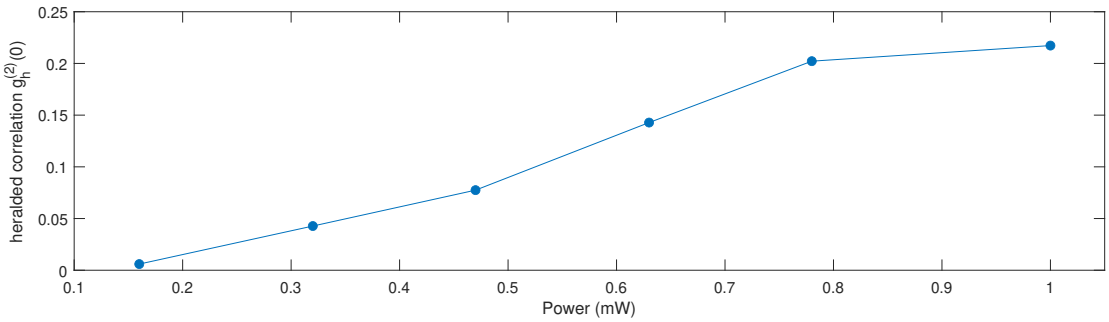

Figure 3.18: Measured $g_h^{(2)}(0)$ with the pump power, which indicates the quality as a heralded single photon source decreases by the increase of pump power.

The heralding process is to remove the zero photon probability for a TMS state, which is expressed as

$$P(0) \gg P(2) \gg P(4) \cdots \gg P(n), n = 2,4,\cdots,\infty \tag{3.71}$$

and make the remaining photon distribution obey a sub-Poissonian statistics. The measured three photon count is accumulated from $P(n > 4)$ and this term increases with the pump power, thus the $g_h^{(2)}(0)$ also increases accordingly as seen in Figure 3.18. Experimentally, lower $g_h^{(2)}(0)$ is preferred for qubit-based quantum computing as this represents a better heralded single photon source (HSPS) quality and a higher fidelity.

The coincidence to accidental ratio (CAR) is to identify the level of noise for a heralding photon source. The corresponding experimental set up is shown in Figure 3.19. The signal and idler photon pair from the TMS state can be directly measured after splitting with the WDM.

The *CAR* defined in Equation 3.23 is the coincidence counts from the heralding

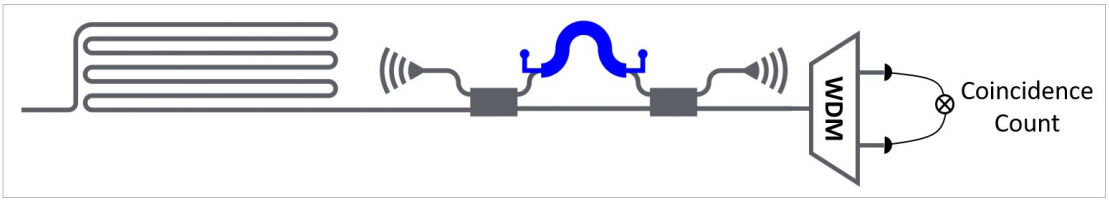

Figure 3.19: Schematic of CAR setup under TMS state. The signal and idler photon is split by a WDM device and the corresponding two channels are coupled to detector for coincidence measurement.

source over the accidental counts. The total coincidence counts is directly measured as $N_{si}(\Delta t)$ the accidental counts for the pulsed pumping scheme can be estimated as

$$R_{acc} = R_s \frac{R_i}{R_p} = \frac{R_s R_i}{R_p} \tag{3.72}$$

where R_s and R_i are single channel count rate of signal and idler photon, R_p is the repetition rate of pulsed laser. This equation can be interpreted as the probability of accidentally detect an idler photon with the existence of signal photon. Therefore, the *CAR* in Equation 3.23 can be simplified as

$$CAR = \frac{R_{si} - \frac{R_s R_i}{R_p}}{\frac{R_s R_i}{R_p}} = \frac{R_{si} R_p}{R_s R_i} - 1 = g_{si}(0) - 1 \tag{3.73a}$$

$$g_{si}(\Delta t) = \frac{R_{si}(\Delta t) R_p}{R_s R_i} \tag{3.73b}$$

The $g_{si}(\Delta t)$ is called the signal-idler cross-correlation. Another simpler way to compute the cross-correlation $g_{si}(0)$ is

$$g_{si}(0) = \frac{R_{si}(0)}{R_{si}(\Delta t \neq 0)} \tag{3.74}$$

where the $R_{si}(\Delta t \neq 0)$ is estimates to be the accidental counts. The *CAR* calculated

from the two methods are very identical with only 1.8% difference. Figure 3.20 shows the measured coincidence counts $N_{si}(\Delta t)$ and $g_{si}(\Delta t)$ with different pump powers. The trend of *CAR* and $R_{si}(0)$ over different pump powers are plotted in Figure 3.21a. The *CAR* drops drastically while the R_{si} increases as the pump power increase, which means the accidental counts, as the noise part, would compromise the theoretical results at high pump power conditions.

The squeeze parameter ξ of the TMS state as shown in Equation 3.13 can also be estimated from the g_{si} given by

$$\frac{\tanh^2(\xi)}{\cosh^2(\xi)} = \frac{1}{g_{si}(0)} \tag{3.75a}$$

$$\tanh^2(\xi) \approx \frac{1}{g_{si}(0)} \tag{3.75b}$$

where the $\cosh^2(\xi)$ is approximated to 1 to simplify the calculation at low pump regime. Figure 3.21b shows the calculated squeeze parameter ξ at different pump powers with the two equation. The two results are similar at low pump power conditions but the estimated squeeze parameter ξ of second equation would be smaller by the increase of pump power.

The quantum circuit performs quantum computation by manipulating the photon interference at the MZIs. The designed quantum circuit is simplified as an MZI to study the interference of two spiral sources under non-degenerated SFWM process as shown in Figure 3.22. The single pump laser at 1550.116 *nm* is injected into the circuit to pump the two on-chip sources. Then the pump laser is filtered out by AMZI and generated signal idler photon pair at 1553.329 *nm* and 1546.917 *nm* would go into the following circuit. The phase shifter ϕ is added at top arm of the generated TMS state

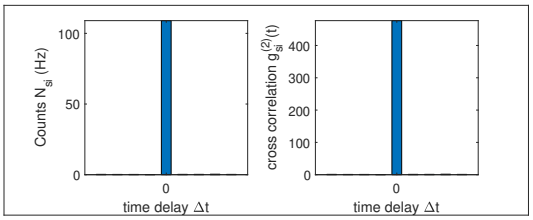

(a) 0.1 mW

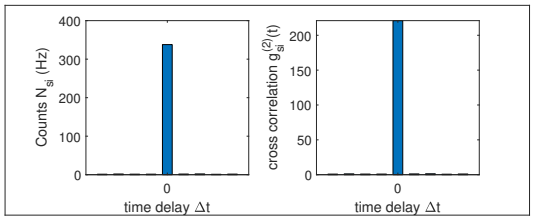

(b) 0.16 mW

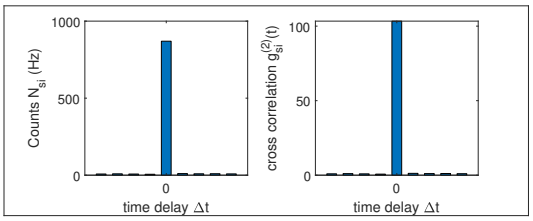

(c) 0.25 mW

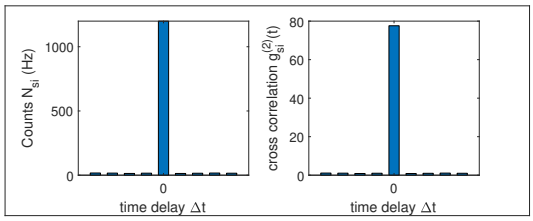

(d) 0.32 mW

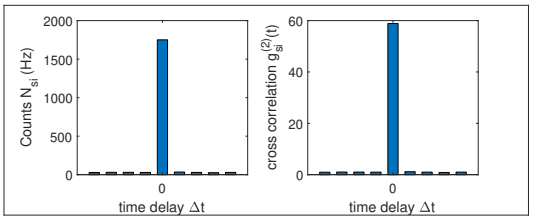

(e) 0.38 mW

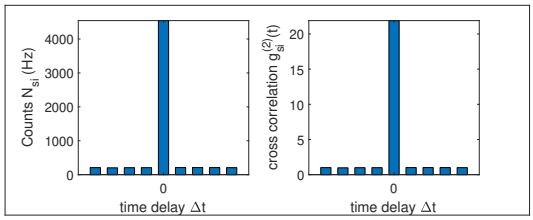

(f) 0.63 mW

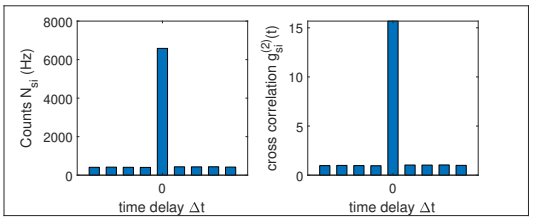

(g) 0.79 mW

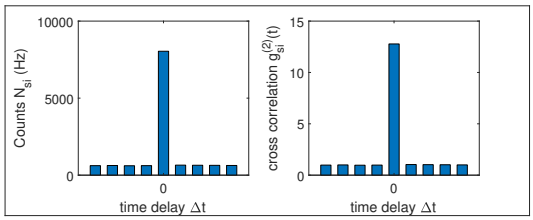

(h) 0.94 mW

Figure 3.20: The measurement results of N_{si} with different input powers. Coincidence counts of N_{si} is measured at different time delays and the $g_{si}(\Delta t)$ is calculated accordingly. The ratio between side peak and main peak is increasing with the increase in power.

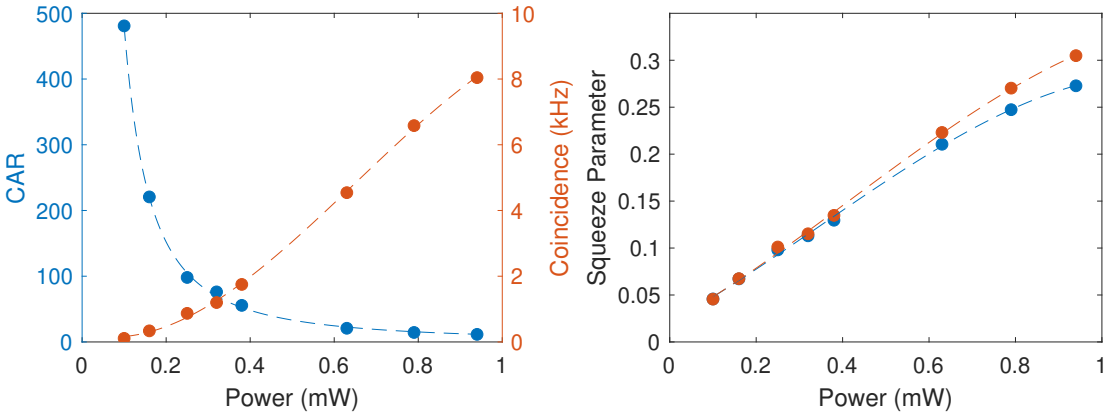

(a) (b)

Figure 3.21: (a) *CAR* and coincidence count over the power increase. Higher CAR means less noise while lower coincidence counts means longer data collection process. (b) The estimated squeezing parameter with different powers calculated from two equations in Equation 3.75.

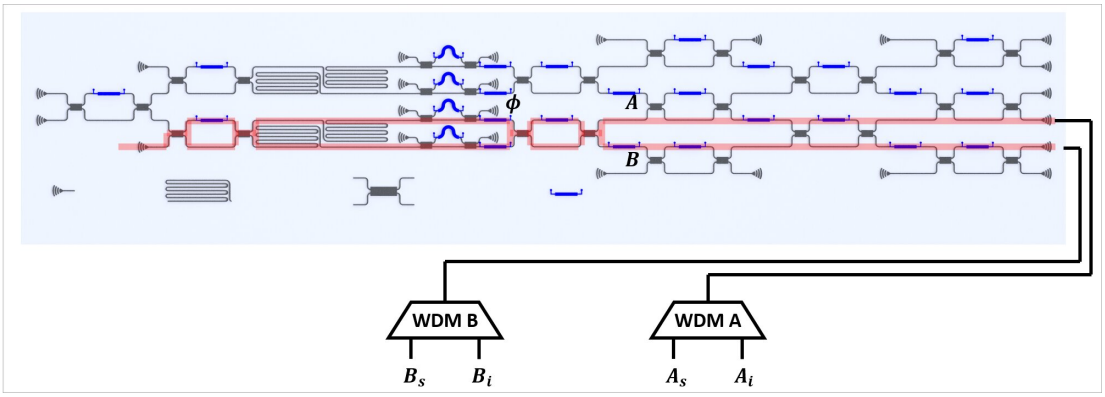

Figure 3.22: Schematic of quantum interference setup. Two spiral waveguides are pumped together to generate photons and interfere with each other at MZI with their relative phase tuned by heater ϕ. The fringe is measured by coupling the output photon to WDM A and B for further analysis as shown in red lines.

and the whole linear optical circuit is tuned to be a Hadamard gate for interference. The equivalent optical circuit is represented in shaded red lines. Finally the output from the two ports would each go to a WDM A and B to measure the signal and idler photon counts with 4 channels of detectors. The corresponding results are denoted as A_s, A_i, B_s, B_i [8].

The quantum states at the end of the circuit evolution are then studied. The two waveguide modes are labeled as mode A and mode B and the creation operator is simplified as a_s, a_i, b_s, b_i. The initial state of the two photon source is in a superposition given by

$$|\psi\rangle = (e^{2i\phi} a_s a_i + b_s b_i)|0\rangle \tag{3.76}$$

The Hadamard gate changes the state as

$$\begin{aligned} |\psi\rangle &= e^{2i\phi}(a_s + b_s)(a_i + b_i)|0\rangle + (a_s - b_s)(a_i - b_i)|0\rangle \\ &= (e^{2i\phi} + 1)(a_s a_i + b_s b_i)|0\rangle + (e^{2i\phi} - 1)(a_s b_i - b_s a_i)|0\rangle \\ &= cos\phi\,|\psi\rangle_{bunch} + sin\phi\,|\psi\rangle_{split} \end{aligned} \tag{3.77}$$

where $|\psi\rangle_{bunch} = e^{i\phi}(a_s a_i + b_s b_i)|0\rangle$, $|\psi\rangle_{split} = ie^{i\phi}(a_s b_i - b_s a_i)|0\rangle$. Therefore, the final state is a superposition of the state $|\psi\rangle_{bunch}$ for two photons taking one mode A or B and $|\psi\rangle_{split}$ for one photon at each mode. The interference of classical light is first measured via a photo diode at mode A and B with the phase $|phi\rangle$ changing from $\pi/2$ to $5\pi/2$. The blue dots are power at mode A and orange dots are power at mode B as shown in Figure 3.23a. The power changes with $|sin(\phi/2)|^2 = (1 - cos(\phi))/2$ with a period of 2π. The average visibility measured is $V = 99.12\%$.

For quantum interference, the Figure 3.23b is the two photon coincidence count rate of $A_s A_i$ and $B_s B_i$ with the change of phase ϕ. It represents the probability of measuring the $|\psi\rangle_{bunch}$ state to be $|cos(\phi)|^2 = (1 + cos(2\phi))/2$, which corresponds to a period of π. The visibility is $V = 98.46\%$. The measured results show the different maximum count rates between fringes. This can be explained by the spurious photons generated at short distance from the input port before entering the photon source. These

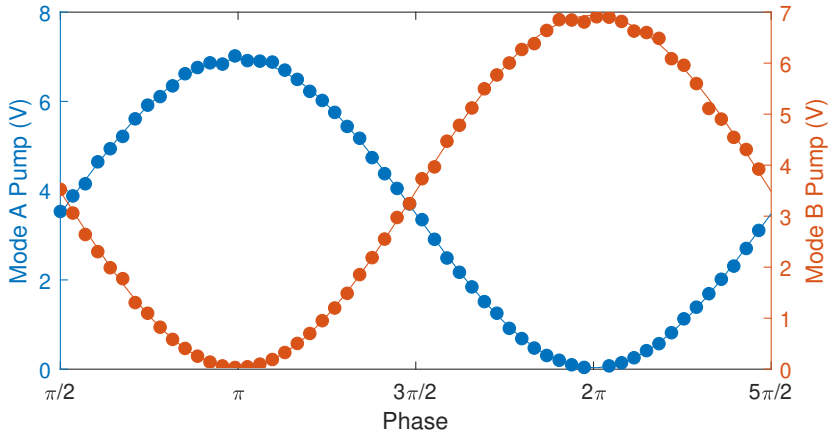

(a)

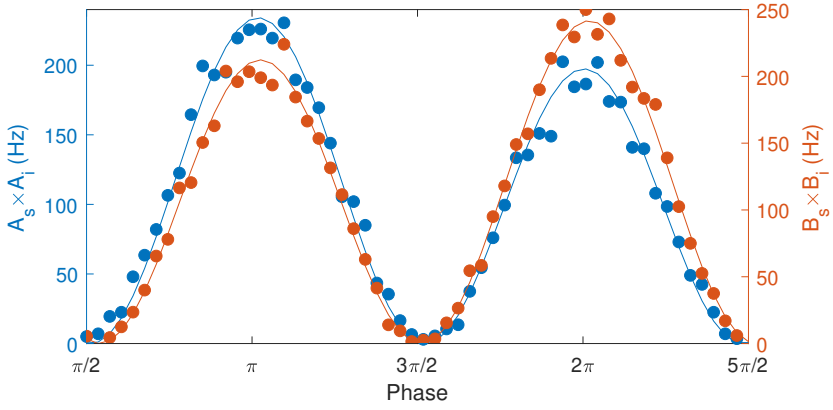

(b)

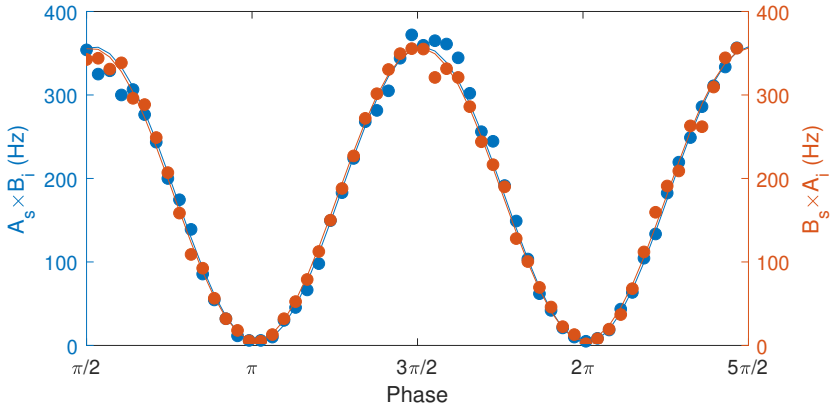

(c)

Figure 3.23: Measurement results of classical interference and quantum interference for TMS state: (a) Interference fringe of classical light, the period is 2π. (b) Interference fringe of $A_s \times A_i$ and $B_s \times B_i$ for $|\psi\rangle_{bunch}$, the period is shrink to π due to the two photon interference and the relative phase change is doubled. (c) Interference fringe of $A_s \times B_i$ and $B_s \times A_i$ for $|\psi\rangle_{split}$.

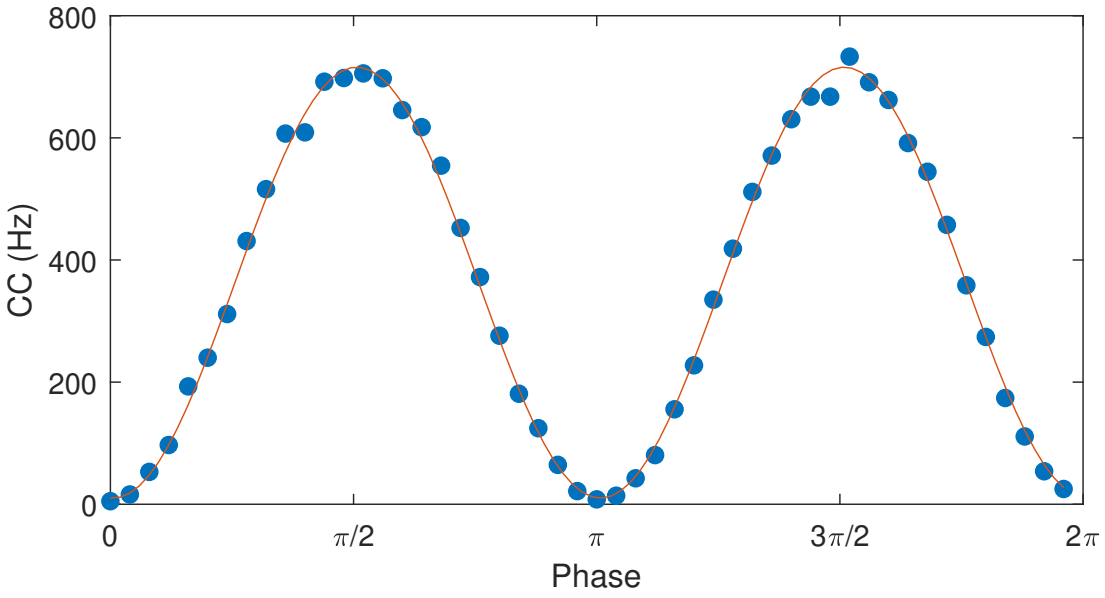

Figure 3.24: Measurement results of quantum interference for SMS state at $|\psi\rangle_{split}$ condition, also known as the $N00N$ state interference. $|\psi\rangle_{bunch}$ cannot be observed here as the photon pair is identical and cannot be discriminated efficiently.

spurious photons follow the interference fringe of classical light with a period of 2π. Its valley does not contribute to the count rate of A_sA_i and B_sB_i while its peak causes an increase in the count rate, which leads to the asymmetric interference fringe. The photon generation rate is proportional to P^2_{pupm} and length of waveguide L. Since the input port waveguide is relatively short, the two peaks only have a difference of 12.01%.

In Figure 3.23c, the coincidence of A_sB_i and A_iB_s is measured, which corresponds to the state $|\psi\rangle_{split}$. The probability is $|sin(\phi)|^2 = (1-cos(2\phi))/2$ with a period of π. The measured average visibility is $V = 98.67\%$. The spurious photon does not change the peak count rate here because at $\phi = \pi$ and $\phi = 2\pi$ points, the spurious photons are all interfered into one of the ports thus there is no coincidence between mode A and B.

If the the quantum state is SMS state with dual pump scheme, similar results can be obtained as seen in Figure 3.24. In SMS condition, the signal and idler photons are

identical with the same wavelength and they cannot be distinguished by a WDM device. The evolution process of TMS quantum state can be directly applied here by mixing the signal and idler creation operator. In this case, only state $|\psi\rangle_{split}$ is observable. The coincidence of CC_{AB} is plot over the phase change with a visibility of $V = 97.21\%$.

The difference in periods between quantum interference and classical light interference is due primarily to the difference in the nature of single photon and coherent light. The phase shifter ϕ corresponds to a phase different $e^{i\phi}$. For the quantum state, there exists two photons $a_s a_i |0\rangle$ (TMS) or $a^2 |0\rangle$ (SMS) at the upper arm, thus the phase difference is actually $(e^{i\phi}a_s)(e^{i\phi}a_i)|0\rangle = e^{2i\phi}a_s a_i |0\rangle$ or $(e^{i\phi}a)^2 |0\rangle = e^{2i\phi}a^2 |0\rangle$, while for coherent light, the general effect of phase shifter is $e^{i\phi}$. Thus, quantum state is more sensitive to the phase change and has a smaller interference period. In addition, it is also possible to obtain a kind of quantum state called N00N state, which is given by

$$\begin{aligned} |N00N\rangle &= |n0\rangle + |0n\rangle \\ &\xrightarrow{\phi} e^{ni\phi}|n0\rangle + |0n\rangle \end{aligned} \tag{3.78}$$

This state can have n times smaller periods than the classical light under photon number basis. If there is a phase perturbation at one arm, it can be amplified n times by observing the interference change under N00N state. The state can be written as $|nm\rangle + |mn\rangle$, which would provide $|n-m|$ times better resolution than coherent light.

For SMS state with dual pump scheme, another important factor to calibrate is the delay time of the two laser pulses, which would affect the efficiency of the degenerated SFWM process. The photon generation rate is first measured by directly connecting the output ports to a detector. The on chip linear optical circuit is set to an identity matrix, which means no photons are split into other ports. A tunable fibre delay line

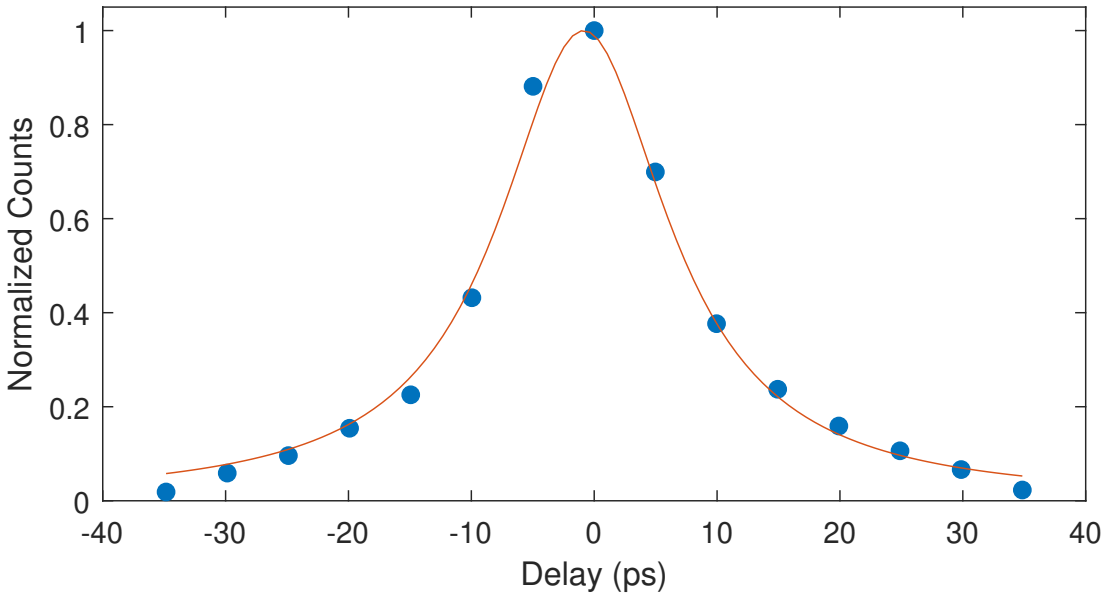

(a)

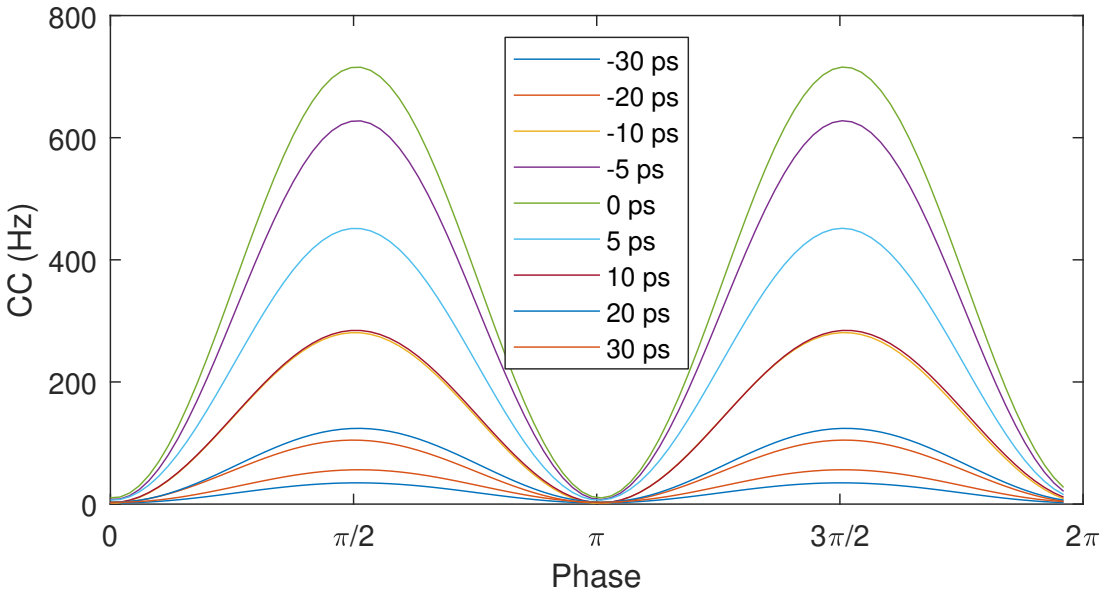

(b)

Figure 3.25: (a) Count rate over the delay between two pumps. The blue dots are measured results and the orange line are Lorentz fit function. A maximum count rate can be obtained with the optimized delay at -2.4 *ps*. (b) $|\psi\rangle_{split}$ state interference with different delays.

is connected between one channel of the WDM device with its delay initialized to 0 so that it allows $\pm 40ps$ tuning range. A fixed delay fibre is first added to ensure the difference between two WDM channels are less than 1 *cm*, which corresponds to 50 *ps*.

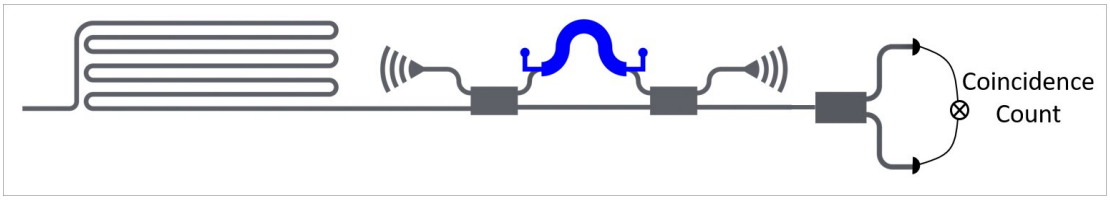

Figure 3.26: Schematic of dual pump squeeze parameter measurement setup. The spiral waveguide is pumped to be SMS state and the photon pair would be split for coincidence count measurement.

Then the delay time is manually adjusted by a tunable fibre delay line and the count rate is measured accordingly. The photon rate is plot over the delay time between two pulses as shown in Figure 3.25a. The blue dots are normalized count rate and the orange line is the Lorentz fitting function. The optimized delay time is estimated to be -2.4 *ps* and the FWHM bandwidth is about 15 *ps*. Figure 3.25b are the measured interference from two photon sources. The linear optical circuit is configured as the set up in 3.22. The maximum two photon coincidence rate for $|\psi\rangle_{split}$ occurs around 0 *ps*.

For SMS state, its squeeze parameter can be measured with the setup shown in Figure 3.26. The generated identical photon pair would go through a beam splitter to be measured in two single photon detectors. The coincidence count rate would be processed by a time tagger with the delays set electrically at one of the data channel. The squeeze parameter of a SMS state can be expressed as

$$2R = \frac{\tanh^2(\xi)}{\cosh(\xi)} \approx \tanh^2(\xi) \tag{3.79a}$$

$$R \approx \frac{R(\Delta t \neq 0)}{R(\Delta t = 0)} \approx \frac{R_1 R_2}{R_p R_{cc}} \tag{3.79b}$$

The squeeze parameter estimation function is very similar to the TMS condition in Equation 3.75. The coefficient 2 is due to the probabilistic splitting of the degenerated

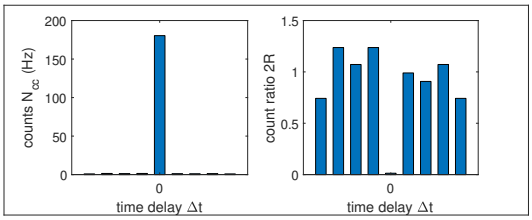

(a) 0.07 mW

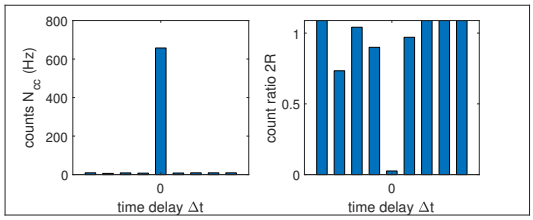

(b) 0.14 mW

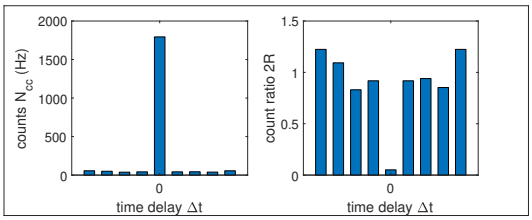

(c) 0.22 mW

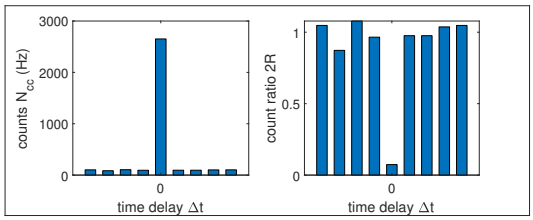

(d) 0.28 mW

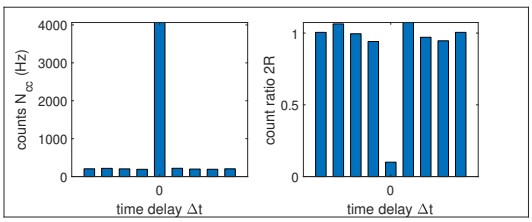

(e) 0.35 mW

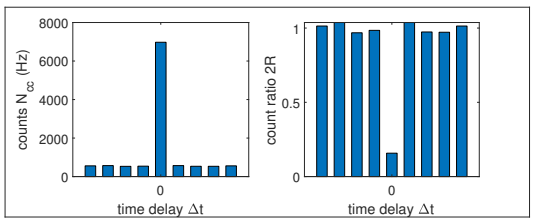

(f) 0.45 mW

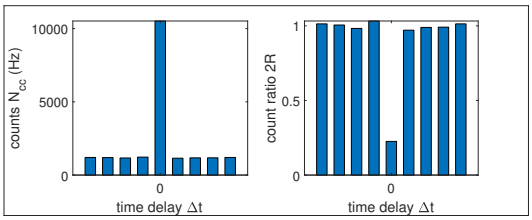

(g) 0.56 mW

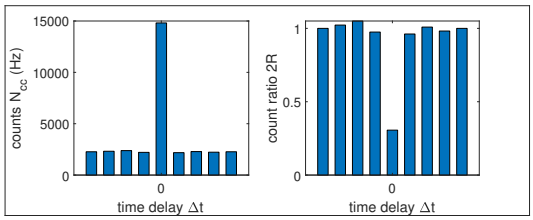

(h) 0.71 mW

Figure 3.27: Measured count N_{cc} and count ratio $2R$ with time difference Δt are plotted at various input power conditions. The corresponding powers are labeled beneath each figure.

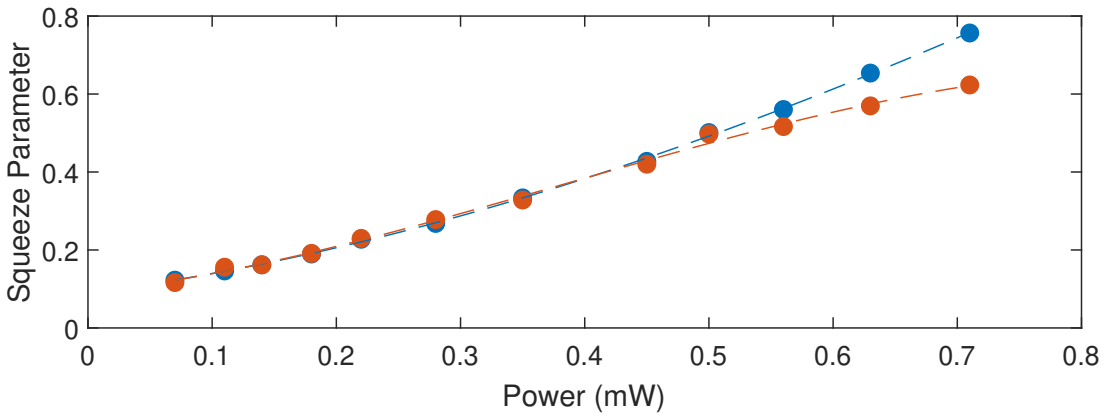

Figure 3.28: Estimated squeeze parameters from Equation 3.79. Blue dots are direct calculation and orange dots are approximated calculation with $\cosh(\xi) = 1$.

mode with beam splitter. Figure 3.27 shows the measured coincidence rates and ratios $2R$ at some particular pump powers, both of them would increase by the pump power. Figure 3.28 is the calculated squeeze parameter. The blue dots are original data while the orange dots take the approximation of $\cosh(\xi) = 1$ at low pump regime. As can be seen, the two results fit well when $\xi < 0.5$.

Finally, the interference visibility with different squeeze parameters is studied. The measurement set up is the same as Figure 3.22 and squeeze parameters are tuned by changing the pump powers. Figure 3.29 shows the interference fringes with different squeeze parameter ξ in a phase range from $\phi = 0$ to $\phi = 2\pi$. Visibility and count rates are plot over the squeeze parameters shown in Figure 3.30. By the increase of squeeze parameter, non-zero photon probability would increase. This would cause the count rate to increase and visibility to decrease. The photonic integrated digital quantum computing requires both accuracy and processing speed and these two points corresponds to the high fidelity and more count rate. There should be a trade off of these two factors in experiment. Usually for proof of principle demonstration, higher fidelity is preferred

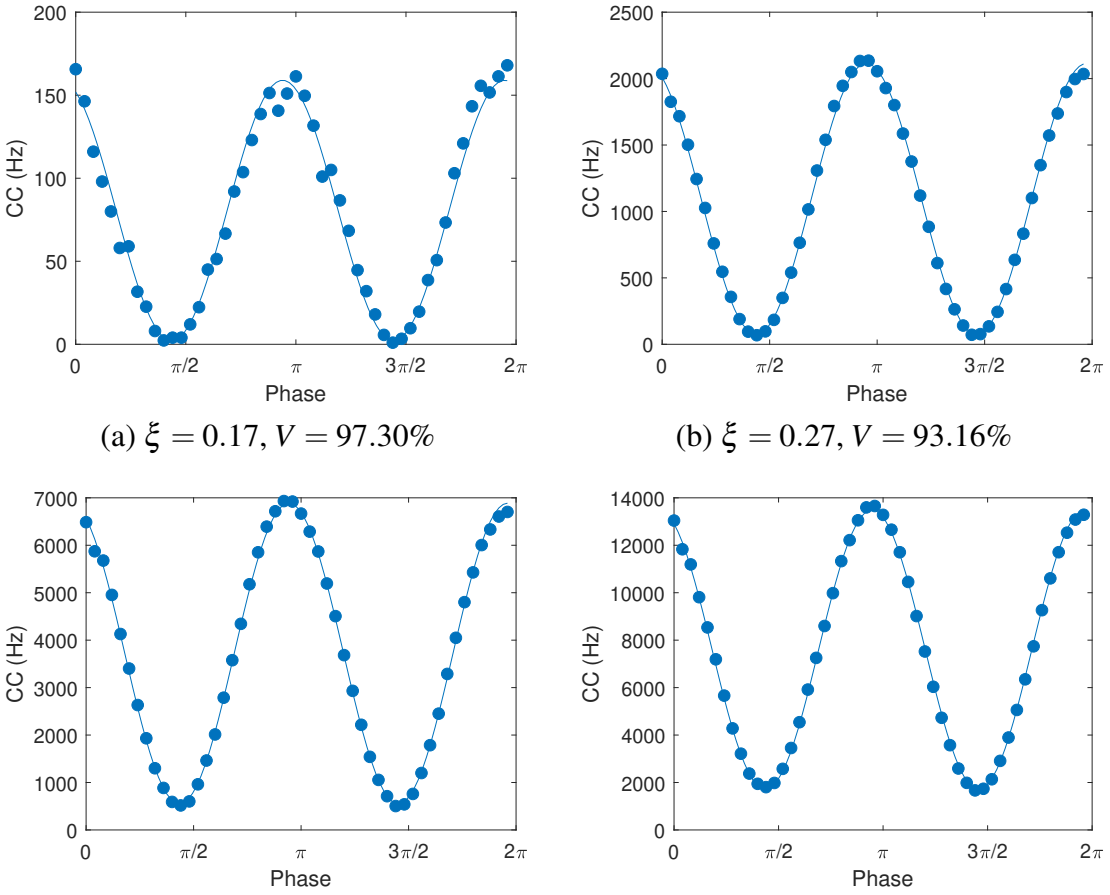

(a) $\xi = 0.17$, $V = 97.30\%$

(b) $\xi = 0.27$, $V = 93.16\%$

(c) $\xi = 0.46$, $V = 85.18\%$

(d) $\xi = 0.62$, $V = 77.38\%$

Figure 3.29: Interference fringe of $|\psi\rangle_{split}$ at different squeeze parameters. The squeeze parameter and visibility are labeled beneath each figure.

so that the squeeze parameter is set to be low in experimental conditions.

For the linear optical circuit, four different unitary matrices are implemented on it by tuning the phase shifters according the square circuit decomposition model. The classical light inputs from the port i can be represented as a column vector I_{in} with its ith element being 1 and the four output port powers are expressed as

$$U \cdot I_{in} = \begin{bmatrix} U_{1i} & U_{2i} & U_{3i} & U_{4i} \end{bmatrix}^T \tag{3.80}$$

which is the ith column vector of the U matrix. The target matrix implementation can

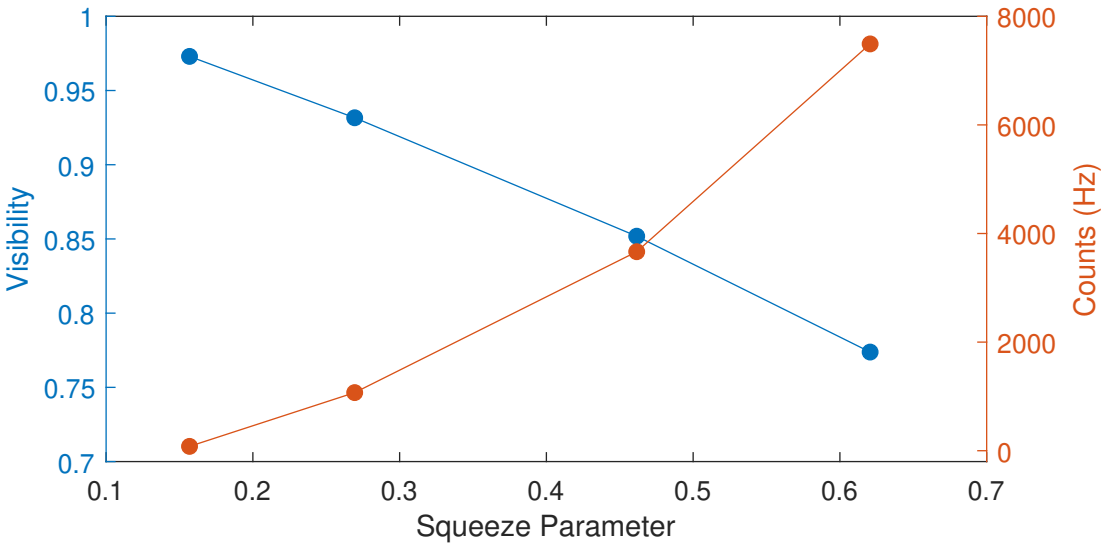

Figure 3.30: Visibility and coincidence count rate over the squeeze parameter. Photon generation probability for both single pair and multi pair would increase and lead to lower interference quality and higher count rate.

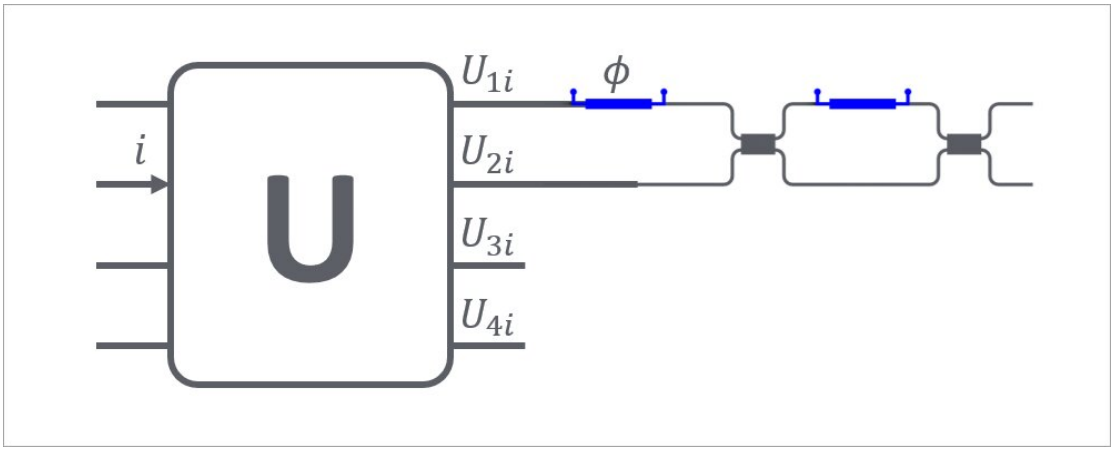

Figure 3.31: Measurement set up for matrix reconstruction. The amplitude is directly measured with detector and relative phase is measured by observing interference fringe with phase shifter ϕ.

be verified by measuring the amplitude and phase of the output classical light. The unitary matrix satisfies the condition as

$$|U_{1i}|^2 + |U_{2i}|^2 + |U_{3i}|^2 + |U_{4i}|^2 = 1 \tag{3.81}$$

and the light intensity is proportional to the amplitude square, which is expressed as

$$I_j \propto |U_{ji}|^2 \tag{3.82}$$

where j is the output port. The amplitude can be estimated as

$$Abs(U_{ji}) = \sqrt{\frac{I_j}{\sum I}} \tag{3.83}$$

For the phase term at each output port, it can be measured by interfering the target light with the adjacent light at a MZI to retrieve the relative phase as shown in Figure 3.31. The output can be expressed as

$$\begin{bmatrix} 1 & 1 \\ 1 & -1 \end{bmatrix} \cdot \begin{bmatrix} e^{i\phi} & 0 \\ 0 & 1 \end{bmatrix} \cdot \begin{bmatrix} U_{1i} \\ U_{2i} \end{bmatrix} = \begin{bmatrix} e^{i\phi}U_{1i} + U_{2i} \\ e^{i\phi}U_{1i} - U_{2i} \end{bmatrix} \tag{3.84}$$

Therefore, the light intensity at upper port can be written as

$$I = |U_{1i}|^2 + |U_{2i}|^2 + e^{i\phi}U_{1i}U_{2i}^{\dagger} + e^{-i\phi}U_{1i}^{\dagger}U_{2i} \tag{3.85}$$

where the U_{1i} and U_{2i} are $U_{1i} = a_1 e^{i\phi_1}$ and $U_{1i} = a_2 e^{i\phi_2}$, respectively. The intensity can be simplified as

$$I = |a_1|^2 + |a_2|^2 + 2|a_1||a_2|\cos(\phi + \phi_1 - \phi_2) \tag{3.86}$$

The phase shifter ϕ has been calibrated previously and the initial phase is solely decided by the relative phase $\phi_1 - \phi_2$ and can be fitted from the interference fringe by changing the heater ϕ. In this way, the phase from output 2, 3, 4 relative to 1 can be measured.

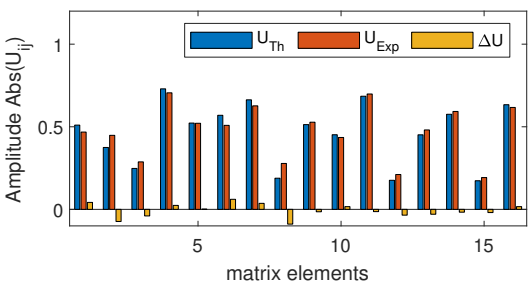

(a) Matrix 1 Abs

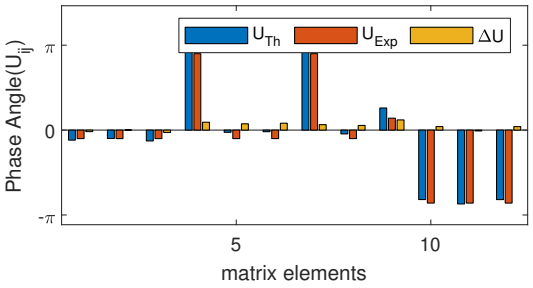

(b) Matrix 1 Angle

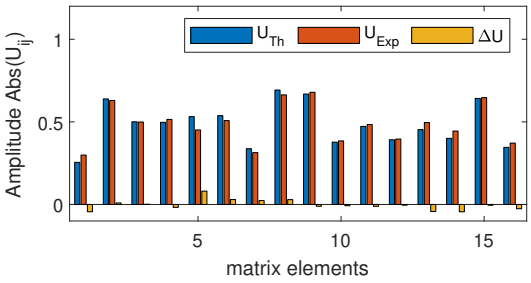

(c) Matrix 2 Abs

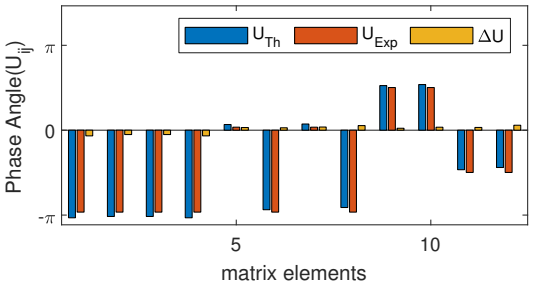

(d) Matrix 2 Angle

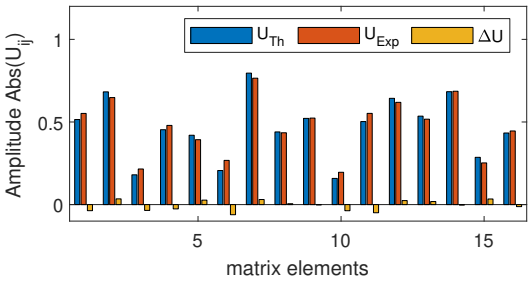

(e) Matrix 3 Abs

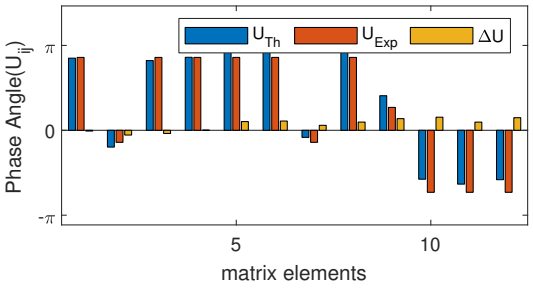

(f) Matrix 3 Angle

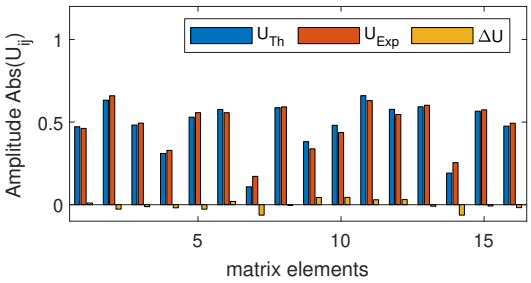

(g) Matrix 4 Abs

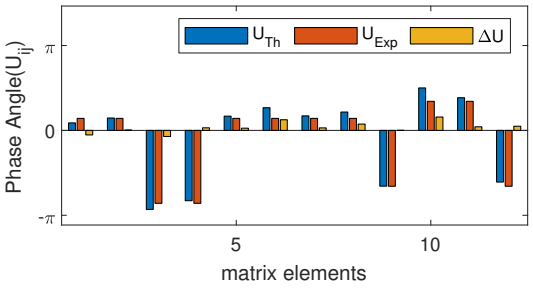

(h) Matrix 4 Angle

Figure 3.32: The 16 amplitudes and 12 phases from 4 different reconstructed unitary matrices are plotted from (a)-(h). Blue bars are theoretical value, orange bars are experimental value and the yellow bars are the error.

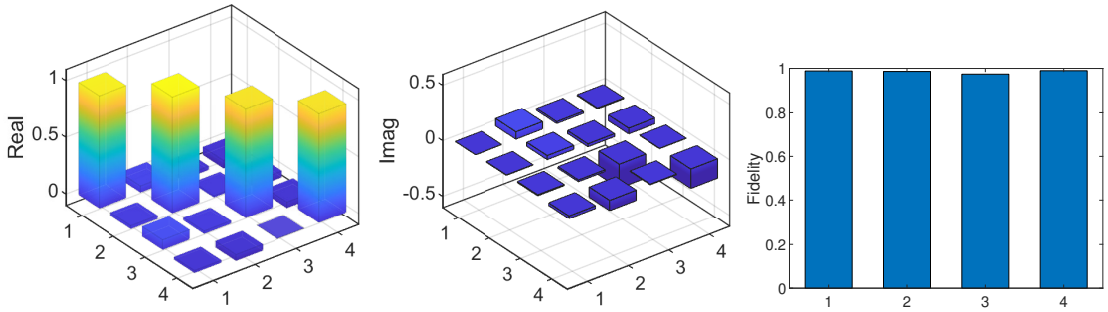

(a) Real (b) Imag (c) Fidelities

Figure 3.33: The visualization of Identity matrix $I = U_{Exp}U_{Th}^{\dagger}$ for (a) Real part and (b) Imag part. (c) Measured similarities of 4 matrices with the theoretical value. The average is $\bar{F} = 98.44\%$.

By switching the input channel i from port 1 to 4, the full matrix of 16 amplitude values and 12 relative phase values can be calibrated. The Figure 3.32 is the plotted amplitude value and phase value from theoretical data (blue bar) and experimental data (orange bar) and their difference (yellow bar) for all 4 sets of configurations.

The data matches very well, which proves the reliability of the circuit and calibration process. To quantify the similarity of the reconstructed unitary matrix and theoretical one, the fidelity is defined as

$$F = \frac{1}{4}Abs(Trace(U_{Exp} \cdot U_{Th}^{\dagger})) \tag{3.87}$$

The optimal matrix product results should be an Identity matrix. Figure 3.33a and Figure 3.33b are the visualized matrix product for the first implementation. The diagonal elements weigh most among all elements and the imaginary part takes almost no value comparing with real part. The fidelities of 4 reconstructed unitary matrices are plot in Figure 3.33c with an average of $\bar{F} = 98.44\%$.

After calibrating all the components of the circuit, the boson sampling and perfect

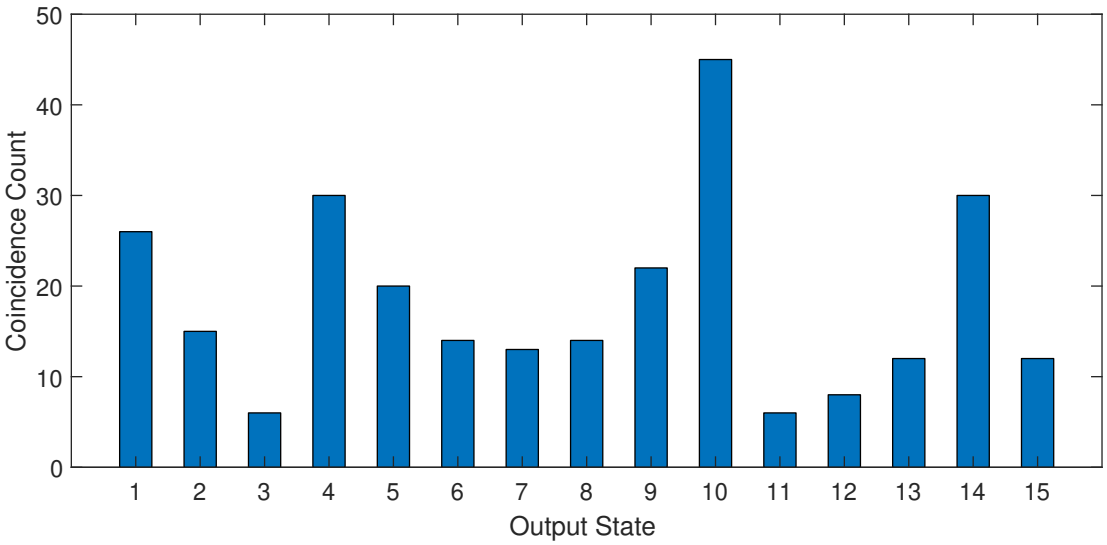

Figure 3.34: Gaussian boson sampling results. 15 combinations of 4 photon clicks are measured from mode $\{0,1,2,3\}$ to mode $\{2,3,4,5\}$. A total of 273 clicks are accumulated in 30 minutes.

matching for a graph is studied. A Gaussian boson sampling is first performed with a 6 mode random unitary matrix and the obtained results are shown in Figure 3.34. The 15 output states are sampling all 4-photon distributions from 6 waveguide modes listed as $\{\{0,1,2,3\},\{0,1,2,4\},\cdots,\{2,3,4,5\}\}$. 273 data points of 4-photon click are accumulated in 30 minutes.

A graph with 6 vertexes are studied here as shown in Figure 3.35a. The connection of vertexes can be expressed with an adjacent matrix M_{adj} as shown in Figure 3.35b. It is a diagonally symmetric matrix with elements 0 and 1. If the two vertexes are connected, the corresponding elements are labeled as 1, else it is 0. Taking SVD decomposition of M_{adj}, it can be expressed as

$$M_{adj} = U \cdot diag(\lambda_1, \lambda_2, \cdots, \lambda_6) \cdot U^{\dagger} \tag{3.88}$$

The unitary matrix of the GBS circuit is set to U and the squeezing parameter at each

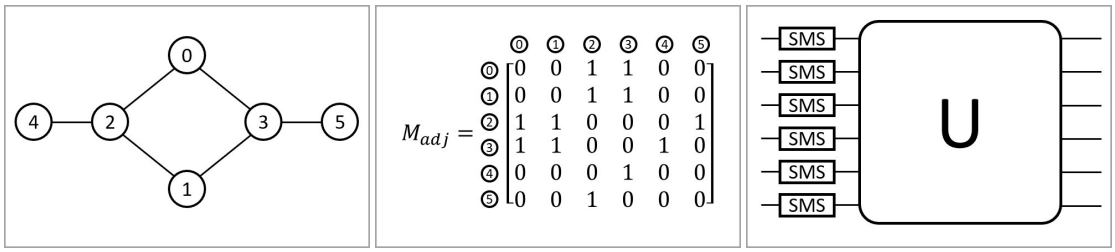

(a) Graph (b) Adjacent Matrix (c) GBS Circuit

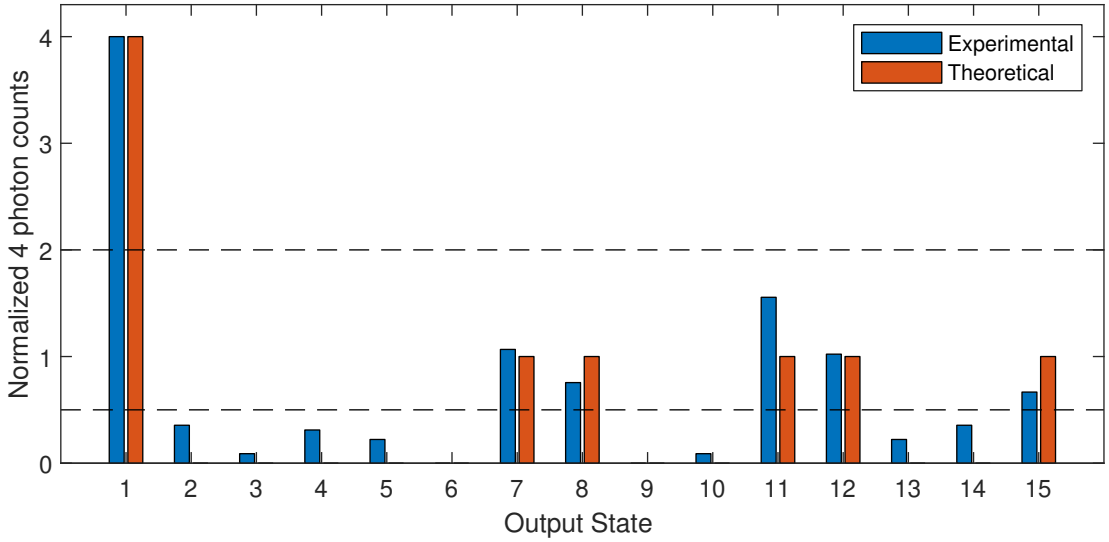

(d) Normalized Distribution

Figure 3.35: GBS for perfect matching. (a) Schematic of a graph with 6 vertex. (b) The adjacent matrix M_{adj} to describe the graph. (c) obtained GBS circuit to calculate perfect matching. (d) Normalized photon distributions for all measured output states.

mode is set to λ_i for mode i. By making measurements at the specific output ports, the perfect matchings of this subgraph can be determined as shown in Figure 3.35c.

The measured results are shown in Figure 3.35d. The x axis is the allowed 15 combinations of 4-photon clicks and the y axis is the normalized count rate. Experimental results D_{exp} are plotted in blue bar and the theoretical results D_{the} are in orange bar. The similarity of the distributions is defined as

$$F = \frac{\vec{D_{exp}} \cdot \vec{D_{the}}}{|\vec{D_{exp}}| \cdot |\vec{D_{the}}|} = 0.9783 \tag{3.89}$$

Two dashed horizontal lines are $y = 0.5$ and $y = 2$ to separate the data into three groups $\{0,1,4\}$, which maps to the perfect matching number of $\{0,1,2\}$. Under this criteria, an accuracy of 100% is achieved for this simple graph.

3.4 Conclusions

In this chapter, the properties of on chip photon source and linear optical circuit is carefully studied. First the SFWM process of on chip photon generation is discussed. Different methods to realize the energy conservation and phase matching condition are listed and calculated. Two matrix decomposition methods are shown as a guide towards realizing arbitrary unitary matrix with linear photonic circuit. For the designed quantum circuit, the photon source properties are carefully studied under both single pump scheme for TMS state and dual pump scheme for SMS state such as the JSI, g_2, CAR, squeeze parameter and so on. Next, the circuit is used to implement unitary matrices and the results are verified experimentally to get a similarity of 98.44%. Finally, a boson sampling is measured with a random unitary set and a perfect matching problem is studied for a 6-vertex graph. GBS circuit is configured to simulate the perfect matching problem and the achieved photon distribution has a similarity of 0.9783 with the theoretical results. The subgraph perfect matching number is also calculated to be identical with the theory.

Chapter 4

Qubit Error Correction for Quantum Computer

In this chapter, the fabrication and implementation of a quantum error correction scheme on a silicon photonic chip is demonstrated. A single qubit quantum information is encoded fully on chip with 4 physical qubits. Three tasks of qubit reconstruction, error type identification and fault-tolerant quantum teleportation are demonstrated with chip scale control of qubits. The experimental results successfully show the functionality of this error correction scheme with higher fidelities than previous demonstration on bulk optics and fiber systems.

4.1 Theory of Qubit Error Correction

Quantum information is fragile. On the one hand, individual subsystems requires to interact sufficiently strongly to perform computations, and on the other hand, each subsystems should be adequately insulated from its environment [16]. Yet, the discovery of quantum error-correcting codes [17–20] convincingly demonstrate the possibility of overcoming memory and transmission errors provided the noise level is below a certain threshold.

Cluster states is a highly entangled resources for one-way quantum computation. Fault-tolerant thresholds for cluster states have been established [156] to ensure the success of the computation. Recently, fault-tolerant one-way quantum computer using cluster states in three dimensions have also been proposed [21]. Stabilizers of the cluster state constitutes a sufficient backbone of fault-tolerant quantum computation [22, 23]. Most error correcting codes are stabilizer codes. There is a general approach to quantum error correction called operator quantum error correction [24], and even for this approach, a stabilizer formalism has also been formulated for it [157].

With the inspiration of previous work [158, 159], a cluster state based quantum error correction code is implemented on an integrated silicon photonic platform to demonstrate its capability to correct or detect a single qubit error. A four-physical-qubit state is generated to encode one logical qubit and its performance against various errors is proved in this section. This scheme also can be applied to identify the error types by measuring the stabilizers and further get extended to demonstrate the fault tolerant quantum teleportation process.

4.1.1 Error-Correction Encoding

The error correction encoding scheme first begins from an experimentally feasible initial state $\frac{1}{\sqrt{2}}(|00\rangle + |11\rangle)|0\rangle$ that can be realized easily on photonic chip. By implementing a fusion operation on qubit 2 and 3 and post selection on the result, a 3-qubit GHZ state $\frac{1}{\sqrt{2}}(|000\rangle + |111\rangle)$ can be realized with a success probability 50%. Then a Hadamard gate H is performed on qubit 2 and 3 to transfer the GHZ state into the form of $\frac{1}{\sqrt{2}}(|0++\rangle + |1--\rangle)$, which is a 3-qubit linear cluster state. The 3-photon 3-qubit state further expands to a higher dimension space of 4 waveguides modes as $|+\rangle \rightarrow |0\rangle + |3\rangle$, $|-\rangle \rightarrow |0\rangle - |3\rangle$ to mimic two qubits with one photon using the mapping given by

$$|0\rangle \rightarrow |00\rangle, |1\rangle \rightarrow |01\rangle, |2\rangle \rightarrow |10\rangle, |3\rangle \rightarrow |11\rangle \tag{4.1}$$

Thus, the final state can be transformed into a 3-photon 5-qubit state, which is expressed as

$$|L_5\rangle = \frac{1}{\sqrt{2}}(|0\phi^+\phi^+\rangle + |1\phi^-\phi^-\rangle) \tag{4.2}$$

where $|\phi^+\rangle = \frac{1}{\sqrt{2}}(|00\rangle + |11\rangle)$ and $|\phi^-\rangle = \frac{1}{\sqrt{2}}(|00\rangle - |11\rangle)$ are the corresponding bell states, and this state is also equivalent to a linear cluster state under local unitary trans-

formation. The whole process can be expressed as

$$\begin{aligned}
|\psi\rangle =& \frac{1}{\sqrt{2}}(|00\rangle + |11\rangle)|0\rangle \\
\rightarrow& \frac{1}{2}(|00\rangle + |11\rangle)(|0\rangle + |1\rangle) \\
\rightarrow& \frac{1}{\sqrt{2}}(|000\rangle + |111\rangle) \\
\rightarrow& \frac{1}{2\sqrt{2}}|0\rangle(|0\rangle + |3\rangle)(|0\rangle + |3\rangle) + \frac{1}{2\sqrt{2}}|1\rangle(|0\rangle - |3\rangle)(|0\rangle - |3\rangle) \\
\rightarrow& \frac{1}{\sqrt{2}}|0\rangle_1 \left|\phi^+_{23}\phi^+_{45}\right\rangle + \frac{1}{\sqrt{2}}|1\rangle_1 \left|\phi^-_{23}\phi^-_{45}\right\rangle
\end{aligned} \tag{4.3}$$

In the quantum error correction code, the logical qubit $|\psi\rangle_L = \alpha|0\rangle_L + \beta|1\rangle_L$ is encoded in a 4-physical-qubit system, which is expressed as [158]

$$|0\rangle_L = \frac{1}{2}(|00\rangle + |11\rangle)_{12}(|00\rangle + |11\rangle)_{34} = \left|\phi^+\phi^+\right\rangle \tag{4.4a}$$

$$|1\rangle_L = \frac{1}{2}(|00\rangle - |11\rangle)_{12}(|00\rangle - |11\rangle)_{34} = \left|\phi^-\phi^-\right\rangle \tag{4.4b}$$

where the subscripts L and $1,2,3,4$ each means logical qubit and physical qubit indices. Quantum information is loaded into the error correction scheme by performing a single qubit operation U, which is expressed as

$$U = \begin{bmatrix} \alpha & \beta \\ \beta & -\alpha \end{bmatrix} \tag{4.5}$$

on the first physical qubit of state $|L_5\rangle$, the evolved state is given by

$$\begin{aligned}
U|L_5\rangle =& \frac{1}{\sqrt{2}}(U|0\rangle \left|\phi^+\phi^+\right\rangle + U|1\rangle \left|\phi^-\phi^-\right\rangle) \\
=& \frac{1}{\sqrt{2}}[|0\rangle(\alpha \left|\phi^+\phi^+\right\rangle) + \beta \left|\phi^-\phi^-\right\rangle + |1\rangle(\beta \left|\phi^+\phi^+\right\rangle) - \alpha \left|\phi^-\phi^-\right\rangle]
\end{aligned} \tag{4.6}$$

and followed by a Z basis measurement to teleport information to the remaining four physical qubits and the encoded state will collapse to the form expressed as

$$|\psi\rangle_{1234} = \alpha \left|\phi^+\phi^+\right\rangle + \beta \left|\phi^-\phi^-\right\rangle \tag{4.7}$$

for measurement result $|0\rangle$ on qubit 1 with the probability of $p = |\frac{1}{\sqrt{2}}|^2 = 0.5$. This 2-photon 4-qubit encoding scheme is robust against single qubit error and how it works on quantum information reconstruction and error type detection will be discussed.

4.1.2 State Reconstruction

For an arbitrary single qubit error at a given location, the encoded quantum information can be reconstructed from the remaining three qubits by applying specific Pauli matrices as correction. Take error at qubit 4 as an example: the quantum state $|\psi\rangle_{1234}$ is expressed as

$$\begin{aligned} |\psi\rangle_{1234} &= \frac{1}{\sqrt{2}}\alpha \left|\phi^+\right\rangle (|00\rangle + |11\rangle) + \frac{1}{\sqrt{2}}\beta \left|\phi^-\right\rangle (|00\rangle - |11\rangle) \\ &= \frac{1}{\sqrt{2}}(\alpha \left|\phi^+\right\rangle + \beta \left|\phi^-\right\rangle)|00\rangle + \frac{1}{\sqrt{2}}(\alpha \left|\phi^+\right\rangle - \beta \left|\phi^-\right\rangle)|11\rangle \end{aligned} \tag{4.8}$$

Due to the error signal at qubit 4, the measurement result is no longer reliable thus the error qubit 4 is traced out, leaving the remaining three qubits to be a mixed state with 50% probability in state $|A\rangle$ expressed as

$$\begin{aligned} 50\% : |A\rangle &= (\alpha \left|\phi^+\right\rangle + \beta \left|\phi^-\right\rangle)_{12} |0\rangle_3 \\ &= \frac{1}{\sqrt{2}} \begin{bmatrix} \alpha+\beta & 0 & 0 & \alpha-\beta & 0 & 0 & 0 & 0 \end{bmatrix}^T \end{aligned} \tag{4.9}$$

and 50% probability in state $|B\rangle$ expressed as

$$\begin{aligned} 50\% : |B\rangle &= (\alpha \left|\phi^{+}\right\rangle - \beta \left|\phi^{-}\right\rangle)_{12} |1\rangle_3 \\ &= \frac{1}{\sqrt{2}} \begin{bmatrix} 0 & 0 & 0 & 0 & \alpha-\beta & 0 & 0 & \alpha+\beta \end{bmatrix}^T \end{aligned} \tag{4.10}$$

It has an equal probability of 50% to be in either state $|A\rangle$ or state $|B\rangle$ and density matrix for the mixed state is expressed as

$$\begin{aligned} \rho &= \frac{1}{2}(|A\rangle \langle A| + |B\rangle \langle B|) \\ &= \frac{1}{2} \begin{bmatrix} \rho_{11} & 0 & 0 & \rho_{14} & 0 & 0 & 0 & 0 \\ 0 & 0 & 0 & 0 & 0 & 0 & 0 & 0 \\ 0 & 0 & 0 & 0 & 0 & 0 & 0 & 0 \\ \rho_{41} & 0 & 0 & \rho_{44} & 0 & 0 & 0 & 0 \\ 0 & 0 & 0 & 0 & \rho_{55} & 0 & 0 & \rho_{58} \\ 0 & 0 & 0 & 0 & 0 & 0 & 0 & 0 \\ 0 & 0 & 0 & 0 & 0 & 0 & 0 & 0 \\ 0 & 0 & 0 & 0 & \rho_{85} & 0 & 0 & \rho_{88} \end{bmatrix} \end{aligned} \tag{4.11}$$

where all these elements are defined as

$$\rho_{11} = |\alpha|^2 + |\beta|^2 + \alpha\beta^* + \alpha^*\beta \tag{4.12a}$$

$$\rho_{14} = |\alpha|^2 - |\beta|^2 - \alpha\beta^* + \alpha^*\beta \tag{4.12b}$$

$$\rho_{41} = |\alpha|^2 - |\beta|^2 + \alpha\beta^* - \alpha^*\beta \tag{4.12c}$$

$$\rho_{44} = |\alpha|^2 + |\beta|^2 - \alpha\beta^* - \alpha^*\beta \tag{4.12d}$$

$$\rho_{55} = |\alpha|^2 + |\beta|^2 - \alpha\beta^* - \alpha^*\beta \tag{4.12e}$$

$$\rho_{58} = |\alpha|^2 - |\beta|^2 + \alpha\beta^* - \alpha^*\beta \tag{4.12f}$$

$$\rho_{85} = |\alpha|^2 - |\beta|^2 - \alpha\beta^* + \alpha^*\beta \tag{4.12g}$$

$$\rho_{88} = |\alpha|^2 + |\beta|^2 + \alpha\beta^* + \alpha^*\beta \tag{4.12h}$$

Then, the Z measurement is performed on qubit 3 and the state can be expressed as

$$|A\rangle \to \alpha\left|\phi^+\right\rangle + \beta\left|\phi^-\right\rangle = \frac{1}{\sqrt{2}}\begin{bmatrix}\alpha+\beta & 0 & 0 & \alpha-\beta\end{bmatrix}^T \tag{4.13a}$$

$$|B\rangle \to \alpha\left|\phi^+\right\rangle - \beta\left|\phi^-\right\rangle = \frac{1}{\sqrt{2}}\begin{bmatrix}\alpha+\beta & 0 & 0 & \beta-\alpha\end{bmatrix}^T \tag{4.13b}$$

$$|A/B\rangle = \alpha\left|\phi^+\right\rangle + (-1)^{m_3}\beta\left|\phi^-\right\rangle \tag{4.13c}$$

The state can be unified given the measurement result $m_3 = 0/1$ on qubit 3. Finally, another X measurement is performed on qubit 2, which are given by

$$\begin{aligned}|A\rangle =& H(\alpha|0\rangle + \beta|1\rangle)|+\rangle + H(\beta|0\rangle + \alpha|1\rangle)|-\rangle \\ \to& HX^{m_2}(\alpha|0\rangle + \beta|1\rangle)\end{aligned} \tag{4.14a}$$

$$\begin{aligned} |B\rangle =& H(\alpha|0\rangle - \beta|1\rangle)|+\rangle - H(\beta|0\rangle - \alpha|1\rangle)|-\rangle \\ \rightarrow& HX^{m_2}(\alpha|0\rangle - \beta|1\rangle) \end{aligned} \tag{4.14b}$$

$$|\varphi\rangle = HX^{m_2}Z^{m_3}(\alpha|0\rangle + \beta|1\rangle) \tag{4.14c}$$

where $m_2 = 0/1$ is the measurement results of qubit 2. Therefore, the final state can be simplified to the form of $|\varphi\rangle$ and the density matrix becomes pure again as $\rho = |\varphi\rangle\langle\varphi|$ given the measurement results of m_2 and m_3. Thus, encoded qubit can be reconstructed from the error with feed forward control on qubit 1. The same process can be applied to arbitrary single qubit error at a known location and the corresponding correction operations can be checked in the Table 4.1. E_i, m_i and Q_i each represents the error, measurement result and correction operator at qubit i.

Table 4.1: Qubit Correction Operator

E_1			E_2			E_3			E_4		
m_2	m_3	Q_4	m_1	m_3	Q_4	m_4	m_2	Q_1	m_3	m_2	Q_1
0	0	H	0	0	H	0	0	H	0	0	H
0	1	HX	0	1	HX	0	1	HX	0	1	HX
1	0	HZ	1	0	HZ	1	0	HZ	1	0	HZ
1	1	HXZ	1	1	HXZ	1	1	HXZ	1	1	HXZ

4.1.3 Error Type Identification

Another function of the scheme is to identify the qubit error type at a given location by measuring the stabilizers. If an operator S keeps the state $|\phi\rangle$ unchanged after performing on it or has an eigenvalue $\lambda_i = 1$, this operator is called the stabilizer of the state $|\phi\rangle_i$, which is given by

$$S|\phi\rangle = |\phi\rangle \tag{4.15}$$

For a cluster state, its stabilizer is represented as $S_i = X_i \otimes \prod_j Z_j$, where i is index for qubit i and j are indices for all the other qubits connected with qubit i. Take $|L_3\rangle$ in Figure 2.4 for example, it has 3 stabilizers expressed as

$$S_1 = X_1 \otimes Z_2 \otimes Z_3 \tag{4.16a}$$

$$S_2 = X_2 \otimes Z_1 \tag{4.16b}$$

$$S_3 = X_3 \otimes Z_1 \tag{4.16c}$$

In the encoding scheme, the state $|\psi\rangle_{1234}$ in Equation 4.7 is composed of $|\phi^+\rangle$ and $|\phi^-\rangle$, which are equivalent to $|L_2\rangle$ under local unitary transform. Therefore, their stabilizers can be deducted as

$$\begin{aligned} \left|\phi^+\right\rangle = H_2 |L_2\rangle = H_2 Z_1 X_2 |L_2\rangle = H_2 Z_1 X_2 H_2 \left|\phi^+\right\rangle = Z_1 Z_2 \left|\phi^+\right\rangle \\ = H_2 X_1 Z_2 |L_2\rangle = H_2 X_1 Z_2 H_2 \left|\phi^+\right\rangle = X_1 X_2 \left|\phi^+\right\rangle \end{aligned} \tag{4.17a}$$

$$\begin{aligned} \left|\phi^-\right\rangle = Z_2 \left|\phi^+\right\rangle = Z_2 Z_1 Z_2 \left|\phi^+\right\rangle = Z_2 Z_1 Z_2 Z_2 \left|\phi^-\right\rangle = Z_1 Z_2 \left|\phi^-\right\rangle \\ = Z_2 X_1 X_2 \left|\phi^+\right\rangle = Z_2 X_1 X_2 Z_2 \left|\phi^-\right\rangle = -X_1 X_2 \left|\phi^-\right\rangle \end{aligned} \tag{4.17b}$$

It is obvious to see that operator $Z_1 \otimes Z_2$ is stabilizer for state $|\phi^+\rangle$ and $|\phi^-\rangle$ while $X_1 \otimes X_2$ is not as it will generate a -1 sign when acting on $|\phi^-\rangle$, but this operator can be performed on both $\left|\phi_{12}^-\right\rangle$ and $\left|\phi_{34}^-\right\rangle$ to cancel the -1 sign. Therefore, the three stabilizers

Table 4.2: Expectation Value of Stabilizers.

Location	1 or 2			3 or 4		
Type	S_1	S_2	S_3	S_1	S_2	S_3
I	1	1	1	1	1	1
X	-1	1	1	1	-1	1
Y	-1	1	-1	1	-1	-1
Z	1	1	-1	1	1	-1

for $|\psi\rangle_{1234}$ can be written as

$$S_1 = Z_1 \otimes Z_2 \otimes I_3 \otimes I_4 \tag{4.18a}$$

$$S_2 = I_1 \otimes I_2 \otimes Z_3 \otimes Z_4 \tag{4.18b}$$

$$S_3 = X_1 \otimes X_2 \otimes X_3 \otimes X_4 \tag{4.18c}$$

The expectation value of state $|\psi\rangle_{1234}$ under stabilizer operator is given by

$$\langle S_i \rangle = \langle \psi | S_i | \psi \rangle_{1234} = 1 \tag{4.19}$$

If there exists error on state $|\psi\rangle_{1234}$, the expectation value of $\langle S_i \rangle$ will be different based on the error type. Take error type X at qubit 1 as an example, the expectation value of $\langle S_1 \rangle$ is expressed as

$$\langle S_1 \rangle = \langle \psi | X_1^* S_1 X_1 | \psi \rangle_{1234} = -1 \tag{4.20a}$$

$$\langle S_2 \rangle = \langle \psi | X_1^* S_2 X_1 | \psi \rangle_{1234} = 1 \tag{4.20b}$$

$$\langle S_3 \rangle = \langle \psi | X_1^* S_3 X_1 | \psi \rangle_{1234} = 1 \tag{4.20c}$$

All the corresponding theoretical values can be calculated similarly and their theoretical values can be obtained from the Table 4.2. All four expectation values are listed

under Identity operator I (no error) and three basic error types X, Y, Z with error qubit location from 1 to 4. It can be seen that the combination of the expectation values for three stabilizers at a known qubit location are unique and this will map to an explicit error type, which is the working principle of this encoding scheme to identify the error types.

Experimentally, the expectation value is measured by counting the multi-photon clicks under different basis. For a d-dimensional single qudit observable operator U, which is a Hermitian operator, the state $|\psi\rangle$ should be measured under the eigenvectors $|v_i\rangle$ of U to calculate the expectation value of $\langle U\rangle$. Since U is Hermitian, it always has a real eigenvalue λ_i for its eigenvector $|v_i\rangle$, so that the operator U can be expressed as

$$U = \sum_{i=0}^{d-1} \lambda_i |v_i\rangle \langle v_i| \tag{4.21}$$

and the corresponding expectation value is given by

$$\begin{aligned} \langle U\rangle &= \langle\psi| U |\psi\rangle \\ &= \sum_{i=0}^{d-1} \lambda_i \langle\psi|v_i\rangle \langle v_i|\psi\rangle \\ &= \sum_{i=0}^{d-1} \lambda_i |\langle\psi|v_i\rangle|^2 \end{aligned} \tag{4.22}$$

Then, the basis transformation matrix T between eigenvector basis v_i and qudit basis $\{|i\rangle\}$ is defined as

$$T = \sum_{i=0}^{d-1} |i\rangle \langle v_i| \tag{4.23a}$$

$$\langle v_i| = \langle i| T \tag{4.23b}$$

The expectation value $\langle U \rangle$ can be expressed as

$$\langle U \rangle = \sum_{i=0}^{d-1} \lambda_i |\langle i|(T\psi)\rangle|^2 \tag{4.24}$$

Therefore, a rotation matrix T is performed after state $|\psi\rangle$ and it is measured under qudit basis $\{|i\rangle\}$ to calculate the expectation values.

For the experimental 4-qubit system, take the expectation value $\langle S_3 \rangle$ for example, the eigensystem of operator X is first calculated as

$$\lambda_0 = 1, |v_0\rangle = \frac{1}{\sqrt{2}} \begin{bmatrix} 1 & 1 \end{bmatrix}^T \tag{4.25a}$$

$$\lambda_1 = -1, |v_1\rangle = \frac{1}{\sqrt{2}} \begin{bmatrix} 1 & -1 \end{bmatrix}^T \tag{4.25b}$$

$$Z_n = \sum_{i=0}^{1} \lambda_{n,i} |v_{n,i}\rangle \langle v_{n,i}| \tag{4.25c}$$

Thus, the stabilizer S_3 can be expressed as

$$S_3 = X_1 \otimes X_2 \otimes X_3 \otimes X_4 = \sum_{i,j,k,l=0}^{1} \lambda_{i,j,k,l} \hat{v}_{i,j,k,l} \tag{4.26a}$$

$$\lambda_{i,j,k,l} = (-1)^{i+j+k+l} \tag{4.26b}$$

$$\hat{v}_{i,j,k,l} = |v_{1,i}\rangle\langle v_{1,i}| \otimes |v_{2,j}\rangle\langle v_{2,j}| \otimes |v_{3,k}\rangle\langle v_{3,k}| \otimes |v_{4,l}\rangle\langle v_{4,l}| \tag{4.26c}$$

The stabilizer S_3 is expanded into 16 terms of 4-qubit operator combinations with eigenvectors $\hat{v}_{i,j,k,l}$ from each operator and expectation value $\langle S_3 \rangle$ under state $|\psi\rangle_{1234}$

is then expressed as

$$\begin{aligned}\langle S_3\rangle &= \sum_{i,j,k,l=0}^{1} \lambda_{i,j,k,l} \langle\psi| \hat{v}_{i,j,k,l} |\psi\rangle_{1234} \\ &= \sum_{i,j,k,l=0}^{1} \lambda_{i,j,k,l} |\langle v_{1,i} \otimes v_{2,j} \otimes v_{3,k} \otimes v_{4,l} | \psi\rangle|^2_{1234}.\end{aligned} \tag{4.27}$$

To calculate the expectation value, each terms in experimental basis $\{|i,j,k,l\rangle\}$ should be measured and the corresponding basis transformation matrix is also the tensor product of each basic operator expressed as

$$\begin{aligned}T_n =& |0\rangle \langle v_{n,0}| + |1\rangle \langle v_{n,1}| \\ =& \frac{1}{\sqrt{2}} \begin{bmatrix} 1 & 1 \\ 1 & -1 \end{bmatrix} = H\end{aligned} \tag{4.28a}$$

$$\begin{aligned}T =& T_1 \otimes T_2 \otimes T_3 \otimes T_4 \\ =& H^{\otimes 4}\end{aligned} \tag{4.28b}$$

Then, the H operation is performed on each qubit of state $|\psi\rangle_{1234}$ and the measurement basis of 4 qubits is changed to

$$|v_{1,i} \otimes v_{2,j} \otimes v_{3,k} \otimes v_{4,l}\rangle \rightarrow |i,j,k,l\rangle . \tag{4.29}$$

The expectation value expression will be expressed as

$$\langle S_3\rangle = \sum_{i,j,k,l=0}^{1} \lambda_{i,j,k,l} |\langle i,j,k,l|T\psi\rangle|^2_{1234}. \tag{4.30}$$

Experimentally, the 4 qubit coincidence counts are recorded under the basis $|i,j,k,l\rangle$ as

$CC_{i,j,k,l}$ and the corresponding expectation value is calculated as

$$\langle S_3 \rangle_{exp} = \sum_{i,j,k,l=0}^{1} \lambda_{i,j,k,l} CC_{i,j,k,l}. \tag{4.31}$$

By changing the stabilizer S_i and simulating different error types, the coincidence counts can be measured and get normalized into expectation values as shown in Table 4.2.

4.1.4 Error Corrected Quantum State Teleportation

Finally, the error correction scheme can be extended to fault tolerant quantum teleportation. The idea of MBQC is to teleport the quantum information by performing measurements on cluster state and the basic unit is a two qubit cluster state $|L_2\rangle = \frac{1}{\sqrt{2}}(|0+\rangle + |1-\rangle)$. An arbitrary single qubit operator U acting on one qubit can be teleported to the other qubit by performing a Z basis measurement on that qubit and a feed-forward control on the other qubit. The teleportation process can be expressed as

$$U = \begin{bmatrix} \alpha & \beta \\ \beta & -\alpha \end{bmatrix} \tag{4.32a}$$

$$\begin{aligned} U|L_2\rangle =& \frac{1}{\sqrt{2}}|0\rangle HU|0\rangle + \frac{1}{\sqrt{2}}|1\rangle HU|1\rangle \\ \rightarrow& \frac{1}{\sqrt{2}} HU|0\rangle + \frac{1}{\sqrt{2}} HUX|0\rangle \\ \rightarrow& HUX^{m_1}|0\rangle \end{aligned} \tag{4.32b}$$

where $m_1 = 0/1$ is the measurement results of first qubit on Z basis. As can be seen that operation U on first qubit is transferred to the second qubit with the measurement result

m_1 as feed forward information. This idea can be used in future quantum network applications like two separate quantum nodes Alice and Bod who are far away from each other would like to connect their quantum networks and perform some quantum operation remotely. Instead of directly operating with each other, they can first share a pair of entangled state $|L_2\rangle$ and perform the target operation U locally. They just need to share the measurement result m_1 through the classical channel to teleport the quantum operation to another side.

Here, a fault tolerant quantum teleportation is demonstrated. The scheme also allows the teleportation process to be discarded or repeated if the measurement fails due to some loss or error. The main idea of this fault tolerance scheme is that performing a Z basis measurement can remove the qubit from the cluster state chain and disentangle the remaining state by cutting the CZ entanglement operation. An n-qubit cluster state can always be written as $|L_n\rangle = |0A\rangle + |1B\rangle$, where state $|A\rangle$ and $|B\rangle$ is defined by the specific state form. Connecting 2 cluster states $|L_n\rangle$ to a vertex $|+\rangle$, a $2n+1$ cluster state is formed as shown in Figure 4.1a, which can be expressed as

$$\begin{aligned} & (|A0\rangle + |B1\rangle)\,|+\rangle\,(|0A\rangle + |1B\rangle) \\ \xrightarrow{CZ_1} & (|A0+\rangle + |B1-\rangle)(|0A\rangle + |1B\rangle) \\ \xrightarrow{CZ_2} & |A0+0A\rangle + |A0-1B\rangle + |B1-0A\rangle + |B1+1B\rangle \end{aligned} \tag{4.33}$$

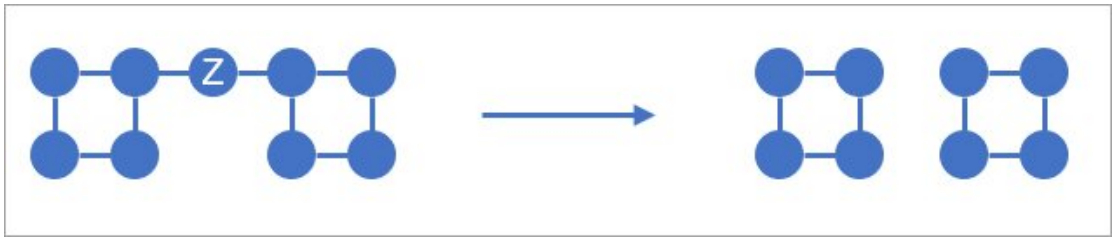

(a)

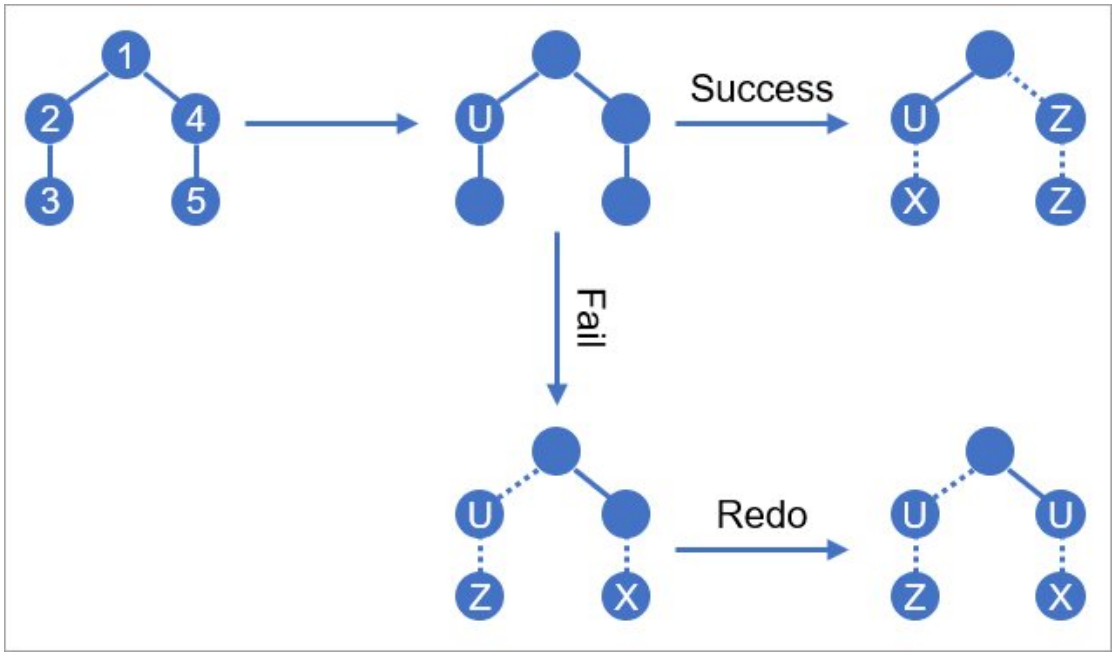

(b)

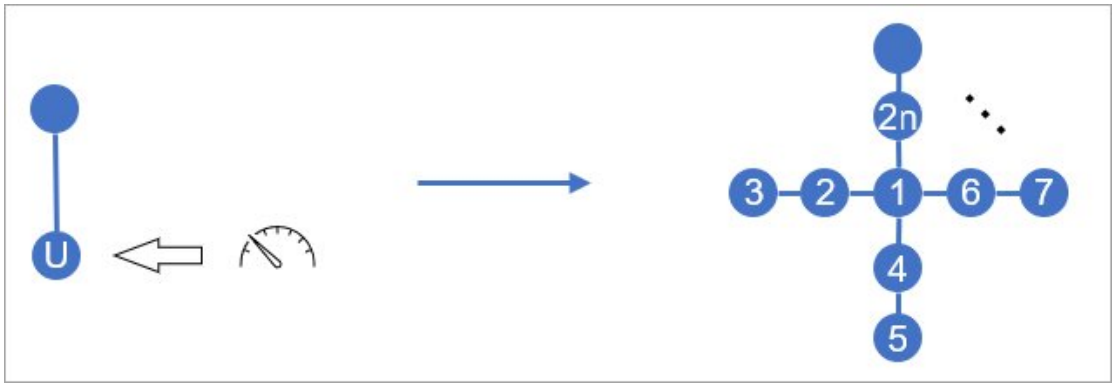

(c)

Figure 4.1: (a) A cluster state can be disentangled by performing Z measurement. (b) Schematic of fault tolerant MBQC. (c) The graph representation for state $|\varphi\rangle_{2n+1}$ that allows $n-1$ times teleportation redo.

By performing Z measurement on the vertex, the state can be expressed as

$$\begin{aligned}|L_{2n+1}\rangle =& |A0+0A\rangle + |A0-1b\rangle + |B1-0A\rangle + |B1+1B\rangle \\ =& (|A0\rangle + |B1\rangle)(|0A\rangle + |1B\rangle)|0\rangle + \\ & (|A0\rangle - |B1\rangle)(|0A\rangle - |1B\rangle)|1\rangle \\ \rightarrow& (|A0\rangle + Z^m|B1\rangle)(|0A\rangle + Z^m|1B\rangle),\end{aligned} \tag{4.34}$$

which is a separable state of two original cluster state $|L_n\rangle$ after correction operator and the entanglement is efficiently removed by Z measurement.

For the error corrected quantum teleportation state $|\psi\rangle$ in Equation 4.3, it is equivalent to a linear cluster state $|L_5\rangle$ under local unitary transform and the similar idea can be applied to disentangle the faulty operations from the state. The unitary operation U can be performed on one of the qubit from 2 to 5 and teleport this qubit to qubit 1. If the teleportation succeeds, the redundant qubits can be removed by some measurement without affecting the current results. If the teleportation process fails, the remaining qubit can be used to reconstruct the $|L_2\rangle$ and perform the teleportation again. Take error at qubit 2 for instance, as can be seen in Figure 4.1b that the target operation U acting on qubit 2 can be expressed as

$$\begin{aligned}|\psi\rangle =& \frac{1}{\sqrt{2}}|0\rangle_1 \left|\phi_{23}^+\phi_{45}^+\right\rangle + \frac{1}{\sqrt{2}}|1\rangle_1 \left|\phi_{23}^-\phi_{45}^-\right\rangle \\ \rightarrow& \frac{1}{2}U_2|00\rangle_{23}\left(\left|0\phi^+\right\rangle + \left|1\phi^-\right\rangle\right)_{145} + \\ & \frac{1}{2}U_2|11\rangle_{23}\left(\left|0\phi^+\right\rangle - \left|1\phi^-\right\rangle\right)_{145}\end{aligned} \tag{4.35}$$

If there is no error, the X measurement can be performed on qubit 3, Z measurement can be performed on qubit 4 and 5 to remove these redundant qubits, which can be

expressed as

$$
\begin{aligned}
|\psi\rangle \xrightarrow{4,5} & \frac{1}{2\sqrt{2}} U_2 |00\rangle_{23} (|000\rangle + |011\rangle + |100\rangle - |111\rangle)_{145} + \\
& \frac{1}{2\sqrt{2}} U_2 |11\rangle_{23} (|000\rangle + |011\rangle - |100\rangle + |111\rangle)_{145} \\
= & \frac{1}{2} U_2 |00\rangle_{23} (|+00\rangle + |-11\rangle)_{145} + \\
& \frac{1}{2} U_2 |11\rangle_{23} (|-00\rangle + |+11\rangle)_{145} \\
\xrightarrow{3} & \frac{1}{2\sqrt{2}} U_2 (|0+\rangle + |0-\rangle)_{23} (|+00\rangle + |-11\rangle)_{145} + \\
& \frac{1}{2\sqrt{2}} U_2 (|1+\rangle - |1-\rangle)_{23} (|-00\rangle + |+11\rangle)_{145} \\
= & \frac{1}{2\sqrt{2}} U_2 (|0+\rangle + |1-\rangle)_{21} |+00\rangle_{345} + \\
& \frac{1}{2\sqrt{2}} U_2 (|0-\rangle + |1+\rangle)_{21} |+11\rangle_{345} + \\
& \frac{1}{2\sqrt{2}} U_2 (|0+\rangle - |1-\rangle)_{21} |-00\rangle_{345} + \\
& \frac{1}{2\sqrt{2}} U_2 (|0-\rangle - |1+\rangle)_{21} |-11\rangle_{345} \\
\rightarrow & U_2 Z_2^{m_3} Z_1^{m_4+m_5} (|0+\rangle + |1-\rangle)_{21}
\end{aligned}
\tag{4.36}
$$

It can be seen that the quantum state on qubit 1 and 2 can always be transformed to $|L_2\rangle$ given the measurement results m_3, m_4, m_5 and the operation U_2 can be transferred from qubit 2 to qubit 1 successfully.

Next, the encoding scheme will be used to recover the teleportation should the operation on qubit 2 fails. Z measurement can be performed on qubit 3 to remove the

U operation from the state, which is given by

$$\begin{aligned}
|\psi\rangle \xrightarrow{U_2} & U_2 |00\rangle_{23} \left(\left|0\phi^+\right\rangle + \left|1\phi^-\right\rangle\right)_{145} + \\
& U_2 |11\rangle_{23} \left(\left|0\phi^+\right\rangle - \left|1\phi^-\right\rangle\right)_{145} \\
\xrightarrow{3} & \frac{1}{2} U_2 |0\rangle_2 |0\rangle_3 \left(\left|0\phi^+\right\rangle + \left|1\phi^-\right\rangle\right)_{145} + \\
& \frac{1}{2} U_2 |1\rangle_2 |1\rangle_3 \left(\left|0\phi^+\right\rangle - \left|1\phi^-\right\rangle\right)_{145} \\
\xrightarrow{m_3} & \frac{1}{\sqrt{2}} Z_1^{m_3} \left(\left|0\phi^+\right\rangle + \left|1\phi^-\right\rangle\right)_{145}
\end{aligned} \tag{4.37}$$

By tracing out the faulty qubit 2, the state $|\psi\rangle$ will become a mixed state. Then the measurement on qubit 3 will correct the mixed state into a pure state $|\psi\rangle = \frac{1}{\sqrt{2}}(|0\phi^+\rangle + |1\phi^-\rangle)_{145}$. Next step of measuring qubit 5 under X basis will collapse the quantum state, which is expressed as

$$\begin{aligned}
|\psi\rangle = & \frac{1}{\sqrt{2}} Z_1^{m_3} (|{+}00\rangle + |{-}11\rangle)_{145} \\
\xrightarrow{5} & \frac{1}{2\sqrt{2}} Z_1^{m_3} (|{+}0{+}\rangle + |{+}0{-}\rangle + |{-}1{+}\rangle - |{-}1{-}\rangle)_{145} \\
= & \frac{1}{2} Z_1^{m_3} (|{+}0\rangle + |{-}1\rangle)_{14} |{+}\rangle_5 + \frac{1}{2} Z_1^{m_3} (|{+}0\rangle - |{-}1\rangle)_{14} |{-}\rangle_5 \\
\xrightarrow{m_5} & \frac{1}{\sqrt{2}} X_1^{m_5} Z_1^{m_3} (|{+}0\rangle + |{-}1\rangle)_{14}
\end{aligned} \tag{4.38}$$

This process forms a linear cluster state $|L_2\rangle$ between qubit 1 and 4 with corrections applied at qubit 1, and further teleportation processes can be repeated as described in Equation 4.32.

Therefore, the error correction encoding scheme allows the reconstruction of teleportation process should the qubit suffers any faulty during computation. Further more, the initial 2-qubit cluster state $|L_2\rangle$ can be expanded into a $(2n+1)$-qubit star shaped

cluster state as

$$|L_{2n+1}\rangle = |0\rangle \left|\phi^{+}\right\rangle^{\otimes n} + |1\rangle \left|\phi^{-}\right\rangle^{\otimes n} \tag{4.39}$$

so that the quantum teleportation process can be done for n times as seen in Figure 4.1c. This fault tolerant quantum state $|L_{2n+1}\rangle$ contains n branches of copies and if the quantum teleportation fails, the involved qubit can be disentangled by Z measurement on the other qubit at the same branch and the operation will be repeated at the next branch until the teleportation succeed, then the unused branch can be removed by the Z measurement.

4.2 Design of Quantum Error Correction Circuits

The error correction encoding scheme has been theoretically modeled in qubit and operator notation. To realize it experimentally on an photonic integrated platform, a silicon photonic chip containing photon generation, qubit entanglement, error correction encoding and measurement parts must be fabricated. The realization of these functions on chip will be illustrated in this section.

4.2.1 Photon Source

The on-chip single photon source is generated via the SFWM process by inducing the non-linearity of silicon waveguides. The laser is first injected into the silicon waveguides (to interact with the silicon) and two pump photons are absorbed to create a pair of signal and idler photon, which is called the two mode squeezed vacuum state.

This process can be expressed as

$$|\phi\rangle = S(\xi)\,|0\rangle = e^{\xi^* \hat{a}\hat{b} - \xi \hat{a}^\dagger \hat{b}^\dagger}\,|0\rangle\,, \tag{4.40}$$

and by writing $\xi = re^{i\phi}$, the state in photon number basis is given by

$$\begin{aligned} |\phi\rangle =& \frac{1}{\cosh r}\sum_{n=0}^{\infty}(-e^{i\phi}\tanh r)^n\,|nn\rangle \\ =& \frac{1}{\cosh r}(|00\rangle - e^{i\phi}\tanh r\,|11\rangle + e^{2i\phi}\tanh^2 r\,|22\rangle + \cdots). \end{aligned} \tag{4.41}$$

Experimentally, the squeezing parameter is chosen to be around $r = 0.1$ and the probabilities for 0 pair, 1 pair and 2 pairs of photons can be expressed as

$$P_0 = |\frac{1}{\cosh r}|^2 = 0.9901 \tag{4.42a}$$

$$P_1 = |\frac{-e^{i\phi}\tanh r}{\cosh r}|^2 = 9.8 \times 10^{-3} \tag{4.42b}$$

$$P_2 = |\frac{e^{2i\phi}\tanh^2 r}{\cosh r}|^2 = 9.8 \times 10^{-5} \tag{4.42c}$$

The higher multi-photon probability will drop about 100 times with every 2 additional photon generated. Based on the squeezing parameter selected, it is reasonable to ignore the multi-photon events and simplify the photon generation equation in photon number basis, which is given by

$$\begin{aligned} |\psi\rangle =& |00\rangle + 0.1\,|11\rangle + 0.01\,|22\rangle \\ =& (1 + 0.1\hat{a}_1\hat{a}_2 + \frac{0.01}{\sqrt{2}}\hat{a}_1^2\hat{a}_2^2)\,|0\rangle \end{aligned} \tag{4.43}$$

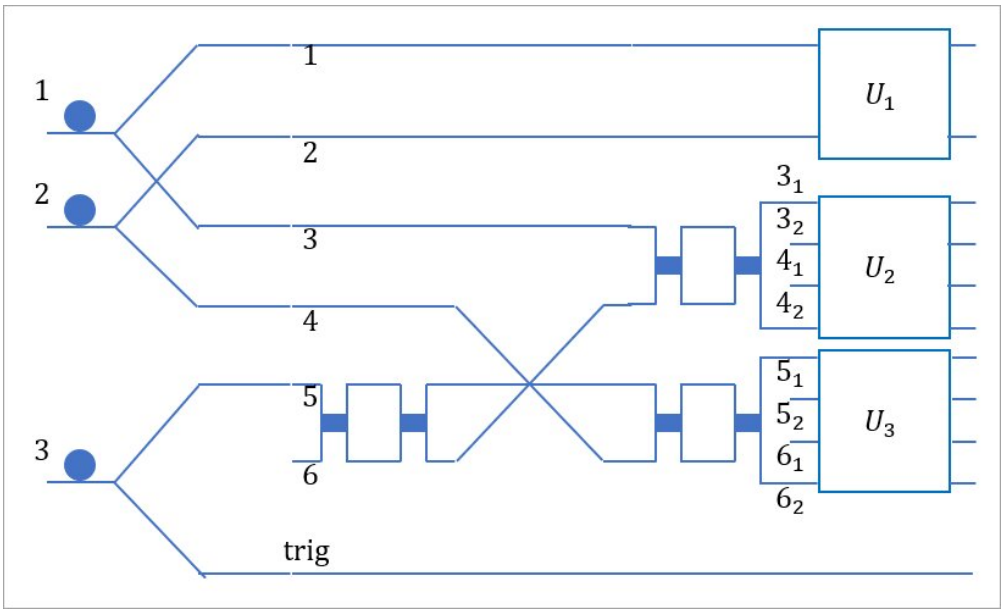

(a)

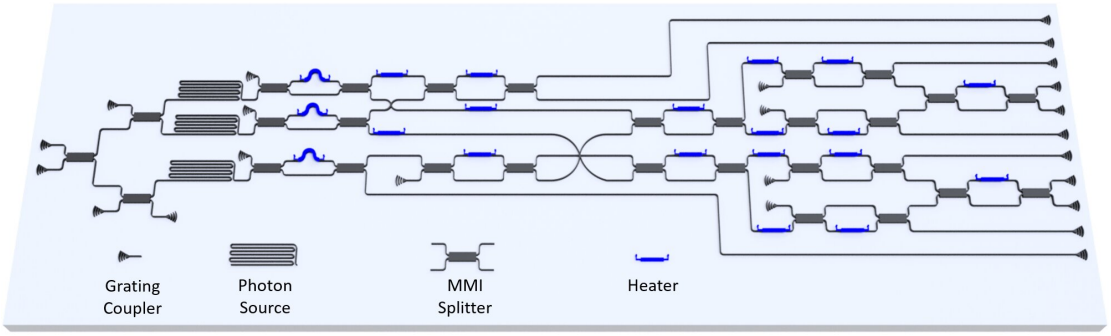

(b)

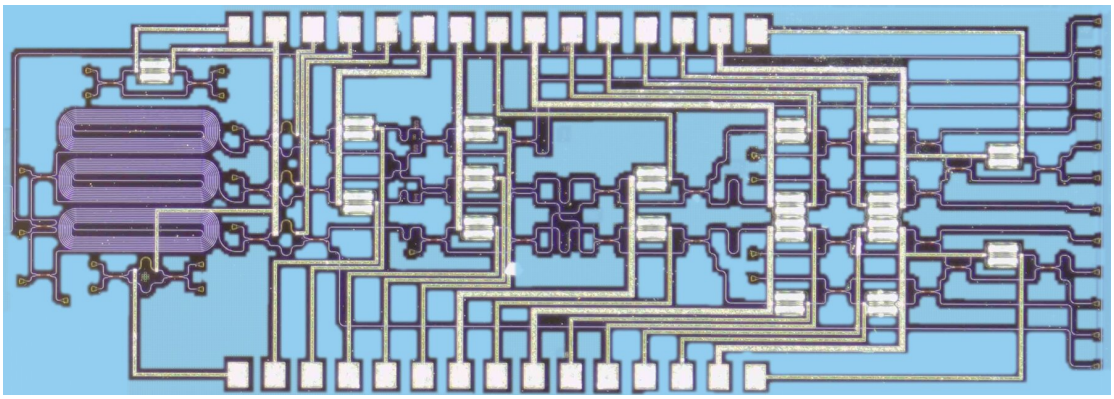

(c)

Figure 4.2: (a) Schematic of the circuit. (b) Design of photonic integrated circuit. (c) Microscope photograph of the fabricated chip.

As seen in Figure 4.2a, the initial three photon source can be expressed as

$$\begin{aligned}
&|\psi\rangle_1 |\psi\rangle_2 |\psi\rangle_3 \\
=&(2+0.1\hat{a}_2\hat{a}_4+0.1\hat{a}_1\hat{a}_3+\frac{0.01}{\sqrt{2}}\hat{a}_2^2\hat{a}_4^2+\frac{0.01}{\sqrt{2}}\hat{a}_1^2\hat{a}_3^2+ \\
&\frac{0.001}{\sqrt{2}}\hat{a}_1\hat{a}_2^2\hat{a}_3\hat{a}_4^2+\frac{0.001}{\sqrt{2}}\hat{a}_1^2\hat{a}_2\hat{a}_3^2\hat{a}_4+\frac{0.0001}{2}\hat{a}_1^2\hat{a}_2^2\hat{a}_3^2\hat{a}_4^2) \\
&\otimes(1+0.1\hat{a}_5\hat{a}_{trig}+\frac{0.01}{\sqrt{2}}\hat{a}_5^2\hat{a}_{trig}^2)|0\rangle
\end{aligned} \tag{4.44}$$

It is a complicated multi-photon state but it can be seen that the probability drops exponentially with the increase of photon numbers. Thus, the effective terms in this state is given by

$$|\psi\rangle = (0.1\hat{a}_2\hat{a}_4+0.1\hat{a}_1\hat{a}_3)\otimes(0.1\hat{a}_5\hat{a}_{trig})|0\rangle \tag{4.45}$$

The qubit is represented by dual rail of waveguides thus the state can be mapped into $(|00\rangle+|11\rangle)|0\rangle|trig\rangle$ with the last photon as trigger signal, which is the initial state in Equation 4.3.

4.2.2 Entanglement Generation

The MZI followed with a swapping operation will evolve the state into the expression as

$$\begin{aligned}
|\psi\rangle =&(\hat{a}_1\hat{a}_3+\hat{a}_2\hat{a}_4)\otimes\hat{a}_5|0\rangle|trig\rangle \\
\xrightarrow{MZI}&(\hat{a}_1\hat{a}_3+\hat{a}_2\hat{a}_4)\otimes(\hat{a}_5+\hat{a}_6)|0\rangle|trig\rangle \\
\xrightarrow{swap}&(\hat{a}_1\hat{a}_3+\hat{a}_2\hat{a}_6)\otimes(\hat{a}_5+\hat{a}_4)|0\rangle|trig\rangle \\
=&(\hat{a}_1\hat{a}_3\hat{a}_5+\hat{a}_2\hat{a}_4\hat{a}_6+\hat{a}_1\hat{a}_3\hat{a}_4+\hat{a}_2\hat{a}_5\hat{a}_6)|0\rangle|trig\rangle \\
\rightarrow&(\hat{a}_1\hat{a}_3\hat{a}_5+\hat{a}_2\hat{a}_4\hat{a}_6)|0\rangle|trig\rangle
\end{aligned} \tag{4.46}$$

The terms $\hat{a}_1\hat{a}_3\hat{a}_5 + \hat{a}_2\hat{a}_4\hat{a}_6$ represent the GHZ state $|000\rangle + |111\rangle$ while the other two term $\hat{a}_1\hat{a}_3\hat{a}_4 + \hat{a}_2\hat{a}_5\hat{a}_6$ represent three photons occupying mode $1,3,4$ and $2,5,6$, which disobey the dual rail definition of qubit concept in the experimental scheme by having two photos at two waveguide modes of a single qubit.

4.2.3 Error Correction Encoding

The error correction encoding part functions as an implementation of the error correction scheme including the simulation of qubit errors and the measurement of qubits in different bases.

The two MZI will evolve the photon into a superposition state and the expansion of waveguide mode to 4 dimension will add more degree of freedoms that allow the single photon to represent more qubits given by

$$\begin{aligned} |\psi\rangle =& (\hat{a}_1\hat{a}_3\hat{a}_5 + \hat{a}_2\hat{a}_4\hat{a}_6)\,|0\rangle\,|trig\rangle \\ \xrightarrow{MZI}& [\hat{a}_1(\hat{a}_3+\hat{a}_4)(\hat{a}_5+\hat{a}_6) + \hat{a}_2(\hat{a}_3-\hat{a}_4)(\hat{a}_5-\hat{a}_6)]\,|0\rangle\,|trig\rangle \\ \xrightarrow{4d}& [\hat{a}_1(\hat{a}_{3_1}+\hat{a}_{4_2})(\hat{a}_{5_1}+\hat{a}_{6_2}) + \hat{a}_2(\hat{a}_{3_1}-\hat{a}_{4_2})(\hat{a}_{5_1}-\hat{a}_{6_2})]\,|0\rangle\,|trig\rangle \end{aligned} \tag{4.47}$$

By taking the mapping of high dimension given by

$$\hat{a}_{3_1}\,|0\rangle = |00\rangle \tag{4.48a}$$

$$\hat{a}_{4_2}\,|0\rangle = |11\rangle \tag{4.48b}$$

$$\hat{a}_{5_1}\,|0\rangle = |00\rangle \tag{4.48c}$$

$$\hat{a}_{6_2}\,|0\rangle = |11\rangle \tag{4.48d}$$

the final state can be expressed as

$$\begin{aligned} |\psi\rangle &= |0\rangle (|00\rangle + |11\rangle)(|00\rangle + |11\rangle) + |1\rangle (|00\rangle - |11\rangle)(|00\rangle - |11\rangle) \\ &= |0\rangle \left|\phi^+\phi^+\right\rangle + |1\rangle \left|\phi^-\phi^-\right\rangle \end{aligned} \tag{4.49}$$

and this is the initial state for the quantum error correction scheme described in Equation 4.2. Further implementations are realized by three unitary matrices U_1, U_2 and U_3 to manipulate qubits and select the appropriate measurement basis.

The schematics of quantum chip to demonstrate the error correction code is shown in Figure 4.2b. It is a fully integrated platform to include the resource preparation, information encoding and state measurement. Silicon photonic chip is used to realize the control of qubits with structures like grating couplers, waveguides, multi-mode interferometers (MMI) and heaters. The 500 MHz, 1550.116 nm pulsed laser is first coupled into the chip using grating coupler structures with specially designed pitches and duty cycles for the TE mode of light and waveguide cross section is also 220 nm $\times$ 500 nm for TE mode propagation only. MMI is used to equally split a beam into two for further process and heaters are working as phase shifters to change the refractive index of the material and cause phase difference between the photons. Two MMIs and a phase shifter in between can form a Mach-Zehnder Interferometer (MZI), which can realize arbitrary beam splitting ratio and function as a single qubit operator. On-chip single photon source is realized by pumping the spiral waveguides to induce the non-linearity properties of the silicon to generate a pair of signal (1555.747 nm, C27) and idler (1544.526 nm, C41) photons in two modes with spontaneous four wave mixing process. These two modes of photons are split by Asymmetric MZI into different waveguides to form the dual-rail qubit. With single qubit operations and post selection,

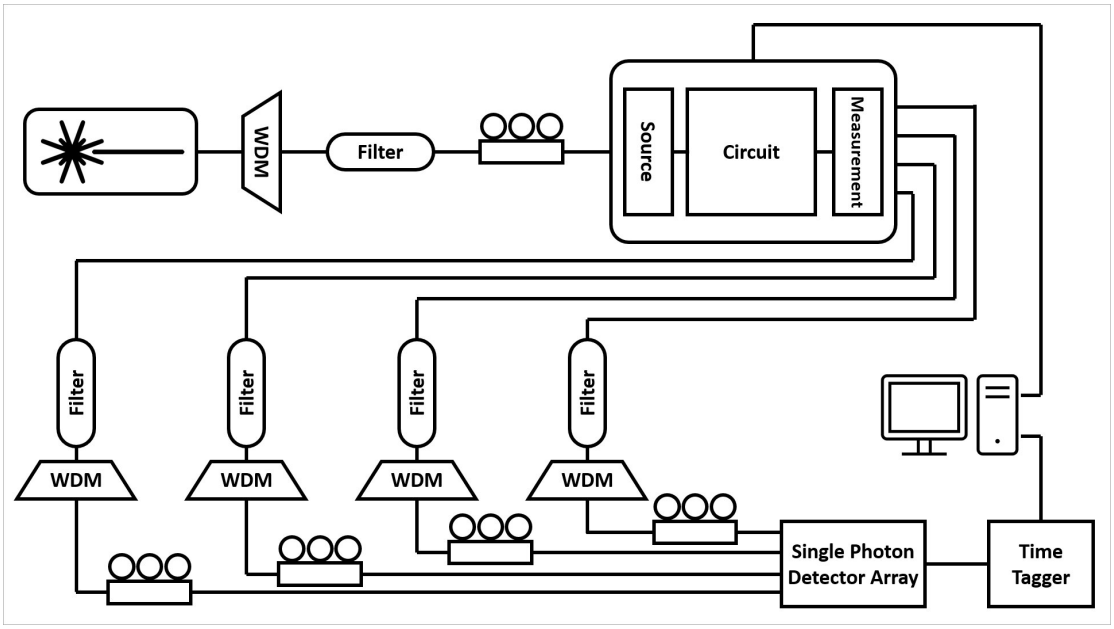

Figure 4.3: Flow chart of experiment setups for error correction encoding scheme.

the error correction scheme can be demonstrated on chip. Then the photon couples outside the chip with another grating coupler and collected by the single photon detector. The microscope photograph of the real chip is shown in Figure 4.2c that the whole scale of the circuit is about 4.5 $mm \times 2.5\ mm$.

4.3 Experimental Results and Discussions

4.3.1 Experimental Set-up

The experimental setup is shown in Figure 4.3. 500MHz pulsed laser is generated from Ultrafast Optical Clock device (PriTel) and go through a WDM device and a filter to adjust the line width of the laser pulse and suppress the unwanted background photons. Then the shaped laser pulse is injected into the chip via fibre grating coupler structures on chip and its polarization is carefully tuned by a three-ring polarization

controller to realize the maximum efficiency. The pump laser will generate photons on chip to perform the designed error correction scheme at circuit part. Next, multiple channels of photons are coupled outside the chip via another set of fibre grating couplers and these photons go through another set of filters and WDMs to remove the pump laser and select the designed signal and idler wavelength channel to ensure the efficiency of the whole system. Afterwards, these photons carrying the quantum information will go through another three-ring polarization controller to realize the maximum detection efficiency when they reaching the polarization sensitive superconducting photon detector array (PhotonSpot). The photons in detector array are converted from optical signal to electrical pulse signal and get transferred to a time tagger (Swabian Instrument) to record the number of pulses and their time tag. These data is processed by the computer to record the coincidence counts of different channels of electrical signals, which corresponds to the measured coincidence clicks of photons under the selected basis and quantum information can be retrieved from these statistic data. Finally, the computer sets another measurement basis by tuning the current in each heater channel via a DAC and repeat the above process to get another results.

4.3.2 System Calibration

The spectra of the input pulsed laser (blue line) is shown in Figure 4.4 that the spectra FWHM is 1.1 *nm*. To ensure a better photon purity, a 100 GHz WDM device is added to select the $C34$ channel with central wavelength at 1550.116 *nm* and FWHM bandwidth of 0.5 *nm* to narrow down the linewidth (orange line). Another advantage is to suppress the background photon at signal and idler channel, The input spectra has an extinction ratio of 40 dB and the background is around -77 dBm, with WDM added,

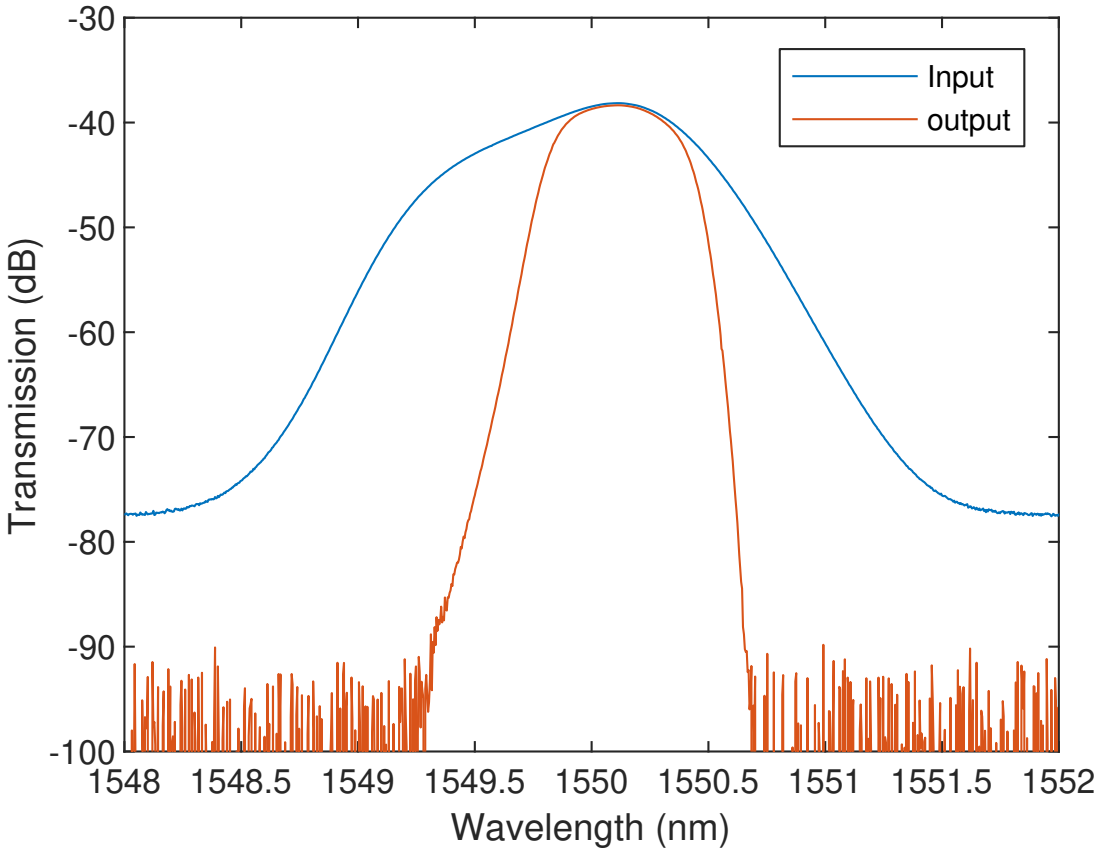

Figure 4.4: Spectra of pump laser. The blue line indicates the pump laser spectra from the laser and the orange line indicates the spectra after the WDM.

the background light is suppressed to the noise level of OSA and the extinction ratio is measured up to 100 dB.

The fibre grating coupler is also calibrated with a broadband laser as seen in Figure 4.5. First, the spectra of the input laser (blue line) is measured and the laser is injected into a simple structure of two grating couplers and a short distance of waveguide to measure the output spectra (orange line). As the length of waveguide is only hundreds of micrometer level, its noise is negligible and the loss of grating coupler is calibrated (yellow line). It can be seen that the optimized centre wavelength is around 1570 nm with loss around 5 dB (for single grating coupler), the loss at the working wavelength 1550 nm is around 6 dB.

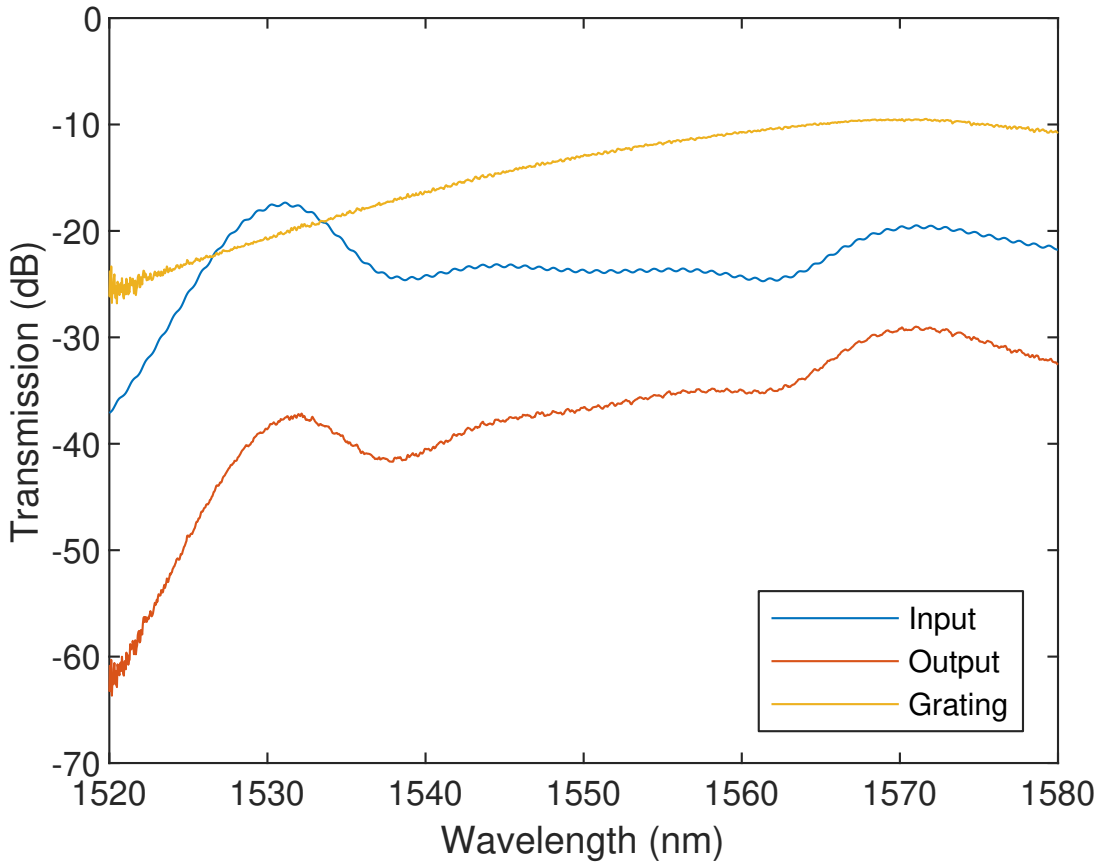

Figure 4.5: Grating coupler spectra. The spectra of input (blue line) and output (orange line) broadband laser is measured from two grating couplers and yellow line is calculated grating coupler spectra.

The AMZI spectra is shown in Figure 4.6.By designing the optical path difference (OPD), it can function as a filter to select different wavelengths from two ports. Its free spectra range is measured to be 22.4 *nm*, which is 28 WDM channels and the extinction ratio to be over 25 *dB*. The signal and idler photon wavelength is designed accordingly with a separtion of 11.2 *nm*, which is exactly half of the FSR. By tuning the heater current at one arm of the AMZI to adjust the temperature, the refractive index of the silicon waveguide is changed and induce the OPD to shift. The wavelength can be adjusted to match the designed WDM channel so that the signal and idler wavelength fall at the peak and valley of the spectra, which corresponds to the two output ports of AMZI, to realize the separation of two photons.

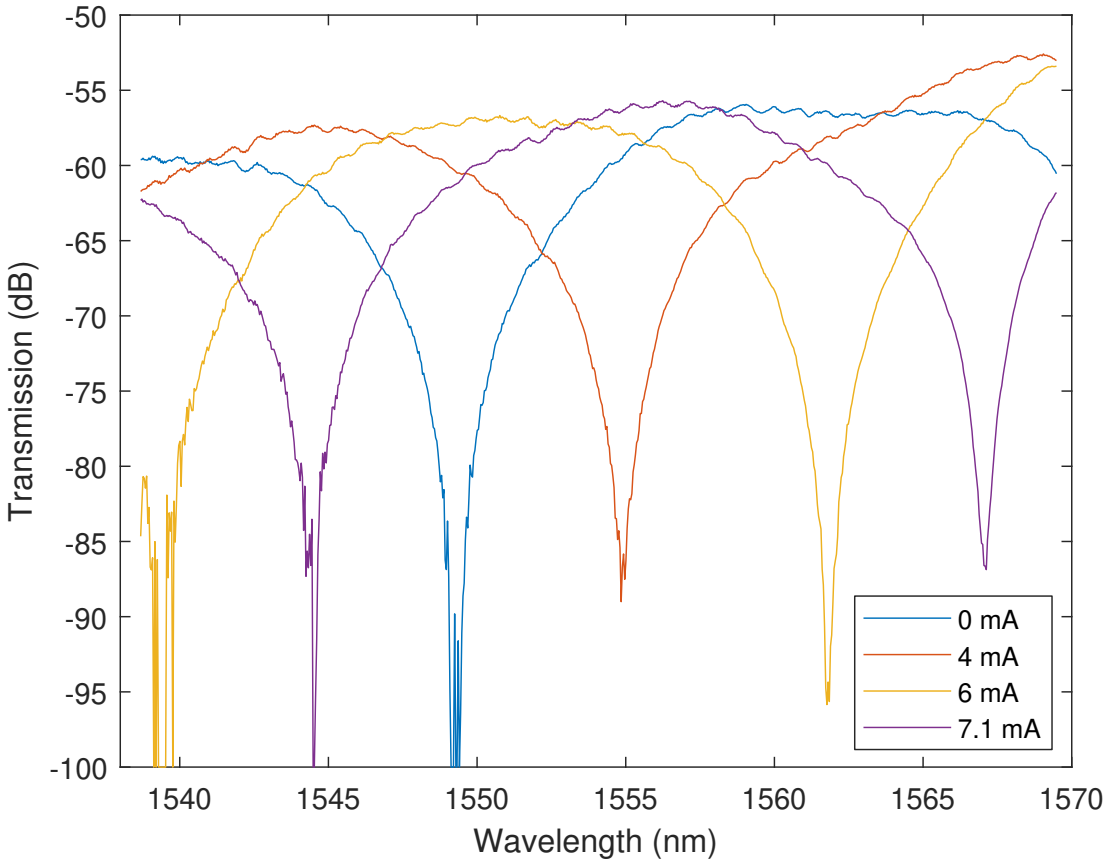

Figure 4.6: AMZI spectra with different heater current. The AMZI FSR is designed to be 25.6 *nm*. By increasing the heater current, the spectra will shift to longer wavelength.

Apart from WDM, extra filters are required to remove the pump laser after the chip. Although its wavelength is fixed, it has the advantage of lower insertion loss. The spectra of filters shown in Figure 4.7 are deducted by the input spectra (blue line) and output spectra (orange line).

The loss of all parts is calibrated and the data is shown in Table 4.3. The propagation loss of the waveguide is 2.3 dB/cm, the crossing structure is 0.024 dB each, the MMI is 0.15 dB each. The WDM loss for each wavelength channel is different and a mean value of 2 dB is assumed for estimation. The average detector efficiency calculated from test data by vendor is 85%. Therefore, the whole loss of the setup is 16.107

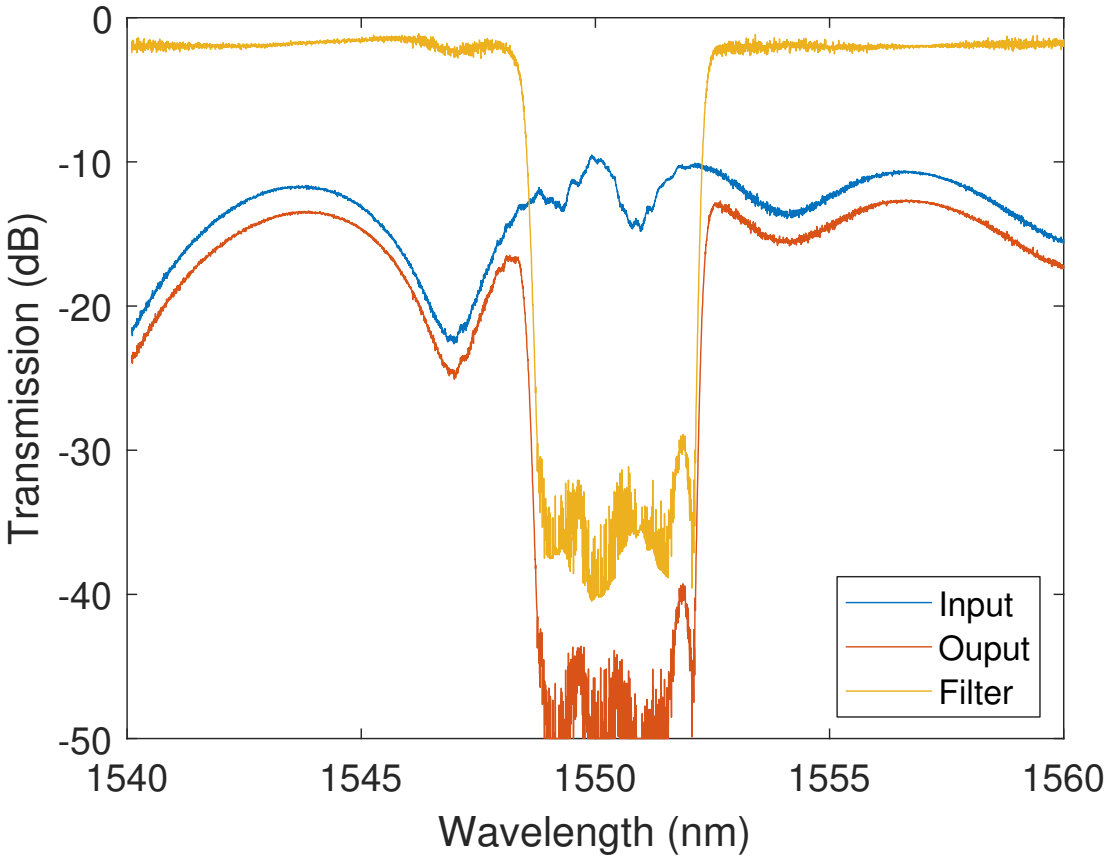

Figure 4.7: Filter spectra. Broadband laser spectra is measured before and after the filter as indicated by blue line and orange line. The spectra of filter is calculated from them. It has the bandwidth of 3 *nm* and extinction ratio of 30 *dB*. The insertion loss is measured to be 0.9 *dB*.

Table 4.3: Loss estimation of the error correction circuit.

	Loss *dB*	No.	*dB*
Grating Coupler	6	1	6
Waveguide	2.3 cm^{-1}	1.75 *cm*	4.025
Crossing	0.024	3	0.072
MMI	0.15	10	1.5
WDM	2	1	2
Filter	0.9	2	1.8
Detector	0.71	1	0.71
			16.107

dB, which corresponds to the system efficiency of 2.47%.

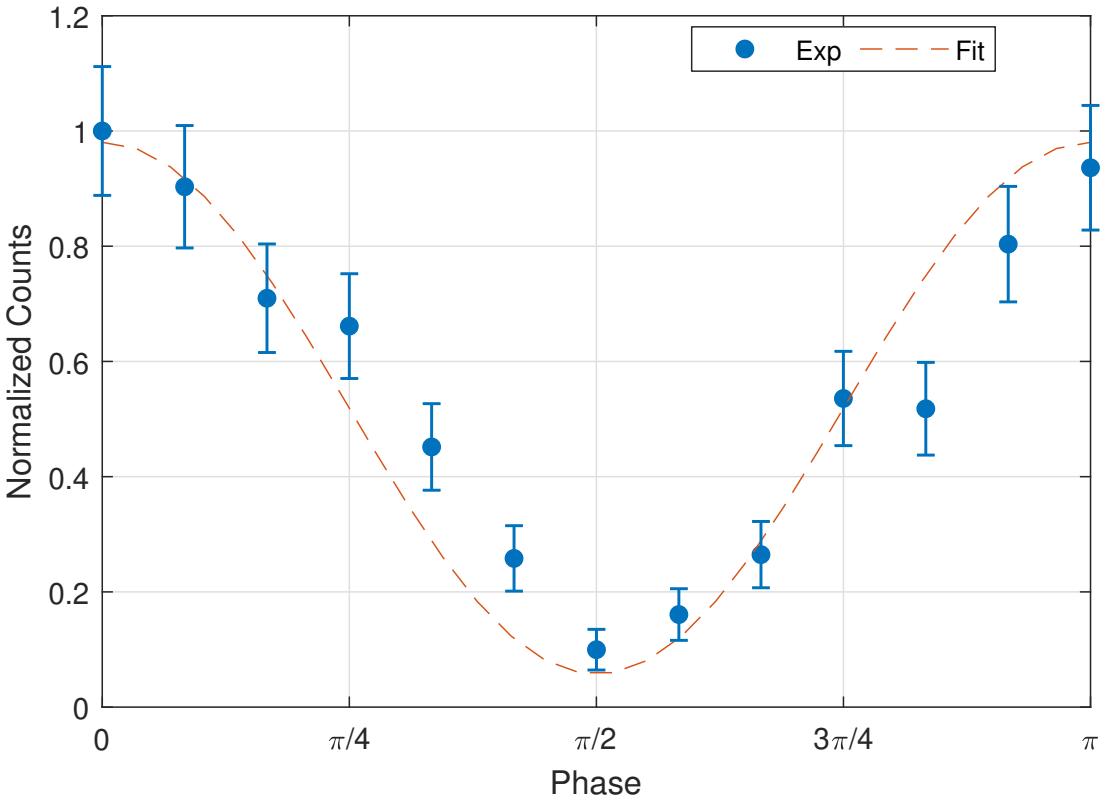

Figure 4.8: HOM Interference of photons from two on chip source. The blue dots are experimental data with error bars and dashed line is the fitting value. Visibility is measured to be $V = 0.89$.

4.3.3 Experimental Results and Discussions

The quality of on chip heralded single photon source is first experimentally tested by performing HOM interference and GHZ state tomography. Then, three main tasks of this error correction scheme: (a) Reconstructing states from errors, (b) Identifying error types and (c) Error protected quantum teleportation are demonstrated in this section.

For Hong-Ou-Mandel (HOM) effect interference, it is first measured to calibrate the in indistinguishability of the photon source. Two signal photons from different spiral structures are merged into a MZI to perform the interference and two idler photons are coupled into detectors directly to function as triggers of signal photon. By tuning the phase difference of the photon at two arm from 0 to π, the 4 photon coincidence count

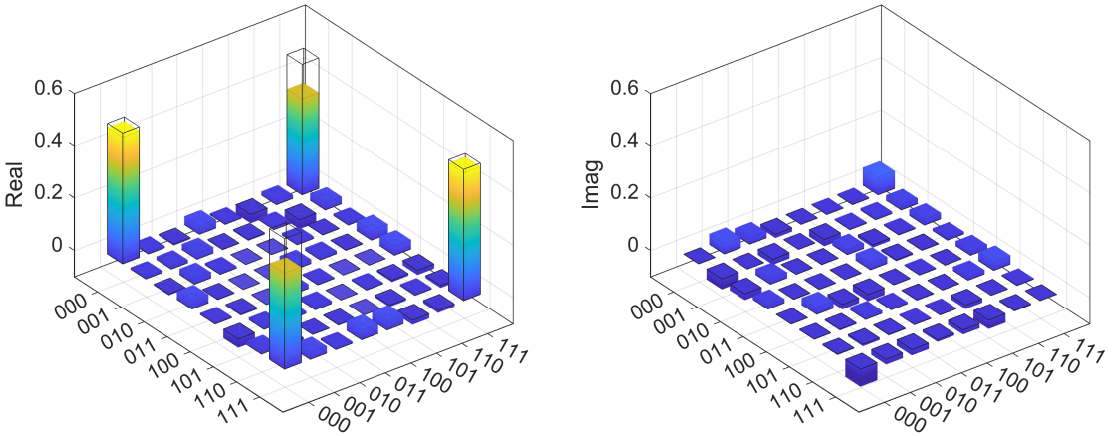

(a) Real (b) Imag

Figure 4.9: (a) Real and (b) imaginary part for density matrix of GHZ state. The experimental results are in color bars while the theoretical results are transparent bars. The fidelity is $F = 0.8524 \pm 0.0141$.

fringe is observed to change from peak to valley and back to peak as seen in Figure 4.8. The blue dots are measured results and dashed line is the fitting function. Interference visibility is calculated to be

$$V = \frac{Max - Min}{Max + Min} = 0.89 \tag{4.50}$$

After proving the feasibility of photon source, the tomography of 3-qubit GHZ state $|GHZ\rangle = \frac{1}{\sqrt{2}}(|000\rangle + |111\rangle)$, which is the key steps of initial state preparation process in Equation 4.3, is performed with theoretical density matrix expressed as

$$\begin{aligned} \rho &= |GHZ\rangle \langle GHZ| \\ &= \begin{bmatrix} 0.5 & \cdots & 0.5 \\ \vdots & & \vdots \\ 0.5 & \cdots & 0.5 \end{bmatrix}_{8\times 8} \end{aligned} \tag{4.51}$$

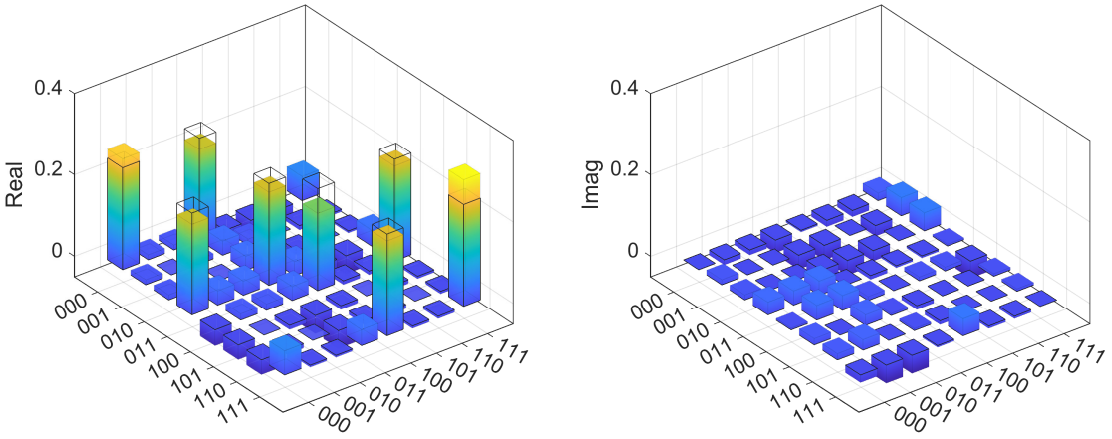

(a) Imag (b) Real

Figure 4.10: (a) Real and (b) imaginary part for density matrix of the mixed state with $\alpha = 1, \beta = 0$. The experimental results are in color bars while the theoretical results are transparent bars. The fidelity is $F = 0.9625 \pm 0.0281$.

Measured real parts and imaginary parts of the density matrix are shown in Figure 4.9a and Figure 4.9b, where the color bars are for experimental results and the transparent bars are for theoretical results. The fidelity recovered from the the tomography process is $F = 0.8524 \pm 0.0141$.

For State Reconstruction from Error, reconstruction of quantum information from error is demonstrated with this encoding scheme. The tomography of mixed state in reconstruction process is first performed as seen in Equation (4.11). By taking $\alpha = 1$, $\beta = 0$, the density matrix can be expressed as

$$|A\rangle = |\phi^+ 0\rangle = \frac{1}{\sqrt{2}} \begin{bmatrix} 1 & 0 & 0 & 1 & 0 & 0 & 0 & 0 \end{bmatrix}^T \tag{4.52a}$$

$$|B\rangle = |\phi^+ 1\rangle = \frac{1}{\sqrt{2}} \begin{bmatrix} 0 & 0 & 0 & 0 & 1 & 0 & 0 & 1 \end{bmatrix}^T \tag{4.52b}$$

$$\begin{aligned}\rho =& \frac{1}{2}|A\rangle\langle A| + \frac{1}{2}|B\rangle\langle B| \\ =& \frac{1}{4}\begin{bmatrix} 1 & \cdots & 1 & 0 & 0 & 0 \\ \vdots & & \vdots & 0 & 0 & 0 \\ 1 & \cdots & 1 & 0 & 0 & 0 \\ 0 & 0 & 0 & 1 & \cdots & 1 \\ 0 & 0 & 0 & \vdots & & \vdots \\ 0 & 0 & 0 & 1 & \cdots & 1 \end{bmatrix}\end{aligned} \tag{4.52c}$$

The measured real part and imaginary part of the density matrix are shown in Figure 4.10a and Figure 4.10b with fidelity of $F = 0.9625 \pm 0.0281$. The colored bars are experimental results and the transparent bars are for theoretical results.

To test the performance of error correction scheme on the integrated platform, 6 initial basic states $|\phi\rangle$ are selected as

$$|H\rangle = |0\rangle \qquad |V\rangle = |1\rangle \tag{4.53a}$$

$$|D\rangle = \frac{1}{\sqrt{2}}(|0\rangle + |1\rangle) \qquad |A\rangle = \frac{1}{\sqrt{2}}(|0\rangle - |1\rangle) \tag{4.53b}$$

$$|R\rangle = \frac{1}{\sqrt{2}}(|0\rangle + i|1\rangle) \qquad |L\rangle = \frac{1}{\sqrt{2}}(|0\rangle - i|1\rangle) \tag{4.53c}$$

which are the eigenvectors for Pauli X, Y, Z operators. The error qubit location is tested on both qubit 1 and qubit 3. By taking Z basis and X basis measurement result as $m_Z = m_X = 0$, the retrieved state from Equation 4.14 can be simplified as $|\phi\rangle = H(\alpha|0\rangle + \beta|1\rangle)$. The tomography on all 12 states are performed as shown in Figure 4.11 and the average fidelity is $\bar{F} = 0.8630$. The blue bars are for error at qubit 1, yellow bars are for error at qubit 3.

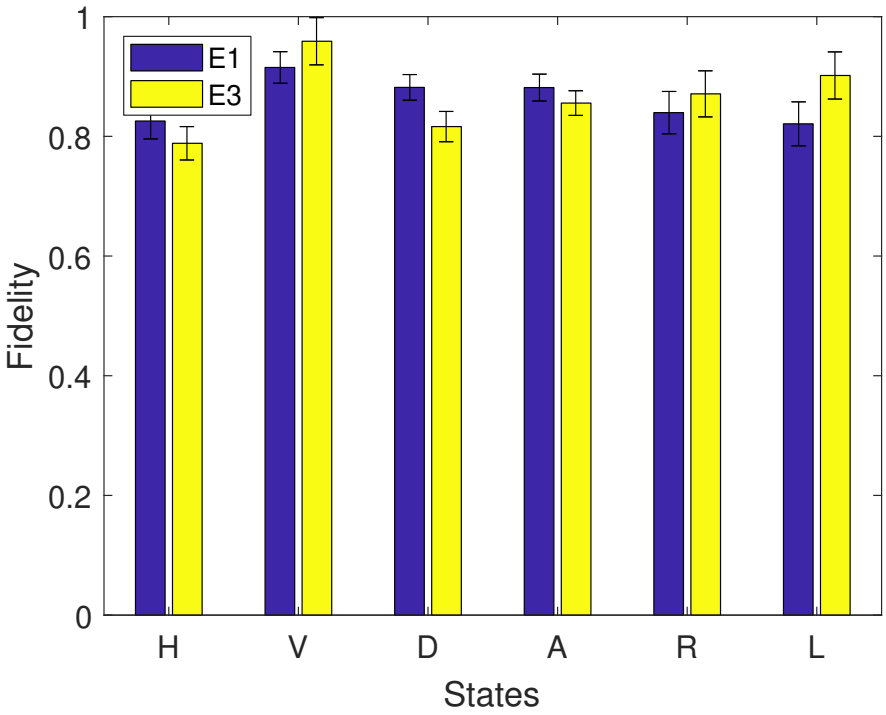

Figure 4.11: Fidelities of the reconstructed state from error qubit. Blue bars E_1 are for error at qubit 1 and yellow bars E_3 are for error at qubit 3. The X axis order is the encoded initial state described in Equation 4.53. An average reconstruction fidelity $\bar{F} = 0.8630$ is achieved.

The detailed density matrix for error at qubit 1 and qubit 3 are shown in Figure 4.12 and Figure 4.13 with fidelities listed below each density matrix. Colored bars are measured results and transparent bars are theoretical results.

For error identification case, error type is identified by measuring expectation values of stabilizer as listed in Equation 4.18. Due to the symmetry of the encoded state $|\psi\rangle_{1234}$, qubit 1 and 2 share one group of stabilizer measurement results while qubit 3 and 4 share another. The stabilizer expectation value $\langle S_2 \rangle$ has a constant value 1 regardless of the error type at qubit 1 or 2, which can be explained by that S_2 has no effect on the first two qubits and there is no entanglement between first two qubits and last two qubits in state $|\psi\rangle_{1234}$. So do the results for $\langle S_1 \rangle$ on qubit 3 and 4. Thus, error at the location of qubit 1 is taken as an example to see how the stabilizer expectation value

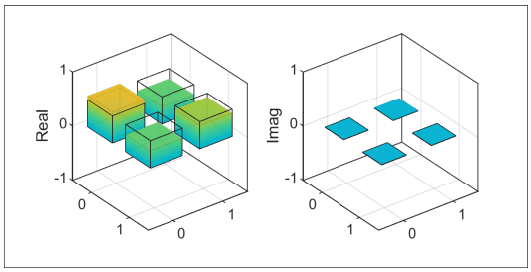

(a) $F_H = 0.8256 \pm 0.0294$

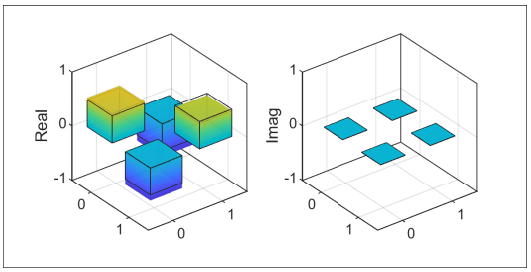

(b) $F_V = 0.9151 \pm 0.0527$

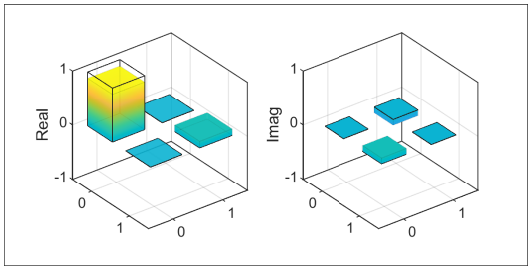

(c) $F_D = 0.8818 \pm 0.0212$

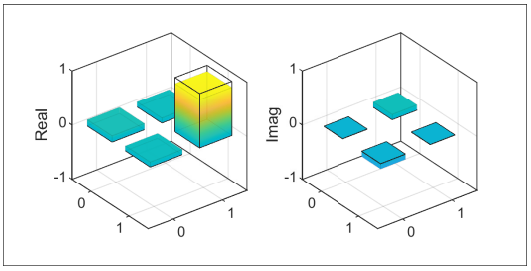

(d) $F_A = 0.8815 \pm 0.0218$

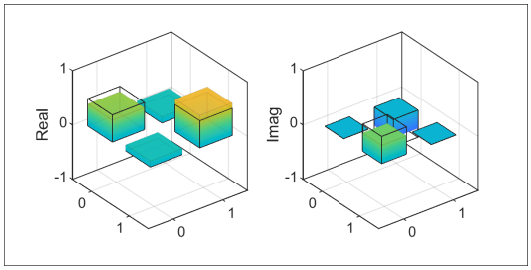

(e) $F_R = 0.8432 \pm 0.0372$

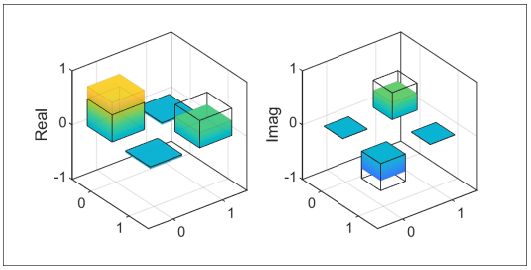

(f) $F_L = 0.8209 \pm 0.0361$

Figure 4.12: Real part and imaginary part of density matrices of reconstructed state for error at qubit 1 with initial state as H, V, D, A, R, L. The colored bars are for theoretical data and the transparent bars are for theoretical data. The corresponding fidelity of each state is listed beneath the density matrix.

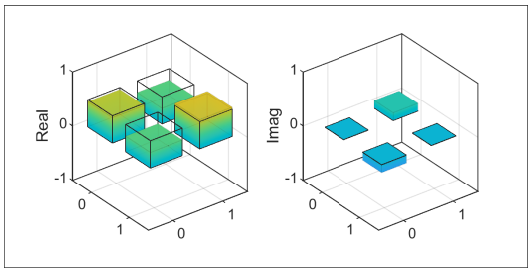

(a) $F_H = 0.7884 \pm 0.0276$

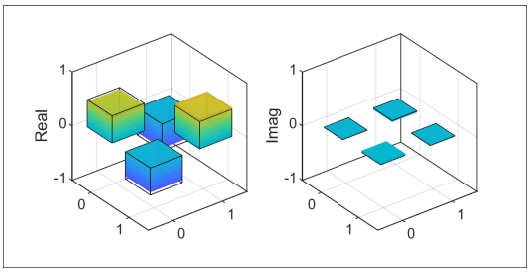

(b) $F_V = 0.9589 \pm 0.0392$

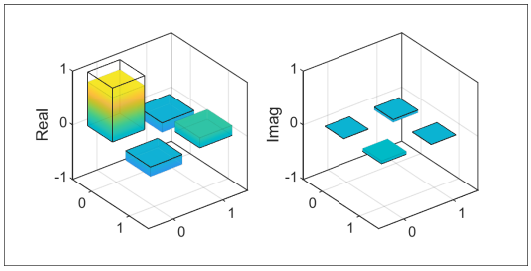

(c) $F_D = 0.8163 \pm 0.0259$

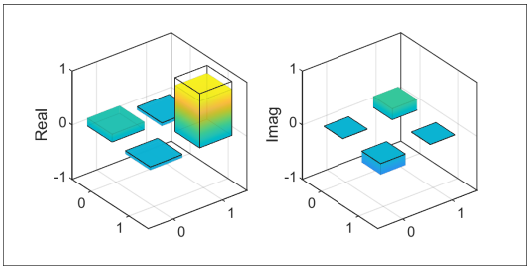

(d) $F_A = 0.8583 \pm 0.0201$

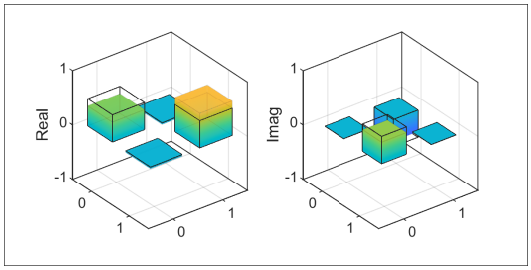

(e) $F_R = 0.8984 \pm 0.0368$

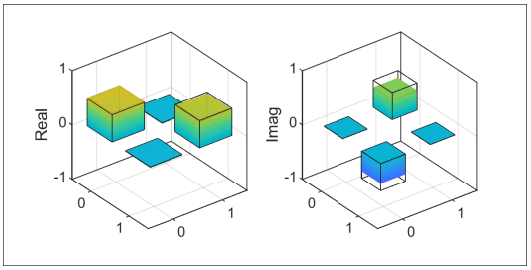

(f) $F_L = 0.8706 \pm 0.0370$

Figure 4.13: Real part and imaginary part of density matrices of reconstructed state for error at qubit 3 with initial state as H, V, D, A, R, L. The colored bars are for theoretical data and the transparent bars are for theoretical data. The corresponding fidelity of each state is listed beneath the density matrix.

$\langle S \rangle$ vary with the error type as seen in Figure 4.14. Blue bars are for stabilizer $\langle S_1 \rangle$ and yellow bars are for $\langle S_3 \rangle$ and the x axis is the corresponding error type I, X, Y, Z. It can be noticed that the experimental results match very well as the theoretical results in Table 4.2, which proves the feasibility of the error correction code to identify the error types.

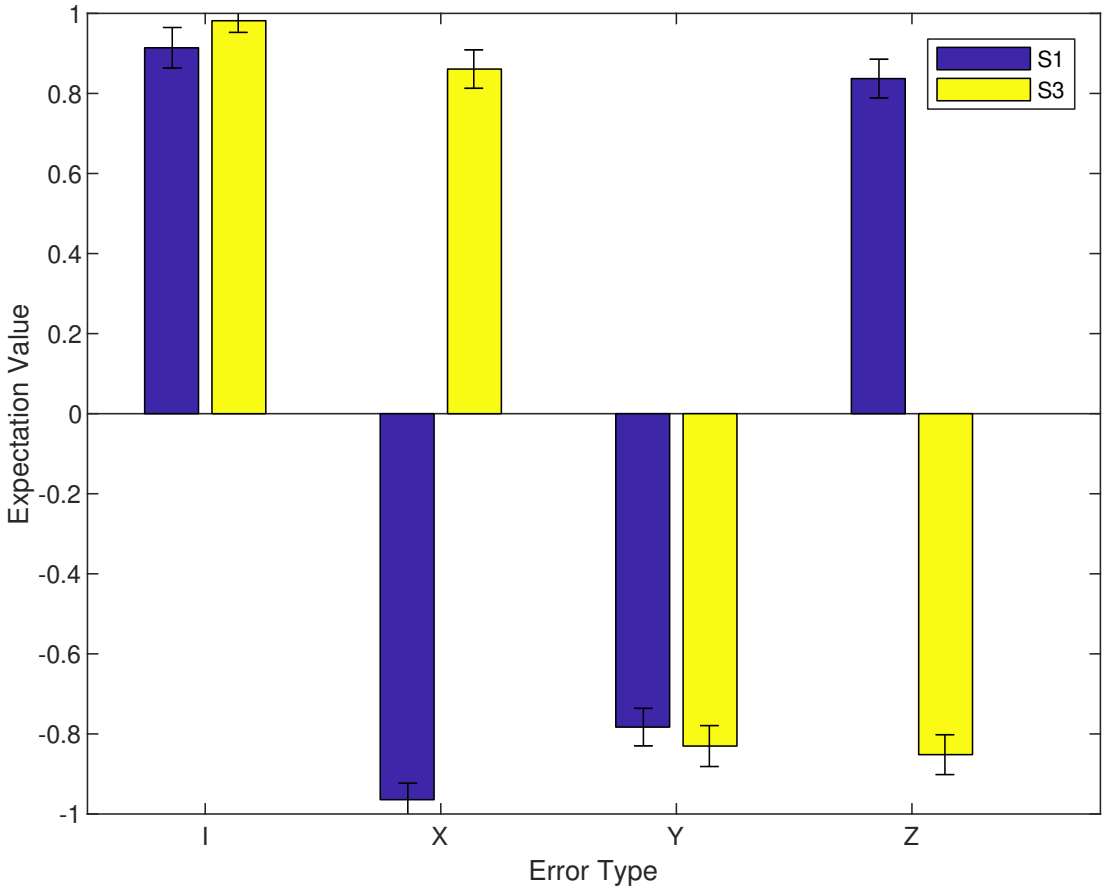

Figure 4.14: Measured expectation values of stabilizer for identifying error types. Errors types of I, X, Y, Z are simulated at qubit 1 as listed on x axis and expectation value $\langle S_1 \rangle$ (blue bar) and $\langle S_3 \rangle$ (yellow bar) are measured accordingly.

Finally, the experimental results of error corrected quantum teleportation are studied. The 2-qubit linear cluster state $|L_2\rangle = \frac{1}{\sqrt{2}}(|0+\rangle + |1-\rangle)$ at qubit 1-4 and 1-2 are reconstructed by simulating errors at qubits 2 and 4. The theoretical density matrix is

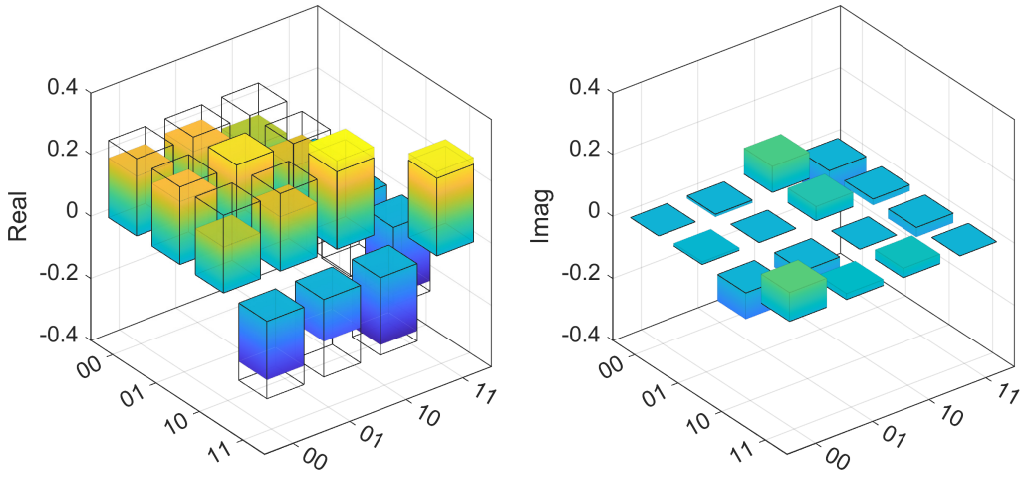

(a) Real part

(b) Imag part

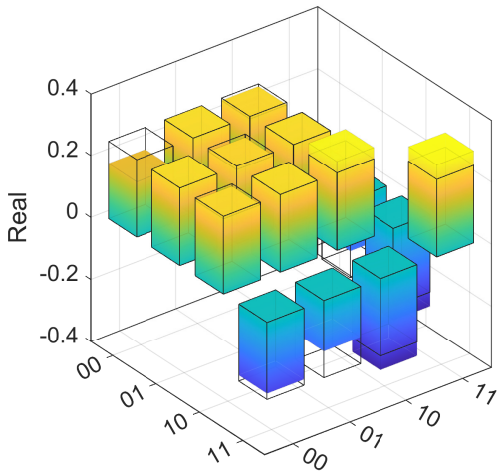

(c) Real part

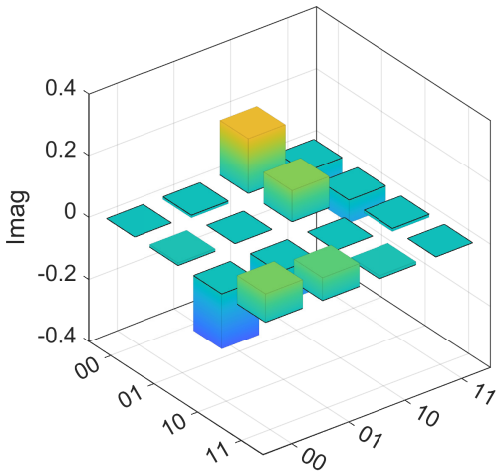

(d) Imag part

Figure 4.15: Tomography on state $|L_2\rangle = \frac{1}{\sqrt{2}}(|0+\rangle + |1-\rangle)$. (a) Real and (b) imaginary part of density matrix for error at qubit 2. (c) Real and (d) imaginary part of density matrix for error at qubit 4.

calculated to be expressed as

$$\begin{aligned}\rho &= |L_2\rangle \langle L_2| \\ &= \frac{1}{4}\begin{bmatrix}1 & 1 & 1 & -1\end{bmatrix}^T \begin{bmatrix}1 & 1 & 1 & -1\end{bmatrix} \\ &= \frac{1}{4}\begin{bmatrix}1 & 1 & 1 & -1 \\ 1 & 1 & 1 & -1 \\ 1 & 1 & 1 & -1 \\ -1 & -1 & -1 & 1\end{bmatrix}\end{aligned} \tag{4.54}$$

The measured density matrices are shown in Figure 4.15 for error at qubit 2 and error at qubit 4. Similarly, the colored bars are measured results and transparent bars are theoretical results and fidelities for this two results are $F_{14} = 0.8522 \pm 0.0232$ and $F_{12} = 0.9656 \pm 0.0283$.

4.4 Conclusions

In this section, the theoretical model of the quantum error correction scheme is studied and its photonic implementation is designed. Then, an photonic integrated circuit is fabricated with on chip photon generation, initial state preparation and qubit operation function to realize the prototype of this error correction encoding scheme. Three applications of quantum state reconstruction, error type identification and error corrected quantum teleportation have been demonstrated on this photonic integrated circuit. The experimental result has proved that the encoding scheme is feasible for protecting the quantum information from the propagation loss or quantum operation error, an average state reconstruction fidelity of $\bar{F} = 0.8630$. Quantum error correction

is a very important topic in the era of Noisy Intermediate Scale Quantum Computer as the further scaling up of quantum circuit model to larger scales would require the error rate level to be maintained beneath a certain threshold to avoid decoherence of quantum states and loss of quantum information.

Chapter 5

On-Chip Quantum Computing with Autoencoder

In this chapter, an efficient method to transfer quantum information via teleportation between quantum photonic chips is proposed. The efficiency of this quantum state transformation process relies on the quantum autoencoder model which is trained with genetic algorithms to compressed a particular set of qutrits to qubits for teleportation and to decode it to qutrit to retrieve the original information.

5.1 Theory of Quantum Teleportation with Autoencoder

Quantum network has played a more and more important role in the development of quantum technologies as it provides a way to build the connection between separate quantum nodes for quantum information sharing and operations among different quantum systems. To realize a practical quantum network, one of the key problems is to deliver the quantum state between quantum nodes. With this motivation, quantum teleportation is invented as a technique to transfer the unknown quantum state over a long distance. However, the two nodes within the network needs a pair of entangled states to share their own unknown quantum information via the quantum channel.

5.1.1 Quantum Teleportation and Bell State Measurement

The quantum teleportation has been demonstrated with many platforms ranging from superconducting qubits [160], trapped atoms [161,162], Nitrogen-vacancy centres [163], to continuous variable states [164, 165] and so on.

Photonic qubit is one of the most promising candidates to build the quantum channel in a quantum network since it is robust against noise environment and the ease of manipulation under room temperature compared to other implementations. Moreover, it can tolerate longer propagation distances without much disturbance from the surrounding environment. Photonic quantum teleportation has been proved experimentally in many ways including free space [166] and fibre systems [167]. The state of the art proof of quantum teleportation is between the Micius satellite and ground station over a distance of 1400 km [168], which paves the way for an interconnected quantum network globally.

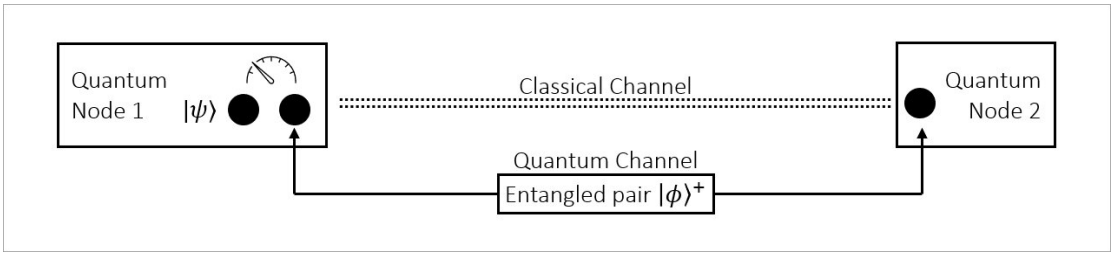

Figure 5.1: Schematic of quantum teleportation.

The fundamental idea of quantum teleportation is to make a joint projective measurement of the unknown state and transmit the classical information of measurement results to the remote party to reconstruct the target unknown state. The involved resources are a pair of entangled photonic state $|\phi\rangle^+ = |00\rangle + |11\rangle$, the unknown state $|\psi\rangle$ to be transferred and the classical information of measurement results as shown in Figure 5.1. The entangled photon pair $|\phi\rangle_{23}^+$ is distributed to two quantum nodes through a quantum channel and the target state to be transferred along with the qubit from entangled photon pair undergo a bell state measurement. Then the measurement result is sent through a classical channel to quantum node 2 where the other qubit of the entangled pair locate and some modification is performed on the state based on this classical information to retrieve the initial state $|\psi\rangle_1$.

The initial state can be written as

$$|\psi\rangle_1 |\phi\rangle_{23}^+ = \alpha|000\rangle + \alpha|011\rangle + \beta|100\rangle + \beta|111\rangle \tag{5.1}$$

The Bell state measurement on qubit 1 and 2 projects the state into one of the four Bell

pairs, which is expressed as

$$|\phi\rangle^{+} = |00\rangle + |11\rangle \tag{5.2a}$$

$$|\phi\rangle^{-} = |00\rangle - |11\rangle \tag{5.2b}$$

$$|\psi\rangle^{+} = |01\rangle + |10\rangle \tag{5.2c}$$

$$|\psi\rangle^{-} = |01\rangle - |10\rangle \tag{5.2d}$$

Thus, the basic two-qubit state is represented as

$$|00\rangle = |\phi\rangle^{+} + |\phi\rangle^{-} \tag{5.3a}$$

$$|11\rangle = |\phi\rangle^{+} - |\phi\rangle^{-} \tag{5.3b}$$

$$|01\rangle = |\psi\rangle^{+} + |\psi\rangle^{-} \tag{5.3c}$$

$$|10\rangle = |\psi\rangle^{+} - |\psi\rangle^{-} \tag{5.3d}$$

and the initial state is represented by Bell state, which is expressed as

$$\begin{aligned} |\psi\rangle_1 |\phi\rangle_{23}^{+} =& \alpha |000\rangle + \alpha |011\rangle + \beta |100\rangle + \beta |111\rangle \\ =& |\phi\rangle^{+} (\alpha |0\rangle + \beta |1\rangle)_3 + |\phi\rangle^{-} (\alpha |0\rangle - \beta |1\rangle)_3 + \\ & |\psi\rangle^{+} (\alpha |1\rangle + \beta |0\rangle)_3 + |\psi\rangle^{-} (\alpha |1\rangle - \beta |0\rangle)_3 \end{aligned} \tag{5.4}$$

Given the measurement results of entangled state at qubit 1 and 2, the initial quantum information is reconstructed at qubit 3 with an appropriate operator depending on the

outcome of the measurement, which is expressed as

$$|\phi\rangle^+ : I_3 \tag{5.5a}$$

$$|\phi\rangle^- : Z_3 \tag{5.5b}$$

$$|\psi\rangle^+ : X_3 \tag{5.5c}$$

$$|\psi\rangle^- : Z_3X_3 \tag{5.5d}$$

Finally, the quantum state at qubit 1 is teleported to qubit 3 with the aid of entangled state and the measurement results.

The remaining problem is how to discriminate the four bell states $|\phi\rangle^+$, $|\phi\rangle^-$, $|\psi\rangle^+$ and $|\psi\rangle^-$. The state in vector form can be expressed as

$$|\phi\rangle^+ = \begin{bmatrix} \frac{1}{\sqrt{2}} \\ 0 \\ 0 \\ \frac{1}{\sqrt{2}} \end{bmatrix}, |\phi\rangle^- = \begin{bmatrix} \frac{1}{\sqrt{2}} \\ 0 \\ 0 \\ -\frac{1}{\sqrt{2}} \end{bmatrix}, |\psi\rangle^+ = \begin{bmatrix} 0 \\ \frac{1}{\sqrt{2}} \\ \frac{1}{\sqrt{2}} \\ 0 \end{bmatrix}, |\psi\rangle^- = \begin{bmatrix} 0 \\ \frac{1}{\sqrt{2}} \\ -\frac{1}{\sqrt{2}} \\ 0 \end{bmatrix}. \tag{5.6}$$

It is easy to check that these states are orthogonal to each other with no overlap and they can be discriminated perfectly theoretically. If the four states can be converted to the vector form expressed as

$$|00\rangle = \begin{bmatrix} 1 \\ 0 \\ 0 \\ 0 \end{bmatrix}, |11\rangle = \begin{bmatrix} 0 \\ 0 \\ 0 \\ 1 \end{bmatrix}, |01\rangle = \begin{bmatrix} 0 \\ 1 \\ 0 \\ 0 \end{bmatrix}, |10\rangle = \begin{bmatrix} 0 \\ 0 \\ 1 \\ 0 \end{bmatrix}, \tag{5.7}$$

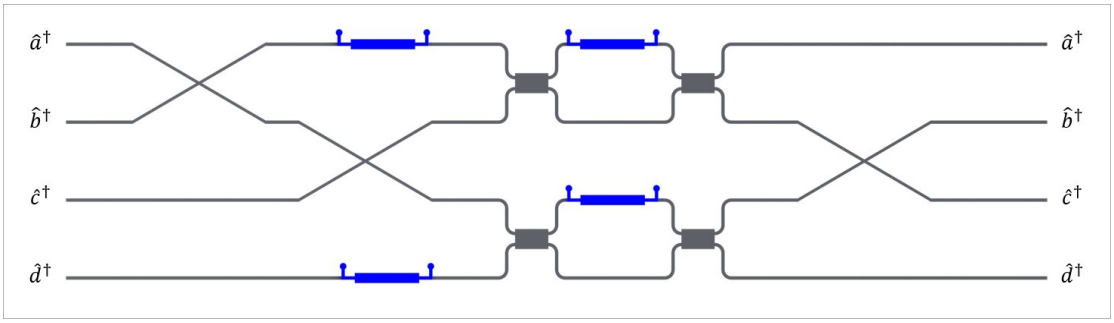

Figure 5.2: Schematic of photonic BSM with 50% success probability.

they can be discriminated efficiently under the experimental basis and the corresponding operator U for conversion is expressed as

$$U = \frac{1}{\sqrt{2}} \begin{bmatrix} 1 & 0 & 0 & 1 \\ 0 & 1 & 1 & 0 \\ 0 & 1 & -1 & 0 \\ 1 & 0 & 0 & -1 \end{bmatrix} \tag{5.8}$$

This operator cannot be decomposed as tensor products of two separable 2×2 sub-matrices, thus it is not able to be performed on photonic integrated systems, but a partial state discrimination can be done.

The partial discrimination scheme of the Bell states on photonic integrated system is shown in Figure 5.2. The four waveguide modes form two dual-rail qubits and the two MZI are set to be a Hadamard gate. If the creation operator on four modes is

represented as $\hat{a}^\dagger$, $\hat{b}^\dagger$, $\hat{c}^\dagger$, $\hat{d}^\dagger$, the four bell state can be expressed as

$$|\phi\rangle^+ = (\hat{a}^\dagger\hat{c}^\dagger + \hat{b}^\dagger\hat{d}^\dagger)\,|0\rangle \tag{5.9a}$$

$$|\phi\rangle^- = (\hat{a}^\dagger\hat{c}^\dagger - \hat{b}^\dagger\hat{d}^\dagger)\,|0\rangle \tag{5.9b}$$

$$|\psi\rangle^+ = (\hat{a}^\dagger\hat{d}^\dagger + \hat{b}^\dagger\hat{c}^\dagger)\,|0\rangle \tag{5.9c}$$

$$|\psi\rangle^- = (\hat{a}^\dagger\hat{d}^\dagger - \hat{b}^\dagger\hat{c}^\dagger)\,|0\rangle \tag{5.9d}$$

The evolution of the creation operator under this circuit is given by

$$\hat{a}^\dagger = \hat{b}^\dagger + \hat{d}^\dagger \tag{5.10a}$$

$$\hat{b}^\dagger = \hat{a}^\dagger + \hat{c}^\dagger \tag{5.10b}$$

$$\hat{c}^\dagger = \hat{a}^\dagger - \hat{c}^\dagger \tag{5.10c}$$

$$\hat{d}^\dagger = \hat{b}^\dagger - \hat{d}^\dagger \tag{5.10d}$$

Thus, the four bell states after the circuit can be expressed as

$$|\phi\rangle^+ \rightarrow (\hat{a}^\dagger\hat{b}^\dagger - \hat{c}^\dagger\hat{d}^\dagger)\,|0\rangle \tag{5.11a}$$

$$|\phi\rangle^- \rightarrow (\hat{a}^\dagger\hat{d}^\dagger - \hat{b}^\dagger\hat{c}^\dagger)\,|0\rangle \tag{5.11b}$$

$$|\psi\rangle^+ \rightarrow (\hat{a}^{\dagger 2} + \hat{b}^{\dagger 2} - \hat{c}^{\dagger 2} - \hat{d}^{\dagger 2})\,|0\rangle \tag{5.11c}$$

$$|\psi\rangle^- \rightarrow (\hat{b}^{\dagger 2} - \hat{a}^{\dagger 2} + \hat{d}^{\dagger 2} - \hat{c}^{\dagger 2})\,|0\rangle \tag{5.11d}$$

For state $|\phi\rangle^+$ and $|\phi\rangle^-$, the evolution results will be two photons either occupying the first two modes or the last two modes, which corresponds to a two photon coincidence counts at mode a and b or mode c and d. For state $|\psi\rangle^+$ and $|\psi\rangle^-$, there will

Table 5.1: Measurement Results of Bell State

Bell State	$\|\phi\rangle^+$	$\|\phi\rangle^-$	$\|\psi\rangle^+$	$\|\psi\rangle^-$
Coincidence Clicks	ab/cd	ad/bc	NA	NA
Transferred State	$\alpha\|0\rangle+\beta\|1\rangle$	$\alpha\|0\rangle-\beta\|1\rangle$	$\alpha\|1\rangle+\beta\|0\rangle$	$\alpha\|1\rangle-\beta\|0\rangle$
Correction Operators	Identity	Z	X	ZX

be photon bunching results that two photons appear in the same modes and cannot be distinguished by the threshold detector, thus the corresponding bell states cannot be effectively discriminated. If the path swapping operation in the circuit model is modified, the results may vary based on the similar deduction above.

So far only one pair of bell states can be discriminated using linear optical circuit and the total successful probability is 50%. The general results for all measurement conditions are listed in Table 5.1.

5.1.2 Autoencoder

To increase the capacity of quantum information transferred in the quantum channel, two schemes of multi qubit [169] and higher dimensional qudit [170, 171] teleportation have been raised and demonstrated. However, these schemes require either more quantum resources like multi-qubit entanglement as quantum channel or more sophisticated measurement basis that scales exponentially with number of qubits or dimensions comparing with the ordinary 2-level qubit teleportation. Thus, the efficient use of the transferred quantum resources in quantum channel to allow more information loaded on it is another optional way to release the stress of teleportation and the compression of quantum information into smaller sizes seems to be a promising solution to save the

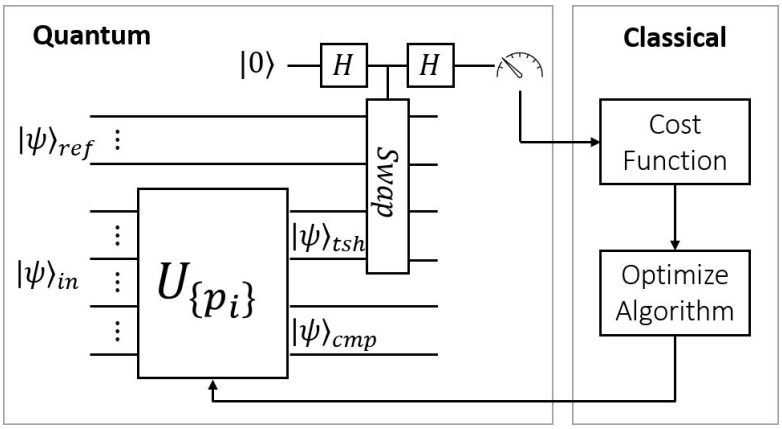

Figure 5.3: Schematic of theoretical model for quantum autoencoder. The input state entering into the autoencoder with free parameters $\{p_i\}$ will be transformed into $|\psi\rangle_{tsh} \otimes |\psi\rangle_{cmp}$. The overlap between $|\psi\rangle_{ref}$ and $|\psi\rangle_{tsh}$ will be measured as cost function to optimize the autoencoder parameter.

quantum resource.

Inspired from the classical autoencoder concept that a machine learning model can be trained to map a higher-dimensional data set to a lower-dimensional data set so that it is used as a compressor for classical information like images or files to save memory space, the quantum autoencoder model is thus proposed to compress the quantum information at higher dimensions into lower dimensions [172–176].

A general quantum autoencoder model is shown in Figure 5.3 that the initial input state is a $(m+n)$-qubit state $|\psi\rangle_{in}$ and it first undergoes a compression operator $U_{\{p_i\}}$ with a series of tunable parameters $\{p_i\}$. The output is a separable state with two parts, the m-qubit trash state $|\psi\rangle_{tsh}$ and the n-qubit compressed state $|\psi\rangle_{cmp}$, which is given by

$$U_{\{p_i\}} |\psi\rangle_{in} = |\psi\rangle_{tsh} \otimes |\psi\rangle_{cmp} . \tag{5.12}$$

Then the trash state $|\psi\rangle_{tsh}$ and the reference state $|\psi\rangle_{ref}$ will go through a controlled swap gate to measure the overlap of the two states. The degree of overlap is used as a

cost function along with the optimization algorithm to update the compression operator parameter sets $\{p_i\}$. The iteration will be repeated until the cost function reaches a convergence.

This process can be understood as the mapping of a $(m+n)$-qubit state from a larger Hilbert space into a smaller Hilbert space as a constant m-qubit state $|\psi\rangle_{ref}$ and a compressed n-qubit state $|\psi\rangle_{cmp}$. The optimization process is to compare the difference between trashed state and reference state until they reach a maximum overlap. The $|\psi\rangle_{cmp}$ contains all the information on the original input state while it requires fewer quantum resource to store the information. The initial state can be retrieved by a reversed operation $U^{\dagger}_{\{p_i\}}$ acting on $|\psi\rangle_{ref}$ and $|\psi\rangle_{cmp}$.

To demonstrate the quantum autoencoder experimentally, the theory is simplified to encode a 3-dimensional qutrit $|3D\rangle$ to a 2-dimensional qubit $|2D\rangle$ given the assumption that the generated qutrit from this quantum node allows compression without any information loss, which indicates that only a specific subset of the universal qutrit Hilbert space can be compressed [175].

5.1.3 Qutrit State Tomography

The quality of the transferred qudit state can be justified by the qutrit state tomography [177], which is similar to qubit tomography with the Pauli Matrix being replaced by 9 matrices under 3-dimensional space. These matrices form the special unitary group of degree 3, denote as $SU(3)$, which is the fundamental concept of Lie group theory [178, 179]. It is also known as the GellMann matrices for the study of strong interaction in physics [180].

These matrices can be written as

$$\lambda_0 = \begin{bmatrix} 1 & 0 & 0 \\ 0 & 1 & 0 \\ 0 & 0 & 1 \end{bmatrix}, \quad \lambda_1 = \begin{bmatrix} 0 & 1 & 0 \\ 1 & 0 & 0 \\ 0 & 0 & 0 \end{bmatrix}, \quad \lambda_2 = \begin{bmatrix} 0 & -i & 0 \\ i & 0 & 0 \\ 0 & 0 & 0 \end{bmatrix},$$
$$\lambda_3 = \begin{bmatrix} 1 & 0 & 0 \\ 0 & -1 & 0 \\ 0 & 0 & 0 \end{bmatrix}, \quad \lambda_4 = \begin{bmatrix} 0 & 0 & 1 \\ 0 & 0 & 0 \\ 1 & 0 & 0 \end{bmatrix}, \quad \lambda_5 = \begin{bmatrix} 0 & 0 & -i \\ 0 & 0 & 0 \\ i & 0 & 0 \end{bmatrix}, \tag{5.13}$$
$$\lambda_6 = \begin{bmatrix} 0 & 0 & 0 \\ 0 & 0 & 1 \\ 0 & 1 & 0 \end{bmatrix}, \quad \lambda_7 = \begin{bmatrix} 0 & 0 & 0 \\ 0 & 0 & -i \\ 0 & i & 0 \end{bmatrix}, \quad \lambda_8 = \begin{bmatrix} 1 & 0 & 0 \\ 0 & 1 & 0 \\ 0 & 0 & -2 \end{bmatrix}.$$

The eigensystem of these matrices are calculated mathematically and represented as

$$\lambda_i \cdot \left|v_{i,j}\right\rangle = s_{i,j} \left|v_{i,j}\right\rangle, i = \{0, \cdots, 8\}, j = \{1,2,3\}, \tag{5.14}$$

where $\left|v_{i,j}\right\rangle$ is the j-th normalized eigenvector for matrix λ_i and $s_{i,j}$ is the corresponding eigenvalue. The density matrix of the target qutrit $|\phi\rangle$ is represented as

$$\rho = \sum_{i=0}^{8} r_i \lambda_i, \tag{5.15}$$

the parameter r_i is the coefficient determined by the eigensystem of λ_i expressed as

$$r_i = \frac{1}{Tr(\lambda_i \lambda_i)} \sum_{j=1}^{3} s_{i,j} \cdot \left\langle v_{i,j}\right| \rho \left|v_{i,j}\right\rangle = \frac{1}{Tr(\lambda_i \lambda_i)} \sum_{j=1}^{3} s_{i,j} \cdot |\left\langle v_{i,j}\middle|\phi\right\rangle|^2 \tag{5.16}$$

where $|\left\langle v_{i,j}\middle|\phi\right\rangle|^2$ is the projection of $|\phi\rangle$ under the basis $\left|v_{i,j}\right\rangle$.

For example, for λ_0, its eigensystem is calculated as

$$s_{0,1} = 1, \left|v_{0,1}\right\rangle = \begin{bmatrix} 1 & 0 & 0 \end{bmatrix}^T \tag{5.17a}$$

$$s_{0,2} = 1, \left|v_{0,2}\right\rangle = \begin{bmatrix} 0 & 1 & 0 \end{bmatrix}^T \tag{5.17b}$$

$$s_{0,3} = 1, \left|v_{0,3}\right\rangle = \begin{bmatrix} 0 & 0 & 1 \end{bmatrix}^T \tag{5.17c}$$

Assuming the qutrit is in the form of $|\phi\rangle = |0\rangle$, the coefficient r_0 is calculated as

$$\begin{aligned} r_0 =& \frac{1}{Tr(\lambda_0\lambda_0)}(s_{0,1}|\left\langle v_{0,1}\middle|\phi\right\rangle|^2 + s_{0,2}|\left\langle v_{0,2}\middle|\phi\right\rangle|^2 + s_{0,3}|\left\langle v_{0,3}\middle|\phi\right\rangle|^2) \\ =& \frac{1}{3}. \end{aligned} \tag{5.18}$$

Experimentally, $|\left\langle v_{i,j}\middle|\phi\right\rangle|^2$ is directly obtained by measuring the coincidence count of state $|\phi\rangle$ under the basis of $\left|v_{i,j}\right\rangle$ and normalizing the data at the end of the measurements.

5.2 Design of Quantum Photonic Autoencoder Circuit

5.2.1 Encoder and Decoder Circuit

The schematic diagram of the chip design is shown in Figure 5.4. It contains two parts: the encoder chip and the decoder chip connected with a quantum channel to teleport the quantum state. The encoder chip generates a pair of entangled qubit and distributes one of the branch to the decoder chip to establish the quantum channel between them. The generated qutrit $|3D\rangle$ is then compressed to the target qubit $|2D\rangle$ by the quantum autoencoder. Along with another qubit from the entangled pair, the two

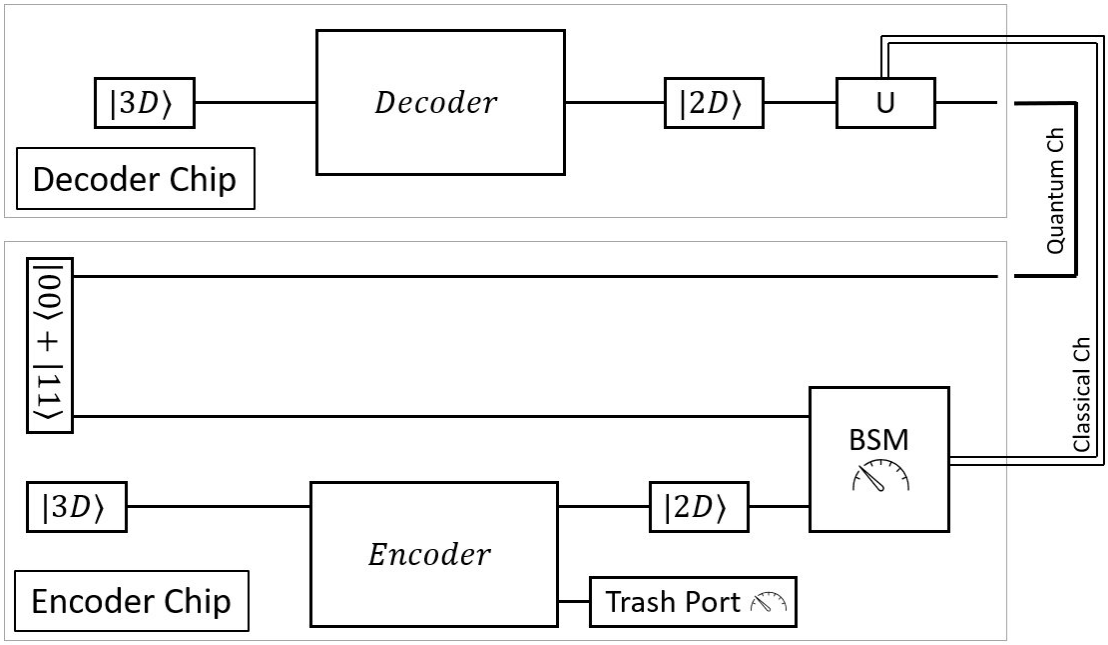

Figure 5.4: Schematic of the teleportation with autoencoder circuit. The qutrit state $|3D\rangle$ is compressed into a qubit state $|2D\rangle$ by autoencoder and get teleport to the decoder chip. Then the original qutrit quantum information is recovered.

qubits go through a Bell state measurement process and the measurement results is communicated as classical information to the decoder chip to reconstruct the compressed quantum state and the original quantum information can be decoded.

The whole system is implemented on an photonic integrated platform as shown in Figure 5.5a. The qubit is encoded in dual rail with a single photon: a photon in one wave guide represents 0 and a photon in another wave guide represents 1. Pump laser is injected into the chip and split equally into three spiral structures to generate photon pair via the SFWM process. The pump power is then filtered out by the first AMZI and the signal/idler photon pair is split into two modes through the second AMZI. The first two spiral sources form a pair of entangled state as $|00\rangle + |11\rangle$. The photon pair from the third spiral structure is used to simulate the quantum information from the network node. The idler photon functions as a trigger to herald the signal photon as a

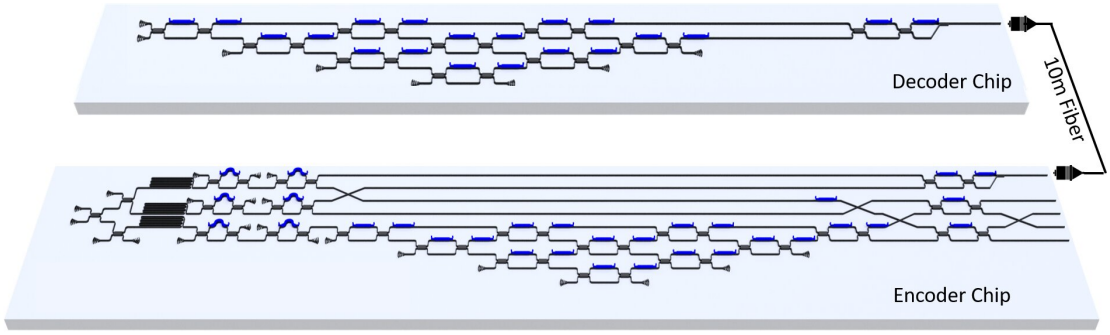

(a)

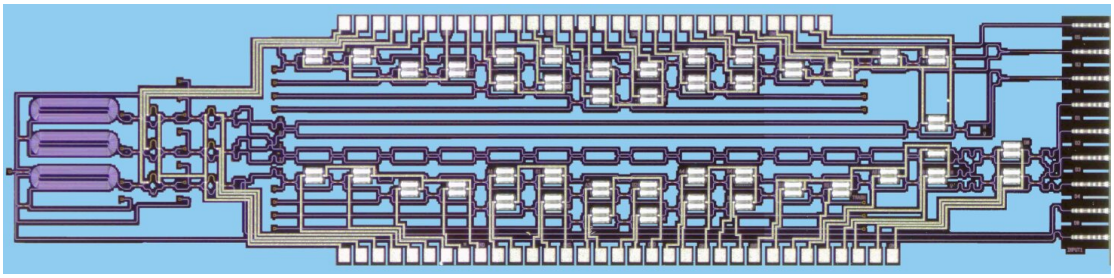

(b)

Figure 5.5: (a) Schematic for integrated quantum photonic teleportation with autoencoder circuit. The encoder and decoder parts are connected by a 10-meter-long fiber to teleport the quantum information. (b) The microscope photograph of the fabricated chip.

single photon source. The following two MZIs encode the signal photon into a qutrit defined in three waveguide modes. Another 3 MZIs in a triangle shape function as the unitary matrix to realize arbitrary unitary transform of the single qutrit, which acts as an autoencoder to compress the qutrit to a qubit. The autoencoder contains eight tunable phase shifters as the free parameters for further training. The bell state measurement is realized with three crossings for waveguide swap and two MZIs as Hadamard gate. The four output is connected into a single photon detector array for coincidence counts measurement. Figure 5.5b is the microscope photograph of the fabricated photonic integrated circuit. The encoder and decoder are fabricated on one unit only for ease of operation. There is no direct waveguide connection between them and the two separated parts are connected with a 10-meter long fiber.

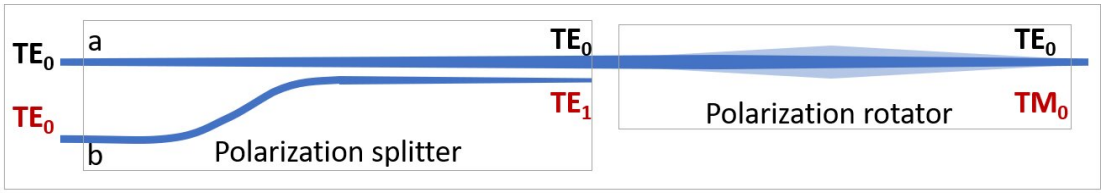

Figure 5.6: Schematic of the PRS. It contains two parts, the polarization splitters and polarization rotator, to realize the conversion of qubit dual rail encoding in chip to polarization encoding in fiber and free space.

5.2.2 Teleportation Channel

The qubit for teleportation at first two waveguides of the encoder chip will be transferred to the decoder chip to deliver the quantum information. The most obvious way is to connect the two waveguide at encoder chip directly to the decoder chip via two fibres. However, the main concern here is to maintain the phase stability of two fibres, which is rather sensitive to the environmental fluctuation.

This problem can be effectively solved if the quantum information can be transferred in a single fibre. Therefore, the on-chip polarization rotator and splitter (PRS) is used to merge the two waveguides labeled with a and b into one and the implemented information on two waveguides can be converted to the two propagation modes TE_0 and TM_0 in the same waveguide. It is a combination of polarization splitter and a polarization rotator. The cross section and coupling length is specially designed that the input TE_0 propagation mode at waveguide a is first converted to TE_1 mode and coupled to the waveguide b by a polarization splitter. The polarization rotator then rotates the TE_1 mode to TM_0 mode by the asymmetry design of waveguide cross section. The TE_0 and TM_0 are two orthogonal propagation modes in waveguide and when coupled to single mode fibres, they can occupy the two orthogonal polarization of H and V so that the quantum information will not merge with each other while their relative phase

can still be maintained.

The evolution of a qubit under the structure of PRS can be written as

$$\begin{aligned} |\psi\rangle =& \alpha|0\rangle + \beta|1\rangle \\ =& \alpha|a\rangle|TE_0\rangle + \beta|b\rangle|TE_0\rangle \\ \xrightarrow{splitter}& \alpha|a\rangle|TE_0\rangle + \beta|a\rangle|TE_1\rangle \\ \xrightarrow{rotator}& \alpha|a\rangle|TE_0\rangle + \beta|a\rangle|TM_0\rangle \\ \xrightarrow{couple}& \alpha|fibre\rangle|H\rangle + \beta|fibre\rangle|V\rangle . \end{aligned} \tag{5.19}$$

where qubit state $|0/1\rangle$ is converted from $|a\rangle|TE_0\rangle / |b\rangle|TE_0\rangle$ with its waveguide position degree of freedom and propagation mode degree of freedom to the polarization degree freedom $|H\rangle / |V\rangle$.

To couple the two propagation modes to fibre simultaneously, the 1D grating coupler array is no longer appropriate as it will reject the TM mode with an extinction ratio up to 20 dB, instead, a spot size converter (SSC) is used as a polarization independent edge coupler structure to guide the light from waveguide to the the single mode fibre. Then a three-ring polarization controller is added to adjust the input polarization to the decoder chip. This can be done by sending a series of $|0\rangle$ and $|1\rangle$ as calibration signals to align the two chips. The qubit coupled from fibre to decoder chip will undergo another unitary matrix evolution to recover the original qudit and the implemented decoder unitary matrix here is the inverse of encoder unitary operator. Finally, the quantum state tomography is performed on the recovered qudit to calculate its fidelity and proves the feasibility of designed circuit.

5.2.3 Training Process

The quantum autoencoder implemented in the designed circuit is to compress a qutrit to a qubit. The autoencoder is a 3×3 linear optical circuit with 3 MZIs. It contains 9 phase shifters but one of the phase shifter canset to be arbitrary phase and functions as the reference of the others without any effect on final results. Thus, the autoencoder model contains 8 free parameters, which are the current added on 8 heaters. The cost function theoretically is the overlap between trash state and reference state as $|\langle \psi_{ref} | \psi_{tsh} \rangle|$. The optimization algorithm will maximize the overlap of two states by tuning the free parameter sets. Experimentally, considering the state overlap requires additional operations and the designed autoencoder only compress a qutrit to a qubit, the experimental reference state can be selected as a vacuum state, which means the occupancy of the trash mode will be 0. Therefore, the optimization process functions to minimize the probability of detecting the photons at trash waveguide mode can be expressed as

$$\alpha_0 |0\rangle + \alpha_1 |1\rangle + \alpha_2 |2\rangle \xrightarrow{autoencoder} \beta_0 |0\rangle + \beta_1 |1\rangle + \beta_2 |2\rangle , \tag{5.20a}$$

$$|\beta_2|^2 \xrightarrow{optimization} 0. \tag{5.20b}$$

Note that the proposed quantum autoencoder is only functional for a particular qutrit set where a universal lossless compression process exists. The initial dataset is prepared by mathematically selecting a constant 3×3 unitary matrix U and randomly generating a large set of 2 dimensional complex vector $\{v_i\}$. When acting the matrix on the 2 dimensional vector $U \cdot v_i$, the initial qutrit space is prepared. The input qutrit is first selected from this dataset and prepared by a heralded single photon source and

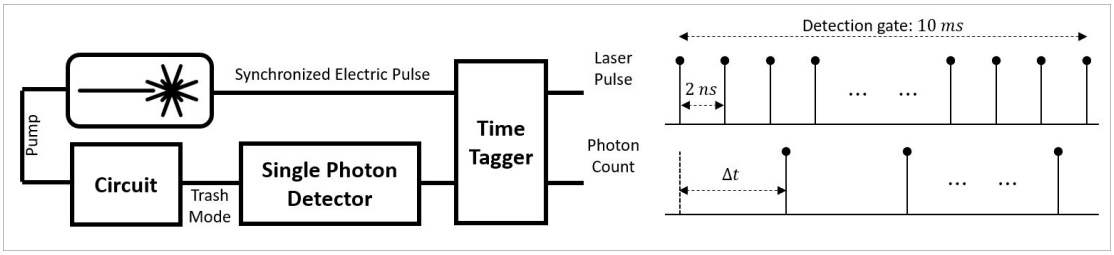

(a)

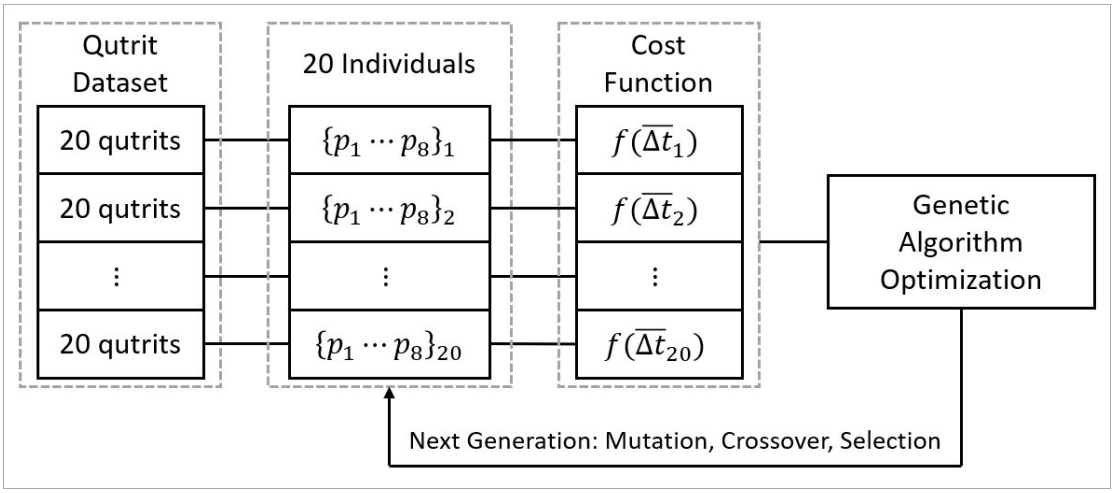

(b)

Figure 5.7: (a) Trash state measurement process for cost function. The time difference of gate start flag and first photon click labeled as Δt is recorded as cost function. (b) The training process is to optimize free parameters in autoencoder and minimize the cost function $f(\Delta t)$ using the genetic algorithm classically.

two MZI structures. Then the qutrit will enter the autoencoder with the trash mode measured to optimize the autoencoder.

Theoretically, the output qutrit from quantum node is unknown. Due to the constraint imposed by the non-cloning principle: a quantum bit cannot be measured twice, a direct measurement of the count rate at trash mode by repeating the qutrit preparation process will violate the non-cloning principle so that it cannot be treated as a cost function parameter for further optimization.

Instead, the time difference Δt of the trigger signal and the first photon click is

chosen to be the cost function parameter as illustrated in Figure 5.7a. The $500MHz$ pump laser generates a synchronized electrical pulse and is inputted into one channel of time tagger as a start trigger for gated detection. Only the photon signal inside the detection gate is measured. The time difference between first photon and gate start trigger is measured as Δt and passed into the evaluation of the cost function. Twenty different initial qutrits are prepared for each set of parameter $\{p_i\}$ to get the averaged $\bar{\Delta t}$. The optimization approach used is a genetic algorithm with the 20 individuals initialized in the first generation. The mutation, crossover and selection process are applied to generate the subsequent generations until one arrives at a convergence of the cost function as shown in Figure 5.7b.

5.3 Experimental Results and Discussions

5.3.1 Experimental Setup

A schematic diagram of the experimental setup is shown in Figure 5.8a. The Ultrafast Optical Clock device (PriTel) is applied here as a laser source to generate a 500 MHz pulsed lasers with line width of around 1.1 nm. It is then sent to a WDM device and a filter to narrow down the line width of the laser pulse to 0.7 nm to suppress the unwanted background photons for a better single-photon quality. The shaped laser pulse is coupled into the chip via a single mode fibre aligning itself to the on-chip grating coupler structure and its polarization is adjusted by a fiber-based three-ring polarization controller to realize the maximum efficiency since the grating coupler is polarization-sensitive. Multiple photon pairs are generated by equally splitting the input pump laser into three spiral waveguides on chip to generate the SFWM process.

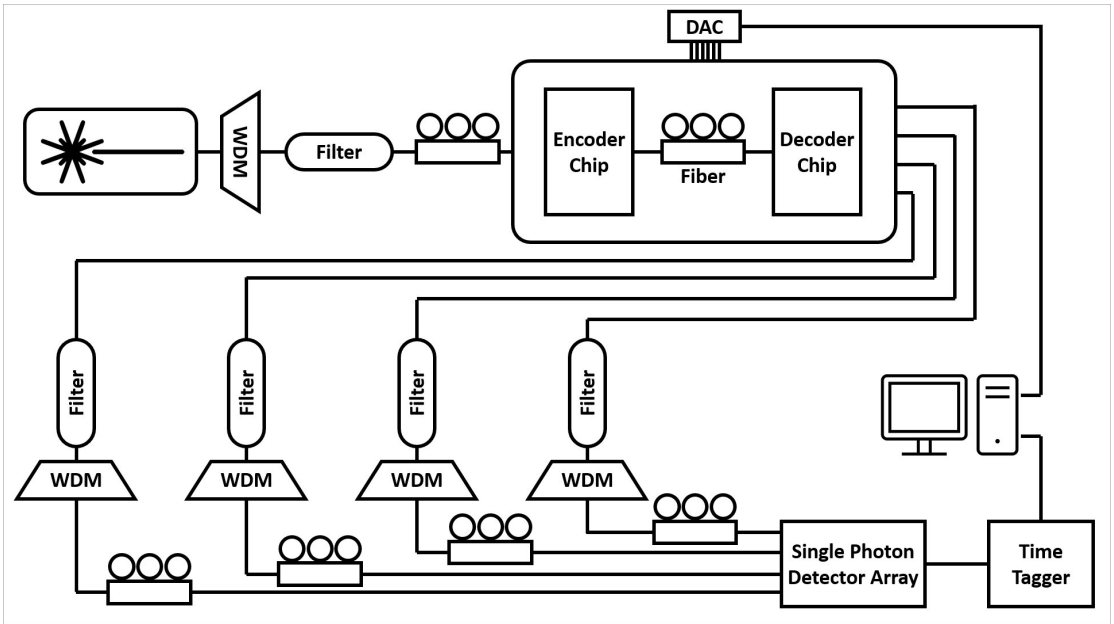

(a)

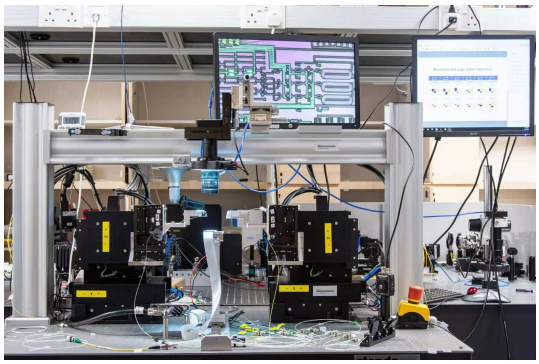

(b)

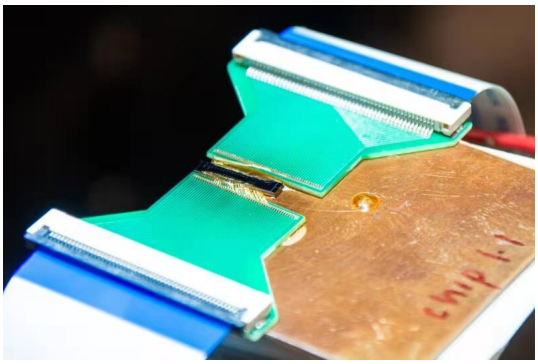

(c)

Figure 5.8: (a) The control flow chart of the experimental system. The qutrit on the encoder chip will be compressed and transformed to the decoder chip via a fiber. The qubit is decoded back to qutrit and get measured. (b) Photograph of the experimental setup. (c) Photograph of the packaged quantum autoencoder chip.

The qutrit compression training and Bell state measurement are performed on the encoder chip and the entangled photon pair is sent to the decoder chip via a single mode fibre by suspended spotsize converter (SSC) edge coupler. Another three-ring polarization controller is applied to align the polarization of two chips. The compressed qubit is sent to decoder chip via this quantum channel and the original qutrit is recovered and

state tomography is performed to verify that the scheme works. The output channels of photons are coupled to a set of fibre arrays via the SSC and each fiber is connected with a filter and a WDM to remove the pump laser and other background photons to increase the fidelity of coincidence counts. Before the photons enter into the detectors, another three-ring polarization controller is connected to maximize the detection efficiency for the superconducting photon detector array (PhotonSpot). The photon signal is then converted to electrical signal and transfers to a time tagger (Swabian Instrument) to measure the coincidence count between the different channels. These data are then processed by the computer to train the circuit or reconstruct the density matrix for calculating the fidelity quantum quantum state. Finally, the computer sends instruction to the DAC to apply the proper current on each heater to control the circuit for further measurement.

A photographic illustration of the full system is shown in Figure 5.8b. The fiber coupling array is controlled by a 12-axis alignment stage with a CCD camera to monitor the chip for coupling adjustment. The chip is centralized at the stage as shown in Figure 5.8c. The copper pad function as a substrate to hold the chip and two PCB boards. The thermalelectral cooler (TEC) pad is added beneath the substrate for temperature stabilization. The chip lies between two PCB boards with golden wires bounded to connect the on-chip heaters to PCB metal pad. The flat blue-white cables are FFC connectors to send the electric signal from DAC to the bonded chip.

5.3.2 System Calibration

The circuit includes two AMZIs to remove the pump power and split the signal and idler photons. The spectra of these two devices and their joint spectra are measured as

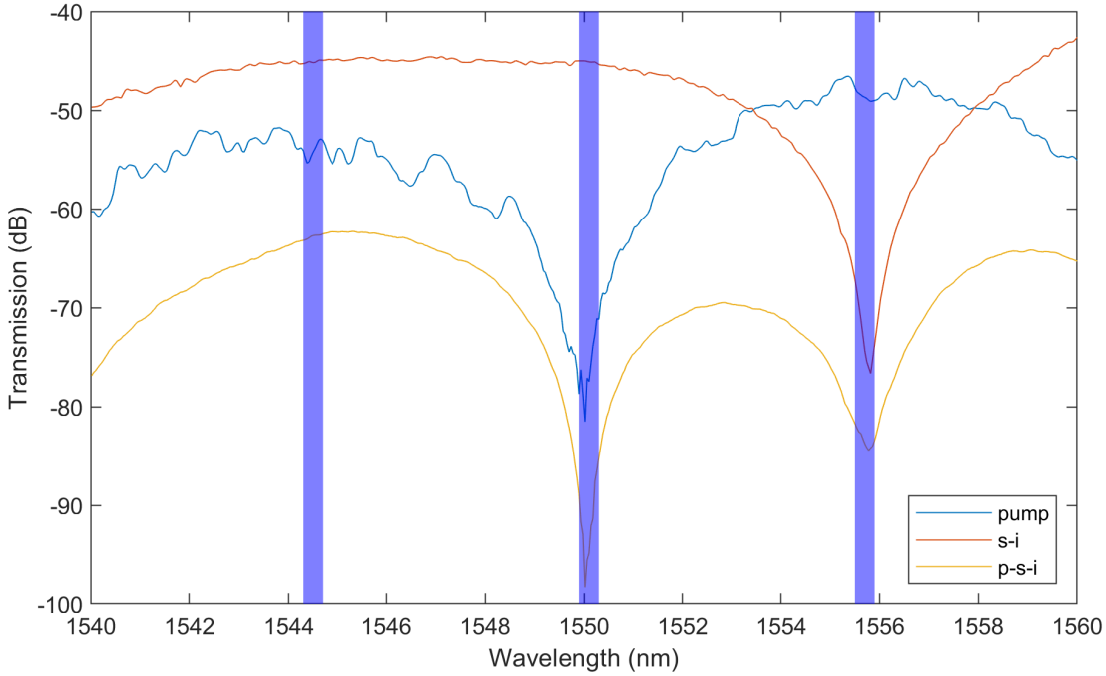

Figure 5.9: The spectra of AMZI. Blue line is the pump AMZI. Its FSR is 11.2 *nm* to keep the signal and idler photon while rejecting the pump power. The red line is the s-i AMZI with FSR of 22.4 *nm* to separate the signal and idler photons into two output ports. The yellow line is the combined spectra of two consecutive AMZI to show that the three wavelength can be well distinguished with up to 20 *dB* extinction ratio. The shaded blue bars are the wavelength for signal, idler and pump.

shown in Figure 5.9. The blue line is for the pump AMZI, the red line is for the signal-idler AMZI and the yellow line is the spectra after passing through these two devices. The three shaded vertical bars indicate the pump and the two photon wavelengths. The average extinction ratio for AMZI is over 25 *dB*. Pump laser wavelength is selected to be 1550.112 *nm*, which is the C34 channel of WDM. The photon pair wavelengths are selected to be 1555.747 *nm* at C27 channel for signal and 1544.526 *nm* at C41 channel for Idler. The first pump AMZI has a FSR of 11.2 *nm* to split the photon pair and pump laser as illustrated with blue line. The pump wavelength (mid bar) falls at the valley of spectra while the signal and idler wavelengths (left and right bars) fall at the peak of

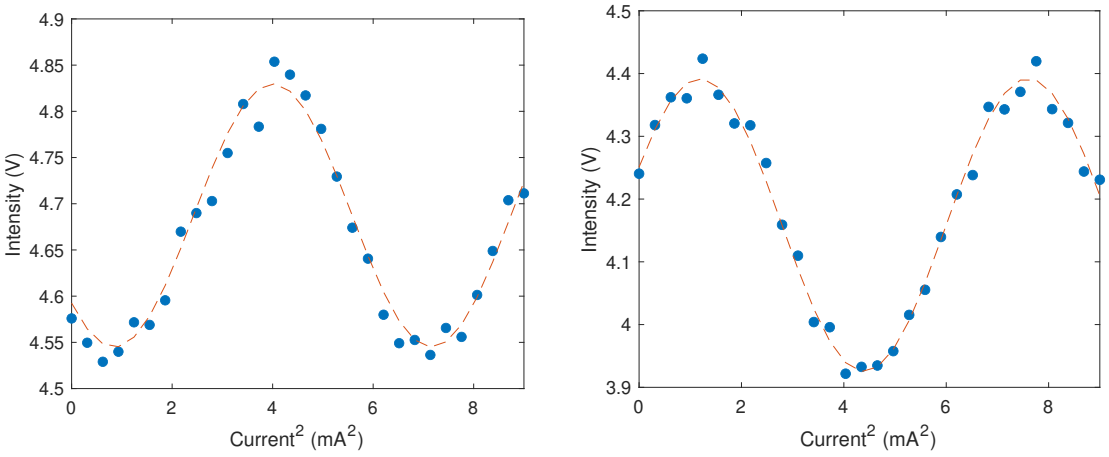

(a) $V_{en} = 0.030$ (b) $V_{de} = 0.056$

Figure 5.10: Measurement results of MZI on PRS at (a) encoder and (b) decoder chip. The loss difference of TE_0 and TM_0 mode can be used to calibrate the MZI connecting to two arms of PRS. By measuring the intensity fluctuations from PRS, the peak corresponds to the TE_0 modes and valley is for TM_0 mode.

the spectra, which indicates they can be separated into different output ports effectively. The signal-idler AMZI has a FSR of 22.4 *nm* to separate the two photon wavelengths by aligning them at the peak and valey of the spectra as shown in red line. It should be noted again that the yellow line is the spectra after two AMZIs with proper phase settings that three wavelengths are all at the peak or valley of the spectra with a high extinction ratio.

The on-chip PRS is a passive structure used to convert the TE_0 mode photon in two waveguides into TE_0 and TM_0 photon in one waveguide. Although the theoretical simulation indicates no loss in conversion, the waveguide cross section is designed for TE_0 mode propagation and TM_0 would suffer slightly higher loss. The MZI connected to PRS can be calibrated by observing the interference fringe of intensity at the single waveguide output. Figure 5.10 is the measured fringe of MZI for PRS on encoder and

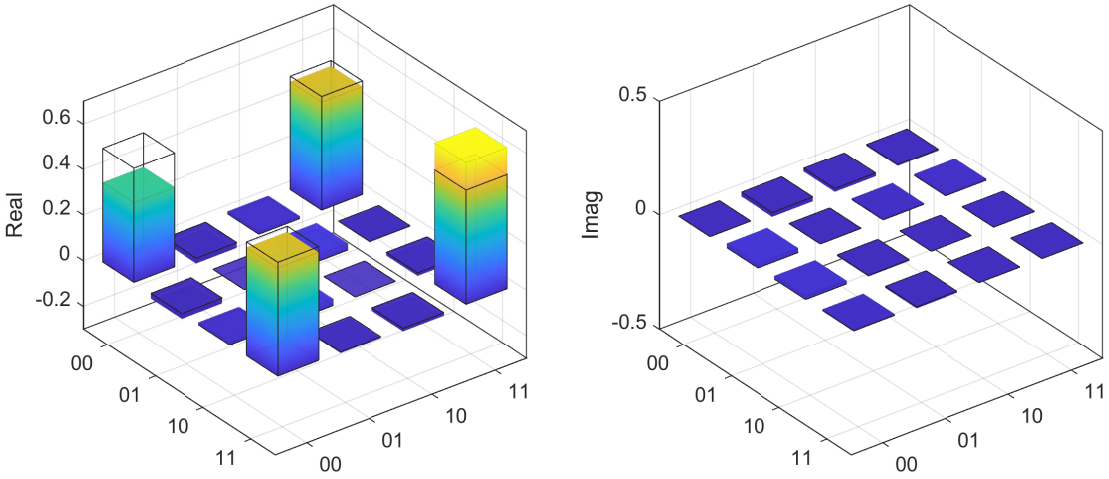

(a) Real part (b) Imag part

Figure 5.11: (a) Real part and (b) imaginary part of density matrix for $|00\rangle + |11\rangle$ with $F = 0.9594 \pm 0.004$. The colored bars are for measured results while the transparent bars are theoretical results.

decoder chip. The visibilities are $V_{en} = 0.030$ and $V_{de} = 0.056$.

The quantum channel for teleportation is built with a pair of entangled state $|00\rangle + |11\rangle$. The state is generated by pumping two spiral waveguides simultaneously and generating entangled photon for the heralded single-photon source, and ignoring multi-photon-pair events. In this experiment, the pump power is set to a low level to reduce the effect of multi-photon events. Quantum state tomography is performed to reconstruct the experimental density matrix and its fidelity is measured to be $F = 0.9594 \pm 0.004$ as shown in Figure 5.11. The colored bars are for experimental results and the transparent bars are theoretical value.

The estimated losses for the whole system are calibrated and the data is shown in Table 5.2. For circuit part, the waveguide propagation loss is 2.3 dB/cm, the crossing structure is 0.024 dB and the MMI loss is 0.15 dB. The SSC coupling loss is slightly better than the grating coupler at 5 dB per facet. For PRS structure, it has a loss around

Table 5.2: Loss estimation of the teleportation with autoencoder chip.

Components	Loss dB	No.	Total dB
SSC Coupler	5	3	15
Waveguide	2.3 cm^{-1}	2.5 cm	5.75
Crossing	0.024	1	0.024
MMI	0.15	20	3
PRS	2	2	4
WDM	2	1	2
Filter	0.9	2	1.8
Detector	0.71	1	0.71
			32.284

1.5 dB and although it has lower propagation loss for TE_0 than TM_0 mode, the difference can be ignored comparing with its own loss. For the off chip devices, 20 channels in WDM have a variant loss from 1 dB to 3 dB and a mean value of 2 dB is considered. The filter has a smaller loss to be 0.9 dB. The average single photon detector efficiency can be assumed to be 85% with the test data from vendor. Other losses like fiber or connectors can be ignored or have been counted into other devices. Therefore, the whole loss of the longest route is 32.284 dB, which corresponds to a system efficiency of 0.052%.

5.3.3 Experimental Results and Discussions

After the calibration of circuit design, the teleportation of quantum state is first tested with the 6 basis states $|H/V\rangle = |0/1\rangle$, $|D/A\rangle = \frac{1}{\sqrt{2}}(|0\rangle \pm |1\rangle)$, $|R/L\rangle = \frac{1}{\sqrt{2}}(|0\rangle \pm i|1\rangle)$. They are prepared from a heralded single photon state and tuning the phase information at the following heaters. The target qubit along with the qubit from entangled photon pair are subject to Bell states measurement (BSM). Due to the limitations of feed forward control of quantum circuit, the BSM results are all post-selected to the $|\phi\rangle^+$ and no correction operations are then required on the transferred qubit. A 10-

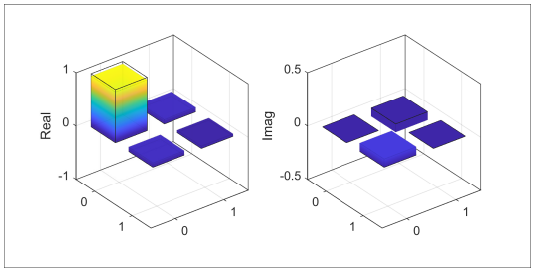

(a) $F_H = 0.9551 \pm 0.009$

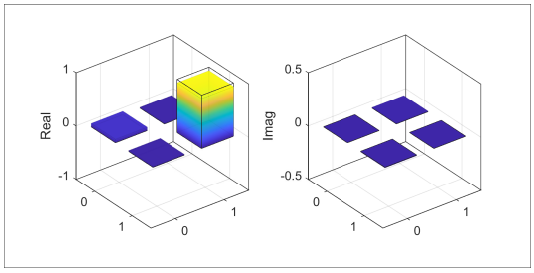

(b) $F_V = 0.9355 \pm 0.011$

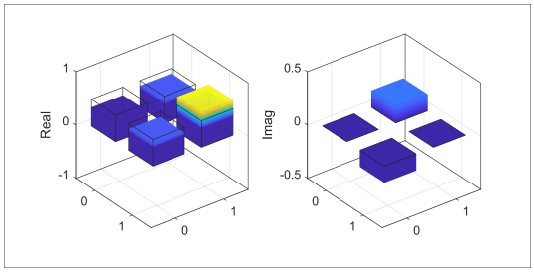

(c) $F_D = 0.9235 \pm 0.025$

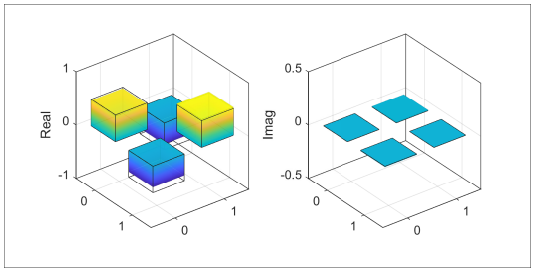

(d) $F_A = 0.9167 \pm 0.031$

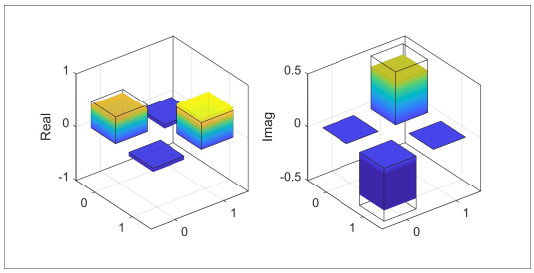

(e) $F_R = 0.9415 \pm 0.024$

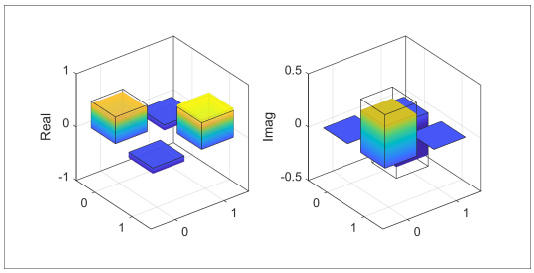

(f) $F_L = 0.9109 \pm 0.030$

Figure 5.12: Density matrices measured at the decoder circuit. The initial state is selected to be (a) H, (b) V, (c) D, (d) A, (e) R, (f) L. The corresponding fidelity of each state is listed beneath each plot with an average of $\bar{F} = 0.935$.

meter-long single mode fiber is connected between encoder and decoder chip to send the entangled qubits as a quantum channel. At the decoder chip, the MZI is set with the state tomography basis and coincidence counts are measured correspondingly to reconstruct the density matrix as shown in Figure 5.12. Real parts and imaginary parts of density for each state is plotted with colored bars for the experimental results and transparent bar for the theoretical results. The fidelity is labeled beneath each plot and the average fidelity is measured to be $\bar{F} = 0.935$.

The time tagger measures the time in the step of ps. The initial average photon count rate without training is at the level of 10^4 Hz and the dark count of the detector is less than 100 Hz, which corresponds to an average time step of 10^8 ps and 10^{10} ps. The cost function is defined as

$$f(x) = 1 - \frac{e^{\frac{x-10^8}{10^{10}}} - 1}{e-1}, \tag{5.21}$$

so that the autoencoder is optimized for the compression of the higher dimensional quantum states into a qubit subspace with the remaining components (the trashable part of the state) reduced to the vacuum state. The measured photon rate is at dark count level of 100 Hz and $\Delta t \approx 10^10 ps$. Also, $f(\Delta t)$ converges to 0. Since the detection window is selected to be 10 ms, if no photon click is detected in this window, the $Deltat$ is defined to be 10^{10} ps.

The training process is shown in Figure 5.13 that for the time difference between trigger and first photon click Δt, each generation consists of 20 individuals, and the Δt for each individual is the averaged results of 20 different qutrit input states selected from some initial dataset. It is easy to see that the time difference convergence to $\Delta t = 10^{10}$

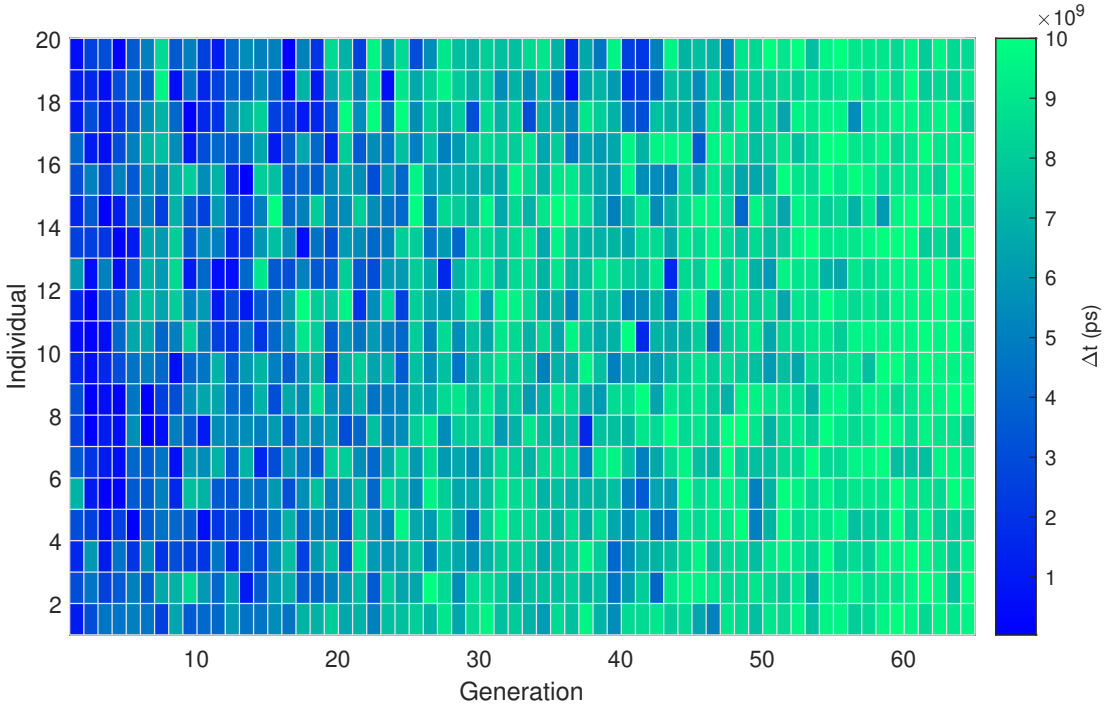

(a)

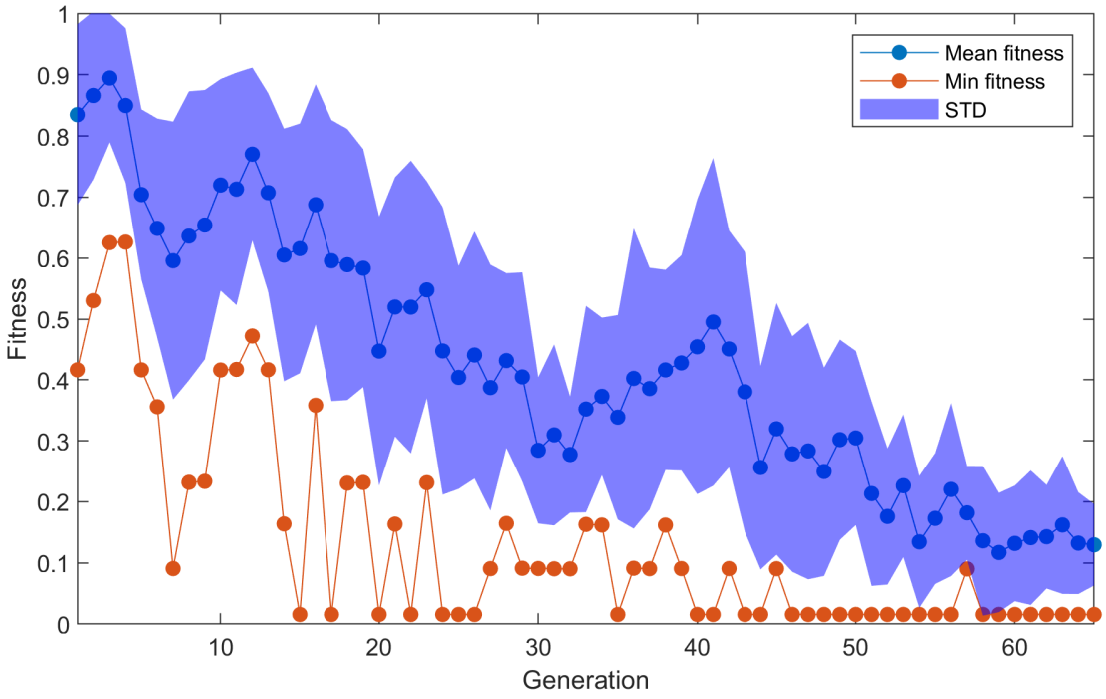

(b)

Figure 5.13: Training Process of the autoencoder. (a) The time difference Δt increase by the generation. (b) The mean fitness (blue dots) converges at the end of training. The shaded blue areas are the std in each generation. The minimum fitness (orange dots) stays to be 0, indicating no photon detected at the end of training.

ps with each generation.

For the fitness function, the average fitness value for all 20 individuals (blue dots) and the minimum of each generation (red dots) are plotted. The shaded area are the standard deviation of fitness value. By the iteration of generation, the fitness converges to 0, which indicates the trash state $|\phi\rangle_{tsh}$ is closed to a vacuum state. The minimum fitness value exhibits some discrete level because Δt for each individual is the averaged result of 20 different qutrits. The parameter for the minimum individual has been optimized so that no click is measured inside the window for most of the qutrits and the Δt is set to be 10^{10} ps. The average can be approximated as $\bar{\Delta t} \approx n/20 \times 10^{10} ps$, where n is the number of non-click qutrits.

The fitness function during the training process does not decrease continuously and shows some fluctuations as in generation 40. The fluctuation is due to the genetic algorithm training process itself and output will jump outside the local minimum via the mutation process.

The comparison of training results at convergence condition with initial results is shown in Figure 5.14. The blue bars are for first generation training results while the orange bars are for last generation. The Δt in all individuals show great increase from $10^9 ps$ level to $10^{10} ps$ level, the corresponding fitness value also decreases from 1 to 0.1.

The statistical distributions of 8 free parameters are also studied. Based on the previous calibration results, 3 mA current is enough to induce a phase change of 2π thus the tuning range of 8 heaters are all set to be slightly larger than 3 mA. In Figure 5.15, the red line for each parameter is the mid number value of 20 individuals. The

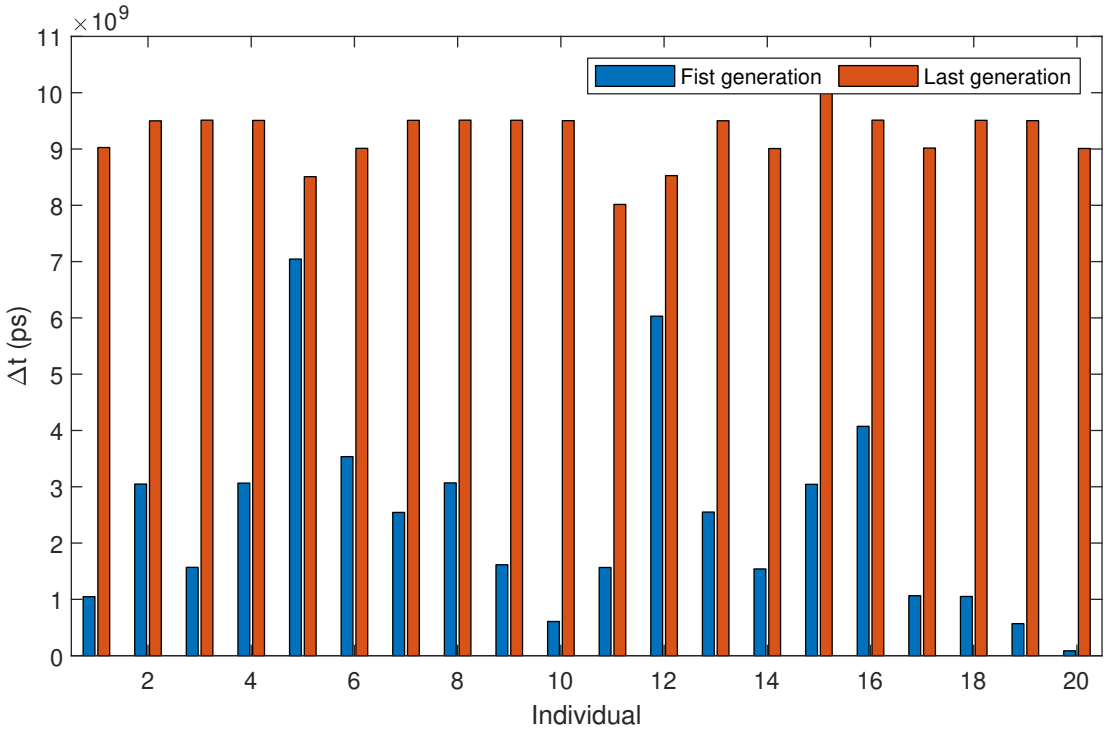

(a)

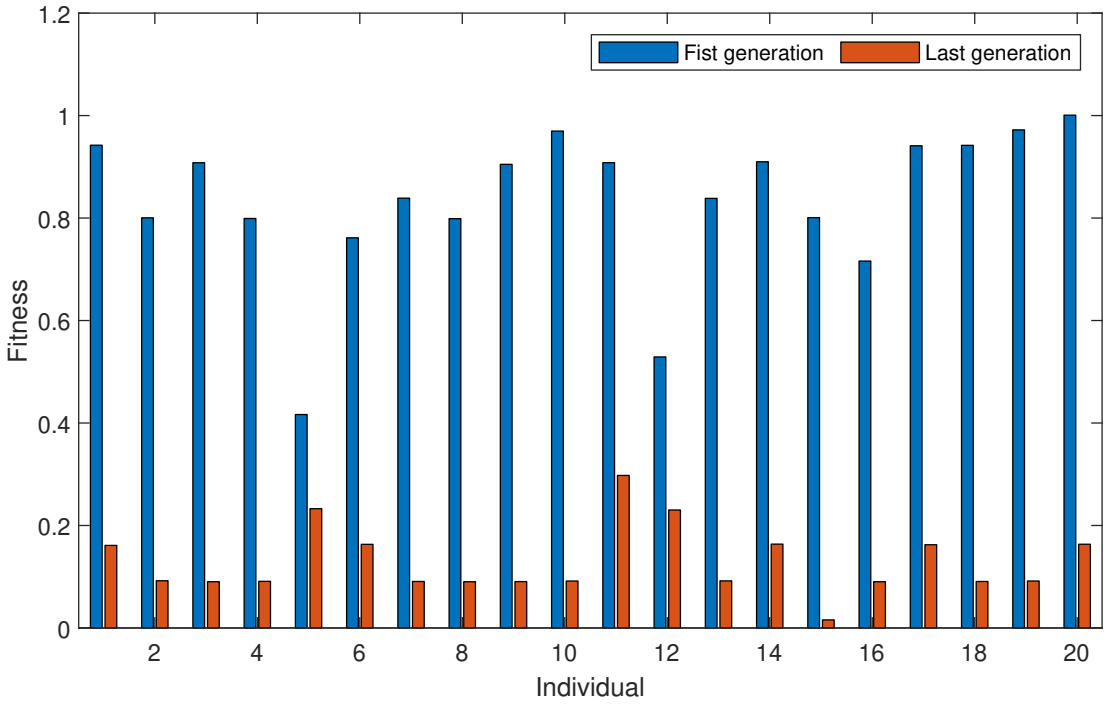

(b)

Figure 5.14: Comparison between the first generation and the last generation for (a) Δt and (b) Fitness. The blue bars are for the first generation and the orange bars are for the last generation.

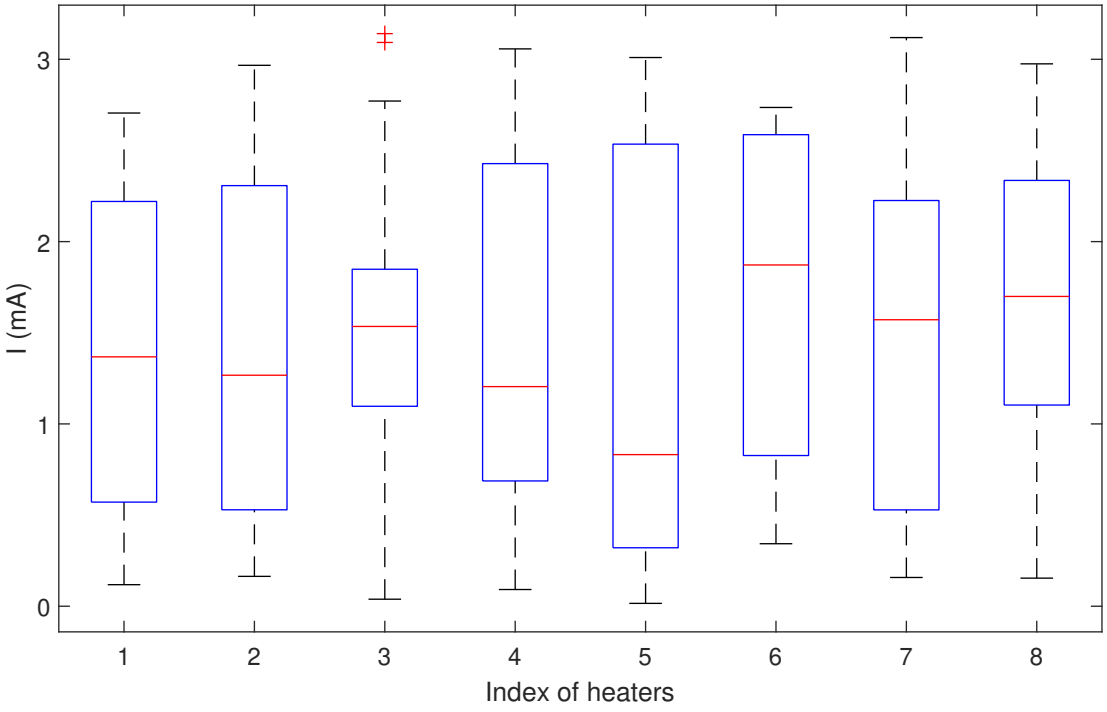

(a)

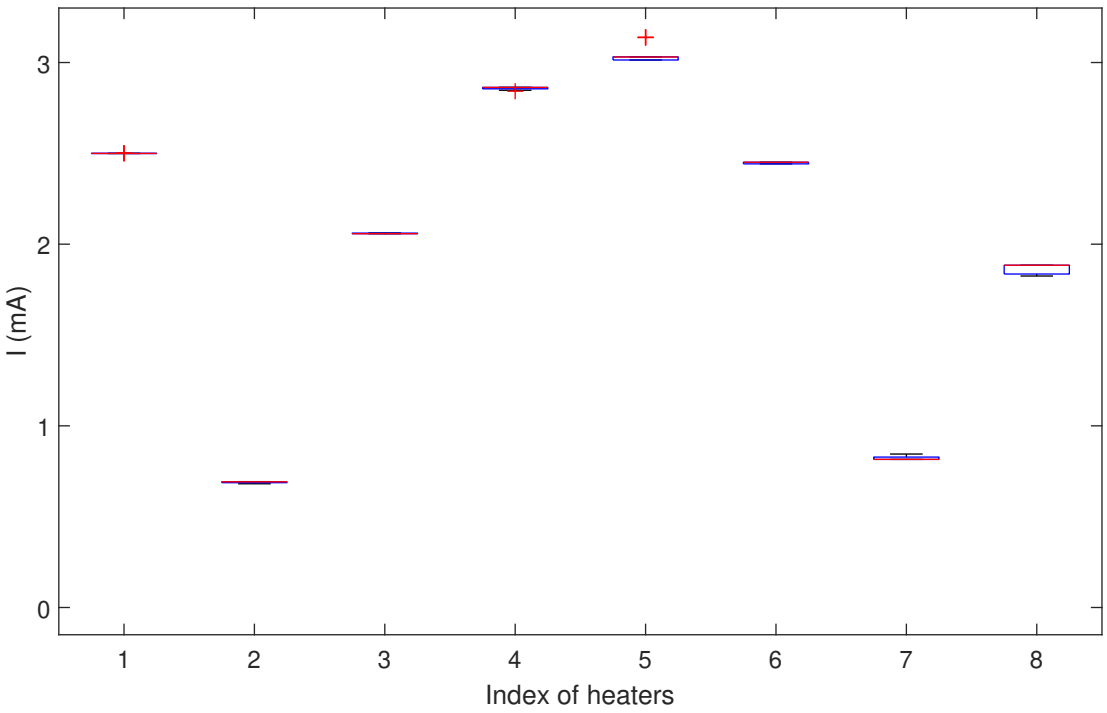

(b)

Figure 5.15: Statistics for 8 free parameters of the autoencoder over 20 individuals at (a) the first generation and (b) the last generation. Red line is the mid number and the blue box covers 25% to 75% percentile. Dashed bar is the upper and lower limit. Red '+' marker is the discarded data.

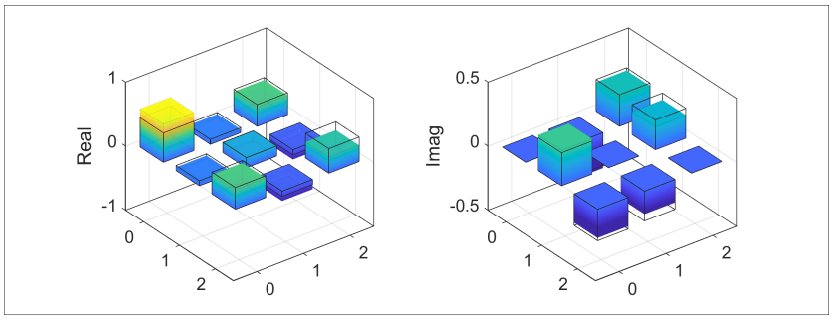

(a) $F_1 = 0.9564 \pm 0.052$

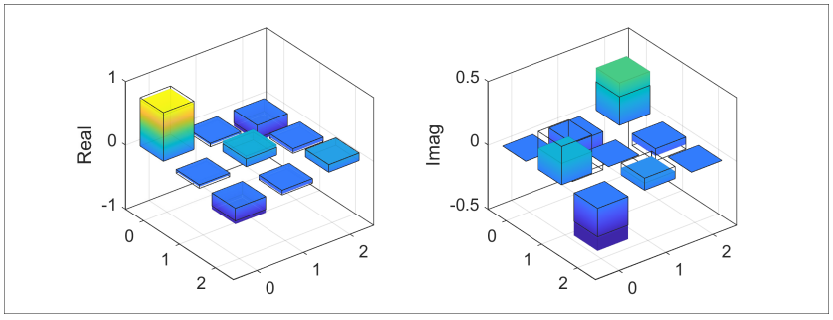

(b) $F_2 = 0.9134 \pm 0.047$

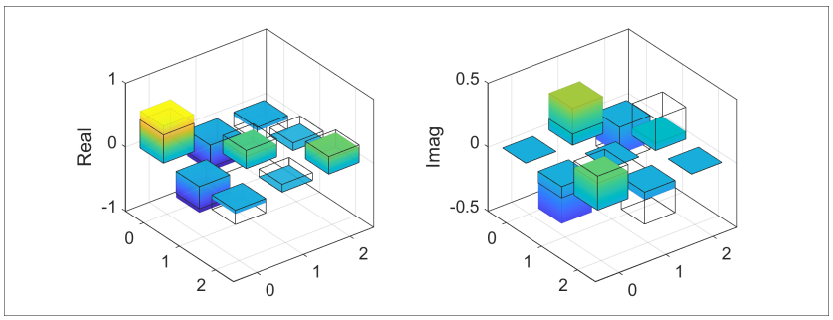

(c) $F_3 = 0.8793 \pm 0.051$

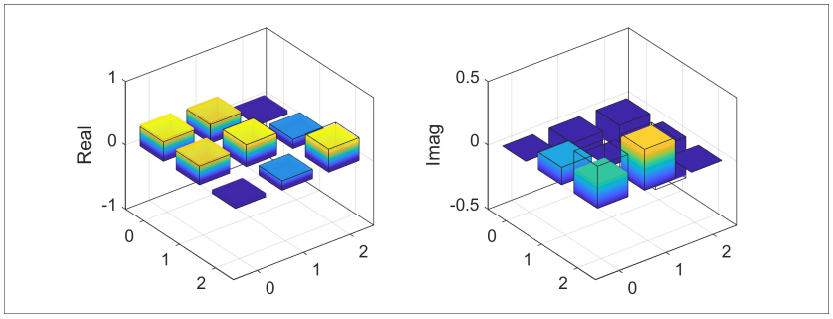

(d) $F_4 = 0.9036 \pm 0.046$

Figure 5.16: Tomography results of 4 random qutrits using decoder chip for reconstructed density matrices (a)-(d). Real and imag parts are plotted with colored bars for experimental data and transparent bars for theoretical data. Fidelity of each qutrit is labeled beneath the plot with an average of $\bar{F} = 0.9132$.

blue box indicates the 25% to 75% percentile range of parameter value distribution in 20 individuals. The dashed lines are the maximum and minimum limit of all parameter values and the red '+' mark is the omitted data are outliers and their values are too far away from other points in the samples. At the first generation of training process, the parameters are not optimized and the statistics of all eight parameters are randomly distributed and their distributions are spread over the 3 mA range. At the last generation, the fitness function has reached the convergence values and each free parameter p_i in all 20 individuals also converges to a stable value with a very narrow distribution, which proves the functionality of autoencoder.

Finally, four random qutrits are selected from the dataset to prove the full teleportation process with autoencoder. With the autoencoder well trained, the current set on each heater is known, thus the corresponding phase information is also decided based on previous calibration process. The decoder is set as the inverse unitary matrix of encoder and the transferred qubit is then decoded to the original qutrit with the decoder circuit. Quantum state tomography is then performed as shown in Figure 5.16. Experimental results for real part and imaginary part of the 4 qutrits are plotted in colored bars and the corresponding theoretical results are plotted in transparent bars for comparison. The fidelities are labeled beneath each plot and the average retrieved fidelity is $\bar{F} = 0.9132$.

5.4 Conclusions

In this chapter, a novel quantum information transferring method consuming less quantum resources is proposed and demonstrated with photonic integrated circuit. The proposed method focuses on a particular dataset of qutrit with an almost lossless com-

pression process to train a quantum autoencoder model with genetic algorithm that maps the qutrit subspace to a qubit space to save the quantum resource. The quantum teleportation of qubit requires in general less quantum resources than qutrit and is demonstrated by transferring the compressed qubit from one photonic integrated circuit to another via a 10-meter-long fiber. The original qutrit is recovered by the inverse process of trained autoencoder and the quantum state tomography is performed with an average fidelity of $\bar{F} = 0.9132$ for four random qutrits to prove the functionality of the full system. This prototype can pave the way for the development of quantum network and high efficiency quantum information sharing.

Chapter 6

Finale

6.1 Recapitulation and Conclusions

In this thesis, the integrated quantum photonic computing circuit is carefully studied and three different quantum computing algorithms are demonstrated experimentally. The theoretical modeling, photonic integrated circuit design and experimental implementation process are described in detail.

In GBS quantum computing section, the properties of on chip photon source and linear optical circuit is carefully studied. First the SFWM process of on chip photon generation is discussed. Different methods to realize the energy conservation and phase matching condition are listed and calculated. Two matrix decomposition methods are shown as a guidance to realize arbitrary unitary matrix with linear photonic circuit. Then, for the designed quantum circuit, the photon source properties are carefully studied under both single pump scheme for TMS state and dual pump scheme for SMS state such as the JSI, g_2, CAR, squeeze parameter and so on. Next, the circuit is used to

implement unitary matrices and the results are verified experimentally to get a similarity of 98.44%. Finally, a boson sampling is measured with a random unitary set and a perfect matching problem is studied for a 6-vertex graph. GBS circuit is configured to simulate the perfect matching problem and the achieved photon distribution has a similarity of 0.9783 with the theoretical results. The subgraph perfect matching number is also calculated to be identical with the theory.

In error correction encoding section, the theoretical model of this scheme is studied and its photonic implementation is designed. Next, a photonic integrated circuit is fabricated with on chip photon generation, initial state preparation and qubit operation function to realize the prototype of this error correction encoding scheme. Three applications of quantum information processing: quantum state reconstruction, error type identification and error corrected quantum teleportation have been demonstrated on this photonic integrated circuit. The experiment result has proved the encoding scheme to be feasible for protecting the quantum information from the propagation loss or quantum operation error, an average state reconstruction fidelity of $\bar{F} = 0.8630$. The success implementation of the quantum error correction encoding on integrated photonic platform is very important in the era of quantum information as it provides a demonstration to maintain the qubit operation error beneath a certain threshold to avoid decoherence of quantum states and loss of quantum information. This would pave the way for further scaling up of quantum circuit model to larger scales.

In teleportation with autoencoder section, a novel quantum information transferring method consuming less quantum resources is proposed and demonstrated with photonic integrated circuit. The proposed method focuses on a particular dataset of qutrit with an existent lossless compression process. A quantum autoencoder model is trained

with genetic algorithm that maps the qutrit subspace to a qubit space. Thus, less quantum resource is required to store the quantum information during the transformation at the quantum network. The quantum teleportation of qubit also requires less quantum resource than qutrit and is demonstrated by transferring the compressed qubit from encoder chip to decoder chip via a 10-meter-long fiber. The original qutrit is recovered by the inverse process of trained autoencoder and the quantum state tomography is performed with an average fidelity of $\bar{F} = 0.9132$ for four random qutrits to prove the functionality of the full system. This prototype can help the development of quantum network and high efficiency quantum information sharing.

The demonstration of some of these quantum algorithms for computation offers a possible solution for taking the advantage of quantum computation power, reducing error rates in computation process and high efficiency quantum information transformation on integrated photonic platform. This would help the future development of integrated quantum photonic computer and quantum network system.

6.2 Recommendations for future works

The demonstrations in thesis have the potential for further improvements. First, the system can be scaled up with more photons and to larger linear optical circuits for more realistic quantum simulation tasks. This may require the optimization of circuit design of higher efficiency and photon number resolving detectors to unlock more computation power.

Second, more general quantum error correction scheme that does not rely on the prerequisite of error type or location but can tolerate more qubit errors should be stud-

ied. Involving more physical qubits to protect a logic qubit and a more efficient way to implement the error correction encoding to quantum algorithms still awaits further exploration.

Third, the quantum autoencoder for quantum information compression should be generalize to support complicated quantum information other than qutrit. Quantum optimization would be studied to see whether it can provide more advantage in classical training process of the autoencoder. The quantum teleportation process can be more efficient with photon number resolving detectors and a quantum network with multiple nodes can be considered.

Author's Publications

1. **L.X. Wan**, B. Wang, H.H. Zhu, H. Zhang, Y. Li, L.C. Kwek and A.Q. Liu, "Perfect matching of Gaussian boson sampling to Solve Graph Problems on Integrated Photonic Chip", *Nature Communication*, 2021 (Submitted).

2. **L. X. Wan**, H. Zhang, T. Haug, D. Mok, H. Cai, F. K. Muhammad, G. Q. Lo, X. S. Luo, B. Dong, D. L. Kwong, L. C. Kwek, and A. Q. Liu, "Quantum autoencoder for teleportation of high-dimensional quantum states", *Nature Physics*, 2021 (Submitted).

3. **L.X. Wan**, L.B. Yan, J.G. Huang, G. Zhang, L.C. Kwek, J. Fitzsimons, Y.D. Chong, J.B. Gong, A. Szameit, X.Q. Zhou, M.H. Yung, X.M. Jin, X.L. Su, W. Ser, W.B. Gao and A.Q. Liu, "A Large-Number and Multilayer Quantum Walk using Silicon Nano-photonic Chip", *CLEO2018*, SanJose, USA. (Oral)

4. **L.X. Wan**, H. Zhang, J.G. Huang, G. Zhang, L.C. Kwek, J. Fitzsimons, Y.D. Chong, J.B. Gong, A. Szameit, X.Q. Zhou, M.H. Yung, X.M. Jin, X.L. Su, W. Ser, W.B. Gao and A.Q. Liu, "Determinating Full Parameters of U-Matrix for Recofigurable Boson Sampling Circuits using Machine Learning", *CLEO2018*, SanJose, USA. (Poster)

5. H.Zhang, **L.X. Wan**, M. Gu, X.D. Jiang, J. Thompson, H. Cai, S. Paesani, R.

Santagati, A. Laing, Y. Zhang, M.H. Yung, F.K. Muhammad, G.Q. Lo, X.S. Luo, B. Dong, D.L. Kwong, L.C. Kwek and A.Q. Liu, ”Efficient Nonlinear Activation in Optical Neural Network”, *CLEO2020*, San Jose, USA. (Poster)

Bibliography

[1] Joonsuk Huh, Gian Giacomo Guerreschi, Borja Peropadre, Jarrod R McClean, and Alán Aspuru-Guzik. Boson sampling for molecular vibronic spectra. *Nature Photonics*, 9(9):615–620, 2015.

[2] Chris Sparrow, Enrique Martín-López, Nicola Maraviglia, Alex Neville, Christopher Harrold, Jacques Carolan, Yogesh N Joglekar, Toshikazu Hashimoto, Nobuyuki Matsuda, Jeremy L O'Brien, et al. Simulating the vibrational quantum dynamics of molecules using photonics. *Nature*, 557(7707):660–667, 2018.

[3] Kamil Brádler, Pierre-Luc Dallaire-Demers, Patrick Rebentrost, Daiqin Su, and Christian Weedbrook. Gaussian boson sampling for perfect matchings of arbitrary graphs. *Physical Review A*, 98(3):032310, 2018.

[4] Juan Miguel Arrazola and Thomas R Bromley. Using gaussian boson sampling to find dense subgraphs. *Physical review letters*, 121(3):030503, 2018.

[5] Jacques Carolan, Christopher Harrold, Chris Sparrow, Enrique Martín-López, Nicholas J Russell, Joshua W Silverstone, Peter J Shadbolt, Nobuyuki Matsuda, Manabu Oguma, Mikitaka Itoh, et al. Universal linear optics. *Science*, 349(6249):711–716, 2015.

[6] Nicholas C Harris, Gregory R Steinbrecher, Mihika Prabhu, Yoav Lahini, Jacob Mower, Darius Bunandar, Changchen Chen, Franco NC Wong, Tom Baehr-Jones, Michael Hochberg, et al. Quantum transport simulations in a programmable nanophotonic processor. *Nature Photonics*, 11(7):447, 2017.

[7] Yichen Shen, Nicholas C Harris, Scott Skirlo, Mihika Prabhu, Tom Baehr-Jones, Michael Hochberg, Xin Sun, Shijie Zhao, Hugo Larochelle, Dirk Englund, et al. Deep learning with coherent nanophotonic circuits. *Nature Photonics*, 11(7):441, 2017.

[8] Joshua W Silverstone, Damien Bonneau, Kazuya Ohira, Nob Suzuki, Haruhiko Yoshida, Norio Iizuka, Mizunori Ezaki, Chandra M Natarajan, Michael G Tanner, Robert H Hadfield, et al. On-chip quantum interference between silicon photon-pair sources. *Nature Photonics*, 8(2):104–108, 2014.

[9] Jianwei Wang, Stefano Paesani, Yunhong Ding, Raffaele Santagati, Paul Skrzypczyk, Alexia Salavrakos, Jordi Tura, Remigiusz Augusiak, Laura Mančinska, Davide Bacco, et al. Multidimensional quantum entanglement with large-scale integrated optics. *Science*, 360(6386):285–291, 2018.

[10] Peter W Shor. Algorithms for quantum computation: discrete logarithms and factoring. In *Proceedings 35th annual symposium on foundations of computer science*, pages 124–134. Ieee, 1994.

[11] Lov K Grover. A fast quantum mechanical algorithm for database search. In *Proceedings of the twenty-eighth annual ACM symposium on Theory of computing*, pages 212–219, 1996.

[12] Evgeny Milanov. The rsa algorithm. *RSA Laboratories*, pages 1–11, 2009.

[13] Marta Arcari, Immo Söllner, Alisa Javadi, S Lindskov Hansen, Sahand Mahmoodian, Jin Liu, Henri Thyrrestrup, Eun Hye Lee, Jin Dong Song, Søren Stobbe, et al. Near-unity coupling efficiency of a quantum emitter to a photonic crystal waveguide. *Physical review letters*, 113(9):093603, 2014.

[14] Emanuel Knill, Raymond Laflamme, and Gerald J Milburn. A scheme for efficient quantum computation with linear optics. *nature*, 409(6816):46–52, 2001.

[15] Wolfram HP Pernice, C Schuck, O Minaeva, M Li, GN Goltsman, AV Sergienko, and HX Tang. High-speed and high-efficiency travelling wave single-photon detectors embedded in nanophotonic circuits. *Nature communications*, 3(1):1–10, 2012.

[16] Emanuel Knill, Raymond Laflamme, and Wojciech H Zurek. Resilient quantum computation: error models and thresholds. *Proceedings of the Royal Society of London. Series A: Mathematical, Physical and Engineering Sciences*, 454(1969):365–384, 1998.

[17] A Robert Calderbank and Peter W Shor. Good quantum error-correcting codes exist. *Physical Review A*, 54(2):1098, 1996.

[18] David P DiVincenzo and Peter W Shor. Fault-tolerant error correction with efficient quantum codes. *Physical review letters*, 77(15):3260, 1996.

[19] Andrew M Steane. Error correcting codes in quantum theory. *Physical Review Letters*, 77(5):793, 1996.

[20] Andrew M Steane. Simple quantum error-correcting codes. *Physical Review A*, 54(6):4741, 1996.

[21] Robert Raussendorf, Jim Harrington, and Kovid Goyal. Topological fault-tolerance in cluster state quantum computation. *New Journal of Physics*, 9(6):199, 2007.

[22] Daniel Gottesman. Stabilizer codes and quantum error correction. *arXiv preprint quant-ph/9705052*, 1997.

[23] Simon J Devitt, William J Munro, and Kae Nemoto. Quantum error correction for beginners. *Reports on Progress in Physics*, 76(7):076001, 2013.

[24] David Kribs, Raymond Laflamme, and David Poulin. Unified and generalized approach to quantum error correction. *Physical Review Letters*, 94(18):180501, 2005.

[25] Vahid Karimipour, Alireza Bahraminasab, and Saber Bagherinezhad. Entanglement swapping of generalized cat states and secret sharing. *Physical Review A*, 65(4):042320, 2002.

[26] Zheng-Da Li, Rui Zhang, Xu-Fei Yin, Li-Zheng Liu, Yi Hu, Yu-Qiang Fang, Yue-Yang Fei, Xiao Jiang, Jun Zhang, Li Li, et al. Experimental quantum repeater without quantum memory. *Nature Photonics*, 13(9):644–648, 2019.

[27] Koji Azuma, Kiyoshi Tamaki, and Hoi-Kwong Lo. All-photonic quantum repeaters. *Nature communications*, 6(1):1–7, 2015.

[28] Albert Einstein, Boris Podolsky, and Nathan Rosen. Can quantum-mechanical description of physical reality be considered complete? *Physical review*, 47(10):777, 1935.

[29] David Bohm. A suggested interpretation of the quantum theory in terms of" hidden" variables. i. *Physical review*, 85(2):166, 1952.

[30] Albert Einstein. *The Collected Papers of Albert Einstein, Volume 13: The Berlin Years: Writings & Correspondence, January 1922-March 1923 (English Translation Supplement)*, volume 13. Princeton University Press, 1987.

[31] John S Bell. On the einstein podolsky rosen paradox. *Physics Physique Fizika*, 1(3):195, 1964.

[32] Stuart J Freedman and John F Clauser. Experimental test of local hidden-variable theories. *Physical Review Letters*, 28(14):938, 1972.

[33] Gregor Weihs, Thomas Jennewein, Christoph Simon, Harald Weinfurter, and Anton Zeilinger. Violation of bell's inequality under strict einstein locality conditions. *Physical Review Letters*, 81(23):5039, 1998.

[34] Markus Ansmann, H Wang, Radoslaw C Bialczak, Max Hofheinz, Erik Lucero, Matthew Neeley, Aaron D O'Connell, Daniel Sank, Martin Weides, James Wenner, et al. Violation of bell's inequality in josephson phase qubits. *Nature*, 461(7263):504–506, 2009.

[35] Marissa Giustina, Alexandra Mech, Sven Ramelow, Bernhard Wittmann, Johannes Kofler, Jörn Beyer, Adriana Lita, Brice Calkins, Thomas Gerrits, Sae Woo Nam, et al. Bell violation using entangled photons without the fair-sampling assumption. *Nature*, 497(7448):227–230, 2013.

[36] Bas Hensen, Hannes Bernien, Anaïs E Dréau, Andreas Reiserer, Norbert Kalb, Machiel S Blok, Just Ruitenberg, Raymond FL Vermeulen, Raymond N

Schouten, Carlos Abellán, et al. Loophole-free bell inequality violation using electron spins separated by 1.3 kilometres. *Nature*, 526(7575):682–686, 2015.

[37] BIG Bell Test Collaboration et al. Challenging local realism with human choices. *Nature*, 557(7704):212–216, 2018.

[38] Michael A Nielsen and Isaac Chuang. Quantum computation and quantum information, 2002.

[39] Richard P Feynman. Simulating physics with computers. *Int. J. Theor. Phys*, 21(6/7), 1982.

[40] Juha J Vartiainen, Mikko Möttönen, and Martti M Salomaa. Efficient decomposition of quantum gates. *Physical review letters*, 92(17):177902, 2004.

[41] Alexander Slepoy. Quantum gate decomposition algorithms. Technical report, Sandia National Laboratories, 2006.

[42] Chi-Kwong Li, Rebecca Roberts, and Xiaoyan Yin. Decomposition of unitary matrices and quantum gates. *International Journal of Quantum Information*, 11(01):1350015, 2013.

[43] Robert Raussendorf and Hans J Briegel. A one-way quantum computer. *Physical Review Letters*, 86(22):5188, 2001.

[44] Philip Walther, Kevin J Resch, Terry Rudolph, Emmanuel Schenck, Harald Weinfurter, Vlatko Vedral, Markus Aspelmeyer, and Anton Zeilinger. Experimental one-way quantum computing. *Nature*, 434(7030):169–176, 2005.

[45] DE Browne and HJ Briegel. One-way quantum computation–a tutorial introduction 2006. *arXiv preprint quant-ph/0603226*, 2006.

[46] Noriaki Horiuchi. One-way quantum computer. *Nature Photonics*, 9(1):7–7, 2015.

[47] Mikkel V Larsen, Xueshi Guo, Casper R Breum, Jonas S Neergaard-Nielsen, and Ulrik L Andersen. Deterministic generation of a two-dimensional cluster state. *Science*, 366(6463):369–372, 2019.

[48] Warit Asavanant, Yu Shiozawa, Shota Yokoyama, Baramee Charoensombutamon, Hiroki Emura, Rafael N Alexander, Shuntaro Takeda, Jun-ichi Yoshikawa, Nicolas C Menicucci, Hidehiro Yonezawa, et al. Generation of time-domain-multiplexed two-dimensional cluster state. *Science*, 366(6463):373–376, 2019.

[49] Mercedes Gimeno-Segovia, Terry Rudolph, and Sophia E Economou. Deterministic generation of large-scale entangled photonic cluster state from interacting solid state emitters. *Physical review letters*, 123(7):070501, 2019.

[50] Ido Schwartz, Dan Cogan, Emma R Schmidgall, Yaroslav Don, Liron Gantz, Oded Kenneth, Netanel H Lindner, and David Gershoni. Deterministic generation of a cluster state of entangled photons. *Science*, 354(6311):434–437, 2016.

[51] Mohan Sarovar, Akihito Ishizaki, Graham R Fleming, and K Birgitta Whaley. Quantum entanglement in photosynthetic light-harvesting complexes. *Nature Physics*, 6(6):462–467, 2010.

[52] Leonardo Banchi, Mark Fingerhuth, Tomas Babej, Christopher Ing, and Juan Miguel Arrazola. Molecular docking with gaussian boson sampling. *Science advances*, 6(23):eaax1950, 2020.

[53] Morten Kjaergaard, Mollie E Schwartz, Jochen Braumüller, Philip Krantz, Joel I-J Wang, Simon Gustavsson, and William D Oliver. Superconducting qubits: Current state of play. *Annual Review of Condensed Matter Physics*, 11:369–395, 2020.

[54] Iulia Georgescu. Trapped ion quantum computing turns 25. *Nature Reviews Physics*, 2(6):278–278, 2020.

[55] Steven Prawer and Andrew D Greentree. Diamond for quantum computing. *Science*, 320(5883):1601–1602, 2008.

[56] Pieter Kok, William J Munro, Kae Nemoto, Timothy C Ralph, Jonathan P Dowling, and Gerard J Milburn. Linear optical quantum computing with photonic qubits. *Reviews of modern physics*, 79(1):135, 2007.

[57] Jeremy L O'brien, Akira Furusawa, and Jelena Vučković. Photonic quantum technologies. *Nature Photonics*, 3(12):687–695, 2009.

[58] Tim C Ralph and Geoff J Pryde. Optical quantum computation. *Progress in optics*, 54:209–269, 2010.

[59] Thaddeus D Ladd, Fedor Jelezko, Raymond Laflamme, Yasunobu Nakamura, Christopher Monroe, and Jeremy Lloyd O'Brien. Quantum computers. *Nature*, 464(7285):45–53, 2010.

[60] Sergei Slussarenko and Geoff J Pryde. Photonic quantum information processing: A concise review. *Applied Physics Reviews*, 6(4):041303, 2019.

[61] Lan-Tian Feng, Guang-Can Guo, and Xi-Feng Ren. Progress on integrated quantum photonic sources with silicon. *Advanced Quantum Technologies*, 3(2):1900058, 2020.

[62] SL Braunstein and S Lloyd. Quantum computation over continuous variables. *Phys. Rev. Lett.*, 82:1789, 1999.

[63] Samuel L Braunstein and Peter Van Loock. Quantum information with continuous variables. *Reviews of modern physics*, 77(2):513, 2005.

[64] Nicolas C Menicucci, Peter Van Loock, Mile Gu, Christian Weedbrook, Timothy C Ralph, and Michael A Nielsen. Universal quantum computation with continuous-variable cluster states. *Physical review letters*, 97(11):110501, 2006.

[65] Francesco Lenzini, Jiri Janousek, Oliver Thearle, Matteo Villa, Ben Haylock, Sachin Kasture, Liang Cui, Hoang-Phuong Phan, Dzung Viet Dao, Hidehiro Yonezawa, et al. Integrated photonic platform for quantum information with continuous variables. *Science advances*, 4(12):eaat9331, 2018.

[66] Stefan F Preble, Michael L Fanto, Jeffrey A Steidle, Christopher C Tison, Gregory A Howland, Zihao Wang, and Paul M Alsing. On-chip quantum interference from a single silicon ring-resonator source. *Physical Review Applied*, 4(2):021001, 2015.

[67] Stefano Paesani, Massimo Borghi, Stefano Signorini, Alexandre Maïnos, Lorenzo Pavesi, and Anthony Laing. Near-ideal spontaneous photon sources in silicon quantum photonics. *Nature communications*, 11(1):1–6, 2020.

[68] Joshua W Silverstone, Raffaele Santagati, Damien Bonneau, Michael J Strain, Marc Sorel, Jeremy L O'Brien, and Mark G Thompson. Qubit entanglement between ring-resonator photon-pair sources on a silicon chip. *Nature communications*, 6(1):1–7, 2015.

[69] Yin-Hai Li, Zhi-Yuan Zhou, Lan-Tian Feng, Wen-Tan Fang, Shi-long Liu, Shi-Kai Liu, Kai Wang, Xi-Feng Ren, Dong-Sheng Ding, Li-Xin Xu, et al. On-chip multiplexed multiple entanglement sources in a single silicon nanowire. *Physical Review Applied*, 7(6):064005, 2017.

[70] Daniel Llewellyn, Yunhong Ding, Imad I Faruque, Stefano Paesani, Davide Bacco, Raffaele Santagati, Yan-Jun Qian, Yan Li, Yun-Feng Xiao, Marcus Huber, et al. Chip-to-chip quantum teleportation and multi-photon entanglement in silicon. *Nature Physics*, 16(2):148–153, 2020.

[71] Alto Osada, Yasutomo Ota, Ryota Katsumi, Masahiro Kakuda, Satoshi Iwamoto, and Yasuhiko Arakawa. Strongly coupled single-quantum-dot–cavity system integrated on a cmos-processed silicon photonic chip. *Physical Review Applied*, 11(2):024071, 2019.

[72] Ryota Katsumi, Yasutomo Ota, Alto Osada, Takuto Yamaguchi, Takeyoshi Tajiri, Masahiro Kakuda, Satoshi Iwamoto, Hidefumi Akiyama, and Yasuhiko Arakawa. Quantum-dot single-photon source on a cmos silicon photonic chip integrated using transfer printing. *APL Photonics*, 4(3):036105, 2019.

[73] Michael Reck, Anton Zeilinger, Herbert J Bernstein, and Philip Bertani. Experimental realization of any discrete unitary operator. *Physical review letters*, 73(1):58, 1994.

[74] Roel Burgwal, William R Clements, Devin H Smith, James C Gates, W Steven Kolthammer, Jelmer J Renema, and Ian A Walmsley. Using an imperfect photonic network to implement random unitaries. *Optics Express*, 25(23):28236–28245, 2017.

[75] William R Clements, Peter C Humphreys, Benjamin J Metcalf, W Steven Kolthammer, and Ian A Walmsley. Optimal design for universal multiport interferometers. *Optica*, 3(12):1460–1465, 2016.

[76] Caterina Taballione, Tom AW Wolterink, Jasleen Lugani, Andreas Eckstein, Bryn A Bell, Robert Grootjans, Ilka Visscher, Dimitri Geskus, Chris GH Roeloffzen, Jelmer J Renema, et al. $8\times$ 8 reconfigurable quantum photonic processor based on silicon nitride waveguides. *Optics express*, 27(19):26842–26857, 2019.

[77] Faraz Najafi, Jacob Mower, Nicholas C Harris, Francesco Bellei, Andrew Dane, Catherine Lee, Xiaolong Hu, Prashanta Kharel, Francesco Marsili, Solomon Assefa, et al. On-chip detection of non-classical light by scalable integration of single-photon detectors. *Nature communications*, 6(1):1–8, 2015.

[78] C Schuck, WHP Pernice, and HX Tang. Nbtin superconducting nanowire detectors for visible and telecom wavelengths single photon counting on si3n4 photonic circuits. *Applied Physics Letters*, 102(5):051101, 2013.

[79] Paul G Kwiat, Klaus Mattle, Harald Weinfurter, Anton Zeilinger, Alexander V Sergienko, and Yanhua Shih. New high-intensity source of polarization-entangled photon pairs. *Physical Review Letters*, 75(24):4337, 1995.

[80] Mario Krenn, Xuemei Gu, and Anton Zeilinger. Quantum experiments and graphs: Multiparty states as coherent superpositions of perfect matchings. *Physical review letters*, 119(24):240403, 2017.

[81] Xi-Lin Wang, Luo-Kan Chen, Wei Li, H-L Huang, Chang Liu, Chao Chen, Y-H Luo, Z-E Su, Dian Wu, Z-D Li, et al. Experimental ten-photon entanglement. *Physical review letters*, 117(21):210502, 2016.

[82] Xi-Lin Wang, Yi-Han Luo, He-Liang Huang, Ming-Cheng Chen, Zu-En Su, Chang Liu, Chao Chen, Wei Li, Yu-Qiang Fang, Xiao Jiang, et al. 18-qubit entanglement with six photons' three degrees of freedom. *Physical review letters*, 120(26):260502, 2018.

[83] Amin Babazadeh, Manuel Erhard, Feiran Wang, Mehul Malik, Rahman Nouroozi, Mario Krenn, and Anton Zeilinger. High-dimensional single-photon quantum gates: concepts and experiments. *Physical review letters*, 119(18):180510, 2017.

[84] Chao Zhang, Yun-Feng Huang, Zhao Wang, Bi-Heng Liu, Chuan-Feng Li, and Guang-Can Guo. Experimental greenberger-horne-zeilinger-type six-photon quantum nonlocality. *Physical review letters*, 115(26):260402, 2015.

[85] Hao Zhang, Chao Zhang, Xiao-Min Hu, Bi-Heng Liu, Yun-Feng Huang, Chuan-Feng Li, and Guang-Can Guo. Arbitrary two-particle high-dimensional bell-state measurement by auxiliary entanglement. *Physical Review A*, 99(5):052301, 2019.

[86] Ming Zhang, Lan-Tian Feng, Zhi-Yuan Zhou, Yang Chen, Hao Wu, Ming Li, Shi-Ming Gao, Guo-Ping Guo, Guang-Can Guo, Dao-Xin Dai, et al. Generation

of multiphoton quantum states on silicon. *Light: Science & Applications*, 8(1):1–7, 2019.

[87] Liangliang Lu, Lijun Xia, Zhiyu Chen, Leizhen Chen, Tonghua Yu, Tao Tao, Wenchao Ma, Ying Pan, Xinlun Cai, Yanqing Lu, et al. Three-dimensional entanglement on a silicon chip. *npj Quantum Information*, 6(1):1–9, 2020.

[88] Levon Chakhmakhchyan and Nicolas J Cerf. Simulating arbitrary gaussian circuits with linear optics. *Physical Review A*, 98(6):062314, 2018.

[89] Jeremy C Adcock, Caterina Vigliar, Raffaele Santagati, Joshua W Silverstone, and Mark G Thompson. Programmable four-photon graph states on a silicon chip. *Nature communications*, 10(1):1–6, 2019.

[90] Justin B Spring, Benjamin J Metcalf, Peter C Humphreys, W Steven Kolthammer, Xian-Min Jin, Marco Barbieri, Animesh Datta, Nicholas Thomas-Peter, Nathan K Langford, Dmytro Kundys, et al. Boson sampling on a photonic chip. *Science*, 339(6121):798–801, 2013.

[91] Matthew A Broome, Alessandro Fedrizzi, Saleh Rahimi-Keshari, Justin Dove, Scott Aaronson, Timothy C Ralph, and Andrew G White. Photonic boson sampling in a tunable circuit. *Science*, 339(6121):794–798, 2013.

[92] Stefano Paesani, Yunhong Ding, Raffaele Santagati, Levon Chakhmakhchyan, Caterina Vigliar, Karsten Rottwitt, Leif K Oxenløwe, Jianwei Wang, Mark G Thompson, and Anthony Laing. Generation and sampling of quantum states of light in a silicon chip. *Nature Physics*, 15(9):925–929, 2019.

[93] Leonardo Banchi, Nicolás Quesada, and Juan Miguel Arrazola. Training gaussian boson sampling distributions. *Phys. Rev. A*, 102:012417, Jul 2020.

[94] Stefano Paesani, Andreas A Gentile, Raffaele Santagati, Jianwei Wang, Nathan Wiebe, David P Tew, Jeremy L O'Brien, and Mark G Thompson. Experimental bayesian quantum phase estimation on a silicon photonic chip. *Physical review letters*, 118(10):100503, 2017.

[95] Gregory R Steinbrecher, Jonathan P Olson, Dirk Englund, and Jacques Carolan. Quantum optical neural networks. *npj Quantum Information*, 5(1):1–9, 2019.

[96] Lin Cao, W Luo, YX Wang, J Zou, RD Yan, H Cai, Yichen Zhang, XL Hu, C Jiang, WJ Fan, et al. Chip-based measurement-device-independent quantum key distribution using integrated silicon photonic systems. *Physical Review Applied*, 14(1):011001, 2020.

[97] Henry Semenenko, Philip Sibson, Andy Hart, Mark G Thompson, John G Rarity, and Chris Erven. Chip-based measurement-device-independent quantum key distribution. *Optica*, 7(3):238–242, 2020.

[98] Gong Zhang, Jing Yan Haw, Hong Cai, Feng Xu, SM Assad, Joseph F Fitzsimons, Xianzhong Zhou, Y Zhang, S Yu, J Wu, et al. An integrated silicon photonic chip platform for continuous-variable quantum key distribution. *Nature Photonics*, 13(12):839–842, 2019.

[99] Armando Perez-Leija, Robert Keil, Alastair Kay, Hector Moya-Cessa, Stefan Nolte, Leong-Chuan Kwek, Blas M Rodríguez-Lara, Alexander Szameit, and Demetrios N Christodoulides. Coherent quantum transport in photonic lattices. *Physical Review A*, 87(1):012309, 2013.

[100] Filippo Caruso, Andrea Crespi, Anna Gabriella Ciriolo, Fabio Sciarrino, and Roberto Osellame. Fast escape of a quantum walker from an integrated photonic maze. *Nature communications*, 7(1):1–7, 2016.

[101] Yao Wang, Zi-Wei Cui, Yong-Heng Lu, Xiao-Ming Zhang, Jun Gao, Yi-Jun Chang, Man-Hong Yung, and Xian-Min Jin. Integrated quantum-walk structure and nand tree on a photonic chip. *Physical Review Letters*, 125(16):160502, 2020.

[102] Xiaogang Qiang, Xiaoqi Zhou, Jianwei Wang, Callum M Wilkes, Thomas Loke, Sean O'Gara, Laurent Kling, Graham D Marshall, Raffaele Santagati, Timothy C Ralph, et al. Large-scale silicon quantum photonics implementing arbitrary two-qubit processing. *Nature photonics*, 12(9):534–539, 2018.

[103] Terry Rudolph. Why i am optimistic about the silicon-photonic route to quantum computing. *APL Photonics*, 2(3):030901, 2017.

[104] Anthony Laing, Alberto Peruzzo, Alberto Politi, Maria Rodas Verde, Matthaeus Halder, Timothy C Ralph, Mark G Thompson, and Jeremy L O'Brien. High-fidelity operation of quantum photonic circuits. *Applied Physics Letters*, 97(21):211109, 2010.

[105] Brian J Smith, Dmytro Kundys, Nicholas Thomas-Peter, PGR Smith, and IA Walmsley. Phase-controlled integrated photonic quantum circuits. *Optics Express*, 17(16):13516–13525, 2009.

[106] Giacomo Corrielli, Andrea Crespi, Riccardo Geremia, Roberta Ramponi, Linda Sansoni, Andrea Santinelli, Paolo Mataloni, Fabio Sciarrino, and Roberto Osel-

lame. Rotated waveplates in integrated waveguide optics. *Nature communications*, 5(1):1–6, 2014.

[107] Linda Sansoni, Fabio Sciarrino, Giuseppe Vallone, Paolo Mataloni, Andrea Crespi, Roberta Ramponi, and Roberto Osellame. Polarization entangled state measurement on a chip. *Physical review letters*, 105(20):200503, 2010.

[108] Andrea Crespi, Roberta Ramponi, Roberto Osellame, Linda Sansoni, Irene Bongioanni, Fabio Sciarrino, Giuseppe Vallone, and Paolo Mataloni. Integrated photonic quantum gates for polarization qubits. *Nature communications*, 2(1):1–6, 2011.

[109] Xiyuan Lu, Qing Li, Daron A Westly, Gregory Moille, Anshuman Singh, Vikas Anant, and Kartik Srinivasan. Chip-integrated visible–telecom entangled photon pair source for quantum communication. *Nature physics*, 15(4):373–381, 2019.

[110] Xiang Zhang, Bryn A Bell, Andri Mahendra, Chunle Xiong, Philip HW Leong, and Benjamin J Eggleton. Integrated silicon nitride time-bin entanglement circuits. *Optics letters*, 43(15):3469–3472, 2018.

[111] Avik Dutt, Kevin Luke, Sasikanth Manipatruni, Alexander L Gaeta, Paulo Nussenzveig, and Michal Lipson. On-chip optical squeezing. *Physical Review Applied*, 3(4):044005, 2015.

[112] Caterina Taballione, Reinier van der Meer, Henk J Snijders, Peter Hooijschuur, Jörn P Epping, Michiel de Goede, Ben Kassenberg, Pim Venderbosch, Chris Toebes, Hans van den Vlekkert, et al. A 12-mode universal photonic processor for quantum information processing. *arXiv preprint arXiv:2012.05673*, 2020.

[113] S Tanzilli, Wolfgang Tittel, Hugues De Riedmatten, Hugo Zbinden, Paolo Baldi, M DeMicheli, Da B Ostrowsky, and Nicolas Gisin. Ppln waveguide for quantum communication. *The European Physical Journal D-Atomic, Molecular, Optical and Plasma Physics*, 18(2):155–160, 2002.

[114] H Jin, FM Liu, P Xu, JL Xia, ML Zhong, Y Yuan, JW Zhou, YX Gong, W Wang, and SN Zhu. On-chip generation and manipulation of entangled photons based on reconfigurable lithium-niobate waveguide circuits. *Physical review letters*, 113(10):103601, 2014.

[115] Jan Philipp Höpker, Moritz Bartnick, Evan Meyer-Scott, Frederik Thiele, Stephan Krapick, Nicola Montaut, Matteo Santandrea, Harald Herrmann, Sebastian Lengeling, Raimund Ricken, et al. Towards integrated superconducting detectors on lithium niobate waveguides. In *Quantum Photonic Devices*, volume 10358, page 1035809. International Society for Optics and Photonics, 2017.

[116] Ruo-Jing Ren, Jun Gao, Wen-Hao Zhou, Zhi-Qiang Jiao, Lu-Feng Qiao, Xiao-Wei Wang, and Xian-Min Jin. 128 identical quantum sources integrated on a single silica chip. *arXiv preprint arXiv:2005.12918*, 2020.

[117] R Adar, MR Serbin, and Victor Mizrahi. Less than 1 db per meter propagation loss of silica waveguides measured using a ring resonator. *Journal of lightwave technology*, 12(8):1369–1372, 1994.

[118] Hiroshi Takahashi. High performance planar lightwave circuit devices for large capacity transmission. *Optics express*, 19(26):B173–B180, 2011.

[119] Minh A Tran, Duanni Huang, Tin Komljenovic, Jonathan Peters, Aditya Malik, and John E Bowers. Ultra-low-loss silicon waveguides for heterogeneously integrated silicon/iii-v photonics. *Applied Sciences*, 8(7):1139, 2018.

[120] Alberto Politi, Martin J Cryan, John G Rarity, Siyuan Yu, and Jeremy L O'brien. Silica-on-silicon waveguide quantum circuits. *Science*, 320(5876):646–649, 2008.

[121] Alberto Politi, Jonathan CF Matthews, and Jeremy L O'brien. Shor's quantum factoring algorithm on a photonic chip. *Science*, 325(5945):1221–1221, 2009.

[122] Alberto Peruzzo, Mirko Lobino, Jonathan CF Matthews, Nobuyuki Matsuda, Alberto Politi, Konstantinos Poulios, Xiao-Qi Zhou, Yoav Lahini, Nur Ismail, Kerstin Wörhoff, et al. Quantum walks of correlated photons. *Science*, 329(5998):1500–1503, 2010.

[123] Peter J Shadbolt, Maria R Verde, Alberto Peruzzo, Alberto Politi, Anthony Laing, Mirko Lobino, Jonathan CF Matthews, Mark G Thompson, and Jeremy L O'Brien. Generating, manipulating and measuring entanglement and mixture with a reconfigurable photonic circuit. *Nature Photonics*, 6(1):45–49, 2012.

[124] Thomas Gerrits, Nicholas Thomas-Peter, James C Gates, Adriana E Lita, Benjamin J Metcalf, Brice Calkins, Nathan A Tomlin, Anna E Fox, Antía Lamas Linares, Justin B Spring, et al. On-chip, photon-number-resolving, telecommunication-band detectors for scalable photonic information processing. *Physical Review A*, 84(6):060301, 2011.

[125] Damien Bonneau, Erman Engin, Kazuya Ohira, Nob Suzuki, Haruhiko Yoshida, Norio Iizuka, Mizunori Ezaki, Chandra M Natarajan, Michael G Tanner,

Robert H Hadfield, et al. Quantum interference and manipulation of entanglement in silicon wire waveguide quantum circuits. *New Journal of Physics*, 14(4):045003, 2012.

[126] Andrea Crespi, Roberto Osellame, Roberta Ramponi, Daniel J Brod, Ernesto F Galvao, Nicolo Spagnolo, Chiara Vitelli, Enrico Maiorino, Paolo Mataloni, and Fabio Sciarrino. Integrated multimode interferometers with arbitrary designs for photonic boson sampling. *Nature photonics*, 7(7):545–549, 2013.

[127] Linda Sansoni, Fabio Sciarrino, Giuseppe Vallone, Paolo Mataloni, Andrea Crespi, Roberta Ramponi, and Roberto Osellame. Two-particle bosonic-fermionic quantum walk via integrated photonics. *Physical review letters*, 108(1):010502, 2012.

[128] Yu-Ming He, Yu He, Yu-Jia Wei, Dian Wu, Mete Atatüre, Christian Schneider, Sven Höfling, Martin Kamp, Chao-Yang Lu, and Jian-Wei Pan. On-demand semiconductor single-photon source with near-unity indistinguishability. *Nature nanotechnology*, 8(3):213–217, 2013.

[129] Alberto Peruzzo, Jarrod McClean, Peter Shadbolt, Man-Hong Yung, Xiao-Qi Zhou, Peter J Love, Alán Aspuru-Guzik, and Jeremy L O'brien. A variational eigenvalue solver on a photonic quantum processor. *Nature communications*, 5(1):1–7, 2014.

[130] Jianwei Wang, Damien Bonneau, Matteo Villa, Joshua W Silverstone, Raffaele Santagati, Shigehito Miki, Taro Yamashita, Mikio Fujiwara, Masahide Sasaki, Hirotaka Terai, et al. Chip-to-chip quantum photonic interconnect by path-polarization interconversion. *Optica*, 3(4):407–413, 2016.

[131] Philip Sibson, Chris Erven, Mark Godfrey, Shigehito Miki, Taro Yamashita, Mikio Fujiwara, Masahide Sasaki, Hirotaka Terai, Michael G Tanner, Chandra M Natarajan, et al. Chip-based quantum key distribution. *Nature communications*, 8(1):1–6, 2017.

[132] Justin B Spring, Paolo L Mennea, Benjamin J Metcalf, Peter C Humphreys, James C Gates, Helen L Rogers, Christoph Söller, Brian J Smith, W Steven Kolthammer, Peter GR Smith, et al. Chip-based array of near-identical, pure, heralded single-photon sources. *Optica*, 4(1):90–96, 2017.

[133] Marco Bentivegna, Nicolò Spagnolo, Chiara Vitelli, Fulvio Flamini, Niko Viggianiello, Ludovico Latmiral, Paolo Mataloni, Daniel J Brod, Ernesto F Galvão, Andrea Crespi, et al. Experimental scattershot boson sampling. *Science advances*, 1(3):e1400255, 2015.

[134] Mario Arnolfo Ciampini, Adeline Orieux, Stefano Paesani, Fabio Sciarrino, Giacomo Corrielli, Andrea Crespi, Roberta Ramponi, Roberto Osellame, and Paolo Mataloni. Path-polarization hyperentangled and cluster states of photons on a chip. *Light: Science & Applications*, 5(4):e16064–e16064, 2016.

[135] Hui Wang, Yu He, Yu-Huai Li, Zu-En Su, Bo Li, He-Liang Huang, Xing Ding, Ming-Cheng Chen, Chang Liu, Jian Qin, et al. High-efficiency multiphoton boson sampling. *Nature Photonics*, 11(6):361–365, 2017.

[136] Jianwei Wang, Stefano Paesani, Raffaele Santagati, Sebastian Knauer, Antonio A Gentile, Nathan Wiebe, Maurangelo Petruzzella, Jeremy L O'Brien, John G Rarity, Anthony Laing, et al. Experimental quantum hamiltonian learning. *Nature Physics*, 13(6):551–555, 2017.

[137] Alberto Politi, Jonathan CF Matthews, Mark G Thompson, and Jeremy L O'Brien. Integrated quantum photonics. *IEEE Journal of Selected Topics in Quantum Electronics*, 15(6):1673–1684, 2009.

[138] Jonathan CF Matthews, Alberto Politi, André Stefanov, and Jeremy L O'brien. Manipulation of multiphoton entanglement in waveguide quantum circuits. *Nature Photonics*, 3(6):346–350, 2009.

[139] Kishor Bharti, Alba Cervera-Lierta, Thi Ha Kyaw, Tobias Haug, Sumner Alperin-Lea, Abhinav Anand, Matthias Degroote, Hermanni Heimonen, Jakob S Kottmann, Tim Menke, et al. Noisy intermediate-scale quantum (nisq) algorithms. *arXiv preprint arXiv:2101.08448*, 2021.

[140] Xiaoping Liu, Bart Kuyken, Gunther Roelkens, Roel Baets, Richard M Osgood Jr, and William MJ Green. Bridging the mid-infrared-to-telecom gap with silicon nanophotonic spectral translation. *Nature Photonics*, 6(10):667, 2012.

[141] P Xu and SN Zhu. Quasi-phase-matching engineering of entangled photons. *AIP Advances*, 2(4):053807, 2012.

[142] S Signorini and L Pavesi. On-chip heralded single photon sources. *AVS Quantum Science*, 2(4):041701, 2020.

[143] Frank Arute, Kunal Arya, Ryan Babbush, Dave Bacon, Joseph C Bardin, Rami Barends, Rupak Biswas, Sergio Boixo, Fernando GSL Brandao, David A Buell, et al. Quantum supremacy using a programmable superconducting processor. *Nature*, 574(7779):505–510, 2019.

[144] Frank Arute, Kunal Arya, Ryan Babbush, Dave Bacon, Joseph C Bardin, Rami Barends, Sergio Boixo, Michael Broughton, Bob B Buckley, David A Buell, et al. Hartree-fock on a superconducting qubit quantum computer. *arXiv preprint arXiv:2004.04174*, 2020.

[145] Stefan Scheel. Permanents in linear optical networks. *arXiv preprint quant-ph/0406127*, 2004.

[146] Scott Aaronson and Alex Arkhipov. The computational complexity of linear optics. In *Proceedings of the forty-third annual ACM symposium on Theory of computing*, pages 333–342, 2011.

[147] Mark R Jerrum, Leslie G Valiant, and Vijay V Vazirani. Random generation of combinatorial structures from a uniform distribution. *Theoretical computer science*, 43:169–188, 1986.

[148] Leslie G Valiant. The complexity of computing the permanent. *Theoretical computer science*, 8(2):189–201, 1979.

[149] Junjie Wu, Yong Liu, Baida Zhang, Xianmin Jin, Yang Wang, Huiquan Wang, and Xuejun Yang. A benchmark test of boson sampling on tianhe-2 supercomputer. *National Science Review*, 5(5):715–720, 2018.

[150] Yuxuan Li, Mingcheng Chen, Yaojian Chen, Haitian Lu, Lin Gan, Chaoyang Lu, Jianwei Pan, Haohuan Fu, and Guangwen Yang. Benchmarking 50-photon gaussian boson sampling on the sunway taihulight. *arXiv preprint arXiv:2009.01177*, 2020.

[151] Max Tillmann, Borivoje Dakić, René Heilmann, Stefan Nolte, Alexander Szameit, and Philip Walther. Experimental boson sampling. *Nature photonics*, 7(7):540–544, 2013.

[152] Jacques Carolan, Jasmin DA Meinecke, Peter J Shadbolt, Nicholas J Russell, Nur Ismail, Kerstin Wörhoff, Terry Rudolph, Mark G Thompson, Jeremy L O'brien, Jonathan CF Matthews, et al. On the experimental verification of quantum complexity in linear optics. *Nature Photonics*, 8(8):621–626, 2014.

[153] JM Arrazola, V Bergholm, K Brádler, TR Bromley, MJ Collins, I Dhand, A Fumagalli, T Gerrits, A Goussev, LG Helt, et al. Quantum circuits with many photons on a programmable nanophotonic chip. *Nature*, 591(7848):54–60, 2021.

[154] Han-Sen Zhong, Hui Wang, Yu-Hao Deng, Ming-Cheng Chen, Li-Chao Peng, Yi-Han Luo, Jian Qin, Dian Wu, Xing Ding, Yi Hu, et al. Quantum computational advantage using photons. *Science*, 370(6523):1460–1463, 2020.

[155] Craig S Hamilton, Regina Kruse, Linda Sansoni, Sonja Barkhofen, Christine Silberhorn, and Igor Jex. Gaussian boson sampling. *Physical review letters*, 119(17):170501, 2017.

[156] Michael A Nielsen and Christopher M Dawson. Fault-tolerant quantum computation with cluster states. *Physical Review A*, 71(4):042323, 2005.

[157] David Poulin. Stabilizer formalism for operator quantum error correction. *Physical review letters*, 95(23):230504, 2005.

[158] Chao-Yang Lu, Wei-Bo Gao, Jin Zhang, Xiao-Qi Zhou, Tao Yang, and Jian-Wei Pan. Experimental quantum coding against qubit loss error. *Proceedings of the National Academy of Sciences*, 105(32):11050–11054, 2008.

[159] BA Bell, DA Herrera-Martí, MS Tame, Damian Markham, WJ Wadsworth, and JG Rarity. Experimental demonstration of a graph state quantum error-correction code. *Nature communications*, 5(1):1–10, 2014.

[160] Lars Steffen, Yves Salathe, Markus Oppliger, Philipp Kurpiers, Matthias Baur, Christian Lang, Christopher Eichler, Gabriel Puebla-Hellmann, Arkady Fedorov, and Andreas Wallraff. Deterministic quantum teleportation with feed-forward in a solid state system. *Nature*, 500(7462):319–322, 2013.

[161] Stephan Ritter, Christian Nölleke, Andreas Neuzner, Andreas Reiserer, Carolin Hahn, and Gerhard Rempe. Efficient teleportation between remote single-atom quantum memories. In *APS Division of Atomic, Molecular and Optical Physics Meeting Abstracts*, volume 2013, pages U6–001, 2013.

[162] S Olmschenk, DN Matsukevich, P Maunz, D Hayes, L-M Duan, and C Monroe. Quantum teleportation between distant matter qubits. *Science*, 323(5913):486–489, 2009.

[163] Wolfgang Pfaff, Bas J Hensen, Hannes Bernien, Suzanne B van Dam, Machiel S Blok, Tim H Taminiau, Marijn J Tiggelman, Raymond N Schouten, Matthew Markham, Daniel J Twitchen, et al. Unconditional quantum teleportation between distant solid-state quantum bits. *Science*, 345(6196):532–535, 2014.

[164] Akira Furusawa, Jens Lykke Sørensen, Samuel L Braunstein, Christopher A Fuchs, H Jeff Kimble, and Eugene S Polzik. Unconditional quantum teleportation. *science*, 282(5389):706–709, 1998.

[165] Noriyuki Lee, Hugo Benichi, Yuishi Takeno, Shuntaro Takeda, James Webb, Elanor Huntington, and Akira Furusawa. Teleportation of nonclassical wave packets of light. *Science*, 332(6027):330–333, 2011.

[166] Xiao-Song Ma, Thomas Herbst, Thomas Scheidl, Daqing Wang, Sebastian Kropatschek, William Naylor, Bernhard Wittmann, Alexandra Mech, Johannes Kofler, Elena Anisimova, et al. Quantum teleportation over 143 kilometres using active feed-forward. *Nature*, 489(7415):269–273, 2012.

[167] Rupert Ursin, Thomas Jennewein, Markus Aspelmeyer, Rainer Kaltenbaek, Michael Lindenthal, Philip Walther, and Anton Zeilinger. Quantum teleportation across the danube. *Nature*, 430(7002):849–849, 2004.

[168] Ji-Gang Ren, Ping Xu, Hai-Lin Yong, Liang Zhang, Sheng-Kai Liao, Juan Yin, Wei-Yue Liu, Wen-Qi Cai, Meng Yang, Li Li, et al. Ground-to-satellite quantum teleportation. *Nature*, 549(7670):70–73, 2017.

[169] Dan Song, Chen He, Zhengwen Cao, and Geng Chai. Quantum teleportation of multiple qubits based on quantum fourier transform. *IEEE Communications Letters*, 22(12):2427–2430, 2018.

[170] Yi-Han Luo, Han-Sen Zhong, Manuel Erhard, Xi-Lin Wang, Li-Chao Peng, Mario Krenn, Xiao Jiang, Li Li, Nai-Le Liu, Chao-Yang Lu, et al. Quantum teleportation in high dimensions. *Physical review letters*, 123(7):070505, 2019.

[171] Xiao-Min Hu, Chao Zhang, Bi-Heng Liu, Yu Cai, Xiang-Jun Ye, Yu Guo, Wen-Bo Xing, Cen-Xiao Huang, Yun-Feng Huang, Chuan-Feng Li, et al. Experimental high-dimensional quantum teleportation. *Physical Review Letters*, 125(23):230501, 2020.

[172] Jonathan Romero, Jonathan P Olson, and Alan Aspuru-Guzik. Quantum autoencoders for efficient compression of quantum data. *Quantum Science and Technology*, 2(4):045001, 2017.

[173] Lucas Lamata, Unai Alvarez-Rodriguez, José David Martín-Guerrero, Mikel Sanz, and Enrique Solano. Quantum autoencoders via quantum adders with genetic algorithms. *Quantum Science and Technology*, 4(1):014007, 2018.

[174] Yongcheng Ding, Lucas Lamata, Mikel Sanz, Xi Chen, and Enrique Solano. Experimental implementation of a quantum autoencoder via quantum adders. *Advanced Quantum Technologies*, 2(7-8):1800065, 2019.

[175] Alex Pepper, Nora Tischler, and Geoff J Pryde. Experimental realization of a quantum autoencoder: The compression of qutrits via machine learning. *Physical review letters*, 122(6):060501, 2019.

[176] Dmytro Bondarenko and Polina Feldmann. Quantum autoencoders to denoise quantum data. *Physical review letters*, 124(13):130502, 2020.

[177] RT Thew, Kae Nemoto, Andrew G White, and William J Munro. Qudit quantum-state tomography. *Physical Review A*, 66(1):012303, 2002.

[178] Brian Hall. *Lie groups, Lie algebras, and representations: an elementary introduction*, volume 222. Springer, 2015.

[179] Francesco Iachello. *Lie algebras and applications*, volume 12. Springer, 2006.

[180] Murray Gell-Mann. Symmetries of baryons and mesons. In *Murray Gell-Mann: Selected Papers*, pages 128–145. World Scientific, 2010.